TECHNISCHE UNIVERSITÄT MÜNCHEN

Lehrstuhl für Numerische Mechanik

Weak Imposition of the General Navier Condition for Cut Finite Elements with Application to Wetting Processes

Magnus Erik Winter

Vollständiger Abdruck der von der Fakultät für Maschinenwesen der Technischen Universität München zur Erlangung des akademischen Grades eines

Doktor-Ingenieurs (Dr.-Ing.)

genehmigten Dissertation.

Vorsitzender:	Prof. Dr.-Ing. Oskar Haidn
Prüfer der Dissertation:	
	1. Prof. Dr.-Ing. Wolfgang A. Wall
	2. Assoc. Prof. André Massing, Ph.D.

Die Dissertation wurde am 12.09.2019 bei der Technischen Universität München eingereicht und durch die Fakultät für Maschinenwesen am 12.08.2020 angenommen.

ACKNOWLEDGMENTS

First, I would like to thank my supervisors Prof. Dr.-Ing. Wolfgang A. Wall and Prof. Dr. Antonio Huerta for giving me the opportunity to participate in the Erasmus Mundus Joint Doctorate "Simulation in Engineering and Entrepreneurship Development" (SEED) program. I remember the time spent at your institutes in Munich and Barcelona fondly. I also want to thank Prof. Dr.-Ing. Oskar Haidn for chairing the examination committee and Assoc. Prof. André Massing for agreeing to be my second examiner.

I want to give a special thanks to my common friends of Nitsche: Benedikt Schott, Christoph Ager and Alexander Seitz. I feel extremely blessed to have worked with such a talented group of people; the discussions with you directly impacted the quality of my work for the better. Furthermore, I want to extend my warmest thanks to Ursula Rasthofer for patiently explaining the internal workings of BACI and the fluid code during my initial time at LNM. For being an inspiration in resilience and perseverance I want to thank my fellow SEED-student Dhrubajyoti Mukherjee; as you started the program a year ahead of me your advice on all things SEED related helped me out tremendously.

At LNM I not only had the pleasure to work with brilliant colleagues, but I am glad to say that I was lucky to work with colleagues whom I can call friends. A sincere thank you to Anna, Andy, Benjamin, Fabian, Karl, Georg, Julien, Julia, Jorge, Martin, Svenja and Sudhakar for the time spent together at – and outside – the institute.

During my stay at LaCàn in Barcelona I was lucky to be welcomed with open arms; a special thanks to Omid, Ceren, Daniel, Albert, Daobing, Boyi, Olga and Alice for making Barcelona feel like home away from home.

Last but not least, I want to thank the people outside of the research bubble: mamma, pappa, Fredrik and Nina for being there and supporting me through the difficult phases of my Ph.D..

München, October 2020 Magnus Winter

ABSTRACT

In the infancy of fluid dynamics, the views on whether a fluid did or did not slip along the tangential plane of a solid boundary diverged. From experimental observations, a consensus could be reached in the late 1800's that on a macroscopic scale the no-slip approximation of a fluid velocity at a boundary reproduced reality the best. Nonetheless, there are some exceptions where a flow may exhibit slip on a macroscopic scale at the boundary. These include, flows over hydrophobic surfaces, geophysical flows, flow over porous media, contact between immersed bodies and wetting processes. To model this tangential slip, a non-standard boundary condition such as the general Navier boundary condition (GNBC) can be employed.

The GNBC consists of a wall-normal Dirichlet condition and a wall-tangential Robin condition. The latter permits the fluid to slip in the wall-tangential direction, where the slip velocity is proportional to the wall-shear stress and the slip length. Contemporary methods impose the GNBC by means of a Galerkin substitution method. The drawback of this approach is the fact that it can not deal with both the Dirichlet and Neumann limits of the tangential Robin condition. This thesis presents a novel method, permitting both limits to be included by imposing this tangential condition through the Nitsche's method. The method remains well conditioned for an arbitrary choice of slip length, i.e. for any linear combination of the Dirichlet and Neumann contributions in the tangential Robin condition. As the GNBC appears in problems where domains may undergo large deformations or topological changes, typical for the already mentioned modeling of contact between immersed bodies, the choice was made to develop the method within an unfitted finite element method framework, here the cut finite element method (CutFEM). This is to provide future works employing the GNBC a solid foundation to rely on even if an unfitted approach is chosen. For this setup, it is shown that the the proposed formulation is inf-sup stable and has optimal order a priori error estimates for the linearized Navier–Stokes equations, i.e. the Oseen equation.

As a piecewise linear approximation of the physical domain is conducted in the CutFEM, geometrical approximation errors need to be considered for the proposed formulation. One well-known source of error in simulations with the GNBC is the so-called Babuška paradox. This paradox describes the reduced order of spatial convergence of the computed solution when using a normal of a piecewise linear boundary to impose the GNBC. An important contribution of this work is a proposed smoothing to create a continuous normal on the boundary, and as such regain optimal order of convergence. Another geometrical approximation error arises from the fact that the approximated and physical boundaries do not coincide. This begs the question, what boundary condition ought to be imposed on the approximated boundary? In particular, in the case when approximations with elements of higher order are employed, the error stemming from this discrepancy can start to dominate the convergence of the computed solution. A boundary value correction method is proposed in this thesis to resolve this issue, and its effectiveness is demonstrated with a numerical example.

It is a well established fact for wetting processes that at the intersection between two fluids and a solid, i.e. at the contact line, the classic no-slip condition is an unfeasible choice of boundary condition, as it leads to divergent shear stresses. A possible choice to solve this issue is to impose a slip type condition in the vicinity of the contact line, such as the GNBC. Given that the contact line can move over time, a method which can impose the continuous range from slip to no-slip is of practical use at these boundaries. In this thesis, the above mentioned novel imposition of the GNBC is used to derive a localized slip method for the moving contact line problem. As the two-phase flow necessitates modeling of discontinuities between the two phases, the CutFEM is used in this thesis for the simulations of wetting processes. The performance of this constellation is validated against both static and dynamic numerical examples.

In conclusion, this thesis has made strides in improving the usability of the general Navier boundary condition. It has given a rigorous mathematical analysis of a novel weak imposition of the GNBC, provided methods to counteract geometrical approximation errors and shown the applicability of the method within a wetting flow context. The results inspire hope that future theoretical works and physical simulations can build upon the foundations of this thesis.

ZUSAMMENFASSUNG

In den Anfängen der Fluiddynamik divergierten die Ansichten darüber, ob eine Flüssigkeit entlang der Tangentialebene einer festen Grenze gleitet oder nicht. Aus experimentellen Beobachtungen ergab sich im späten 19. Jahrhundert ein Konsens, dass auf einer makroskopischen Skala die Haft-Randbedingung an einem Rand der Realität am besten entspricht. Dennoch gibt es einige Ausnahmen, bei denen eine Strömung ein Gleiten auf makroskopischer Ebene an einem Rand aufweisen kann. Dazu gehören u.a. die Überströmung von hydrophoben Oberflächen, geophysikalische Strömung über poröse Medien, Kontakt zwischen eingetauchten Körpern und Benetzungsverfahren. Um dieses tangentiale Gleiten zu modellieren, wird eine von der Norm abweichende Randbedingung wie die allgemeine Navier-Randbedingung (GNBC) verwendet.

Die GNBC besteht aus einer wandnormalen Dirichlet-Bedingung und einer wandtangentialen Robin-Bedingung. Letztere lässt die Flüssigkeit in wandtangentiale Richtung gleiten, wobei die Gleitgeschwindigkeit proportional zur Wandschubspannung und der Gleitlänge ist. Zeitgenössische Methoden erzwingen die GNBC mittels einer Galerkin-Substitutionsmethode. Der Nachteil dieses Ansatzes ist die Tatsache, dass nicht mit der Dirichlet-Grenze der tangentialen Robin-Bedingung umgegangen werden kann. Diese Arbeit stellt eine neuartige Methode vor, die es erlaubt, beide Grenzen einzubeziehen, indem diese tangentiale Bedingung durch die Nitsche-Methode aufgebracht wird. Die Methode bleibt bei einer beliebigen Wahl der Gleitlänge, d.h. für jede beliebige lineare Kombination der Dirichlet- und Neumann-Beiträge in der tangentialen Robin-Bedingung gut konditioniert. Die GNBC tritt bei Problemen auf, bei denen Gebiete große Verformungen oder topologische Veränderungen aufweisen können, beispielsweise beim Kontakt eingetauchter Körpern. Aus diesem Grund wird die Methode innerhalb einer nicht-randkonformen Finite-Elemente-Methode, hier die Cut-Finite-Elemente-Methode (CutFEM), entwickelt. Das Ziel dabei ist es, für zukünftige Arbeiten mit GNCB eine verlässliche Grundlage zu schaffen, falls ein nicht-randkonformen Ansatz gewählt wird. Für dieses Setup wird gezeigt, dass die vorgeschlagene Formulierung inf-sup stabil ist und eine a priori Fehlerschätzung optimaler Ordnung für die linearisierten Navier–Stokes-Gleichungen, d.h die Oseen-Gleichung, hat.

Da in der CutFEM eine stückweise lineare Approximation des physikalischen Gebiets durchgeführt wird, müssen für die vorgeschlagene Formulierung geometrische Approximationsfehler berücksichtigt werden. Eine bekannte Fehlerquelle bei Simulationen mit der GNCB ist das sogenannte Babuška-Paradoxon. Dieses Paradoxon beschreibt die reduzierte Ordnung der räumlichen Konvergenz der berechneten Lösung bei der Verwendung der stückweise konstante Normale einer stückweisen linearen Oberfläche zur Aufbringung der GNBC. Ein wichtiger Beitrag dieser Arbeit ist der Vorschlag einer Glättung zur Erzeugung einer kontinuierlichen Normalen auf der Oberfläche, und dadurch die optimale Konvergenzordnung zurückzuerlangen. Ein weiterer geometrischer Approximationsfehler ergibt sich aus dem Nichtübereinstimmen der approximierten und physikalischen Ränder. Dies wirft die Frage auf, welche Randbedingung dem approximierten Rand aufgebracht werden soll. Insbesondere bei der Approximation mit

Elementen höherer Ordnung kann der aus der Diskrepanz resultierende Fehler die Konvergenz der berechneten Lösung dominieren. Um dieses Problem zu lösen wird in dieser Arbeit eine Randwertkorrekturmethode vorgeschlagen. Ihre Wirksamkeit wird anhand eines numerischen Beispiels demonstriert.

Für Benetzungsprozesse ist bekannt, dass an der Schnittstelle zwischen zwei Flüssigkeiten und einem Festkörper, d.h. an der Kontaktlinie, die klassische Haftbedingung eine nicht realisierbare Wahl der Randbedingung darstellt, da sie zu divergierenden Schubspannungen führt. Eine Möglichkeit dieses Problem zu lösen ist es, in der Nähe der Kontaktlinie eine Gleitzustandsbedingung aufzubringen, z.B. die GNBC. Da sich die Kontaktlinie im Laufe der Zeit bewegen kann, ist eine Methode, die den kontinuierlichen Bereich von Gleiten bis Haften aufbringen kann, an diesen Ränder von praktischem Nutzen. In dieser Arbeit wird die oben erwähnte neuartige Aufbringung der GNBC verwendet, um eine lokalisierte Gleitmethode für das Problem der beweglichen Kontaktlinie herzuleiten. Da die Zweiphasenströmung die Modellierung von Diskontinuitäten zwischen den beiden Phasen erfordert, wird in dieser Arbeit die CutFEM für die Simulation von Benetzungsprozessen verwendet. Die Leistungsfähigkeit dieser Konstellation wird an statischen und dynamischen numerischen Beispielen überprüft.

Zusammenfassend lässt sich sagen, dass diese Arbeit zur Verbesserung der Anwendbarkeit der allgemeinen Navier-Randbedingung beigetragen hat. Es wurde eine strikte mathematische Analyse für die schwache Auferlegung der GNBC durchgeführt. Des Weiteren wurden Methoden vorgestellt, um geometrischen Approximationsfehlern entgegenzuwirken, und es wurde die Anwendbarkeit der Methode im Kontext eines Benetzungsflusses gezeigt. Die Ergebnisse geben Anlass zur Hoffnung, dass zukünftige theoretische Arbeiten und physikalische Simulationen auf dem Grundstein dieser Arbeit aufbauen können.

TABLE OF CONTENTS

NOMENCLATURE

Abbreviations

ALE	Arbitrary-Lagrangian–Eulerian
BACI	Bavarian Advanced Computational Initiative
BDDC	Balancing Domain Decomposition Constraints
CFD	Computational Fluid Dynamics
CFEM	Continuous Finite Element Method
CFL	Courant–Friedrichs–Lewy condition
CIP	Continuous Interior Penalty
CutFEM	Cut Finite Element Method
DG	Discontinuous Galerkin
FDM	Finite Differences Method
FSI	Fluid-Structure Interaction
FVM	Finite Volume Method
GLS	Galerkin-Least Squares method
GNBC	General Navier Boundary Condition
GP	Gauss Point
HDG	Hybridizable Discontinuous Galerkin
LBM	Lattice-Boltzmann Method
LHS	Left-Hand Side
LS	Level-Set
LSIC	Least-Squares Incompressibility Constraint
NSE	Navier–Stokes Equations
PDE	Partial Differential Equation
PSPG	Pressure-Stabilizing Petrov–Galerkin
PUM	Partition of Unity Method
RB	Residual-Based
RHS	Right-Hand Side
SPR	Super convergent Patch Recovery
SUPG	Streamline Upwind Petrov–Galerkin
USFEM	Unusual Stabilized Finite Element Method
VOF	Volume-Of-Fluid
XFEM	eXtended Finite Element Method

Dimensionless Numbers

Bo	Bond's number
Ca	Capillary number
Ma	Mach number
Re	Reynolds number
Re_T	element Reynolds number

Greek Symbols

$\boldsymbol{\beta}, \boldsymbol{\beta}_h$	continuous/discrete convective velocity
$\delta_{\Gamma_{\mathrm{FF}}}$	thickness of interface region between two immiscible fluids
ε	slip length
$\varepsilon_i, \varepsilon_o$	slip length at the inner/outer boundary for the Taylor–Couette problem
$\varepsilon_{\max}$	maximum slip length at the contact line
$\boldsymbol{\epsilon}(\boldsymbol{u})$	symmetric strain rate tensor
γ^n, γ^t	Nitsche penalty parameter in normal and tangential direction
$\gamma_\sigma, \gamma_\nu$	stabilization parameters for reactive/viscous ghost penalties
$\gamma_u, \gamma_p, \gamma_\beta$	stabilization parameters for the CIP/GP stabilizations
γ_{upw}	upwinding parameter
Γ	boundary of the domain
Γ_{D}	Dirichlet boundary/general Navier boundary with $\varepsilon = 0$
Γ_{FF}	interface between two phases
Γ_{G}	general Navier boundary
$\Gamma_{\mathrm{G}}^{\varepsilon}$	general Navier boundary with $\varepsilon \in [0, \infty)$
Γ_h	mesh dependent interface approximation
Γ_i, Γ_o	inner and outer boundary for the Taylor–Couette problem
Γ_{in}	inflow boundary
Γ_{N}	Neumann boundary
κ	curvature
$\kappa(\boldsymbol{A})$	condition number of matrix $\boldsymbol{A}$
μ	dynamic viscosity
ν	kinematic viscosity
Ω	domain
$\overline{\Omega}$	closure of the domain
Ω_h	mesh dependent domain approximation
Ω_h^*	fictitious domain
$\widehat{\Omega}$	union of positive and negative domains $\Omega^+ \cup \Omega^-$
$\widehat{\Omega}_h$	union of discrete positive and negative domains $\Omega_h^+ \cup \Omega_h^-$

Ω^+, Ω^-	positive and negative domain
ϕ, ϕ_h	continuous/discrete level-set function
$\phi_u, \phi_p, \phi_\beta$	element-wise scaling functions for the CIP/GP stabilizations
ρ	density
$\rho^{\Gamma_{\mathrm{FF}}}$	surface mass density
σ	reactive coefficient
σ	surface tension between two fluids
σ_{s+}, σ_{s-}	surface tension force between positive/negative phase and the solid
$\boldsymbol{\sigma}(\boldsymbol{u}, p)$	Cauchy stress tensor
τ_C	stabilization parameter for the LSIC term
τ_{LS}	stabilization parameter for the SUPG term in the level-set equation
$\tau_{M,u}, \tau_{M,p}$	stabilization parameter for the SUPG and PSPG terms
θ_a	apparent contact angle
θ_d	dynamic contact angle
θ_e	equilibrium contact angle
Θ	parameter for the one-step theta time integration scheme
$\boldsymbol{\xi}$	local element coordinate
ζ_u	term determining whether a formulation is adjoint-(in)consistent

Roman Symbols

a, a_h	viscous, convective and reactive contributions of the continuous/discrete formulation for the Oseen equation
a^*, a_h^*	viscous contribution of the continuous/discrete formulation for the NSE
$\boldsymbol{a}$	acceleration
A_h	left-hand side of the discrete formulation for the Oseen equation
$\mathscr{A}_{\Delta t}$	left-hand side of the time discrete formulation for the NSE
$\mathscr{A}, \mathscr{A}_h$	left-hand side of the continuous/discrete formulation for the NSE
b, b_h	pressure/continuity contribution of the continuous/discrete formulation for the Oseen equation
b^*, b_h^*	pressure/continuity contribution of the continuous/discrete formulation for the NSE
$\mathscr{B}$	geometrical approximation error arising from $\Omega_h \setminus \Omega$
$\mathscr{B}_h^{\mathcal{N}^k}$	geometrical approximation error arising from the boundary imposition
c^*, c_h^*	convective contribution of the continuous/discrete formulation for the NSE
$\boldsymbol{c}$	advective velocity for the level-set equation
C_P	Poincaré constant
$\mathscr{C}_{\Gamma_{\mathrm{D}}}$	Dirichlet condition operator
$\mathscr{C}_h^{\Gamma_{\mathrm{FF}}}$	coupling term for the interface between two phases
$\mathscr{C}_h^{\partial\Gamma_{\mathrm{FF}}}$	coupling term for the contact line in two phase flow

$\mathscr{C}_{\Gamma^n}^{T_k}, \mathscr{C}_{\Gamma^t}^{T_k}$	extended boundary condition operator by means of a Taylor expansion in the normal and tangential direction
$\mathscr{C}_{\Gamma_{\mathrm{G}}^n}, \mathscr{C}_{\Gamma_{\mathrm{G}}^t}$	general Navier condition operator in the normal and tangential direction
d	spatial dimension of the domain
$d_{\boldsymbol{n}}, d_{\boldsymbol{n}_h}$	distance functions for the boundary value correction
E	extension operator for functions in $W^{k,p}(\Omega)$ to the fictitious domain Ω^*
$\mathscr{E}_h$	linear extension of solution based on jumps on facets
$\boldsymbol{f}$	body force
$\boldsymbol{f}_\sigma$	surface tension force between two phases
$\boldsymbol{f}_{\theta_d}$	out-of-balance surface tension force
F	facet between two elements
$\mathscr{F}_\Gamma$	set of facets adjacent to cut elements close to the interface/boundary
$\mathscr{F}_h$	set of all facets of the mesh
$\mathscr{F}_i$	interior facets of the mesh
g_β, g_u, g_p	CIP related ghost penalty operators
g_σ, g_ν	reactive and viscous ghost penalty operators
$g_{\theta,i}, g_{\theta,o}$	radial velocity at the inner/outer radius for the Taylor–Couette problem
$\boldsymbol{g}$	Dirichlet boundary velocity
G_h	ghost penalty operator for the Oseen equation
$\boldsymbol{G}$	covariant metric tensor
$\mathscr{G}_h$	ghost penalty operator
h	element size
$h_{\theta,i}, h_{\theta,o}$	radial traction at the inner/outer radius for the Taylor–Couette problem
$\boldsymbol{h}$	Neumann boundary flux
$\mathscr{H}_n^*$	operator comprising history terms at time t^n
$\mathscr{H}_n^{\mathrm{RB}}, \mathscr{H}_n^{\mathrm{CIP}}$	residual-based and continuous interior penalty history operators
$\mathscr{H}_{\mathscr{J}}^*$	operator comprising history specific terms for the stabilization terms
$\mathscr{H}_{\mathscr{J}}^{\mathrm{RB}}, \mathscr{H}_{\mathscr{J}}^{\mathrm{CIP}}$	residual-based and continuous interior penalty specific history operators
$\boldsymbol{I}$	identity mapping
$\mathscr{I}_h$	continuous piecewise linear approximation
$\mathbb{I}$	time interval $[0, t_{\mathrm{end}})$
$\mathbb{I}_n$	partitioned time interval $[t^n, t^{n+1})$
l_ε	distance of smeared slip around the contact line
l, l_h	right-hand side of the continuous/discrete formulation for the Oseen equation
l^*, l_h^*	right-hand side of the continuous/discrete formulation for the NSE
l_σ	capillary length
$l^{\mathrm{ST}}, l^{\mathrm{LB}}$	right-hand side of the surface tension force
L_h	right-hand side of the discrete formulation for the Oseen equation
$\mathscr{L}_{\Delta t}$	right-hand side of the time discrete formulation for the NSE
$\mathscr{L}^{\partial\Gamma_{\mathrm{FF}}}$	right-hand side of the contact line force term

$\mathscr{L}_h^{\Gamma_\mathrm{G},n}, \mathscr{L}_h^{\Gamma_\mathrm{G},t}$	right-hand side terms for a weak imposition of a GNBC
$\mathscr{L}_h^{\Gamma_\mathrm{N}}$	right-hand side terms for a weak imposition of a Neumann condition
$\mathscr{L}, \mathscr{L}_h$	right-hand side of the continuous/discrete formulation for the NSE
$\mathscr{L}_h^{\mathscr{N}}$	right-hand side of Nitsche imposition operator
$\boldsymbol{m}, \boldsymbol{m}_S$	unit vectors at the contact line
$\mathrm{n}_{\mathrm{ele}}$	number of elements in active mesh $\mathscr{T}_h$
n_{GP}	number of Gauss points
$\mathrm{n}_{\mathrm{node}}$	number of nodes in active mesh $\mathscr{T}_h$
$\boldsymbol{n}, \boldsymbol{n}_h$	outward pointing normal to physical/approximated domain
$\boldsymbol{n}_F$	unit normal on inter-element facets
$\boldsymbol{n}_\Gamma$	normal of the interface Γ_{FF}
N_A	global basis function at node A
$\mathscr{N}_h^{\Gamma_\mathrm{G},n}, \mathscr{N}_h^{\Gamma_\mathrm{G},t}$	left-hand side terms for a weak imposition of a GNBC
$\mathscr{N}_h^{\Gamma_\mathrm{N}}$	left-hand side terms for a weak imposition of a Neumann condition
$\mathscr{N}_h$	Nitsche imposition operator
$\mathscr{N}_h^k$	Nitsche imposition operator including corrections with Taylor expansion terms up to order k
p_A	value of the pressure at node A
p, p_h	continuous/discrete pressure
$\mathfrak{p}_{\boldsymbol{n}_h}, \mathfrak{p}_{\boldsymbol{n}}, \mathfrak{p}_{\phi_h}$	projection operators for the boundary value correction
$\mathfrak{p}(\boldsymbol{x})$	closest point projection
$\boldsymbol{P}^n, \boldsymbol{P}^t$	normal and tangential projection matrices
$\mathbb{P}^k(T)$	set of polynomials on d-simplices of order k
$\pi_h^*, \boldsymbol{\pi}_h^*, \Pi_h^*$	Clément interpolation operator
q, q_h	continuous/discrete pressure test function
$\mathscr{Q}, \mathscr{Q}_0$	trial/test function spaces for the pressure
$\mathscr{Q}_h, \mathscr{Q}_{h,0}$	discrete trial/test function spaces for the pressure
$\mathbb{Q}^k(T)$	set of polynomials on d-rectangles of order k
r	adjoint pressure
r_C	residual of the continuity equation
r_i, r_o	radius of inner/outer cylinder for the Taylor–Couette problem
r_{LS}	residual of the level-set equation
$\boldsymbol{r}_M$	residual of the momentum equation
RM	space of rigid body motion
$\mathscr{R}$	space of symmetric rotations
s_u, s_p, s_β	CIP operators for incompressibility, pressure and streamline derivative
S_d	space of anti-symmetric matrices
S_h	domain stabilization operator for the Oseen equation
$\mathscr{S}_h^*$	domain stabilization term for the NSE
$\mathscr{S}_h^{\mathrm{RB}}, \mathscr{S}_h^{\mathrm{CIP}}$	residual-based and continuous interior penalty domain stabilization

t	time
Δt	time-step length
t_{end}	end time
t^n	discrete time levels for the time-stepping
T	finite element
∂T	boundary of element T
$T^{\boldsymbol{n}}_{m,k}$	Taylor expansion operator in $\boldsymbol{n}$ direction for the derivatives m to k
$\omega(T)$	set of elements T sharing at least one vertex
$\mathscr{T}_\Gamma$	set of finite elements intersected by the interface/boundary
$\mathscr{T}_h$	active part of the finite element mesh with mesh size parameter h
$\widetilde{\mathscr{T}}_h$	computational mesh with mesh size parameter h
u_r, u_θ	radial and rotational velocity
$\boldsymbol{u}_0$	initial velocity vector
$\boldsymbol{u}_A$	value of the velocity at node A
$\boldsymbol{u}_\Gamma$	interface velocity
$\boldsymbol{u}, \boldsymbol{u}_h$	continuous/discrete velocity vector
U_δ	tubular region
U, U_h	product of continuous/discrete velocity and pressure solution
$\boldsymbol{v}, \boldsymbol{v}_h$	continuous/discrete velocity test function
V, V_h	product of continuous/discrete velocity and pressure test functions
V_e^+, V_e^-	positive/negative volume cells
$\mathscr{V}, \mathscr{V}_0, \mathscr{V}_{\boldsymbol{g}}$	trial/test function spaces for the velocity
$\mathscr{V}_h, \mathscr{V}_{h,0}, \mathscr{V}_{h,\boldsymbol{g}}$	discrete trial/test function spaces for the velocity
$\mathbb{V}^k(T)$	set of polynomials on d-simplices and d-rectangles of order k
w, w_h	continuous/discrete level-set test function
$\boldsymbol{w}$	adjoint velocity
$\mathscr{W}, \mathscr{W}_0, \mathscr{W}_{\boldsymbol{g}}$	trial/test function spaces for the velocity-pressure product space
$\mathscr{W}_h, \mathscr{W}_{h,0}, \mathscr{W}_{h,\boldsymbol{g}}$	discrete trial/test function spaces for the velocity-pressure product space
$\boldsymbol{x}$	global coordinate
$\mathscr{X}_h$	continuous function space consisting of piecewise polynomials
$\mathscr{X}_h^{\text{dc}}$	discontinuous functions space consisting of piecewise polynomials

Function Spaces, Inner Products and Norms

$(\cdot,\cdot)_{m,U}$	inner product associated with $H^m(U)$ defined in a domain U
$(\cdot,\cdot)_U$	inner product associated with $L^2(U)$ defined in a domain U
$\langle\cdot,\cdot\rangle_{m,U}$	inner product associated with $H^m(U)$ defined on a face or an interface U
$\langle\cdot,\cdot\rangle_U$	inner product associated with $L^2(U)$ defined on a face or an interface U
$\|\cdot\|_{k,p,U}$	norm associated with $W^{k,p}(U)$
$\|\cdot\|_{m,U}$	norm associated with $H^m(U)$

$\|\cdot\|_U$	norm associated with $L^2(U)$
$C^0(U)$	continuous function space on U
$H^m(U)$	standard Sobolev space of order $m \in \mathbb{R}$ on U
$H^{div}(U)$	Sobolev space of L^2-functions on U for which their divergence is in $L^2(U)$
$L^2(U)$	Sobolev space of order $m = 0$ on U
$L^2_0(U)$	$L^2(U)$ space with average 0 on U
$\mathbb{N}$	integers
$\mathbb{R}$	real numbers
$\mathbb{R}^+$	positive real numbers
$W^{k,p}(U)$	Sobolev space up to order k based on L^p-semi-norms on U

Symbols, Subscripts, Superscripts and other Quantifiers

$(\cdot)^d, [\cdot]^d$	dimension of vector-valued quantities
$(\cdot)^{n+1}, (\cdot)^n$	superscript indicating current and previous time step
$(\cdot)_h$	discrete quantity
$(\cdot)^i$	defining fluid phases for two-phase flows, $i \in \{-, +\}$
$\widetilde{(\cdot)}$	smoothed quantity

Operators

$(\cdot) \circ (\cdot)$	concatenation of operators
$[\![\cdot]\!]$	jump operator
$\langle\cdot\rangle$	inverse weighted average operator
$\{\cdot\}$	weighted average operator
$\oplus$	operator for composing function spaces
$\times$	operator for product spaces
$a \lesssim b$	equivalent to $a \leqslant Cb$ for some positive generic constant C
$\nabla\cdot$	divergence operator
∇	gradient operator
∇_Γ	tangential derivative operator
$D^j_{\boldsymbol{n}}$	normal derivative operator
abs	absolute value
dist	distance function
lim	limit
meas	measure of set
sign	sign function
span	linear span of a set
supp	support
tr	trace operator

Chapter 1

Introduction

In computations, boundary conditions cause most of the problems

– Kreiss and Lorenz [173]

1.1 Motivation

Defining and imposing boundary conditions remains one of the most important tasks in the modeling of flow problems. Most text books on fluid dynamics treat the standard Dirichlet and Neumann boundary conditions in detail. However, most of the time little, or no, attention is given to non-standard boundary conditions, such as the general Navier boundary condition (GNBC). This does not make this boundary condition any less important, as it appears in the modeling of a multitude of problems: such as flows over hydrophobic surfaces, geophysical flows, flow over porous media, contact between immersed bodies and in wetting processes in the vicinity of the contact line, i.e. where two fluids intersect at a solid wall.

The general Navier boundary condition can be decomposed into a wall-normal Dirichlet condition and a wall-tangential Robin condition. This boundary condition, and how it is to be imposed in a computational framework, was studied in detail by Verfürth [269, 271, 272] in the late 1980's and early 1990's. Apart from a recent publication by Urquiza *et al.* [267], where a Nitsche imposition is compared to the proposed Lagrange multiplier methods suggested by Verfürth, no large difference in methodology to the works by Verfürth have been presented. What the existing methods from literature have in common, is the inability to combine the Dirichlet (no-slip) and Neumann (slip) limits of the tangential Robin condition under a unified framework, as they impose this condition with a Galerkin substitution method. This incompatibility of limits is an obvious drawback of current methods. For instance, considering the case of wetting processes. In the proximity of the contact line, almost full slip is observed, whereas further away from the contact line the no-slip condition is retained, as reported by Qian *et al.* [214]. Given that the position of the contact line changes over time, a formulation which can handle both the no-slip and slip limits of the tangential Robin condition is of practical importance. A goal of this thesis is to remedy this, and present a formulation which imposes a general Navier condition, valid in both the Dirichlet and Neumann limits for the wall-tangential Robin

condition. In addition, this thesis aims at applying this proposed formulation for a moving contact line problem, as to determine its potential for these types of problems.

Given that the equations governing the motion of fluids can not be solved by any analytic expression, except in some trivial cases, an approximation of the true solution is sought in a subspace of the continuous one. To achieve this approximation, a spatial discretization of the computational domain can be undertaken. One group of such discretization techniques are so-called unfitted finite element methods. Arguably the main advantage of these methods is that they are not restricted to creating conforming discretizations of the physical domain. The unfitted finite element method of choice in this thesis is the so-called cut finite element method (CutFEM) [64], stemming from the well-known eXtended Finite Element Method (XFEM) [31, 192]. This method has shown its merit in problems ranging from simplifying meshing processes, fluid-structure interaction and multiphase flows. In the CutFEM, a background mesh covering the physical domain is cut, creating a computational domain which is a piecewise linear approximation of the physical domain. Given this approximation of the domain, errors are consequently introduced in the weak formulation. One well-known error appearing for the GNBC is the so-called Babuška paradox [12]. This paradox stems from the the fact that in a piecewise linear domain, the normal of the boundary is piecewise constant, which is incompatible with a continuous wall-tangential velocity at the boundary. Another error introduced from this piecewise linear approximation, is the fact that the computational and physical domain do not coincide. Thus, the question naturally arises what boundary condition to impose on the discretized boundary, to guarantee optimal order of convergence for the solution. These issues need to be addressed for any formulation with the GNBC to be considered applicable, as geometrical approximations of physical domains will always be present in computations. As such, another objective of this thesis is to suggest a remedy for these geometrical errors, as to retain optimal order of convergence for the proposed imposition of the GNBC within the CutFEM framework utilized in this thesis.

1.2 Contribution of this Work

The present thesis was carried out within the projects "Interdisciplinary Modeling of Biofilms"[1] of the International Graduate School for Science and Engineering (IGSSE) and "Erasmus Mundus Joint Doctorate SEED project"[2] at the Institute for Computational Mechanics headed by Prof. Dr.-Ing. Wolfgang A. Wall of the Technical University of Munich and at the Laboratori de Càlcul Numèric under the supervision of Prof. Ph.D. Antonio Huerta of Universitat Politècnica de Catalunya.

The contributions of this work aims at developing a weak imposition of the general Navier boundary condition fulfilling the requirements of being applicable in both the no-slip and slip limits. Furthermore, the proposed method needs to also adhere to the requirements regarding geometrical approximation errors, given the piecewise linear approximation of the CutFEM. Accordingly, the main contributions of this work are the following:

[1]Support via the International Graduate School for Science and Engineering (IGSSE) of the Technical University of Munich (TUM) is gratefully acknowledged.
[2]Support from the European Commission with grant Ref. 2013-0043 is acknowledged.

A Nitsche CutFEM for the Navier–Stokes equations with GNBC: This proposed formulation constitutes the first stable method of imposing a general Navier boundary condition for an arbitrary choice of slip length, i.e. any linear combination of the Dirichlet and Neumann parts of the tangential Robin condition, on unfitted meshes. It postulates that instead of imposing the tangential Robin condition with a Galerkin substitution method, a weak imposition with the Nitsche's method is ought to be done instead. To demonstrate the stability and convergence property of the formulation, the linearized Navier–Stokes equations, i.e. the Oseen equation, are considered instead of the Navier–Stokes equations. This is due to the fact that standard analysis techniques are not applicable to the non-linear Navier–Stokes equation, hence, the linearized equivalency is thoroughly analyzed instead. In addition to this, the Oseen equation appears in the discrete solution process of the Navier–Stokes equation, making it an important sub-problem for rigorous analysis. Inf-sup stability is proven for the Oseen equation with general Navier boundaries, which guarantees existence and uniqueness of the obtained discrete solution. An a priori error analysis is also conducted for this formulation, and optimal order of convergence is obtained in the usual norms. Furthermore, when viscous dominated flow is considered, it is shown that the discrete velocity solution convergence in a L^2-norm, with one order of magnitude higher than the obtained order for the usual norm. The mathematical proofs are corroborated by a numerical example to illustrate the well-posedness in comparison to the Galerkin substitution method and to investigate the stability and conditioning constraints of the proposed method.

The proofs for the inf-sup stability and a priori estimates of the Oseen equation with general Navier boundaries were already published in the author's previous work Winter *et al.* [279] and will be presented in this thesis with only minor modifications. The numerical example to corroborate the results of the analysis is the same as in the aforementioned publication. Nonetheless, the discretization of the problem is conducted with different elements in this thesis. In [279] bi-linear quadrilaterals were used, whereas linear triangles were used in this thesis, making this part also interesting for readers already familiar with the publication.

Geometrical approximation errors for the Nitsche imposition of the GNBC: Given the piecewise linear approximation of the physical domain, it is known that if the discontinuous normals of the boundary from this approximation is used to impose the GNBC, it leads to the Babuška paradox [12]. This paradox describes the reduced order of convergence stemming from the usage of a piecewise constant normal to impose the GNBC. To overcome this paradox, a smoothing of the normal vectors on the boundary is proposed. As the domain is described with an implicit domain description, in the form of a level-set field, the gradients of this level-set field are smoothed to attain a continuous normal field on the discretized boundary. The improvement of the convergence for curved domains is demonstrated by comparing the results to an analytic solution for a two-dimensional problem. This proposition of describing the general Navier boundary with an implicit domain description, and utilizing this implicit domain description to overcome the Babuška paradox, is presented in this thesis for the first time.

Another error introduced by the piecewise linear approximation is the fact that the discretized boundary and the boundary of the physical domain do not necessarily coincide. This leads to problems regarding what boundary condition ought to be imposed on the discretized boundary, as to not have geometrical errors dominate the solution. Especially in simulations with higher order elements, resolving this error becomes quintessential to attain optimal order of conver-

gence. In this thesis the method of boundary value correction for the Poisson equation with Dirichlet boundaries by Burman *et al.* [66], is extended to the Navier–Stokes equation for general Navier boundary conditions, for the first time. The improved convergence with this method is demonstrated for a numerical example with quadratic elements. Important to emphasize here, is the fact that formulations given for a general Navier boundary condition, contain the classical Dirichlet condition. Thus far, the here proposed boundary value correction technique has not been presented for neither Dirichlet nor general Navier boundary conditions for the Navier–Stokes equation, thus making the proposed formulation in this thesis the first to do so. This thesis also identified strong connections between the convergence of the overall problem and the convergence of the normal of the approximated boundary for higher order discretizations. This requirement on the order of convergence for the normal vector appearing in the GNBC is studied for the first time in this thesis. In addition, heuristic arguments on the necessary order of convergence for the normal vector on the approximated boundary, as to retain optimal order of convergence for the problem, are made.

As a disclaimer, it is important to note that the above claims of the proposed methods being presented in this thesis for the first time, are made to the best of the author's knowledge.

A localized slip formulation for multiphase flows with moving contact lines: The physics behind the motion of contact lines in multiphase flows is still an active topic of research. What has been shown early on though, is the fact that the classic no-slip condition is not an applicable boundary condition at the contact line, see Dussan V and Davis [104]. In literature, different approaches have been applied to resolve this issue. However, to this date, a consensus of a best practice for simulations of these types of flows does no exist. In this thesis, the observation of high apparent slip in the vicinity of the contact line, but no-slip further away, by Qian *et al.* [214] motivates a localized slip approach. This approach encompasses the imposition of slip close to the contact line and no-slip further away. Consequently, the need to cover both the Dirichlet and Neumann limits of the tangential Robin condition in the GNBC arises. The previously mentioned method of imposing the general Navier boundary condition by means of the Nitsche's method is employed to carry this out, as this method permits both limits in contrast to the classic Galerkin substitution method. In addition to this, the CutFEM is employed for the first time in the context of the moving contact line problem. As this method can depict discontinuities in the velocity gradient and pressure solutions between the two fluid phases, this leads to the ability to accurately simulate flows with large contrasts in material parameters. This use of a CutFEM and the imposition of a localized slip method with the Nitsche's method, to simulate flows with moving contact lines, make a novel contribution to this field. In particular, this sets the work in this thesis apart from the recent publication by Reusken *et al.* [222], which utilizes an XFEM for the pressure field, but only employs a classic continuous finite element method for the velocity field. In addition to this, the publication does also not consider localized slip in the vicinity of the contact line.

The proposed localized slip formulation is applied to a static droplet and a spreading droplet problem to evaluate its strengths and weaknesses.

The above contributions have been carried out in the parallel finite element software environment Bavarian Advanced Computational Initiative (BACI), see [277].

1.3 Outline of the Thesis

The structure of this thesis is organized as follows. Starting with Chapter 2, the necessary prerequisites are introduced for the ensuing use of the CutFEM in subsequent chapters. This encompasses, first, a recap on the stabilized equal-order finite element formulation for a fitted mesh with Dirichlet and Neumann boundary conditions. Second, an introduction into defining a computational domain implicitly with a level-set method and how to carry out a piecewise linear explicit approximation of this domain. Following this, the CutFEM is introduced and the addition of necessary interface stabilization terms, so-called ghost penalty terms, are explained. Closing off the chapter, methods for the integration of arbitrary shaped polyhedrons are presented, and time integration schemes for the CutFEM with moving boundaries are discussed.

In Chapter 3 the novel weak imposition of a general Navier boundary condition by means of a Nitsche's method for the Navier–Stokes equations is presented. The logic behind this formulation is explained, and its superior conditioning for low slip lengths are demonstrated against the Galerkin substitution method. Also, the mathematical analysis for inf-sup stability and a priori error estimates for the linearized Navier–Stokes equations, i.e. the Oseen equation, from Winter *et al.* [279] is presented here. The results from this analysis are corroborated by a numerical example, which concludes the chapter.

Chapter 4 starts out by introducing the concept of variational crimes in simulations with finite elements. One of these crimes is the approximation made of the geometry when approximating the physical domain. This geometrical approximation error manifests itself in two distinct ways for a general Navier boundary, namely, in the piecewise constant normal of the approximated boundary (given a piecewise linear approximation of the domain) and that the approximated and physical domains do not necessarily coincide. First, the issue of the non-continuity of normals on piecewise linear domains, the so called Babuška paradox, for the general Navier condition is demonstrated. A practical method to solve this problem, for an implicit domain description with a level-set, is suggested and its effectiveness demonstrated with a numerical example. Next, the error stemming from the fact that the approximated boundary and the physical boundary are not coinciding, is addressed. A boundary value correction is proposed here for a general Navier condition which retains optimal order of convergence also for higher-order discretizations. The improved convergence with this boundary value correction method is demonstrated in a numerical example with bi-quadratic elements.

The localized slip formulation for multiphase flows with moving contact lines is presented in Chapter 5. Starting off, the physics surrounding the phenomena of capillarity is presented, and a brief excursion into the difficulties surrounding the modeling of contact lines is made. Existing numerical methods are briefly summarized and compared to the method of choice in this thesis. The proposed localized slip formulation is combined with a CutFEM for the two-phase flow, permitting large contrasts in material parameters of the two fluids. This formulation is first applied to a stationary droplet problem, where different formulations of imposing the capillary forces are evaluated for their effectiveness. The chapter is concluded with an application of the suggested method to a dynamic wetting process, in the form of a spreading droplet. The results are evaluated, and the strengths and weaknesses of the method are highlighted.

Lastly, Chapter 6 summarizes the findings of this thesis and gives an outlook into possible areas of improvement, which could be pursued in future research projects.

Chapter 2

Prerequisites and Notation of the CutFEM for the Navier–Stokes Equations

In the case of fitted domain approaches, i.e. when the computational mesh conforms to the domain, the Navier–Stokes equations have been solved by a plethora of different discretization methods. Some mentionable methods include, the Finite Difference Method (FDM) [213], the Lattice-Boltzmann Method (LBM) [215, 252], the Finite Volume Method (FVM) [274] or, which has quite recently been applied to the Navier–Stokes equations, the Discontinuous Galerkin (DG) [144] and Hybridizable Galerkin Methods (HDG) [203]. However interesting these approaches may be, this thesis will limit itself to the case of continuous finite elements.

In the case of fitted domain approaches, the application of a continuous finite element method (CFEM) for incompressible flow problems is a well studied field of research, see for instance Ferziger and Peric [112] and the references therein. Nonetheless, there arises situations where a fitted domain approach is undesirable, or even unfeasible. This includes problems where creating conforming computational meshes are a tedious and time consuming processes, or problems where domains undergo large deformation or topological changes, such as in multiphase flows or fluid-structure interaction problems. In these cases it might be more suitable to use an unfitted domain approach such as the extended finite element method (XFEM), see the review article by Fries and Belytschko [119], or methods derived from the XFEM, such as the cut finite element method (CutFEM) [64]. However, before being able to apply this method, some fundamental tools need to be introduced; such as the stabilization of the discretized equations, the definition of the domain in an unfitted domain approach and the imposition of boundary conditions on non-fitted boundaries. This chapter aims at introducing these concepts to the reader, to facilitate the reading of subsequent chapters.

Starting with an initial introduction in Section 2.1 to the use of continuous finite elements for discretizing the Navier–Stokes equations on fitted meshes with Dirichlet and Neumann boundaries. Here, the weak form of the equations and necessary stabilizations are presented for the case of a discretization with equal-order continuous finite elements for the velocity and the pressure. In Section 2.2, the description of the computational domain for unfitted mesh methods is explained. In particular implicit domain description methods, such as the level-set method, are treated in more detail. Lastly, the CutFEM for the incompressible Navier–Stokes equations is presented in Section 2.3. The necessary weak imposition of boundary conditions with this

method and the introduced ill-conditioning from specific cut elements are explained and well established solutions from literature are conferred. In addition, a brief introduction into the issues appearing for the CutFEM with moving domains is discussed, and solutions from literature are demonstrated.

2.1 A Stabilized Finite Element Formulation for an Incompressible Fluid

This section begins with the introduction of the governing equations for a single phase incompressible Newtonian fluid with standard Dirichlet and Neumann boundary conditions. Next, the weak form and its discretization is presented. As this discretized formulation necessitates stabilizations, these are also introduced here. The following results are well documented and can be read about in more detail in one of the following text books by Cuvelier *et al.* [79], Donea and Huerta [94], Gresho and Sani [129, 130] or Ferziger and Peric [112].

2.1.1 Strong Form of the Navier–Stokes Equations

For an incompressible Newtonian fluid in a bounded and connected domain $\Omega \subset \mathbb{R}^d$, $d \in \{2, 3\}$, with the boundary Γ, illustrated in Figure 2.1, the following Navier–Stokes equations holds,

$$\rho \frac{\partial \boldsymbol{u}}{\partial t} + \rho \boldsymbol{u} \cdot \nabla \boldsymbol{u} - \nabla \cdot \boldsymbol{\sigma} = \boldsymbol{f} \quad \text{in } \Omega \times (0, t_{\text{end}}), \tag{2.1}$$

$$\nabla \cdot \boldsymbol{u} = 0 \quad \text{in } \Omega \times (0, t_{\text{end}}), \tag{2.2}$$

$$\boldsymbol{u} = \boldsymbol{g} \quad \text{on } \Gamma_{\text{D}} \times (0, t_{\text{end}}), \tag{2.3}$$

$$\boldsymbol{\sigma} \cdot \boldsymbol{n} = \boldsymbol{h} \quad \text{on } \Gamma_{\text{N}} \times (0, t_{\text{end}}), \tag{2.4}$$

$$\boldsymbol{u} = \boldsymbol{u}_0 \quad \text{in } \Omega \times \{0\}, \tag{2.5}$$

where the Cauchy stress tensor $\boldsymbol{\sigma}$ is defined as

$$\boldsymbol{\sigma}(\boldsymbol{u}, p) = -p\boldsymbol{I} + 2\mu\boldsymbol{\epsilon}(\boldsymbol{u}),$$

with the rate-of-strain tensor $\boldsymbol{\epsilon}(\boldsymbol{u}) = \frac{1}{2}\left(\nabla \boldsymbol{u} + (\nabla \boldsymbol{u})^T\right)$. The variables in the equations (2.1)–(2.5) are defined as $\boldsymbol{u}, \boldsymbol{f} : \Omega \times [0, t_{\text{end}}) \to \mathbb{R}^d$, $p : \Omega \times [0, t_{\text{end}}) \to \mathbb{R}$ and $\rho, \mu : \Omega \times [0, t_{\text{end}}) \to \mathbb{R}^+$. These variables have a physical interpretation in that, $\boldsymbol{u}$ is the velocity $[\text{m/s}]$, p the pressure $[\text{N/m}^2]$, ρ the density $[\text{kg/m}^3]$ and μ the dynamic viscosity $[\text{kg/(s} \cdot \text{m)}]$ of the fluid. The body force $\boldsymbol{f}$ acting on the fluid has the dimensions $[\text{N/(m}^3)]$. As such, the dimension of the momentum equation (2.1) is $[\text{kg/(m}^2 \cdot \text{s}^2)] = [\text{N/(m}^3)]$ and the continuity equation (2.2) has the dimension $[1/\text{s}]$. From this it is clear that the terms on the boundary, $\boldsymbol{g}$ and $\boldsymbol{h}$ are defined as a velocity $[\text{m/s}]$ and a traction $[\text{N/m}^2]$, respectively, and are functions defined as $\boldsymbol{g} : \Gamma_{\text{D}} \times [0, t_{\text{end}}) \to \mathbb{R}^d$ and $\boldsymbol{h} : \Gamma_{\text{N}} \times [0, t_{\text{end}}) \to \mathbb{R}^d$.

Equations (2.1)–(2.5) define the Navier–Stokes equations with Dirichlet and Neumann boundaries Γ_{D} and Γ_{N}. The open domain Ω defines the physical domain and its closure $\overline{\Omega} = \Omega \cup \Gamma$ is the union of the domain and the boundary, where the boundary is partitioned as $\Gamma = \Gamma_{\text{D}} \cup \Gamma_{\text{N}}$ and restricted to the condition $\Gamma_{\text{D}} \cap \Gamma_{\text{N}} = \emptyset$. The Dirichlet condition (2.3) imposes a fixed velocity $\boldsymbol{g}$

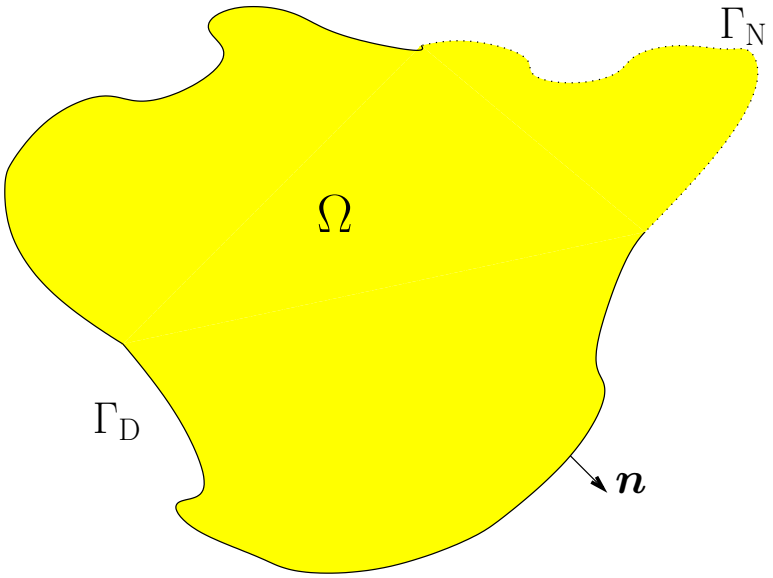

Figure 2.1: The physical domain is defined by the open set Ω with the boundary $\Gamma = \Gamma_D \cup \Gamma_N$, where an outward pointing normal $\boldsymbol{n}$ is defined on the boundary.

on the boundary Γ_D, whereas a fixed traction $\boldsymbol{h}$ is set on the Neumann part (2.4) of the boundary Γ_N. Lastly, the initial velocity field (2.5) is required to be divergence-free, i.e. $\nabla \cdot \boldsymbol{u}_0 = 0$, and fulfill the boundary conditions at $t = 0$.

2.1.2 Weak Form of the Navier–Stokes Equations

Before deriving the weak form, some functional spaces and notations need to be introduced. A brief overview of these spaces are given, and the interested reader can find more in, for instance, the textbook by Lax [175]. First, the standard Sobolev spaces of order $m \in \mathbb{R}_0^+$ are defined as $H^m(U)$ and $[H^m(U)]^d$ for $U \in \{\Omega, \Gamma\}$. The corresponding norm for these spaces is written as $\|\cdot\|_{m,U}$. Inner products are written as $(\cdot,\cdot)_{m,U}$ for measurable subsets $U \subseteq \mathbb{R}^d$ and $\langle\cdot,\cdot\rangle_{m,U}$ for subsets $U \subseteq \mathbb{R}^{d-1}$. In the case of $m = 0$, i.e. for norms and inner products corresponding to $L^2(U)$, the subscript is omitted and instead norms are written as $\|\cdot\|_U$ and inner products are written as $(\cdot,\cdot)_U$ and $\langle\cdot,\cdot\rangle_U$. Fractional Sobolev spaces $[H^s(Y)]^d$ with $s \in \mathbb{R}^+$ will be employed in the following to specify boundary data functions $Y \subseteq \mathbb{R}^{d-1}$ on the boundary Γ, see McLean [187, Ch. 3] for definitions and the most relevant properties. Finally, the space $L_0^2(U)$ defines the space consisting of functions in $L^2(U)$ with zero average on U. The spaces for the functions in the weak form are presented in the following. Assume that the volume force is in $\boldsymbol{f} \in [L^2(\Omega)]^d$ and the values defined on the boundary are in

$$\boldsymbol{g} \in [H^{3/2}(\Gamma_D)]^d \qquad \text{and} \qquad \boldsymbol{h} \in [H^{1/2}(\Gamma_N)]^d. \tag{2.6}$$

For the velocity, the following space will be utilized,

$$\mathcal{V}_{\boldsymbol{g}} := \{\boldsymbol{u} \in [H^1(\Omega)]^d \mid \boldsymbol{u} = \boldsymbol{g} \text{ on } \Gamma_D\}, \tag{2.7}$$

whereas the space for the pressure is set as

$$\mathcal{Q} := \begin{cases} L^2(\Omega) & \text{if } \Gamma_{\mathrm{N}} \neq \emptyset \\ L^2_0(\Omega) & \text{if } \Gamma_{\mathrm{N}} = \emptyset. \end{cases} \tag{2.8}$$

The different choice of pressure space when a Neumann boundary exists to when it does not, stems from the fact that the pressure is only specified up to a constant for a pure Dirichlet problem. This can be deduced directly from the strong form, which only contains the pressure gradient and not the pressure, making only differences in pressure important.

From these definitions, the weak form is defined as: find $U = (u, p) \in \mathcal{V}_{\boldsymbol{g}} \times \mathcal{Q}$ for all $t \in (0, t_{\text{end}}]$ such that for all $V = (\boldsymbol{v}, q) \in \mathcal{V}_{\boldsymbol{0}} \times \mathcal{Q}$

$$(\rho \frac{\partial \boldsymbol{u}}{\partial t}, \boldsymbol{v})_\Omega + a^*(\boldsymbol{u}, \boldsymbol{v}) + c^*(\boldsymbol{u}; \boldsymbol{u}, \boldsymbol{v}) + b^*(p, \boldsymbol{v}) - b^*(q, \boldsymbol{u}) = l^*(\boldsymbol{v}), \tag{2.9}$$

where

$$a^*(\boldsymbol{u}, \boldsymbol{v}) := (2\mu\boldsymbol{\epsilon}(\boldsymbol{u}), \boldsymbol{\epsilon}(\boldsymbol{v}))_\Omega \tag{2.10}$$
$$c^*(\boldsymbol{\beta}; \boldsymbol{u}, \boldsymbol{v}) := (\rho(\boldsymbol{\beta} \cdot \nabla)\boldsymbol{u}, \boldsymbol{v})_\Omega \tag{2.11}$$
$$b^*(p, \boldsymbol{v}) := -(p, \nabla \cdot \boldsymbol{v})_\Omega \tag{2.12}$$
$$l^*(\boldsymbol{v}) := (\boldsymbol{f}, \boldsymbol{v})_\Omega + \langle \boldsymbol{h}, \boldsymbol{v} \rangle_{\Gamma_{\mathrm{N}}}. \tag{2.13}$$

It is clear that the left-hand-side (LHS) of (2.9) constitutes a non-linear operator, owing to the inclusion of the convective term (2.11). As such, standard techniques from functional analysis for linear operators are not applicable to deduce existence, uniqueness and *a priori* estimates. In Chapter 3, a linearized version of the Navier–Stokes equations will be analyzed, where the standard techniques from functional analysis can be applied.

As to shorten the notation for subsequent sections the following operators are introduced,

$$\mathscr{A}(U, V) = \mathscr{L}(V), \tag{2.14}$$

where

$$\mathscr{A}(U, V) = (\rho \frac{\partial \boldsymbol{u}}{\partial t}, \boldsymbol{v})_\Omega + a^*(\boldsymbol{u}, \boldsymbol{v}) + c^*(\boldsymbol{u}; \boldsymbol{u}, \boldsymbol{v}) + b^*(p, \boldsymbol{v}) - b^*(q, \boldsymbol{u}) \tag{2.15}$$
$$\mathscr{L}(V) = l^*(\boldsymbol{v}). \tag{2.16}$$

2.1.3 A Discrete Stabilized Formulation for the Navier–Stokes Equations

Before a discretized version of the weak form can be formulated, some spaces and notations for a computational finite element mesh need to be introduced. In Figure 2.2 an illustration is given of the partition of the domain Ω into a computational domain Ω_h, with boundary $\Gamma_h = \Gamma_{\mathrm{N},h} \cup \Gamma_{\mathrm{D},h}$, to facilitate the understanding of the introduced notation. As is clear from the figure, Ω does not necessary need to coincide with Ω_h, especially if the partitioned mesh $\mathcal{T}_h$ consists of linear elements. This geometrical approximation error will be further investigated in Chapter 4. For now, the assumption is made that the physical and discretized domains coincide, i.e. $\overline{\Omega_h} = \overline{\Omega}$, to

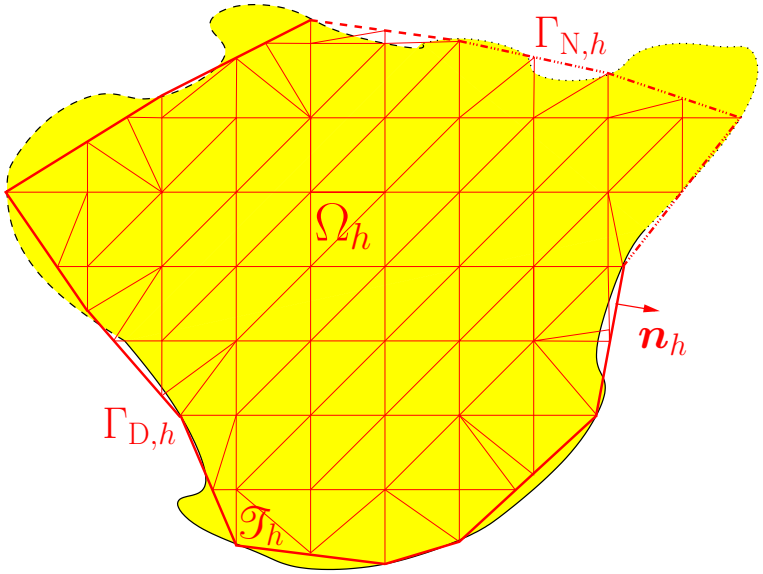

Figure 2.2: The computational domain is defined by the open set Ω_h with the boundary $\Gamma_h = \Gamma_{\mathrm{D},h} \cup \Gamma_{\mathrm{N},h}$, where an outward pointing normal $\boldsymbol{n}_h$ is defined on the boundary. A partition $\mathcal{T}_h$ of the computational domain Ω_h into finite elements is also illustrated in the figure.

simplify the formulations. The discretized geometry Ω_h consists of a partitioned mesh $\mathcal{T}_h$ which is a union of non-overlapping, isoparametric finite elements $T \in \mathcal{T}_h$ such that

$$\Omega_h = \cup_{T \in \mathcal{T}_h} T \tag{2.17}$$

The number of nodes in $\mathcal{T}_h$ is denoted as $\mathrm{n_{node}}$ and the number of elements as $\mathrm{n_{ele}}$. The discrete solution for the velocity and pressure is approximated by equal-order polynomial shape functions N_A as

$$\boldsymbol{u}_h := \sum_{A=0}^{\mathrm{n_{node}}} N_A(\boldsymbol{x}) \boldsymbol{u}_A(t), \tag{2.18}$$

$$p_h := \sum_{A=0}^{\mathrm{n_{node}}} N_A(\boldsymbol{x}) p_A(t), \tag{2.19}$$

where the variables $\boldsymbol{u}_A$ and p_A are the velocity and pressure degrees of freedom at the node A. The shape function space can be formulated as a continuous isoparametric space for piecewise polynomials of order k, which for a given mesh can be defined as

$$\mathcal{X}_h = \left\{ v_h \in C^0(\Omega_h) : v_h|_T \in \mathbb{V}^k(T) \; \forall \; T \in \mathcal{T}_h \right\}. \tag{2.20}$$

Here $\mathbb{V}^k(T)$ is a polynomial functions space on the element T, and either $\mathbb{P}^k$ or $\mathbb{Q}^k$, i.e. simplices or rectangles, will be employed in this thesis. As such, the functional spaces for the discretized velocity and pressure can be defined as

$$\mathcal{V}_{h,\boldsymbol{g}} = [\mathcal{X}_h]^d \cap \mathcal{V}_{\boldsymbol{g}} \qquad \text{and} \qquad \mathcal{Q}_h = \mathcal{X}_h. \tag{2.21}$$

This makes it possible to define the formulation for the stabilized discrete formulation as: find $U_h = (\boldsymbol{u}_h, p_h) \in \mathcal{W}_{h,\boldsymbol{g}}$ such that for all $V_h = (\boldsymbol{v}_h, q_h) \in \mathcal{W}_{h,\mathbf{0}}$

$$\mathcal{A}(U_h, V_h) + \mathcal{S}_h^*(U_h, V_h) = \mathcal{L}(V_h). \tag{2.22}$$

The test function and trial space for the velocity and pressure pair is defined as $\mathcal{W}_{h,\boldsymbol{g}} = \mathcal{V}_{h,\boldsymbol{g}} \times \mathcal{Q}_h$ and $\mathcal{W}_{h,\mathbf{0}} = \mathcal{V}_{h,\mathbf{0}} \times \mathcal{Q}_h$ in the above. The addition of a stabilization term $\mathcal{S}_h^*$ in (2.22) sets this formulation apart from the weak form introduced in (2.14). The necessity to add this term to the discrete formulation stems from three sources of instability.

- The choice of equal-order interpolation spaces for the velocity and pressure leads to a violation of the discrete inf-sup condition. As such the formulation is not guaranteed to be stable, as first shown by Brezzi and Fortin [47].
- The element Reynolds number is defined as

  $$\mathrm{Re}_T = \frac{\rho ||\boldsymbol{u}||_{0,\infty,T} h_T}{\mu},$$

  where h_T is a specific element length. When Re_T becomes large, non-physical oscillatory behavior can be observed in the numerical solution. This originates from insufficient control of the convective term in the weak formulation.
- In the limiting case when $\mu \to 0$, additional stabilization of the divergence is required as the velocity solution space changes from $H^1(\Omega)$ to $H^{\mathrm{div}}(\Omega)$.

Different stabilization methods can be introduced to deal with these three sources of instability, of which an overview can be found in Braack *et al.* [40]. In this thesis two of these methods will be used, the *residual-based stabilization* and the *continuous interior penalty method*. These stabilization techniques are introduced in the subsequent sections 2.1.3.1 and 2.1.3.2, respectively.

2.1.3.1 Residual-based Stabilization

Given the existence of the three sources of instability for the proposed discrete formulation (2.22), measures need to be taken to resolve these. In the case of a residual-based stabilization method, three terms are added to resolve this issue. These three terms are: a pressure-stabilizing Petrov–Galerkin (PSPG) term, which permits the usage of equal order interpolation between velocity and pressure, a streamline upwind Petrov–Galerkin (SUPG) term to counteract the convection dominated instability and a least-squares incompressibility constraint (LSIC) term to handle the Darcy limit where the velocity solution space changes to H^{div}. Additional terms which appear in for instance the Galerkin-least-squares method (GLS) or the unusual stabilized finite element method (USFEM) will not be covered here, but can be viewed in the publication by Franca and Frey [117]. Interpretations of the added terms in a multiscale sense can be viewed in for instance, Hughes [149] and Hughes *et al.* [148]. The connection of these terms to the variational multiscale modeling of turbulence can be found in, for instance, Rasthofer [218], Gamnitzer [121] or Henke [143] and the references therein.

The stabilization term, in the case of a residual based stabilization, is given as

$$\mathcal{S}_h^*(U_h, V_h) = \mathcal{S}_h^{\mathrm{RB}}(U_h, V_h),$$

where

$$\mathscr{S}_h^{\mathrm{RB}}(U_h, V_h) = \sum_{T\in\mathscr{T}_h} (\tau_{M,u}\boldsymbol{r}_M(\boldsymbol{u}_h, p_h), \rho(\boldsymbol{u}_h\cdot\nabla)\boldsymbol{v}_h)_T \tag{2.23}$$

$$+ \sum_{T\in\mathscr{T}_h} (\tau_{M,p}\boldsymbol{r}_M(\boldsymbol{u}_h, p_h), \nabla q_h)_T \tag{2.24}$$

$$+ \sum_{T\in\mathscr{T}_h} (\tau_C\boldsymbol{r}_C(\boldsymbol{u}_h), \nabla\cdot\boldsymbol{v}_h)_T. \tag{2.25}$$

The above term can be divided into a SUPG (2.23), PSPG (2.24) and LSIC (2.25) term with the residuals defined as

$$\boldsymbol{r}_M(\boldsymbol{u}_h, p_h) = \rho\frac{\partial\boldsymbol{u}_h}{\partial t} + \rho(\boldsymbol{u}_h\cdot\nabla)\boldsymbol{u}_h + \nabla p_h - 2\mu\nabla\cdot\boldsymbol{\epsilon}(\boldsymbol{u}_h) - \boldsymbol{f} \tag{2.26}$$

$$\boldsymbol{r}_C(\boldsymbol{u}_h) = \nabla\cdot\boldsymbol{u}_h. \tag{2.27}$$

The scalings $\tau_{M,u} = \tau_{M,p}$ and τ_C are chosen in accordance with Taylor *et al.* [260] and Whiting and Jansen [278] as

$$\tau_{M,u} = \frac{1}{\sqrt{C_1\frac{\rho^2}{\Delta t^2} + \rho\boldsymbol{u}_h\cdot\boldsymbol{G}\rho\boldsymbol{u}_h + C_3\mu^2\boldsymbol{G}:\boldsymbol{G}}} \tag{2.28}$$

$$\tau_C = \frac{1}{\tau_{M,u}\,\mathrm{tr}(\boldsymbol{G})}, \tag{2.29}$$

where $\mathrm{tr}(\boldsymbol{G})$ is the trace of the covariant metric tensor tensor $\boldsymbol{G}$, defined as

$$G_{ij} = \sum_{k=1}^{d}\frac{\partial\xi_k}{\partial x_i}\frac{\partial\xi_k}{\partial x_j}, \tag{2.30}$$

which is related to the mapping between global, $\boldsymbol{x}$, and local element coordinates $\boldsymbol{\xi}$. The constants in (2.28) and (2.29) are chosen as $C_1 = 4.0$ and $C_3 = 36.0$ for linear elements and $C_3 = 144.0$ for quadratic ones.

Remark 2.1 *To verify the validity of the added terms, a short dimensional analysis is conducted. Given that the test functions v_h and q_h are dimensionless, it is clear that the momentum equation (tested with v_h) has the dimension $[N]$ and the continuity equation $[m^3/s]$, as an integration over the domain Ω_h is conducted. As such, the SUPG (2.23) and LSIC (2.25) terms need to have the dimension $[N]$, whereas the PSPG (2.24) has to have the dimension $[m^3/s]$. The dimensions of the following terms can easily be verified to be*

$$\boldsymbol{G} = [1/m^2],\quad \tau_{M,u} = [s\cdot m^3/kg],\quad \tau_C = [kg/(s\cdot m)],\quad \boldsymbol{r}_M = [kg/(m^2\cdot s^2)]\quad \boldsymbol{r}_C = [1/s]$$

Consequently, the dimensions of the following terms can be calculated as

$$(\tau_{M,u}\boldsymbol{r}_M(\boldsymbol{u}_h, p_h), \rho(\boldsymbol{u}_h\cdot\nabla)\boldsymbol{v}_h)_T = [s\cdot m^3/kg]\cdot[kg/(m^2\cdot s^2)]\cdot[kg/(m^3\cdot s)]\cdot[m^3] = [N]$$
$$(\tau_C\boldsymbol{r}_C(\boldsymbol{u}_h), \nabla\cdot\boldsymbol{v}_h)_T = [kg/(s\cdot m)]\cdot[1/s]\cdot[1/m]\cdot[m^3] = [N]$$
$$(\tau_{M,p}\boldsymbol{r}_M(\boldsymbol{u}_h, p_h), \nabla q_h)_T = [s\cdot m^3/kg]\cdot[kg/(m^2\cdot s^2)]\cdot[1/m]\cdot[m^3] = [m^3/s].$$

These dimensions are in accordance with the equations, and as such are added in a fashion adhering to the dimensions of the problem.

2.1.3.2 Continuous Interior Penalty (CIP) Stabilization

An alternative to the residual-based stabilization method, is the so-called continuous interior penalty (CIP) method. The idea of adding interior penalties to stabilize a discretized weak formulation, was first suggested by Douglas and Dupont [97]. These interior penalties are not evaluated in the elements as in the residual-based stabilization. Instead the terms are evaluated on the faces between elements to penalize jumps in gradients between them, and in such a way retain stability of the discretized form. This stabilization method was picked up by Burman and Hansbo [56] and employed on the advection-diffusion-reaction equation. Later, this method of stabilizing discretized equations was extended in ensuing publications to the generalized Stokes problem by Burman and Hansbo [57], the Stokes and Darcy's problem by Burman and Hansbo [58], the Oseen equation by Burman *et al.* [63] and the Navier–Stokes equations by Burman and Fernández [53].

In this thesis, the CIP stabilization is formulated as

$$\mathscr{S}_h^*(U_h, V_h) = \mathscr{S}_h^{\text{CIP}}(U_h, V_h) = s_\beta(\boldsymbol{u}_h; \boldsymbol{u}_h, \boldsymbol{v}_h) + s_u(\boldsymbol{u}_h; \boldsymbol{u}_h, \boldsymbol{v}_h) + s_p(\boldsymbol{u}_h; p_h, q_h), \tag{2.31}$$

with the stabilization operators defined as

$$s_\beta(\boldsymbol{\beta}; \boldsymbol{u}_h, \boldsymbol{v}_h) := \gamma_\beta \sum_{F \in \mathscr{F}_i} \phi_{\beta,F} \rho h \langle [\![\boldsymbol{\beta} \cdot \nabla \boldsymbol{u}_h]\!], [\![\boldsymbol{\beta} \cdot \nabla \boldsymbol{v}_h]\!] \rangle_F, \tag{2.32}$$

$$s_p(\boldsymbol{\beta}; p_h, q_h) := \gamma_p \sum_{F \in \mathscr{F}_i} \phi_{p,F} \rho^{-1} h \langle [\![\boldsymbol{n}_F \cdot \nabla p_h]\!], [\![\boldsymbol{n}_F \cdot \nabla q_h]\!] \rangle_F, \tag{2.33}$$

$$s_u(\boldsymbol{\beta}; \boldsymbol{u}_h, \boldsymbol{v}_h) := \gamma_u \sum_{F \in \mathscr{F}_i} \phi_{u,F} \rho h \langle [\![\nabla \cdot \boldsymbol{u}_h]\!], [\![\nabla \cdot \boldsymbol{v}_h]\!] \rangle_F. \tag{2.34}$$

Notice the fact that the sums in (2.32)–(2.34) are not over all elements in the partition $\mathscr{T}_h$, but over the set of interior facets $\mathscr{F}_i$ in the partition. An interior facet is defined as a facet F, which is shared by two elements, denoted T_F^+ and T_F^-. The jump operator between interior facets is defined as

$$[\![f(\boldsymbol{x})]\!] = f^+(\boldsymbol{x}) - f^-(\boldsymbol{x}) \tag{2.35}$$

where $f^\pm(\boldsymbol{x}) := \lim_{t \to 0} f^\pm(\boldsymbol{x} \pm t\boldsymbol{n}_F)$, with $\boldsymbol{n}_F$ being the unit normal vector on the facet F for $\boldsymbol{x} \in F$. The direction of $\boldsymbol{n}_F$ is defined by the orientation of the facet, determined by the enumeration of the partition $\mathscr{T}_h$, making it well-defined. The element size h is construed from the maximum distance to the facet F from the adjacent elements T_F^+ and T_F^-, as explained in Schott [232]. Furthermore, a quantity defined on the facet is constructed by the average of the quantity between the two adjacent elements, i.e. $f_F(\boldsymbol{x}) = \frac{1}{2}(f_F^+(\boldsymbol{x}) + f_F^-(\boldsymbol{x}))$. The terms $\gamma_\beta, \gamma_u, \gamma_p$ need to be chosen as sufficiently large positive constants, as prescribed in Burman and Fernández [53], Burman *et al.* [63] and Massing *et al.* [184]. The element-wise constant scaling functions are defined as in Massing *et al.* [184] as

$$\phi_{u,T} = \nu + c_u(\|\boldsymbol{\beta}\|_{0,\infty,T} h_T) + c_\sigma(\sigma h_T^2), \tag{2.36}$$

$$\phi_{p,T} = \phi_{\beta,T} = \frac{h_T^2}{\phi_{u,T}} \tag{2.37}$$

where $\nu = \mu/\rho$ and the reactive term $\sigma = 1/(\theta\Delta t)$ when a one-step theta discretization is used for the temporal discretization. For a deeper discussion on the temporal discretization with a CIP stabilization, see Burman and Fernández [54], Burman *et al.* [65] and D'Angelo and Zunino [80]. The convective and reactive scaling shifts are applied as suggested in Schott and Wall [229] and Schott *et al.* [231] as

$$c_u = \frac{1}{6} \quad \text{and} \quad c_\sigma = \frac{1}{12}.$$

The terms introduced for the CIP stabilization can be correlated to the terms in the residual-based stabilization. An equivalency can be drawn between (2.32) and the SUPG stabilization, (2.33) and the PSPG stabilization and (2.34) and the LSIC stabilization, as they alleviate the same instabilities in the discretized formulation.

Remark 2.2 *Similarly as was done for the residual-based terms in Remark 2.1, a short dimensional analysis to verify the validity of the added terms is conducted. The dimensions of the element-wise scaling function are readily deduced from observation to be*

$$\phi_{u,T} = [m^2/s], \quad \phi_{\beta,T} = \phi_{p,T} = [s].$$

From this, the following dimensions can be computed for the terms,

$$\begin{aligned}
&\phi_{\beta,F}\rho h\langle[\![\boldsymbol{\beta}\cdot\nabla\boldsymbol{u}_h]\!],[\![\boldsymbol{\beta}\cdot\nabla\boldsymbol{v}_h]\!]\rangle_F = [s]\cdot[kg/m^2]\cdot[m/s^2]\cdot[1/s]\cdot[m^2] = [N],\\
&\phi_{u,F}\rho h\langle[\![\nabla\cdot\boldsymbol{u}_h]\!],[\![\nabla\cdot\boldsymbol{v}_h]\!]\rangle_F = \cdot[m^2/s]\cdot[kg/m^2]\cdot[1/s]\cdot[1/m]\cdot[m^2] = [N],\\
&\phi_{p,F}\rho^{-1}h\langle[\![\boldsymbol{n}_F\cdot\nabla p_h]\!],[\![\boldsymbol{n}_F\cdot\nabla q_h]\!]\rangle_F = [s]\cdot[m^4/kg]\cdot[kg/(s^2\cdot m^2)]\cdot[1/m]\cdot[m^2] = [m^3/s],
\end{aligned}$$

which confirms that the added terms have the the correct dimensions.

2.1.4 Time Integration of the Discretized Equations

As the Navier–Stokes equations evolves in time, not only a spatial discretization is needed, but also a temporal one. Temporal discretization can be split up in either the use of space-time methods or time-stepping methods. In the case of a space-time method, a weak form in time is employed. Accordingly, a four-dimensional discretization of the problem is necessitated, where the time is partitioned in predetermined intervals on $[0, t_{\text{end}})$. Here t_{end} signifies the end time of the simulation. This temporal discretization has been used in for instance the publications by Bonnerot and Jamet [39], Jamet and Bonnerot [157] and Tezduyar *et al.* [262, 263]. Even though this method seems like a natural extension of the FEM in the temporal direction, it has the drawback of creating large discrete systems.

The alternative is to employ a semi-discretization (or time-stepping) method for the temporal discretization instead. For these approaches, the order in which the equations are discretized can become important, as is discussed in Gamnitzer [121]. Mainly in cases when a residual based stabilization is employed this becomes critical. Therefore, even though a spatial discretization has been shown first, the equations in this thesis are discretized in time and then space in accordance with the method first proposed by Rothe [224]. The alternative would be to use the so-called *method of lines*, for which more information, can be found in Ascher and Petzold [7].

The Navier–Stokes equations can be rewritten as

$$\rho\frac{\partial \boldsymbol{u}}{\partial t} = \boldsymbol{\alpha}(t, \boldsymbol{u}, p) \tag{2.38}$$

$$0 = \lambda(t, \boldsymbol{u}), \tag{2.39}$$

where $\boldsymbol{\alpha}(t, \boldsymbol{u}, p) = -\rho\boldsymbol{u}\cdot\nabla\boldsymbol{u} - \nabla\cdot(-p\boldsymbol{I} + 2\mu\boldsymbol{\epsilon}(\boldsymbol{u})) + \boldsymbol{f}$ and $\lambda(t, \boldsymbol{u}) = \nabla\cdot\boldsymbol{u}$. From this shortened formulation, it becomes apparent that the pressure does not have a time derivative. As such, when discretizing the equations in time, it becomes important to define where the conditions for the pressure (or more accurately, the continuity equation) are to be fulfilled. In accordance with the formulation by Ascher and Petzold [7], the following temporal discretization is made with the *one-step theta* method: given a partition $0 = t^0 < t^1 < \ldots < t^n < t_{\text{end}}$ of the time interval of interest $\mathbb{I} = [0, t_{\text{end}})$, where $\mathbb{I}_n = [t^n, t^{n+1})$ is the n-th interval, the following holds,

$$\rho\frac{\boldsymbol{u}^{n+1} - \boldsymbol{u}^n}{\Delta t} - \Theta\boldsymbol{\alpha}(t^{n+1}, \boldsymbol{u}^{n+1}, p^{n+1}) - (1-\Theta)\boldsymbol{\alpha}(t^n, \boldsymbol{u}^n, p^n) = 0 \tag{2.40}$$

$$0 = g(t^{n+1}, \boldsymbol{u}^{n+1}), \quad 0 = g(t^n, \boldsymbol{u}^n), \tag{2.41}$$

where $\Delta t = t^{n+1} - t^n$. An alternative to the above approach is to only evaluate the pressure at p^{n+1}, as done in for instance John *et al.* [164]. Nonetheless, this approach will not be considered further in the following, and the interested reader is referred to [164] and the references therein. A version to rewrite the equation (2.40) can be done by introducing an acceleration $\boldsymbol{a} = \frac{\partial \boldsymbol{u}}{\partial t}$, where

$$\boldsymbol{a}^{n+1} = \frac{\boldsymbol{u}^{n+1} - \boldsymbol{u}^n}{\Theta\Delta t} - \frac{1-\Theta}{\Theta}\boldsymbol{a}^n. \tag{2.42}$$

This makes it possible to reformulate (2.40) as

$$\rho\frac{\boldsymbol{u}^{n+1} - \boldsymbol{u}^n}{\Delta t} - \Theta\boldsymbol{\alpha}(t^{n+1}, \boldsymbol{u}^{n+1}, p^{n+1}) - \rho(1-\Theta)\boldsymbol{a}^n = 0. \tag{2.43}$$

If $\boldsymbol{a}^0$ and $\boldsymbol{u}^0$ are given, then the by solving for $\boldsymbol{u}^{n+1}$ in (2.43) and updating the acceleration $\boldsymbol{a}^{n+1}$ in (2.42) the system of equations are solvable. Consequently, the evaluation of $f(t^n, \boldsymbol{u}^n, p^n)$ becomes superfluous with this reformulation. The above presented formulation is actually a special case of the *generalized-alpha* scheme by Jansen *et al.* [159], and has also been applied to fluid-structure interaction by Förster [115] and two-phase flows by Schott *et al.* [230].

Applying a spatial discretization to (2.43), the discretized Navier–Stokes equations are given as: find $\boldsymbol{u}_h(t^{n+1}) \in \mathcal{V}_h$ and $p_h(t^{n+1}) \in \mathcal{Q}_h$ such that

$$\mathcal{A}_{\Delta t}(U_h^{n+1}, V_h) + \mathcal{S}_h^*(U_h^{n+1}, V_h) = \mathcal{L}_{\Delta t}(V_h) - \mathcal{H}_n^*(V_h) \tag{2.44}$$

$$\mathcal{A}_{\Delta t}(U_h, V_h) = (\rho\frac{\boldsymbol{u}_h}{\Delta t}, \boldsymbol{v}_h)_\Omega + \Theta\left(a^*(\boldsymbol{u}_h, \boldsymbol{v}_h) + c^*(\boldsymbol{u}_h; \boldsymbol{u}_h, \boldsymbol{v}_h) + b^*(p_h, \boldsymbol{v}_h) - b^*(q_h, \boldsymbol{u}_h)\right) \tag{2.45}$$

$$\mathcal{L}_{\Delta t}(V_h) = (\boldsymbol{f}^{n+1}, \boldsymbol{v}_h)_\Omega + \langle \boldsymbol{h}^{n+1}, \boldsymbol{v}_h\rangle_{\Gamma_{\text{N}}}. \tag{2.46}$$

$$\mathcal{H}_n^*(V_h) = -(\rho\frac{\boldsymbol{u}_h^n}{\Delta t}, \boldsymbol{v}_h)_\Omega - (\rho(1-\Theta)\boldsymbol{a}_h^n, \boldsymbol{v}_h)_\Omega + \mathcal{H}_{\mathcal{I}}^*(V_h), \tag{2.47}$$

with $\mathcal{H}_n^* \in \{\mathcal{H}_n^{\text{RB}}, \mathcal{H}_n^{\text{CIP}}\}$, $\mathcal{H}_{\mathcal{I}}^* \in \{\mathcal{H}_{\mathcal{I}}^{\text{RB}}, \mathcal{H}_{\mathcal{I}}^{\text{CIP}}\}$ and the domain stabilization term $\mathcal{S}_h^*$ defined as in Section 2.1.3.1 for $\mathcal{S}_h^{\text{RB}}$ and Section 2.1.3.2 for $\mathcal{S}_h^{\text{CIP}}$. In the case when a CIP-stabilization

is employed, the term $\mathscr{S}_h^{\text{CIP}}(U_h^{n+1}, V_h)$ is straightforward to define. However, in the case of a residual-based stabilization $\mathscr{S}_h^{\text{RB}}$, the residual $\boldsymbol{r}_M$ needs to be specified as it contains a time derivative of the primary variable. Instead of using $\boldsymbol{r}_M$ defined in (2.26) a temporal discretization of the residual is conducted as

$$\boldsymbol{r}_M(\boldsymbol{u}_h^{n+1}, p_h^{n+1}) = \rho\frac{\boldsymbol{u}_h^{n+1}}{\Delta t} + \Theta(\rho(\boldsymbol{u}_h^{n+1}\cdot\nabla)\boldsymbol{u}_h^{n+1} + \nabla p_h^{n+1} - 2\mu\nabla\cdot\boldsymbol{\epsilon}(\boldsymbol{u}_h^{n+1}) - \boldsymbol{f}^{n+1}) \quad (2.48)$$

which leads to the additional term for the previous time step,

$$\mathscr{H}_{\mathscr{S}}^{\text{RB}}(V_h) = (-\rho\frac{\boldsymbol{u}_h^n}{\Delta t} - \rho\Delta t(1-\Theta)\boldsymbol{a}_h^n, \tau_{M,u}^{n+1}(\rho\boldsymbol{u}_h^{n+1}\cdot\nabla)\boldsymbol{v}_h + \tau_{M,p}^{n+1}\nabla q_h)_\Omega. \quad (2.49)$$

By contrast, in the case of a CIP stabilization, the term $\mathscr{H}_{\mathscr{S}}^{\text{CIP}}(V_h) = 0$.

Even though the proposed formulation (2.44) removes the need to evaluate terms at the previous time step, it necessitates a larger memory usage as $\boldsymbol{a}_h^n$ has to be stored in addition to $\boldsymbol{u}_h^{n+1}$, $\boldsymbol{u}_h^n$ and p_h^{n+1}. Furthermore, an initial acceleration needs to be prescribed to start the algorithm (unless $\Theta = 1$ is chosen).

A more thorough analysis of time-integration schemes for a stabilized finite element methods for incompressible flow can be found in the publication by Dettmer and Perić [88]. As this thesis is mainly concerned with first order time integration schemes, the interested reader is referred to Karniadakis *et al.* [167], Montlaur *et al.* [196] and the references therein for higher-order temporal discretizations.

2.2 Defining the Computational Domain

In the case of an unfitted finite element method, the background mesh $\widehat{\mathscr{T}}_h$ does not conform to the domain Ω, as depicted in Figure 2.3. As the mesh does not define the domain, another method to determine the computational domain Ω_h needs to be utilized. The way of defining this domain, can be split up into two camps: explicit domain descriptions and implicit domain descriptions. An explicit domain description, also known as a front-tracking method, employs a Lagrangian interface tracking for the interface Γ_h, and as such defines the computational domain Ω_h. As an explicit domain description is sparsely used in this thesis, the interested reader can find more on this topic in the thesis by Schott [232].

An implicit domain description has been used extensively in the field of computational fluid dynamics, and in particular for multiphase flows. These methods include, for instance, the Volume-of-fluid (VOF) method, as presented in Hirt and Nichols [146] and Noh and Woodward [206], and the level-set method, explained in, for instance, the textbooks by Sethian [235] or Fedkiw and Osher [109]. In this thesis, the level-set method will be primarily utilized. As such, a more thorough explanation of this method is given in the ensuing sections.

2.2.1 Implicit Domain Description, the Level-Set Method

A level-set function describes a $(d-1)$-dimensional manifold, by defining a scalar function $\phi(\boldsymbol{x}, t)$ in the d-dimensional domain $\widehat{\Omega}$. The zero contour of this function defines the manifold Γ as

$$\Gamma(t) := \{\boldsymbol{x} \in \widehat{\Omega} \mid \phi(\boldsymbol{x}, t) = 0\}. \quad (2.50)$$

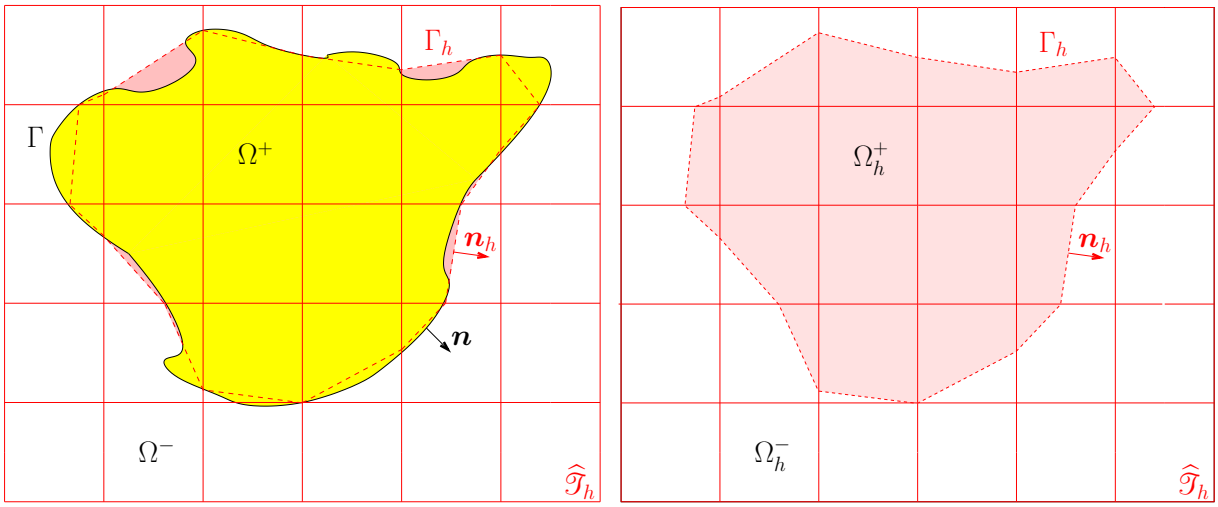

(a) Continuous domain (b) Cut domain

Figure 2.3: The decomposition of the domain $\widehat{\Omega} = \Omega^+ \cup \Omega^-$ is displayed in a) for the continuous problem, and in b) for the discretized, cut problem with $\widehat{\Omega}_h = \Omega_h^+ \cup \Omega_h^-$. The physical domain Ω, is defined by the positive domain Ω^+. Equivalently, the computational domain Ω_h is defined by the positive domain Ω_h^+, approximated by the level-set $\phi_h > 0$.

The level-set function also splits the domain $\widehat{\Omega}$ into two specific domains Ω^+ and Ω^-, where the intersection of the two, defines the interface Γ. The domain Ω^+ is defined where the level-set function ϕ is positive and the domain Ω^- where it is negative, hence, the following connections between the manifolds and the level-set can be made,

$$\phi(\boldsymbol{x},t) = \begin{cases} > 0 & \forall \boldsymbol{x} \in \quad \Omega^+(t), \\ = 0 & \forall \boldsymbol{x} \in \quad \Gamma(t), \\ < 0 & \forall \boldsymbol{x} \in \quad \Omega^-(t). \end{cases} \tag{2.51}$$

A more general construction for the level-set function, where an arbitrary amount of domains can be defined, is demonstrated in the works by Merriman *et al.* [190], Smith *et al.* [241], Zhao *et al.* [286] or Zlotnik and Díez [290]. Nonetheless, in this work, only two domains at most will be utilized, making (2.51) sufficient for the intended use.

The level-set function is usually defined as being a signed distance functions, that is

$$\phi(\boldsymbol{x},t) = \begin{cases} - \min\limits_{\widehat{\boldsymbol{x}} \in \Gamma(t)} (|\boldsymbol{x} - \widehat{\boldsymbol{x}}|) \text{ if } \operatorname{sign}((\boldsymbol{x} - \widehat{\boldsymbol{x}}) \cdot \boldsymbol{n}) \geq 0 \\ \min\limits_{\widehat{\boldsymbol{x}} \in \Gamma(t)} (|\boldsymbol{x} - \widehat{\boldsymbol{x}}|) \text{ if } \operatorname{sign}((\boldsymbol{x} - \widehat{\boldsymbol{x}}) \cdot \boldsymbol{n}) < 0, \end{cases} \tag{2.52}$$

where the normal vector $\boldsymbol{n}$, defined on the interface Γ, points from the positive domain Ω^+ into the negative domain Ω^-. The effect of this signed distance property is that

$$|\nabla \phi(\boldsymbol{x},t)| = 1, \tag{2.53}$$

and

$$\boldsymbol{n}(\boldsymbol{x}) = -\frac{\nabla \phi}{|\nabla \phi|}, \quad \text{for } \boldsymbol{x} \in \Gamma, \tag{2.54}$$

that is, the normal of Γ can be defined by the gradient of the level-set function. Another important geometric quantity, which arises in two-phase flows with surface tension, is the mean curvature of the interface $\Gamma(t)$. This quantity can be computed as

$$\kappa = -\nabla \cdot \boldsymbol{n} = \nabla \cdot \left(\frac{\nabla \phi}{|\nabla \phi|} \right) = \left(\frac{\Delta \phi}{|\nabla \phi|} - \frac{\nabla \phi \cdot \nabla |\nabla \phi|}{|\nabla \phi|^2} \right). \tag{2.55}$$

The above equations are sufficient to define a surface Γ if it is not evolving in time. However, in plenty of applications the surface will evolve in time, which is the case in, for instance, two-phase flows. Consequently, a transport equation for the level-set is needed to determine its evolution in time. This time-dependency can be described by a standard advection equation as

$$\frac{\partial \phi}{\partial t} + \boldsymbol{c} \cdot \nabla \phi = 0 \quad \text{in } \widehat{\Omega} \times (0, T), \tag{2.56}$$

$$\phi = \phi_0 \quad \text{in } \widehat{\Omega} \times \{0\}, \tag{2.57}$$

where $\boldsymbol{c}$ is the advective velocity propagating the level-set in time. In simulations of two-phase flows, the advective velocity is normally prescribed as the velocity of the fluid flow.

The discretized form of the level-set equation (2.56) will be presented here without much discussion on the weak form and its intricacies. For a deeper discussion on the weak form and discretization of the advection equation, the interested reader is referred to Donea and Huerta [94] and Gresho and Sani [129] and the references therein. Introducing the function space for the variational form of the level-set equation

$$\mathscr{P}_{\phi_{\text{in}}} = \left\{ \phi \in H^1(\Omega) \mid \phi = \phi_{\text{in}} \text{ on } \Gamma_{\text{in}} \right\}, \tag{2.58}$$

where Γ_{in} defines a boundary with inflow, i.e. $(\boldsymbol{n} \cdot \boldsymbol{c}) < 0$. The semi-discrete weak form is given for a partition $\mathscr{T}_h$ as: find $\phi_h \in \mathscr{X}_h \cap \mathscr{P}_{\phi_{\text{in}}}$ such that for all $w_h \in \mathscr{X}_h \cap \mathscr{P}_0$

$$\left(w_h, \frac{\partial \phi_h}{\partial t} \right)_{\widehat{\Omega}_h} + (w_h, \boldsymbol{c} \cdot \nabla \phi_h)_{\widehat{\Omega}_h} + \sum_{T \in \widehat{\mathscr{T}}_h} (\boldsymbol{c} \cdot \nabla w_h, \tau_{\text{LS}} r_{\text{LS}}(\phi_h))_T = 0, \tag{2.59}$$

The parameters for the SUPG stabilization is chosen in accordance with Taylor *et al.* [260] as

$$r_{LS}(\phi_h) = \frac{\partial \phi_h}{\partial t} + \boldsymbol{c} \cdot \nabla \phi_h, \tag{2.60}$$

$$\tau_{LS} = \frac{1}{\sqrt{\frac{4}{\Delta t^2} + \boldsymbol{c} \cdot \boldsymbol{G} \boldsymbol{c}}}. \tag{2.61}$$

where the covariant metric tensor $\boldsymbol{G}$ is defined the same way as in (2.30). The time discretization of (2.59) is done in an identical manner as was done for the Navier–Stokes equation in Section 2.1.4 with a one-step theta discretization.

2.2.1.1 Piecewise Linear Approximation of Γ

In the previous section, it was shown how to depict an interface Γ with a level-set function ϕ in (2.51). This equation still holds true when the discretized level-set function ϕ_h is considered, but

now an approximation Γ_h of Γ is received instead. The issue here is that Γ_h is only described implicitly, which becomes an issue if terms are to be evaluated on Γ_h. This is for instance the case when boundary condition are imposed weakly for the CutFEM. Hence, an explicit description to enable this evaluation is needed. The question then arises, how to construe a explicit interface description Γ_h from the level-set function ϕ_h, and through this also define the decomposition of $\widehat{\Omega}_h$ into Ω_h^+ and Ω_h^-. In this thesis, piecewise linear approximations $\mathcal{I}(\phi_h)$ of ϕ_h on regular refinements and subdivisions of non-planar interface segments, as done in Groß and Reusken [131] and Groß *et al.* [134], are applied. The explicit description of the interface can then be defined as

$$\Gamma_h = \left\{ \boldsymbol{x} \in \widehat{\Omega} \mid \mathcal{I}(\phi_h)(\boldsymbol{x}, t) = 0 \right\}, \tag{2.62}$$

and the domains Ω_h^+ and Ω_h^- are defined by the positive and negative parts of $\mathcal{I}(\phi_h)$, respectively.

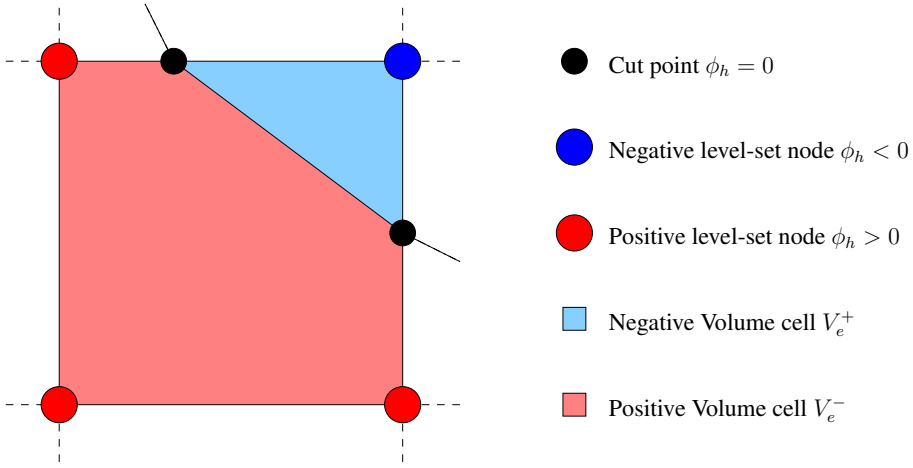

Figure 2.4: A cut bi-linear quadrilateral element T, intersected by the interface Γ is depicted in this figure. The nodes of the element are colored either blue for a negative level-set value, or red for a positive one. On the edges, the cut points calculated from a linear interpolation between the nodes is denoted in black. The ensuing decomposition into the volume cell V_e^- and V_e^+, is depicted in blue and red, and the interface Γ_h is obtained at the intersection of these two volume cells.

The mapping $\mathcal{I}(\phi_h)$ might at first seem superfluous for linear elements. However, in the case of bi-linear elements, ϕ_h is not linear in the interior of the element owing to the mixed terms. Accordingly, the piecewise linear approximation $\mathcal{I}(\phi_h)$ of ϕ_h has merit in this case. The process of defining the explicit surface Γ_h with $\mathcal{I}(\phi_h)$ for a bi-linear quadrilateral element is illustrated in Figure 2.4. The process can be explained as follows, cut points (where $\phi_h = 0$) are found along edges of the elements by linear interpolation between the nodes on the edges. These cut points are then connected and volume cells V_e^- and V_e^+ are formed, as well as the interface $\Gamma_h|_T$ between these volumes. This procedure is carried out in a similar fashion as in Henke [143], however, in this work the cut of an element is performed in global coordinates, and not as in the aforementioned work, in the local configuration of the element.

As this thesis will make use of quadratic elements as well, a method to create an explicit description of Γ_h from ϕ_h is also needed. The procedure here is to decompose the quadratic element into its linear equivalency, and then apply the method described in the above paragraph

for linear elements on this decomposition. Consequently, a bi-quadratic quadrilateral element is divided into four bi-linear quadrilateral elements on which the above procedure is conducted, as demonstrated in Figure 2.5. This method, for creating explicit descriptions of the interface Γ_h and domains Ω_h^+ and Ω_h^-, suffers from the disadvantages that it only leads to a linear approximation of domains, regardless of the order of elements used in $\mathscr{P}_h$. This introduced geometrical approximation error can start to dominate the solution when higher order elements are employed, and will be further investigated in Chapter 4.

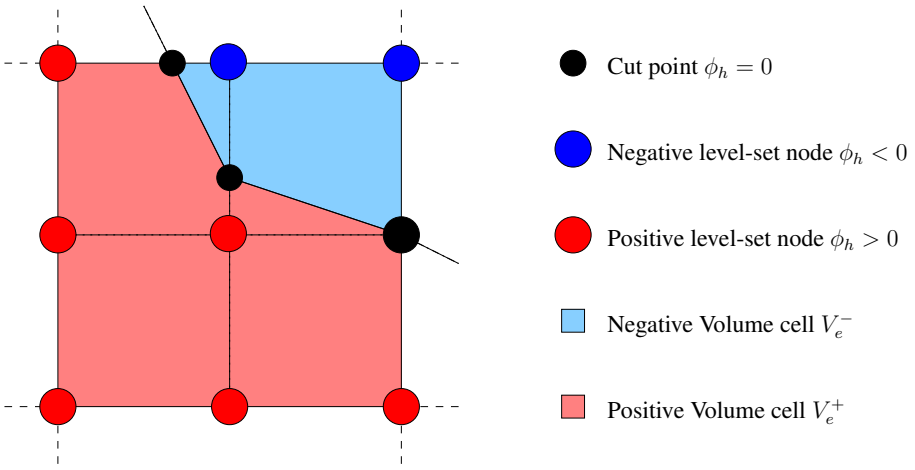

Figure 2.5: A cut bi-quadratic quadrilateral element T, intersected by the interface Γ is depicted in this figure. The nodes of the element are colored either blue for a negative level-set value, red for a positive one or black for a value of zero. As depicted with dotted lines, the quadratic element is decomposed into four sub-elements with each four nodes. These sub-elements are treated as bi-linear elements, and the process depicted in Figure 2.4 is carried out in each sub-element. The ensuing decomposition into the volume cell V_e^- and V_e^+, is depicted in blue and red, and the interface Γ_h is obtained at the intersection of these two volume cells.

2.2.1.2 Reinitialization of the Level-Set

In general, when a level-set field is advected by a velocity $\boldsymbol{c}$ it loses its signed distance property. This makes the calculations of the normal $\boldsymbol{n}$ (2.54) and the curvature κ (2.55) with the level-set function no longer valid. Furthermore, depending on the velocity $\boldsymbol{c}$, large gradients in the level-set may form and deteriorate the solution of the level-set.

Two different approaches can be undertaken to prevent the loss of the signed distance property and the creation of large gradients in the level-set solution. One option is to modify the advection velocity $\boldsymbol{c}$ of the level-set. This is for instance done by Adalsteinsson and Sethian [1], where the advective field is extracted on the surface Γ_h and extensions from this surface, which preserve the signed distance property, are made. The other option is to reinitialize the signed distance property of the level-set at regular intervals. This reinitialization can be done in various ways. A fast marching method can be applied where the Eikonal equation $|\nabla\phi| = 1$ is solved, as originally introduced by Sethian [234]. Another method is a reinitialization technique first suggested by Li *et al.* [179], which recently Basting and Kuzmin [22] reformulated as an elliptic partial differential equation, making it ideal for the FEM. Finally, a geometric reinitialization can be used, where distances to the explicit interface description Γ_h are calculated to reinitialize the level-set.

For this geometric reinitialization, the idea is to find the shortest distance to the piecewise linear surface Γ_h. This surface Γ_h is first tessellated into triangles (assuming here the three dimensional case), thus creating extra nodes on the surface apart from the already introduced cut points in Figure 2.4 and Figure 2.5. Edges make up the boundary of these triangles, and the triangles themselves are here named as boundary cells. The shortest distance to Γ_h is found by computing the minimum distance for a node in the computational mesh to a node, edge and boundary cell on this surface and then taking the minimum of these as the shortest distance. The Algorithm 2.1 displays this geometric reinitialization algorithm in more detail.

Algorithm 2.1 Geometric reinitialization of a level-set function

1: INPUT: Approximated boundary Γ_h and level-set function ϕ_h at time t.
2: **for** All nodes $\boldsymbol{x}^*$ in $\widehat{\mathcal{T}}_h$ **do**
3: **for** All nodes $\boldsymbol{x}_{\Gamma_h}$ in Γ_h **do**
4: Find minimum to node on cut surface
 $d_{\text{min}}^{\text{node}}(\boldsymbol{x}^*) = \min_{\boldsymbol{x}_{\Gamma_h} \in \Gamma_h} (d_{\text{min}}^{\text{node}}(\boldsymbol{x}^*), |\boldsymbol{x}^* - \boldsymbol{x}_{\Gamma_h}|)$
5: **end for**
6: **for** All boundary cells $\Gamma_h|_T$ in Γ_h **do**
7: Calculate if a projection to the node can be made with the normal $\boldsymbol{n}_h$ from the boundary cell $\Gamma_h|_T$ i.e. solve
 $\boldsymbol{x} + \alpha \boldsymbol{n}_h - \boldsymbol{x}^* = 0 \;\; \text{for } \boldsymbol{x} \in \Gamma_h|_T$
8: Set minimum for for all projections where solution exists
 $d_{\text{min}}^{\text{surface}}(\boldsymbol{x}^*) = \min_{\Gamma_h|_T \in \Gamma_h} (d_{\text{min}}^{\text{surface}}(\boldsymbol{x}^*), |\boldsymbol{x}^* - \boldsymbol{x}|)$
9: **end for**
10: **for** All edges of boundary cells $\epsilon_h|_T$ in Γ_h **do**
11: Find if minimum exists to an edge. First calculate
 $s = (\boldsymbol{x}_2 - \boldsymbol{x}_1)(\boldsymbol{x}^* - \boldsymbol{x}_1)$,
 where $\boldsymbol{x}_1, \boldsymbol{x}_2$ are the coordinates of the two vertexes of the edge.
12: **if** $s > 0$ && $s < |\boldsymbol{x}_2 - \boldsymbol{x}_1|$ **then**
13: $d_{\text{min}}^{\text{edge}}(\boldsymbol{x}^*) = \min_{\epsilon_h|_T \in \Gamma_h} (d_{\text{min}}^{\text{edge}}(\boldsymbol{x}^*), |(\boldsymbol{x}^* - \boldsymbol{x}_1) - s(\boldsymbol{x}_2 - \boldsymbol{x}_1)|)$
14: **end if**
15: **end for**
16: $d_{\text{min}}(\boldsymbol{x}^*) = \min(\{d_{\text{min}}^{\text{node}}(\boldsymbol{x}^*), d_{\text{min}}^{\text{surface}}(\boldsymbol{x}^*), d_{\text{min}}^{\text{edge}}(\boldsymbol{x}^*)\})$
17: $\phi_h^{\text{new}}(\boldsymbol{x}^*) = \text{sign}(\phi_h(\boldsymbol{x}^*)) d_{\text{min}}(\boldsymbol{x}^*)$
18: **end for**
19: OUTPUT: The redistanced level-set field ϕ_h^{new}.

2.2.1.3 Mass Conservation

Owing to under resolution of the computational mesh to depict corners or thin films of the level-set, a loss or gain of mass in one of the subdomains Ω_h^+ or Ω_h^- can occur. Furthermore, the numerical diffusion stemming from the solution of the transport equation (2.59) can distort the interface Γ_h. Lastly, the redistancing of the level-set function can also introduce numerical

artifacts which perturb the interface. To preserve the mass, or volume, of the initial domain Ω_h^+ or Ω_h^- at $t = 0$, correction methods can be imposed. This can be done in a global way, where a measure of the initial volume for the respective domain is introduced. The change of volume for one of the subdomains Ω_h^+ or Ω_h^- determines a value to be added to the level-set. An example of such an update is the following,

$$\widehat{\phi}(t_{n+1}) = \phi(t_{n+1}) - \frac{V(\Omega^+(t_{n+1})) - V(\Omega^+(t_0))}{A(\Gamma(t_{n+1}))}, \tag{2.63}$$

where $\widehat{\phi}(t_{n+1})$ is the updated level-set field, $V(\Omega^+(t_{n+1})$ the volume of the positive domain and $A(\Gamma(t_{n+1}))$ the area of the interface separating the positive and negative phases at time t_{n+1}. This global way of preserving the mass of each subdomain has been employed in the works by Rasthofer [218], Croce *et al.* [78] and Lee *et al.* [176]. More information on this method can be found in the references within these works. Nonetheless, this global way of correcting the level-set field is only viable in a limited number of cases, as it implies that even though a loss of mass occurs in a small local region, it will effect the entire level-set function.

To conduct corrections in a local fashion, the hybrid-particle level-set method was proposed by Enright *et al.* [107]. This method suggests adding Lagrangian particles in the vicinity of the interface to enhance the accuracy and local mass-conservation in this region. A thorough explanation of how this method works in practice can be found in the thesis by Rasthofer [218].

2.2.1.4 Smoothing of Gradients

Given that continuous finite elements are employed for the discretization of the level-set, the gradient $\nabla\phi_h$ will be discontinuous between elements, making normals calculated with (2.54) discontinuous. In addition to this, if linear elements are used for the discretization of the level-set, the gradient $\nabla\phi_h$ will be constants in parts of the element. Also the piecewise linear surface Γ_h created from the discretized level-set equation, as explained in Section 2.2.1.1, leads to a discontinuous (more precisely, piecewise constant) normal $\boldsymbol{n}_h$ on the surface.

Now, if the curvature of a surface is to be evaluated with equation (2.55), which is needed in the modeling of two-phase flows in Chapter 5, neither the normal $\boldsymbol{n}_h$ from the surface Γ_h nor the gradient $\nabla\phi_h$ computed with a linear element can be used, as they always return a zero curvature. Additionally, when imposing a Navier-slip type boundary condition, a continuous normal on the surface Γ_h is needed to overcome the so-called Babuška paradox [12], which is further investigated in Chapter 4.

Consequently, the need arises to transform the discontinuous gradient field $\nabla\phi_h$ into a continuous smoothed field $\widetilde{\nabla\phi_h}$. Three possible methods to conduct this transformation are mentioned here.

Mean-value averaging This way of constructing a continuous gradient field can be done in various ways, here the method employed in the thesis by Henke [143] is briefly presented. The smoothed field $\widetilde{\nabla\phi_h}$ is created by averaging the gradients at a node A from all $n_{\mathrm{e},A}$ adjacent elements, which can be summarized to

$$\widetilde{\nabla\phi_h}_A = \frac{1}{n_{\mathrm{e},A}} \sum_{j=1}^{n_{\mathrm{e},A}} \nabla\phi_h(\boldsymbol{x}_A)|_{\mathrm{e}=j}. \tag{2.64}$$

The newly calculated gradient is continuous, i.e. $\widetilde{\nabla\phi_h} \in C^0$ and is evaluated as

$$\widetilde{\nabla\phi_h}(\boldsymbol{x}) := \sum_{A=0}^{\mathrm{n_{node}}} N_A(\boldsymbol{x})\widetilde{\nabla\phi_h}_A, \tag{2.65}$$

where $\widetilde{\nabla\phi_h}_A$ is the value at the node A of the smoothed gradient, $\mathrm{n_{node}}$ is the number of nodes in the computational mesh and N_A is the shape function of the elements from the partition of the computational mesh.

L^2-projection Another way to create a continuous gradient field, is to utilize a L^2-projection from the discontinuous space onto a continuous one. This approach has been applied successfully in, for instance, Jansen *et al.* [158]. However, in contrast to the previously introduced mean-value averaging, where only a small local system needed to be calculated, a global system of equations needs to be solved for the L^2-projection to obtain the smoothed gradient. The following system of equations need to be solved for $i = 1, 2$ and 3, where i defines the spatial direction, to obtain the L^2-projection of the gradient $\nabla\phi_h$ as

$$(w_h, (\boldsymbol{b}_h)_i)_{\widehat{\Omega}} = (w_h, (\nabla\phi_h)_i)_{\widehat{\Omega}}. \tag{2.66}$$

The vector $\boldsymbol{b}_h$ is here defined by (2.65), and by solving for the values $\widetilde{\nabla\phi_h}_A$ at the nodes of the computational mesh, the smoothed gradient field $\widetilde{\nabla\phi_h}$ can be constructed.

Super convergent patch recovery Lastly, a method first introduced by Zienkiewicz and Zhu [287, 288], called super convergent patch recovery (SPR), can be employed for the gradient smoothing. This method creates patches around a node on the mesh and fits a polynomial to the Gauss points, i.e. the super convergent points, of this patch. On the aforementioned patches the gradients are reconstructed as

$$\widetilde{\nabla\phi_h}(\boldsymbol{x}) = \boldsymbol{P}(\boldsymbol{x})\boldsymbol{A}, \tag{2.67}$$

where the polynomial of choice for linear elements will be $\boldsymbol{P} = [1, x_1, x_2, x_3]$ with the coefficients $\boldsymbol{A}_i = [a_0^i, a_1^i, a_2^i, a_3^i]$. The chosen polynomial $\boldsymbol{P}$ could also include bi-linear and tri-linear terms (in the case of bi-linear quadrilateral elements or tri-linear hexahedral elements), nonetheless, in this thesis only linear terms will be utilized regardless of the underlying element. To find the coefficients $\boldsymbol{A}$, the polynomial of the patch is fitted to the values of the gradient $\nabla\phi_h$ at the super convergent Gauss points of the elements in the patch. As such, the following function is to be minimized for each spatial direction $i \in \{0, 1, 2\}$,

$$F(\boldsymbol{A}_i) = \sum_{k=1}^{\mathrm{n_{GP}}} \left((\nabla\phi_h)_i(\boldsymbol{x}_{\mathrm{GP}}^k) - \boldsymbol{P}(\boldsymbol{x}_{\mathrm{GP}}^k)\boldsymbol{A}_i\right)^2, \tag{2.68}$$

with $\boldsymbol{x}_{\mathrm{GP}}^k$ being the k-th Gauss point and $\mathrm{n_{GP}}$ representing the number of Gauss points in the element; see Figure 2.6 for an illustration of a patch consisting of bi-linear quadrilateral elements. The minimum of equation (2.68) is obtained when

$$\sum_{k=1}^{\mathrm{n_{GP}}} \boldsymbol{P}(\boldsymbol{x}_{\mathrm{GP}}^k)^T\boldsymbol{P}(\boldsymbol{x}_{\mathrm{GP}}^k)\boldsymbol{A}_i = \sum_{k=1}^{\mathrm{n_{GP}}} \boldsymbol{P}(\boldsymbol{x}_{\mathrm{GP}}^k)^T(\nabla\phi_h)_i(\boldsymbol{x}_{\mathrm{GP}}^k), \tag{2.69}$$

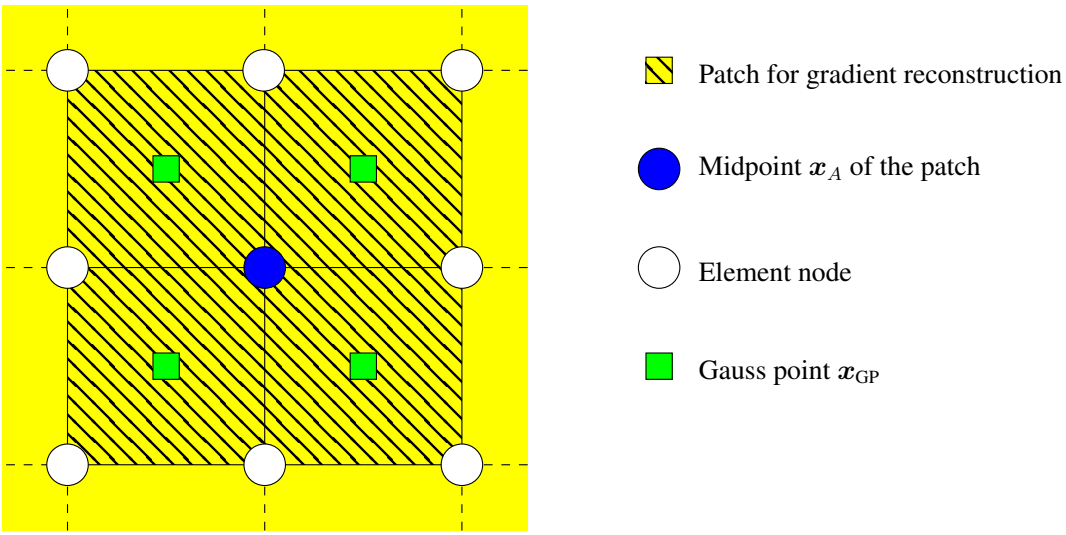

Figure 2.6: A patch for reconstruction of a gradient, for a partition consisting of quadrilateral bi-linear elements. In the figure, the patch is visually marked to contain four elements. Each element contributes with one Gauss point $\boldsymbol{x}_{\text{GP}}$, marked in green, hence $\text{n}_{\text{GP}} = 4$. The gradient is reconstructed at the midpoint $\boldsymbol{x}_A$ of the patch, marked in blue.

which is a linear system of equations of the form $\boldsymbol{B}\boldsymbol{A}_i = \boldsymbol{b}_i$, with $\boldsymbol{B} = \sum_{k=1}^{\text{n}_{\text{GP}}} \boldsymbol{P}(\boldsymbol{x}_{\text{GP}}^k)^T \boldsymbol{P}(\boldsymbol{x}_{\text{GP}}^k)$ and $\boldsymbol{b}_i = \sum_{k=1}^{\text{n}_{\text{GP}}} \boldsymbol{P}(\boldsymbol{x}_{\text{GP}}^k)^T (\nabla \phi_h)_i(\boldsymbol{x}_{\text{GP}}^k)$. The matrix $\boldsymbol{B}$ is small (only depending on the number of terms in the polynomial $\boldsymbol{P}$), and as such it can be inverted to directly solve for $\boldsymbol{A}_i$. From this, the reconstructed gradient at a node A in the background mesh can be evaluated as

$$\widetilde{\nabla \phi_h}_A = \boldsymbol{P}(\boldsymbol{x}_A)\boldsymbol{A}, \tag{2.70}$$

where the smoothed gradient $\widetilde{\nabla \phi_h}(\boldsymbol{x})$ is given by (2.65). The above procedure takes care of the inner nodes of the mesh, however, at the boundary nodes there does not exist a sufficient amount of surrounding elements to solve the system of equations in (2.69). Owing to this, the nodes on the boundaries are reconstructed from a patch created by the closest interior node. For a more thorough discussion on this method see the publication by Zienkiewicz and Zhu [288].

2.3 Extension to a CutFEM Formulation for an Incompressible Fluid

In Section 2.1, a fitted FEM formulation for the incompressible Navier–Stokes equations was presented. This approach is valid in a multitude of cases, however, at times a fitted mesh approach might be undesirable or unfeasible for the problem at hand. For instance, creating a conform computational mesh can be a tedious and time consuming process, as demonstrated in the creation of a fully 3D mesh from biological image data by Antiga *et al.* [6], or in the creation of conforming computational meshes from geological image data, where complex large scale networks of fractures might exists, as demonstrated in Dassi *et al.* [82].

The issue with creating a conforming mesh becomes particularly pronounced if the geometry of the model undergoes large changes in the course of the simulation. This is the case in

simulations of fluid-structure interaction (FSI) or multiphase flows problems, where domains may undergo large deformation and in some cases even topological changes. These issues can make conventional Arbitrary-Lagrangian–Eulerian (ALE) based methods undesirable to use for these kinds of problems, as costly remeshing may be necessitated. A way to resolve these issues, can be done by employing an unfitted finite element method approach instead, of which the CutFEM is introduced in more detail in the following.

2.3.1 Introducing Discontinuities into Solution Spaces

Discontinuities may appear in the modeling of physical fields when fields change drastically over small length scales. This type of problems include, immiscible two-phase flows, fluid structure interaction and flow over porous media. In addition, discontinuities can be a construct of how the discretization of the problem is done. Given a single field problem, an unfitted mesh approach can be utilized for the discretization. This introduces a discontinuity between the physical field in the domain of interest, and void outside of it.

To represent these discontinuities in the solution space, an unfitted finite element method, such as the CutFEM can be used. The CutFEM originates from the eXtended Finite Element Method (XFEM) proposed by Belytschko and Black [31] and Moës *et al.* [192] to simulate crack growth without the necessity to perform remeshing. This was achieved by providing an enhanced function basis, capable of representing discontinuities in the solution space. Other methods which utilize a similar approach are the Partition of Unity Method (PUM) [11, 188] and the General Finite Element Method (GFEM) [99, 250]. The naming convention of defining the aforementioned methods as XFEM, was done in the context of fracture mechanics by Dolbow *et al.* [93]. A comprehensive review on the XFEM, can be found in Fries and Belytschko [119] and Belytschko *et al.* [33].

Since the introduction of the XFEMs, they have been applied to a variety of problems. For material modeling, a comprehensive review making use of these methods was carried out by Belytschko *et al.* [32]. In the case of simulation of solidification processes, the XFEMs have been successfully put to use, as demonstrated by Chessa *et al.* [71], Ji *et al.* [160] and Merle and Dolbow [189]. The methods have also had success in the field of fluid-structure interaction (FSI) as in, for instance, Gerstenberger and Wall [126], Legay *et al.* [177] Zilian and Legay [289], Burman and Fernández [55] and Wagner *et al.* [276]. Approaches with embedding meshes around immersed structures, to better resolve the boundary layer of the surrounding fluid, have been developed by Shahmiri *et al.* [238] and extended to the case of fluid-structure interaction in Massing *et al.* [186] and Schott *et al.* [231]. Also in the field of multiphase flows, the XFEMs have enjoyed great success. Originally introduced by Chessa and Belytschko [70] to this field of study, a plethora of publications appeared afterwards, exploring different enrichment approaches to capture the strong discontinuity for the pressure and the weak discontinuity for the velocity. The publications by Minev *et al.* [191], Groß and Reusken [132], Rasthofer *et al.* [217], Sauerland and Fries [228], Diez *et al.* [90] and Schott *et al.* [230] provide an overview of the different approaches to model two-phase flows with the XFEMs. The extension to premixed combustion was done by Van der Bos and Gravemeier [268] and Henke [143], where also a strong discontinuity for the velocity forms at the flame front. Lastly, also in the modeling of biofilm growth the XFEM has been successfully utilized, as done in for instance the publication by Duddu *et al.* [100].

The unfitted finite element method employed in this thesis is the cut finite element method (CutFEM) by Burman *et al.* [64]. This method has a direct link to the XFEM, as it can be viewed as such a method with a Heaviside function enrichment. The difference between the CutFEM and XFEM lies in how this enrichment is viewed. In the XFEM, an enriched function spaces is thought of as a standard function space with the addition of enrichment functions in elements containing discontinuities. By contrast, in the CutFEM, function spaces are not thought of as enriched, rather, a standard finite element space is considered, which support is cut-off outside the given computational domain. As such, the terminology can be used interchangeably, but throughout this thesis the CutFEM perspective will be pursued. For a detailed explanation on the connection between the two, see Schott [232].

As such, it remains to define how the function space and support of the finite element space works in a CutFEM approach.

2.3.1.1 Brief Introduction on Notation for the CutFEM

Given an unfitted background mesh $\widehat{\mathcal{T}}_h$ with mesh size parameter $h > 0$, covering the computational domain, i.e. $\overline{\Omega^+} \subset \widehat{\mathcal{T}}_h$, as shown in Figure 2.7a; the mesh can then be decomposed into useful components to define the CutFEM. First of all, an active mesh $\mathcal{T}_h$ is the subset of elements of the unfitted background mesh $\widehat{\mathcal{T}}_h$ which are covered at least partially by the domain Ω^+. This can be expressed as follows,

$$\mathcal{T}_h := \left\{ T \in \widehat{\mathcal{T}}_h : T \cap \Omega^+ \neq \emptyset \right\}. \tag{2.71}$$

Equivalently the inactive part is defined from the elements not contained in $\mathcal{T}_h$ but in $\widehat{\mathcal{T}}_h$. A fictitious domain can also be introduced as $\Omega_h^{+,*}$, which is the union of the minimal subset $\mathcal{T}_h \subset \widehat{\mathcal{T}}_h$ covering Ω^+. A mesh $\mathcal{T}_h$ is called a *fitted mesh* if $\overline{\Omega^+} = \overline{\Omega_h^{+,*}}$ and an *unfitted mesh* if $\overline{\Omega^+} \subsetneq \overline{\Omega_h^{+,*}}$. Furthermore, the subset of elements intersecting the boundary Γ is defined as

$$\mathcal{T}_\Gamma := \{ T \in \mathcal{T}_h : T \cap \Gamma \neq \emptyset \}. \tag{2.72}$$

The active mesh $\mathcal{T}_h$, the fictitious domain $\Omega_h^{+,*}$ and the set of intersected elements are visualized in Figure 2.7b. Given the definition of $\mathcal{T}_h$, the same finite element approximation space $\mathcal{X}_h$ can be applied for the active mesh $\mathcal{T}_h$ as was done for a fitted mesh in (2.20). Other important sets, when considering cut meshes, are the different sets of facets. A facet is defined as the edge of an element, that is, a line for a two-dimensional element or a surface for a three-dimensional one. The set of all facets on $\widehat{\mathcal{T}}_h$ are defined by $\mathcal{F}_h$. An important subset of $\mathcal{F}_h$, is the set of interior facets $\mathcal{F}_i$. This subset contains facets sharing two elements, denoted by T_F^+ and T_F^-, which belong to the active mesh $\mathcal{T}_h$. Another important subset of $\mathcal{F}_h$, is the set of intersected facets $\mathcal{F}_\Gamma$. This set is defined by the set of all interior facets $\mathcal{F}_i$ belonging to elements intersected by the boundary Γ as

$$\mathcal{F}_\Gamma = \left\{ F \in \mathcal{F}_i : T_F^+ \cap \Gamma \neq \emptyset \vee T_F^- \cap \Gamma \neq \emptyset \right\}. \tag{2.73}$$

These introduced subsets of $\mathcal{F}_h$ are demonstrated in Figure 2.7b.

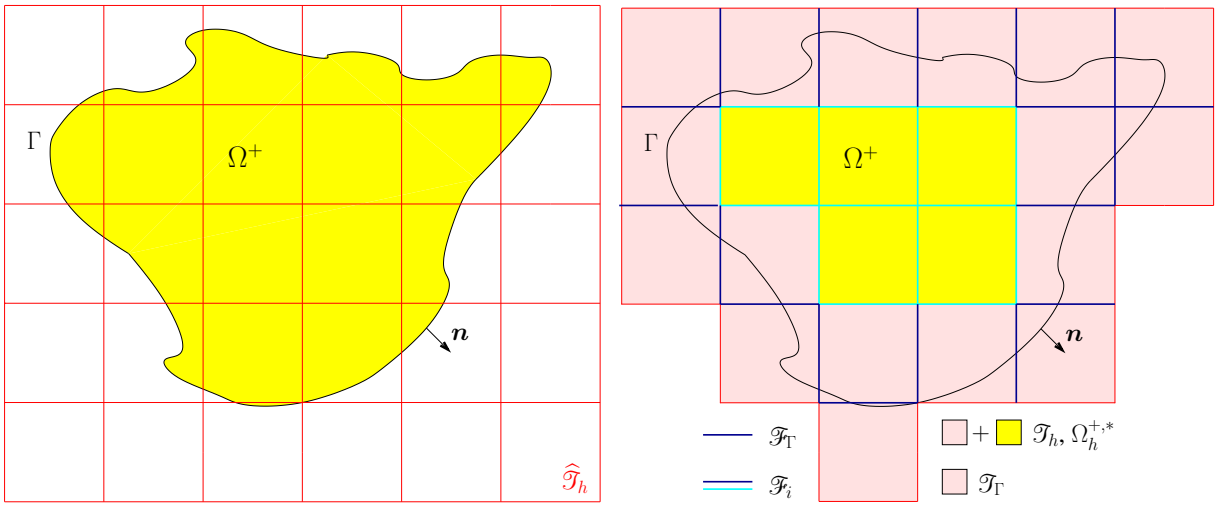

(a) Domain with computational mesh $\widehat{\mathcal{T}}_h$

(b) Active mesh $\mathcal{T}_h$ for positive domain Ω^+

Figure 2.7: Important definitions for a computational domain in the CutFEM visualized. In a) The background mesh $\widehat{\mathcal{T}}_h$ with the computational domain Ω^+ is displayed before the cut. Accordingly, in b) after performing the cut, the fictitious domain $\Omega_h^{+,*}$ and the active mesh $\mathcal{T}_h$ are displayed in yellow and pink. The cut elements are shown in pink and defined as $\mathcal{T}_\Gamma$. Additionally, the set of facets cut by the boundaries $\mathcal{F}_\Gamma$, shown in blue, and the set of interior facets $\mathcal{F}_i$ is shown in red and teal.

From the introduced concept of volume cells in Section 2.2.1, the computational domain Ω_h^+ can be defined as

$$\Omega_h^+ = \bigcup_{T \in \mathcal{T}_h} V_e^+, \tag{2.74}$$

where $V_e^+ = T$ for an uncut element in Ω_h^+. Furthermore, from the constructed volume cells, the approximated boundary Γ_h is naturally defined from the boundaries of the volume cells in the cut elements, i.e.

$$\Gamma_h = \bigcup_{T \in \mathcal{T}_\Gamma} \Gamma_h|_T \cap V_e^+. \tag{2.75}$$

2.3.2 A Discretized Unfitted CutFEM for the Navier–Stokes Equations

Using the definitions of Ω_h^+ and Γ_h from (2.74) and (2.75), a CutFEM for the Navier–Stokes equations can be formulated in Ω_h^+. To shorten the notation in the following, the positive domain will be shortened to $\Omega = \Omega^+$ and $\Omega_h = \Omega_h^+$. Then the following discretized form for a CutFEM for the Navier–Stokes equation can be formulated as: find $U_h \in \mathcal{W}_h$ such that for all $V_h \in \mathcal{W}_h$ it holds that

$$\mathcal{A}_h(U_h, V_h) + \mathcal{S}_h^*(U_h, V_h) + \mathcal{G}_h(U_h, V_h) + \mathcal{N}_h(U_h, V_h) = \mathcal{L}_h(V_h) + \mathcal{L}_h^{\mathcal{N}}(V_h) \tag{2.76}$$

where

$$\begin{aligned}\mathscr{A}_h(U_h, V_h) =&(\rho\frac{\partial \boldsymbol{u}_h}{\partial t}, \boldsymbol{v}_h)_{\Omega_h} + (2\mu\boldsymbol{\epsilon}(\boldsymbol{u}_h), \boldsymbol{\epsilon}(\boldsymbol{v}_h))_{\Omega_h} + (\rho(\boldsymbol{u}_h \cdot \nabla)\boldsymbol{u}_h, \boldsymbol{v}_h)_{\Omega_h} \\ &- \langle(2\mu\boldsymbol{\epsilon}(\boldsymbol{u}_h) - p_h\boldsymbol{I})\boldsymbol{n}, \boldsymbol{v}_h\rangle_{\Gamma_{\mathrm{D},h}} \\ &- (p_h, \nabla \cdot \boldsymbol{v}_h)_{\Omega_h} + (q_h, \nabla \cdot \boldsymbol{u}_h)_{\Omega_h} \qquad (2.77)\\ \mathscr{L}_h(V_h) =&(\boldsymbol{f}, \boldsymbol{v}_h)_{\Omega_h} + \langle \boldsymbol{h}, \boldsymbol{v}_h\rangle_{\Gamma_{\mathrm{N},h}} \qquad (2.78)\end{aligned}$$

and $\mathscr{S}_h^*(U_h, V_h) \in \{\mathscr{S}_h^{\mathrm{CIP}}(U_h, V_h), \mathscr{S}_h^{\mathrm{RB}}(U_h, V_h)\}$. Similar function spaces are employed as in the fitted mesh case from Section 2.1.3, where $\mathscr{W}_h = \mathscr{V}_h \times \mathscr{Q}_h$ with $U_h = (\boldsymbol{u}_h, p_h) \in \mathscr{W}_h$ and $V_h = (\boldsymbol{v}_h, q_h) \in \mathscr{W}_h$. The function space $\mathscr{V}_h$ is defined here as

$$\mathscr{V}_h := [\mathscr{X}_h]^d, \qquad (2.79)$$

$\mathscr{Q}_h$ as in (2.21) and $\mathscr{X}_h$ as in (2.20). Keep in mind that the support of $\mathscr{X}_h$ is in Ω_h, making it possible to use the same space for the fitted and unfitted cases. Some differences to the fitted mesh approach in Section 2.1.3 become immediately apparent. Primarily, the chosen solution space of the velocity is different to the one employed in equation (2.22). The difference here stems from the fact, that the Dirichlet boundaries are not imposed strongly, i.e. the function space of the solution and test function are not modified. Instead, boundary conditions will be imposed weakly by the addition of the terms $\mathscr{N}_h(U_h, V_h)$ on the left-hand-side and $\mathscr{L}_h^{\mathscr{N}}(V_h)$ on the right-hand-side. Owing to the weak imposition of the Dirichlet boundary, the consistency term $\langle(2\mu\boldsymbol{\epsilon}(\boldsymbol{u}_h) - p_h\boldsymbol{I})\boldsymbol{n}, \boldsymbol{v}_h\rangle_{\Gamma_{\mathrm{D},h}}$ remains in the formulation, as seen on the second line of (2.77). In the case of a strong imposition of Dirichlet boundaries this term disappears as $\boldsymbol{v}_h = 0$ on $\Gamma_{\mathrm{D},h}$, however, when imposed weakly, this term remains as the test function $\boldsymbol{v}_h$ does not disappear here. This weak imposition of a Dirichlet condition is further explored in Section 2.3.2.1.

Moreover, the term $\mathscr{G}_h(U_h, V_h)$ is added in (2.76), whereas it is clearly absent in the fitted formulation of (2.22). This term is a necessary addition owing to conditioning and stability issues of the CutFEM. These stem from pathological cut cases of the background mesh, coming from the decomposition of cut elements into volume cells V_e^+. This so-called ghost penalty operator, as first introduced by Burman [49], up heave these issues and will be further explored in Section 2.3.2.2.

2.3.2.1 Weak Imposition of Essential Boundary Conditions

To impose a Dirichlet conditions, the common approach of manipulating the test function space and prescribing Dirichlet values on the nodes of the boundary, is not a practical solution when it comes to the CutFEM. The determination of boundary values in regard to the interface position is not a trivial task, especially if the domain $\Omega_h^{+,*}$ deforms and number of nodes in the active mesh changes. An alternative to manipulating the test function space, is to enforce a boundary condition weakly. That is, terms are added to the weak form which impose the desired boundary condition. In some fitted mesh cases, a weak imposition of a Dirichlet condition might even be superior to a strong enforcement. This can be the case in for example simulations of turbulent flows. In the vicinity of a wall, steep gradients form in the boundary layer, and unless this boundary layer is fully resolved, spurious currents can appear. Accordingly, for an under resolved mesh, a weakened fulfillment of the boundary condition at the wall might be preferable.

For further discussions on this topic, the works of Bazilevs and Hughes [24] and Gamnitzer [121] are recommended.

Different approaches to impose a Dirichlet condition weakly, while retaining existence and uniqueness of the solution of the discretized system, have been proposed in the literature. One of the first suggested approaches was the classical method of Lagrange multipliers, proposed by Babuška [13] and Brezzi [46]. This method requires that the space of the Lagrange multiplier and its corresponding test function are chosen delicately, such that the system of equations retains inf-sup stability. This, in practice, boils down to how the Lagrange multiplier is discretized on the boundary, which for unfitted meshes can be quite a tedious task. For fitted meshes this constraint was studied in more detail by Pitkäranta [211, 212] and in the case of unfitted meshes for two-dimensional problems by Moës *et al.* [193] and Béchet *et al.* [26], and for three-dimensional problems by Hautefeuille *et al.* [139].

To circumvent the limited choices of Lagrange multiplier spaces, stabilized Lagrange multiplier methods were developed. Different techniques to carry out this stabilization of the Lagrange multiplier space exist. One of the more popular methods, is the residual-based stabilized Lagrange multiplier method, originally proposed by Barbosa and Hughes [19, 20] and later improved by Stenberg [248], for a fitted mesh. This method has also been employed on unfitted meshes by Mourad *et al.* [197]. Alternatively, the Lagrange multiplier space can be stabilized with an interior-penalty method proposed by Burman and Hansbo [59] or a projection stabilization as introduced by Burman [51]. A different way to achieve stability is to add an additional bulk stress field as proposed by Gerstenberger and Wall [125] in the so-called mixed/hybrid stress-based Lagrange multiplier method. This method was first introduced in the context of unfitted meshes for incompressible flow, but a symmetric version was developed for the Stokes equation by Baiges *et al.* [15] and for boundary fitted meshes it was employed for imposing boundary conditions in turbulent flows by Gamnitzer [121].

Another popular method to impose boundary conditions weakly is the Nitsche's method by Nitsche [204]. This method is closely related to the stabilized Lagrange multiplier methods. In a review article by Stenberg [248], on different methods of imposing weak boundary conditions, a connection between the residual-based stabilized Lagrange multiplier approach and the Nitsche's method is made. Furthermore, in the work by Baiges *et al.* [15] it is shown that the mixed/hybrid stress-based Lagrange multiplier method can also be used to derive the Nitsche's method. As was concluded by Stenberg [248] that *"the Nitsche's method is the most straightforward method to use"* it has become a popular method for imposing boundary conditions. In particular the simplicity of the method is cherished, as no extra variables are introduced, which is the case in Lagrange multiplier methods. In the Nitsche's method the Lagrange multiplier variable is replaced by its physical representation in the form of the boundary flux. As such, no extra discretization on the boundary, subjugated to rigid demands on stability, are necessary to introduce. This property makes this method of imposing boundary conditions suitable to use in the case of unfitted meshes.

The Nitsche's method was first introduced in the context of unfitted meshes for elliptic interface problems by Hansbo and Hansbo [136]. It was later extended to weak and strong discontinuities in elasticity problems in Hansbo and Hansbo [137] and incompressible elasticity problems in Becker *et al.* [28]. In the case of fitted meshes, the Nitsche's method has been successfully employed to deal with boundary conditions at walls in turbulent flows, as demonstrated in Becker [27] and Burman [48] and later improved with the addition of wall functions by Bazilevs *et al.*

[23]. Also in the case of mesh-free methods the usefulness of the Nitsche's method in imposing essential boundary condition has been demonstrated by Fernández-Méndez and Huerta [111].

For the case of imposing conditions on interfaces between fields the Nitsche's method has been applied in a plethora of problems and methods. In the publication of Burman and Hansbo [58], Stokes and Darcy flow were coupled at an interface, by means of an unfitted finite element method with the Nitsche's method. This was done in a similar fashion for Darcy flow through fractured porous media on unfitted meshes by D'Angelo and Scotti [105]. Fluid-structure interaction couplings have also had success by employing the Nitsche's method, as demonstrated in Hansbo *et al.* [138] for a fitted mesh, which was later extended to unfitted meshes in Burman and Fernández [55]. In the case of two-phase flows, Reusken and Nguyen [221] introduced coupling of strong discontinuities in a advection-diffusion context by means of the Nitsche's method. Lastly, a review for unfitted meshes by Burman and Zunino [62] on the usefulness of employing the Nitsche's method to impose constraints on interfaces separating fields with large contrasts in material parameters for the advection-diffusion-reaction equation, is recommended to the interested reader.

Weak imposition of boundary conditions with the Nitsche's method. In this thesis, the Nitsche's method will be the sole method used to impose boundary and interface conditions weakly. As such, the method is here briefly presented in the context of the incompressible Navier–Stokes equation (see equations (2.1)–(2.5)), by defining the terms $\mathcal{N}_h(U_h, V_h)$ and $\mathcal{L}_h^{\mathcal{N}}(V_h)$ as the following for the weak imposition of a Dirichlet condition

$$\begin{aligned}\mathcal{N}_h(U_h, V_h) =& \langle \frac{\rho\phi_u}{\gamma^n h}\boldsymbol{u}_h\boldsymbol{P}^n, \boldsymbol{v}_h\rangle_{\Gamma_{\mathrm{D},h}} + \langle \frac{\mu}{\gamma^t h}\boldsymbol{u}_h\boldsymbol{P}^t, \boldsymbol{v}_h\rangle_{\Gamma_{\mathrm{D},h}} \\ &- \langle \boldsymbol{u}_h, \zeta_u 2\mu\boldsymbol{\epsilon}(\boldsymbol{v}_h)\boldsymbol{n} + q_h\boldsymbol{n}\rangle_{\Gamma_{\mathrm{D},h}} \\ &- \langle (\rho\boldsymbol{u}_h\cdot\boldsymbol{n})(\boldsymbol{u}_h - \boldsymbol{g}), \boldsymbol{v}_h\rangle_{\Gamma_{\mathrm{in}}} \qquad (2.80)\\ \mathcal{L}_h^{\mathcal{N}}(V_h) =& \langle \frac{\rho\phi_u}{\gamma^n h}\boldsymbol{g}\boldsymbol{P}^n, \boldsymbol{v}_h\rangle_{\Gamma_{\mathrm{D},h}} + \langle \frac{\mu}{\gamma^t h}\boldsymbol{g}\boldsymbol{P}^t, \boldsymbol{v}_h\rangle_{\Gamma_{\mathrm{D},h}} \\ &- \langle \boldsymbol{g}, \zeta_u 2\mu\boldsymbol{\epsilon}(\boldsymbol{v}_h)\boldsymbol{n} + q_h\boldsymbol{n}\rangle_{\Gamma_{\mathrm{D},h}} \qquad (2.81)\end{aligned}$$

Here, ϕ_u is defined in the same way as for the CIP-stabilization in (2.36)–(2.37) with

$$\phi_{u,T} = \nu + c_u(\|\boldsymbol{u}_h\|_{0,\infty,T}h_T) + c_\sigma(\sigma h_T^2), \qquad (2.82)$$

and the normal and tangential projection matrices are defined as $\boldsymbol{P}^n = \boldsymbol{n}\otimes\boldsymbol{n}$ and $\boldsymbol{P}^t = \boldsymbol{I} - \boldsymbol{P}^n$, respectively. The terms, $\gamma^n, \gamma^t \in (0, \infty)$ are the so-called Nitsche penalty parameters for the normal and tangential directions, respectively. These need to be chosen with care to preserve the stability of the method. The term $\zeta_u \in \{-1, 1\}$ defines whether the Nitsche terms are added adjoint-consistent ($\zeta_u = -1$) or adjoint-inconsistent ($\zeta_u = 1$), with the choice affecting the stability properties of the formulation. In equation (2.80) the first line adds the Nitsche penalty terms and the second line the adjoint term. On the third line an inflow stabilization term needs to be added, if there exists inflow at the boundary; where an inflow boundary is defined as $\Gamma_{\mathrm{in}} := \{\boldsymbol{x} \in \Gamma_h \mid \boldsymbol{u}_h\cdot\boldsymbol{n} < 0\}$. The equivalent terms are added on the right-hand-side as introduced in (2.81), which concludes the standard method of imposing a Dirichlet condition by means of the Nitsche's method.

The difference in scaling of the normal terms in comparison to the tangential terms is apparent from the definition of ϕ_u in (2.82) and the added Nitsche penalty terms in (2.80). This difference is a property of the way weak impositions of boundary conditions are performed. It is known that in the convective and reactive limits no tangential condition is to be imposed, which makes this condition dependent on only viscous contributions. Consequently, when the viscous terms become smaller in comparison to other contributions, the length scale where viscous effects dominate, shrink. As such, if the mesh is not properly resolved in the vicinity of the interface, the tangential terms have a minuscule contribution to the system of equations and, hence, the solution will permit deviations from this condition. On the contrary, in the normal direction, the condition is scaled accordingly for all possible flow regimes, and as a consequence will always be enforced. The above mentioned terms will be further investigated for the Oseen equation in Section 3.3.

What might not be immediately apparent from the presentation in (2.80) and (2.81), is that the Nitsche's method is inherently a consistent method and follows a simple logic for the addition of the terms. Introducing the condition desired to be imposed as $\mathscr{C}_{\Gamma_\mathrm{D}}(\boldsymbol{u}_h) = \boldsymbol{u}_h - \boldsymbol{g}$, where the fulfillment of this condition is true when $\mathscr{C}_{\Gamma_\mathrm{D}} = \mathbf{0}$. Then the imposition with the Nitsche's method can be rewritten as

$$\begin{aligned}\mathcal{N}_h(U_h, V_h) - \mathcal{L}_h^{\mathcal{N}}(V_h) =& \langle \frac{\rho\phi_u}{\gamma^n h}\mathscr{C}_{\Gamma_\mathrm{D}}(\boldsymbol{u}_h)\boldsymbol{P}^n, \boldsymbol{v}_h\rangle_{\Gamma_{\mathrm{D},h}} + \langle \frac{\mu}{\gamma^t h}\mathscr{C}_{\Gamma_\mathrm{D}}(\boldsymbol{u}_h)\boldsymbol{P}^t, \boldsymbol{v}_h\rangle_{\Gamma_{\mathrm{D},h}} \\ &- \langle \mathscr{C}_{\Gamma_\mathrm{D}}(\boldsymbol{u}_h), \zeta_u 2\mu\boldsymbol{\epsilon}(\boldsymbol{v}_h)\boldsymbol{n} + q_h\boldsymbol{n}\rangle_{\Gamma_{\mathrm{D},h}} \\ &- \langle (\rho\boldsymbol{u}_h\cdot\boldsymbol{n})\mathscr{C}_{\Gamma_\mathrm{D}}(\boldsymbol{u}_h), \boldsymbol{v}_h\rangle_{\Gamma_\mathrm{in}}. \end{aligned} \tag{2.83}$$

From (2.83), it is clear that all added terms disappear when the condition at the boundary is fulfilled, i.e. $\mathscr{C}_{\Gamma_\mathrm{D}} = \mathbf{0}$, making the Nitsche's method a consistent method.

2.3.2.2 Instabilities Stemming from Cut Meshes

It is well known that without additional measures, cut finite element methods exhibit stability and conditioning issues depending on the position of the cut interface Γ_h, which is observed in for instance the publication by Reusken [220] and Sauerland and Fries [228]. In particular, the so-called pathological cut cases, leading to these problems, can be divided into *dotted cut* and *sliver cut* cases. A dotted cut in a element occurs when the cut elements volume $|\Omega \cap T|$ and boundary area $|\Gamma \cap T|$ are much smaller than the uncut elements volume $|T|$ and area $|\partial T|$, respectively. Whereas a sliver cut transpires when the volume of the cut element is much smaller than the element volume, i.e. $|\Omega \cap T| << |T|$, but the boundary area is of comparable size, i.e. $|\Gamma \cap T| \approx |\partial T|$. An overview how these pathological cut cases impact the conditioning and stability of the system can be found in more detail in Schott [232].

The issue of deteriorating condition number and stability issues stemming from the position of the interface Γ, makes the CutFEM, without modification, unfeasible to use. As these problems lead to loss of performance for iterative solvers, and makes the system of equations sensitive to minor perturbation of data. Recently, however, methods have arisen to remedy these issues. One preconditioning method proposed by Reusken [220] is to remove basis functions which have small physical support from the function space. A further promising preconditioning method has been proposed by Badia and Verdugo [14] where the balancing domain decomposition by constraints (BDDC) framework is utilized to ensure a well conditioned system of equations.

Nevertheless, it is unclear whether this method can be extended from an elliptic problem to a saddle point problem, which is not inherently coercive, as mentioned by Guzmán and Olshanskii [135]. Another method to upheave the problems stemming from pathological cut cases, was introduced by Babuška and Banerjee [10] with the stable generalized finite element method, where the enrichment functions are modified. This has proven to be a viable method when weak discontinuities in solution spaces are considered, however, it has been shown by Henke [143] that it is not able to accurately depict strong discontinuities. Finally, the ghost penalty technique, introduced by Burman [49], can be applied to remove the ill-conditioning problem for the CutFEM. It achieves this by adding terms on the facets of cut elements, i.e. $\mathscr{F}_\Gamma$, and has become a popular method for unfitted mesh approaches.

For the weak imposition of boundary conditions with the Nitsche's method in fictitious domain problems, the ghost penalty method was successfully applied for both an elliptic problem [60] and the Stokes problem by Burman and Hansbo [61]. This was further extended to the three dimensional case of the Stokes problem by Massing *et al.* [185]. A first attempt at utilizing these interface stabilizing terms for high Reynolds number flows was conducted by Schott and Wall [229]. This was followed by works on domain decomposition problems for incompressible flows by Schott *et al.* [231] and on multiphysics problem such as for two-phase flows by Schott *et al.* [230] and fluid-structure interaction by Burman and Fernández [55] and Shahmiri [237].

In the ensuing paragraph the ghost penalty terms are introduced as they appear in the weak form of the Navier–Stokes equations (2.76).

Stabilization with the addition of ghost penalty terms. Recently a rigorous mathematical analysis was performed by Massing *et al.* [184] on the linearized version of the Navier–Stokes equations, i.e. the Oseen equation, for a CutFEM, which makes use of ghost penalties to stabilize the pathological cut situations. In the aforementioned work, inf-sup stability and optimal a-priori error estimates are demonstrated for both the convection dominated and viscous dominated regimes, for problems with Dirichlet boundaries. This analysis was later extended to general Navier boundaries by Winter *et al.* [279], which will be further explored in Chapter 3. Building on the knowledge gained in [184], the following ghost penalty terms for incompressible flow are added to the weak form as suggested in Schott [232]. As such, the term $\mathscr{G}_h(U_h, V_h)$ takes the following shape in equation (2.76),

$$\mathscr{G}_h(U_h, V_h) = g_\sigma(\boldsymbol{u}_h, \boldsymbol{v}_h) + g_\nu(\boldsymbol{u}_h, \boldsymbol{v}_h) + g_\beta(\boldsymbol{u}_h; \boldsymbol{u}_h, \boldsymbol{v}_h) + g_u(\boldsymbol{u}_h; \boldsymbol{u}_h, \boldsymbol{v}_h) + g_p(\boldsymbol{u}_h; p_h, q_h) \tag{2.84}$$

with

$$g_\sigma(\boldsymbol{u}_h, \boldsymbol{v}_h) := \gamma_\sigma \sum_{F\in\mathscr{F}_\Gamma} \sum_{1\leqslant j\leqslant k} \sigma\rho h^{2j+1} \langle [\![\partial_{\boldsymbol{n}}^j \boldsymbol{u}_h]\!], [\![\partial_{\boldsymbol{n}}^j \boldsymbol{v}_h]\!] \rangle_F, \tag{2.85}$$

$$g_\nu(\boldsymbol{u}_h, \boldsymbol{v}_h) := \gamma_\nu \sum_{F\in\mathscr{F}_\Gamma} \sum_{1\leqslant j\leqslant k} \nu\rho h^{2j-1} \langle [\![\partial_{\boldsymbol{n}}^j \boldsymbol{u}_h]\!], [\![\partial_{\boldsymbol{n}}^j \boldsymbol{v}_h]\!] \rangle_F, \tag{2.86}$$

$$g_\beta(\boldsymbol{\beta}; \boldsymbol{u}_h, \boldsymbol{v}_h) := \gamma_\beta \sum_{F\in\mathscr{F}_\Gamma} \sum_{0\leqslant j\leqslant k-1} \phi_{\beta,F}\rho h^{2j+1} \langle [\![\boldsymbol{\beta}\cdot\nabla\partial_{\boldsymbol{n}}^j \boldsymbol{u}_h]\!], [\![\boldsymbol{\beta}\cdot\nabla\partial_{\boldsymbol{n}}^j \boldsymbol{v}_h]\!] \rangle_F, \tag{2.87}$$

$$g_u(\boldsymbol{\beta}; \boldsymbol{u}_h, \boldsymbol{v}_h) := \gamma_u \sum_{F\in\mathscr{F}_\Gamma} \sum_{0\leqslant j\leqslant k-1} \phi_{u,F}\rho h^{2j+1} \langle [\![\nabla\cdot\partial_{\boldsymbol{n}}^j \boldsymbol{u}_h]\!], [\![\nabla\cdot\partial_{\boldsymbol{n}}^j \boldsymbol{v}_h]\!] \rangle_F, \tag{2.88}$$

$$g_p(\boldsymbol{\beta}; p_h, q_h) := \gamma_p \sum_{F\in\mathscr{F}_\Gamma} \sum_{1\leqslant j\leqslant k} \phi_{p,F}\rho^{-1} h^{2j-1} \langle [\![\partial_{\boldsymbol{n}}^j p_h]\!], [\![\partial_{\boldsymbol{n}}^j q_h]\!] \rangle_F, \tag{2.89}$$

where the j-th normal derivative $\partial_{\boldsymbol{n}}^j v$ is given by $\partial_{\boldsymbol{n}}^j v = \sum_{|\alpha|=j} D^\alpha v(\boldsymbol{x})\boldsymbol{n}^\alpha$ for multi-index $\alpha = (\alpha_1, \ldots, \alpha_d)$, $|\alpha| = \sum_i \alpha_i$ and $\boldsymbol{n}^\alpha = n_1^{\alpha_1} n_2^{\alpha_2} \cdots n_d^{\alpha_d}$. The scalings, ϕ_u, ϕ_p and ϕ_β are chosen in the same fashion as done in the case of the CIP-stabilization, i.e.

$$\phi_{u,T} = \nu + c_u(\|\boldsymbol{\beta}\|_{0,\infty,T} h_T) + c_\sigma(\sigma h_T^2), \tag{2.90}$$

$$\phi_{p,T} = \phi_{\beta,T} = \frac{h_T^2}{\phi_{u,T}}, \tag{2.91}$$

where $\boldsymbol{\beta} = \boldsymbol{u}_h$ in (2.90). From initial observation, the terms (2.85)–(2.89) have a lot in common with the already introduced CIP stabilization terms s_β, s_u and s_p ((2.32)–(2.34)). For starters, the terms g_β, g_u and g_p ((2.87)–(2.89)) have the same form as the the introduced terms for the CIP-stabilization. The difference between the two, lies in the fact that the ghost penalty terms also consider higher order normal derivatives, thus controlling not only first order terms, but the entire polynomial of the polynomial space. An interpretation on the connection between these three ghost penalty terms and the CIP-stabilization terms, is that they extend their respective stabilization onto the enlarged domain $\Omega_h^{+,*}$. The reactive g_σ (2.86) and viscous g_ν (2.86) ghost penalties are added to keep control of the L^2- and H^1-norms over the enlarged domain.

The reactive coefficient σ in (2.85) has the same interpretation as in the case of the CIP-stabilization, i.e. $\sigma = 1/(\theta\Delta t)$ when a one-step theta discretization is used for the temporal discretization. Further analysis on the form of the presented ghost penalty terms can be found in Massing *et al.* [184].

2.3.2.3 Integration of Arbitrary Shaped Polyhedrons

To solve the discretized weak form, integrals over the computational domain are required to be evaluated. For uncut elements a straight forward approach can be pursued, which employs Gauss quadrature with weights readily available for hexahedrons, tetrahedrons, wedges or other standard shapes of elements. Nevertheless, in the CutFEM, elements in the vicinity of the interface are cut, which results in polyhedrons of non-standard shapes. Consequently, standard Gauss quadrature methods for integrating these volume cells do not exist. To overcome this problem, different methods to evaluate the integrals over these polyhedrons need to be considered. The tessellation method and the direct-divergence method are utilized in this thesis, and are as such

briefly explained here. Nevertheless, it should be mentioned that these are not the only possible options available for integrating arbitrary shaped polyhedrons, the interested reader can find an overview of such methods in Sudhakar [255].

The method to subdivide a volume cell polyhedron into simple shaped polyhedrons such as tetrahedrons or hexahedrons, for which there exists integration rules, is called *tessellation* or subtetrahedralization. Algorithms for this method have been suggested, e.g. by Sukumar *et al.* [258]. These simple polyhedrons are called integration cells, and as they are only used for integrating the weak form, they are not used in the creation of the function space $\mathscr{X}_h$. Hence, the aspect ratio of these cells does not influence the solution as demonstrated in Pereira *et al.* [210]. Accordingly, more freedom is granted in subdividing the volume cell, than given in the creation of a computational mesh. The drawback of this method to integrate polyhedrons, is the lack of numerical robustness for the case of concave polyhedrons, which was investigated by Sudhakar and Wall [253].

An alternative to using tessellation is the *direct-divergence* method, as introduced by Sudhakar *et al.* [254]. This method makes use of the divergence theorem to shift the integration over a volume onto the areas (facets) of the volume cell. To permit the integration of generalized functions, one-dimensional Gauss quadrature rules are applied as done in Sommariva and Vianello [244] and Hematiyan [141]. By employing this method to evaluate integrals over volume cells, the complexity is drastically reduced in comparison with the tessellation method for three-dimensional elements. For more details on the specifics of the method, the reader is referred to the original publication by Sudhakar *et al.* [254].

2.3.3 Time Integration for the CutFEM with Moving Interfaces

Time integration for fitted meshes was introduced in Section 2.1.4, in this section the differences for a CutFEM formulation will be highlighted. First, if the boundary Γ does not move in time, the same techniques can be applied as in the aforementioned section. However, when the boundary moves, CutFEM methods with semi-discretization approaches face some challenges in the time integration. The fundamental problem resides in the fact that $\Omega_h^n \neq \Omega_h^{n+1}$, which implies $\mathscr{W}_h^n \neq \mathscr{W}_h^{n+1}$, i.e. the function spaces for the solution at the new time step $U^{n+1} \in \mathscr{W}_h^{n+1}$ is not the same as for the old $U^n \in \mathscr{W}_h^n$. This obviously leads to issues in the evaluation of inner products on Ω_h^{n+1} for quantities of the previous time step $\boldsymbol{u}^n$ and $\boldsymbol{a}^n$. In essence, a projection from the previous values $\widehat{\boldsymbol{u}}^n, \widehat{\boldsymbol{a}}^n \in \mathscr{V}_h^n$ to the new function space $\boldsymbol{u}^n, \boldsymbol{a}^n \in \mathscr{V}_h^{n+1}$ has to be undertaken. A profound explanation of these projections has already been given in Schott [232], as such, only a summary will be given here.

First, the case when the interface Γ only moves within an element in the allotted time slot $[t^n, t^{n+1}]$, is considered. This case implies that $\Omega_h^{*,n} = \Omega_h^{*,n+1}$, i.e. that the fictitious domains remain the same between the time steps, even though the computational domains Ω_h^n and Ω_h^{n+1} might not. As the fictitious domains are the same, the active meshes $\mathscr{T}_h^n$ and $\mathscr{T}_h^{n+1}$ are as well. Owing to this, in this thesis, if no element boundary is crossed, the values of the previous time are copied onto the new domain, i.e. $\boldsymbol{u}_h^n = \widehat{\boldsymbol{u}}_h^n$ and $\boldsymbol{a}_h^n = \widehat{\boldsymbol{a}}_h^n$.

Next, the more problematic case will be considered, that is, when the interface Γ crosses an element boundary. This implies that apart from $\Omega_h^n \neq \Omega_h^{n+1}$, also the fictitious domains $\Omega_h^{*,n}$ and $\Omega_h^{*,n+1}$ and the active meshes $\mathscr{T}_h^n$ and $\mathscr{T}_h^{n+1}$ are not the same anymore. To make the algorithms used for the projection of $\widehat{\boldsymbol{u}}_h^n$ to $\boldsymbol{u}_h^n$ tangible, an illustration of a moving interface Γ separating

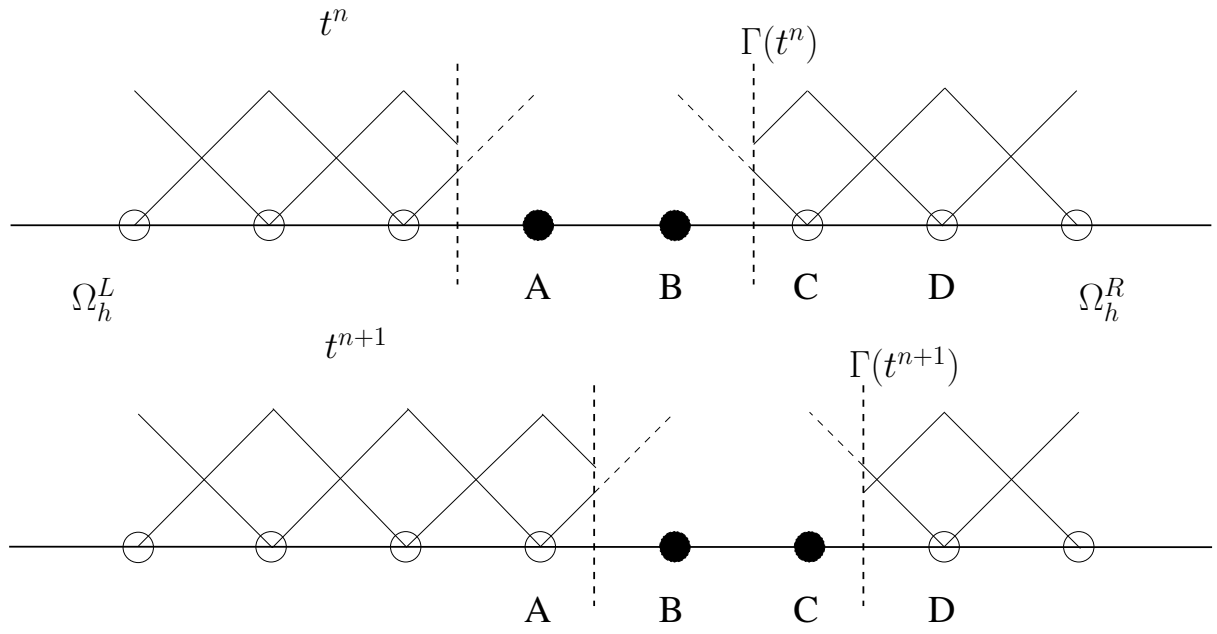

Figure 2.8: CutFEM time integration illustrated in a 1-D problem. The white dots on the left of the interface represent the domain Ω_h^L and on the right the domain Ω_h^R. The black nodes between this domain consist of void and are not part of any physical domain. As such, four distinct transitions for the nodes can be identified as the interface changes its position: **A:** Ghost-value to standard-value, **B:** Void to Ghost-value, **C:** Standard-value to Ghost-value and **D:** Standard-value to standard-value

two domains Ω_h^L and Ω_h^R with a section of void, is depicted in Figure 2.8. In this one-dimensional illustration, the white nodes on the left side make up the domain Ω_h^L and the white nodes on the right side make up the domain Ω_h^R. The black nodes separating these two domains are void, and not part of the domains Ω_h^R and Ω_h^L. Nevertheless, the adjacent void node to these domains belong to their fictitious domain, and as such its active mesh. At the time $t = t^n$ in Figure 2.8, the node **A** resides in $\Omega_h^{L,*}$ and **B** in $\Omega_h^{R,*}$. Owing to the motion of Γ, this changes at time $t = t^{n+1}$, such that now node **A** belongs to Ω_h^L and **B** belongs to $\Omega_h^{L,*}$. Furthermore, for the domain on the right, the node **B** has left its fictitious domain $\Omega_h^{R,*}$ and instead **C** has entered it, from previously residing in Ω_h^R. From this simplified one-dimensional example four possible problematic cases can be illustrated. The following letters **A**, **B**, **C** and **D** refer to the nodes in the aforementioned figure.

Ghost-value to Standard-value At time t^n, the node **A** resides within the fictitious domain $\Omega_h^{L,*}$, and as such also in the active mesh $\mathcal{T}_h^L$, but outside of the domain Ω_h^L. The value at the node **A** at time t^n can be viewed as an extension of the solution in Ω_h^L to $\Omega_h^{*,L}$. Owing to this, the value at this node is henceforth referred to as a *ghost-value*. In the ensuing configuration at time t^{n+1}, the node **A** now lies in Ω_h^L. The value at this node is now in the domain of interest, and its value will be referred to in the following as a *standard value*. The projection of the values in the configuration t^n to t^{n+1}, is here made by copying the previous values to the new time step as $\boldsymbol{u}_h^n = \widehat{\boldsymbol{u}}_h^n$ and $\boldsymbol{a}_h^n = \widehat{\boldsymbol{a}}_h^n$. This copying of the previous values is motivated by the fact that the ghost-values are extensions of the solution,

and can as such be copied to the new configuration. An alternative to this would be to use a semi-Lagrange method as suggested by Henke *et al.* [142].

Void to Ghost-value The node **B** is at t^n not part of neither the fictitious domain $\Omega_h^{*,L}$ nor Ω_h^L. The value at this node is not part of the domain of interest nor the active mesh $\mathcal{T}_h^L$ and is henceforth described as *void*. At the time t^{n+1} the node **B** has now entered the fictitious domain $\Omega_h^{*,L}$ and is as such part of the active mesh. Consequently, a projection to obtain the value $\boldsymbol{u}^n$ in the current configuration of t^{n+1} needs to be found. A copying approach as done in the case of node **A** can not be opted for here, as no previous value $\widehat{\boldsymbol{u}}_h^n$ exists. Instead, to calculated $\boldsymbol{u}^n$ the following extension equation is solved,

$$\mathcal{E}_h(\boldsymbol{u}_h^n, \boldsymbol{v}_h) = \sum_{F \in \mathcal{F}_\Gamma^{n+1}} \sum_{0 \leq j \leq k} \left\langle [\![\partial_{\boldsymbol{n}}^j \boldsymbol{u}_h^n]\!], [\![\partial_{\boldsymbol{n}}^j \boldsymbol{v}_h]\!] \right\rangle_F = 0, \tag{2.92}$$

where k is the order of the chosen polynomial function space $\mathcal{X}_h$. This step is conducted after the cases *Ghost-value to standard-value* (Node **A**), *Standard-value to Ghost-value* (Node **C**) and *Standard-value to standard-value* (Node **D**) have been performed. The already known values of $\boldsymbol{u}_h^n$ and $\boldsymbol{a}_h^n$ in $\Omega_h^{*,L}$, are set as Dirichlet values in the global equation (2.92), and as such the only unknowns solved for are nodes of type **B**. As such this extends the previous solution $\boldsymbol{u}_h^n$ and $\boldsymbol{a}_h^n$ from the domain Ω_h^L onto $\Omega_h^{*,L}$, by restricting jumps in gradients between elements. Another way of determining this unknown is to preserve the jump or the kink in the solution from the previous time-step by means of a semi-Lagrange method as done in Henke *et al.* [142].

Standard-value to Ghost-value Node **C**, resides in the domain Ω_h^R at time t^n and leaves Ω_h^R but still remains in $\Omega_h^{*,R}$ at time t^{n+1}. Consequently, the value at node **C** goes from a standard value to a ghost value. Given that a ghost-value is only a extension of the solution into the domain $\Omega_h^{*,R}$, copying the standard value at t^n to be the ghost-value at t^{n+1} is a feasible approach, i.e. $\boldsymbol{u}_h^n = \widehat{\boldsymbol{u}}_h^n$ and $\boldsymbol{a}_h^n = \widehat{\boldsymbol{a}}_h^n$.

Standard-value to Standard-value Lastly, in the case of node **D**, it stays in the domain Ω_h^R at both times t^n and t^{n+1}. In this particular case the node belongs to a cut element, but it is still within the domain Ω_h^R. Thus, the cut does not effect the strategy at this node per se, and a standard copy method from the t^n to t^{n+1} can be applied, that is $\boldsymbol{u}_h^n = \widehat{\boldsymbol{u}}_h^n$ and $\boldsymbol{a}_h^n = \widehat{\boldsymbol{a}}_h^n$.

Summarized, a copy strategy is employed for three out of the four cases (i.e. nodes **A**, **C** and **D**) and an extension of the primary variable field is done for the last case (i.e. node **B**). It becomes apparent that in the case of nodes **A** and **B** the proposed techniques are only a viable option as long as the motion of the interface adheres to a Courant–Friedrichs–Lewy (CFL) like condition, i.e.

$$|\boldsymbol{u}_\Gamma| \Delta t < h \tag{2.93}$$

where $\boldsymbol{u}_\Gamma$ is defined as the velocity at the interface. If the interface crosses over more than one node in a time step, the node which enters into the domain Ω_h, was previously void and carries no previous information with it. A possibility to circumvent this restriction is by using the already mentioned semi-Lagrange method by Henke *et al.* [142]. Nevertheless, in this thesis the copy

and extension techniques will be used exclusively for moving domain problems. As such, care has to be taken to not chose a too large time step, as to not violate the CFL-condition.

For a more thorough discussion on the time-integration of moving interfaces in the CutFEM, the aforementioned dissertation by Schott [232] and the references therein are recommended.

Chapter 3

A Weak Imposition of a General Navier Boundary Condition

As has been demonstrated in the previous Chapter 2, the imposition of standard Dirichlet and Neumann conditions are well documented for unfitted mesh approaches. However, non-standard boundary conditions such as the Robin and general Navier boundary conditions (GNBC) have as of yet not been explored as extensively in this setting. This thesis will focus on improving the knowledge of the general Navier boundary condition in an unfitted finite element setting. This condition stems from the proposed Navier slip condition originally proposed by Navier [200], where a Dirichlet condition is imposed in wall-normal direction and a Robin condition in wall-tangential direction. A Robin condition consists of a linear combination of a Dirichlet and Neumann condition, and is regulated in this particular instance by a slip length ε [m]. A slip length of $\varepsilon = 0$ defines a pure Dirichlet condition, whereas a choice of $\varepsilon = \infty$ gives a pure Neumann condition. This condition arises in a number of problems, such as modeling of wetting processes Huh and Mason [150] (which will be further discussed in Chapter 5), immersed contact between rigid bodies Gérard-Varet *et al.* [123] and modeling of rough surfaces Basson and Gérard-Varet [21], to mention a few.

Current approaches of imposing the GNBC, by means of a Galerkin substitution, do not incorporate both the Dirichlet and Neumann limits of this condition. They face conditioning issues when the Dirichlet limit is approached, that is when small slip lengths are considered. This inability to incorporate both limits poses an issue in the modeling of certain flows, as is arguably the case for wetting processes with moving contact lines. In the immediate vicinity of the contact line almost full slip can be measured whereas further away the classical no-slip condition is observed, as reported in Qian *et al.* [214]. Hence, the region where slip and no-slip is to be imposed changes with time for a moving contact line. Owing to this, a stable and robust method to impose this boundary condition allowing for both the Dirichlet and Neumann limits in wall-tangential direction is desirable. An initial step towards such a formulation was proposed by Juntunen and Stenberg [166] for a weak imposition of a Robin condition for the Poisson equation. This approach was later extended to the linearized Navier–Stokes equations, the Oseen equations, in Winter *et al.* [279] for a general Navier boundary condition. This proposed method is in this chapter extended to the non-linear Navier–Stokes equations. As the GNBC can not be analyzed for stability and error convergence in a Navier–Stokes setting, owing to its non-linear

nature, important insights on these properties from the linearized formulation are drawn from [279].

What the aforementioned publication [279] did not consider, were geometrical approximation errors arising from the domain approximation. This source of error is well-known when trying to impose a GNBC, and it is in particularly pronounced for a polygonal approximation of the physical domain. If the piecewise constant normal of the polygonal domain is chosen to impose the general Navier condition, convergence issues become apparent. This problem of convergence, for piecewise constant boundary normals, is also known as the Babuška paradox [12]. In this chapter these geometrical approximation errors will be forgone, and instead the assumption is made that the physical and approximated domains coincide, i.e. $\Omega_h = \Omega$, $\Gamma_h = \Gamma$ and $\boldsymbol{n}_h = \boldsymbol{n}$. These issues will instead be dealt with in the subsequent Chapter 4.

The chapter starts with Section 3.1 by introducing the general Navier boundary condition for the Navier–Stokes equations, and its field of application are presented in more detail. Next, in Section 3.2, the contemporary method of imposing this boundary condition with a Galerkin substitution method is explored. The conditioning issues appearing in the case of small slip lengths, i.e. in the no-slip limit, are explained and the cause why this approach can not resolve these issues highlighted. The insights gained from the analysis of the substitution method and the publication by Juntunen and Stenberg [166], provides the foundation for the creation of a novel method to impose the general Navier boundary condition, which is well-defined in both the Dirichlet and Neumann limits. This method imposes the GNBC by means of the Nitsche's method, and is here presented for the Navier–Stokes method based on the formulation for the Oseen equation by Winter *et al.* [279]. The formulation will be given in a CutFEM-framework, however, the application to a fitted mesh is readily received by dropping the ghost penalty terms. Finally in Section 3.3, a thorough mathematical analysis of the Oseen equation with the general Navier boundary condition is conducted. In this analysis, inf-sup stability and optimal a priori error estimates are proven for an arbitrary choice of slip length. In addition, numerical examples are conducted to corroborate the findings from the numerical analysis. The mathematical analysis was previously described in Winter *et al.* [279] and Section 3.3 is closely related to this publication.

3.1 The General Navier Boundary Condition

For an incompressible Newtonian fluid in the domain $\Omega \subset \mathbb{R}^d$, $d \in \{2, 3\}$, which is bounded and connected and has the boundary $\Gamma = \Gamma_{\mathrm{G}} \cup \Gamma_{\mathrm{N}}$, the following Navier–Stokes equations with a general Navier boundary condition hold,

$$\rho \frac{\partial \boldsymbol{u}}{\partial t} + \rho \boldsymbol{u} \cdot \nabla \boldsymbol{u} - \nabla \cdot (2\mu \boldsymbol{\epsilon}(\boldsymbol{u})) + \nabla p = \boldsymbol{f} \quad \text{in } \Omega \times (0, t_{\text{end}}), \tag{3.1}$$

$$\nabla \cdot \boldsymbol{u} = 0 \quad \text{in } \Omega \times (0, t_{\text{end}}), \tag{3.2}$$

$$(-p\boldsymbol{I} + 2\mu \boldsymbol{\epsilon}(\boldsymbol{u})) \cdot \boldsymbol{n} = \boldsymbol{h} \quad \text{on } \Gamma_{\mathrm{N}} \times (0, t_{\text{end}}) \tag{3.3}$$

$$(\boldsymbol{u} - \boldsymbol{g})\, \boldsymbol{P}^n = \boldsymbol{0} \quad \text{on } \Gamma_{\mathrm{G}} \times (0, t_{\text{end}}), \tag{3.4}$$

$$(\varepsilon(2\mu \boldsymbol{\epsilon}(\boldsymbol{u})\boldsymbol{n} - \boldsymbol{h}) + \mu(\boldsymbol{u} - \boldsymbol{g}))\, \boldsymbol{P}^t = \boldsymbol{0} \quad \text{on } \Gamma_{\mathrm{G}} \times (0, t_{\text{end}}), \tag{3.5}$$

where $\boldsymbol{\epsilon}(\boldsymbol{u}) := \frac{1}{2}(\nabla \boldsymbol{u} + (\nabla \boldsymbol{u})^T)$, $\boldsymbol{u}, \boldsymbol{g}, \boldsymbol{h} : \Omega \times [0, t_{\text{end}}) \to \mathbb{R}^d$, $p : \Omega \times [0, t_{\text{end}}) \to \mathbb{R}$ and $\rho, \mu : \Omega \times [0, t_{\text{end}}) \to \mathbb{R}^+$. Here $\boldsymbol{u}$ is the velocity, p the pressure and μ the dynamic viscosity

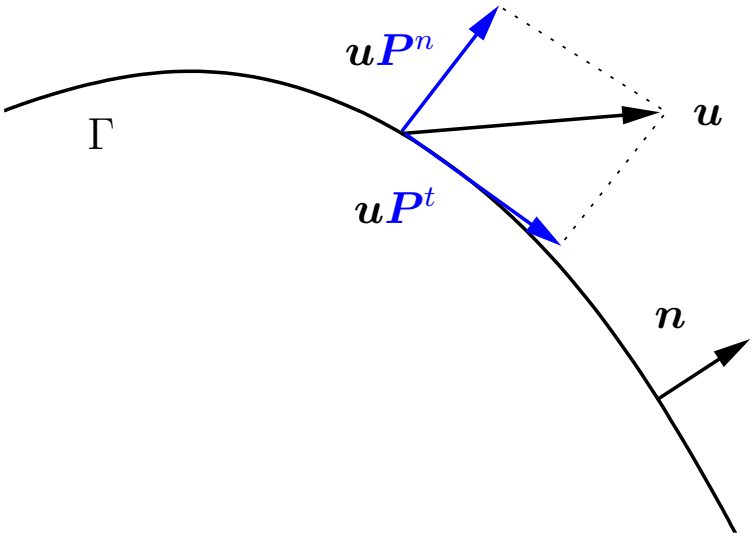

Figure 3.1: The effect of applying the projection matrices $\boldsymbol{P}^n$ and $\boldsymbol{P}^t$ on a vector quantity $\boldsymbol{u}$ defined on the boundary Γ with normal $\boldsymbol{n}$, is illustrated in this figure.

of the fluid. The terms $\boldsymbol{g}$ and $\boldsymbol{h}$ are the velocity and traction prescribed at the boundary Γ. The projection matrices ($\boldsymbol{P}^n, \boldsymbol{P}^t \in \mathbb{R}^{d\times d}$), employed in the imposition of the general Navier boundary condition (3.4)–(3.5), are constructed from the outward pointing unit normal $\boldsymbol{n}$ of the boundary Γ. The projection in normal direction is defined as $\boldsymbol{P}^n := \boldsymbol{n} \otimes \boldsymbol{n}$ and the projection onto the tangential plane of the surface as $\boldsymbol{P}^t := \boldsymbol{I} - \boldsymbol{n} \otimes \boldsymbol{n}$, where $\boldsymbol{I}$ is the $d \times d$ identity matrix. This decomposition in normal and tangential direction of vector components by means of projection matrices, is demonstrated in Figure 3.1.

In comparison to the equations introduced for the standard incompressible Navier–Stokes equation in Chapter 2, the absence of a Dirichlet condition, i.e. (2.3), is apparent in the above formulation. In its stead the general Navier boundary condition (3.4)–(3.5) is prescribed. However, in practice the Dirichlet condition is contained in the GNBC, and as such the boundary condition imposed here is of a more general kind than was previously introduced. The GNBC prescribes a Dirichlet condition in the normal direction (3.4), where the normal velocity of the fluid needs to be the same as the normal velocity prescribed at the boundary. In the tangential plane (3.5), a Robin condition is imposed, which is a condition comprised of a linear combination of a Dirichlet and Neumann condition. The slip length $\varepsilon : \Gamma_{\mathrm{G}} \to \mathbb{R}_0^+ \cup \{\infty\}$ determines the influence of the two parts in the tangential direction, and has the dimension of $[\mathrm{m}]$. In the limiting case where $\varepsilon = 0$, the formulation reduces to the classic Dirichlet condition (provided that $\mu > 0$) $\boldsymbol{u} = \boldsymbol{g}$ on

$$\Gamma_{\mathrm{D}} := \{\boldsymbol{x} \in \Gamma_{\mathrm{G}} \text{ with } \varepsilon = 0\} \tag{3.6}$$

and in the case where $\varepsilon \to \infty$, a combination of a Dirichlet condition in normal direction $\boldsymbol{u}\boldsymbol{P}^n = \boldsymbol{g}\boldsymbol{P}^n$ and a Neumann condition in tangential direction $(2\mu\boldsymbol{\epsilon}(\boldsymbol{u})\boldsymbol{n})\boldsymbol{P}^t = \boldsymbol{h}\boldsymbol{P}^t$ is enforced. Other important sets of interest on the boundary are the inflow boundary

$$\Gamma_{\mathrm{in}} := \{\boldsymbol{x} \in \Gamma_{\mathrm{G}} \mid \boldsymbol{u} \cdot \boldsymbol{n} < 0\} \tag{3.7}$$

and the part of the general Navier boundary Γ_{G} which still contains a Dirichlet contribution

$$\Gamma_{\mathrm{G}}^{\varepsilon} := \{\boldsymbol{x} \in \Gamma_{\mathrm{G}} \text{ with } \varepsilon \in [0, \infty)\}\,. \tag{3.8}$$

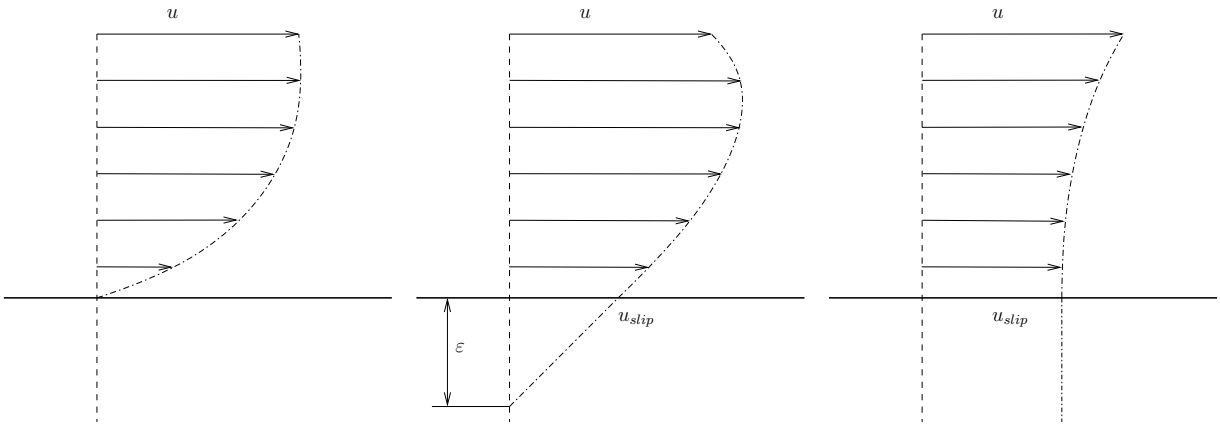

(a) No-slip (b) Navier slip (c) Full slip

Figure 3.2: Effects of different choices of slip lengths on the velocity profile in the vicinity of a wall when $\boldsymbol{g} = \boldsymbol{0}$ and $\boldsymbol{h} = \boldsymbol{0}$ are illustrated here. The slip length for the different cases are set as a) $\varepsilon = 0$, b) $\varepsilon \in (0, \infty)$ and c) $\varepsilon = \infty$, and u_{slip} denotes a non-zero velocity at the boundary in the subfigures.

This type of boundary condition was first proposed by Navier [200] in 1823, with $\boldsymbol{g} = \boldsymbol{h} = \boldsymbol{0}$ as a boundary condition for incompressible fluids at solid walls, and is usually referred to as a Navier slip condition. For this condition, the slip length ε has a natural physical interpretation. In Figure 3.2, a visualization of the flow in the vicinity of a wall is illustrated for different choices of slip lengths. In the case of Figure 3.2a the slip length is $\varepsilon = 0$ and as such a no-slip condition is enforced. In the other extreme case of Figure 3.2c, i.e. $\varepsilon = \infty$, there exists no traction between the fluid and the wall in the tangential direction and as such full slip along the wall is imposed. When the choice is done somewhere between these two extreme cases the slip length can be interpreted as the distance from the wall to the point where the linear extension of the tangential velocity profile intersects with the zero velocity line, as demonstrated in Figure 3.2b. This motivates the dimension of the slip length as $[\mathrm{m}]$, and a physical distance can be interpreted into the choice of slip length.

Even though the Navier slip condition was a promising contender to be the boundary condition of choice at rigid walls for fluid flows, it was shown by experimental observation that in the majority of cases the no-slip boundary condition is an adequate choice of boundary condition. The slip length is in most problems of interest negligibly small and as such $\varepsilon = 0$ is the standard choice in the modeling of fluid flows today. For an account on the acceptance of the no-slip boundary condition, the article by Day [83] or the book by Panton [208] is recommended to the interested reader. Nevertheless, there are some cases where a Navier slip type model has merit. In the experimental work on ultrahydrophobic surfaces by Ou *et al.* [207], significant drag reduction in microchannels was observed and apparent slip lengths larger than 20 μm were measured. In the field of biomimetics, i.e. the process of designing materials which mimic materials found in nature, surfaces have been developed to reduce the drag of flow, as presented in for instance Jung and Bhushan [165], and slip lengths up to 100 μm have been measured. A

review on experimental studies on slip at boundaries for Newtonian fluids can be found in the review article by Neto *et al.* [201]. Another field where a Navier slip model has been employed is to model rough surfaces. In this context a "rough" surface is to be understood as a surface, which variations are small to the typical length of the problem. Instead of discretizing all small cavities, a wall law can be imposed, that is an artificial boundary is imposed inside the domain. This approach has been used extensively in the simulations of geophysical flows as mentioned in Pedlosky [209]. Numerical analysis, comparing the Dirichlet and Navier slip conditions for rough surfaces, can be found in the works of Basson and Gérard-Varet [21] and Jäger and Mikelić [155, 156]. Furthermore, on the interface between a fluid and a porous medium the standard no slip assumption is changed to a Beavers–Josephs condition, as first introduced by Beavers and Joseph [25], and for which a simplified version was later suggested by Saffman [226]. These conditions are in the wall-tangential direction of the porous medium, in essence, a Navier slip type boundary condition. In the vanishing viscosity limit it becomes pertinent to use a Navier slip boundary condition, as with a no-slip condition the Navier–Stokes equations do not converge to the Euler equations, which has been investigated by Clopeau *et al.* [72]. This is also a well known fact with the experimental evidence given in Serrin [233], on high Reynolds number flows of gasses, that their observed motion adhere to a Navier slip condition. Given this connection to high Reynolds number flow, it is quite natural that the Navier boundary condition has also appeared in turbulence modeling. In large eddy simulations (LES), this boundary condition is proposed to be used for the large scales by Galdi and Layton [120]. From a physical perspective this makes sense, as an example given on this by John [161] is that the main vortices in a hurricane do not stick to the boundary, but rather move on it and lose energy while moving (i.e. through friction). Furthermore, in the k-ϵ turbulence model, the Navier slip condition also appears owing to the use of wall law models, where the relation of the two is highlighted by Mohammadi and Pironneau [195]. To model contact between smooth rigid bodies immersed in an incompressible fluid, the no-slip condition is not a feasible choice of boundary condition as shown by Hillairet and Takahashi [145]. An option to resolve the problem can be to make use of a Navier slip boundary condition at the boundaries of the rigid bodies, which has been demonstrated to be a viable path by Neustupa and Penel [202] and Gérard-Varet *et al.* [123]. For polymer melts, slip type conditions play a role in describing their motions as highlighted in the review article by Denn [87] and the references therein. Lastly, the modeling of moving contact lines in multiphase flows necessitates the use of a different boundary condition than the standard no-slip one. If used, the no-slip condition yields non-physical infinite dissipation in the vicinity of the contact line, as shown by Huh and Scriven [151]. An option in overcoming this problem, is to make use of a Navier slip type boundary condition for the motion of the contact line, which was first suggested by Huh and Mason [150].

3.2 A Weak Imposition of a GNBC by means of the Nitsche's Method

As the general Navier boundary condition introduced in (3.4)–(3.5) is usually only mentioned in passing in standard text books on fluid dynamics, an introduction in how it is imposed will be given here. A few different methods have been attempted, where their main difference reside

in the way they treat the normal no-penetration condition. In the work done by Verfürth [269] the wall-normal condition (3.4) is imposed strongly in an ansatz space where the boundary flux condition is satisfied at each node. However, the convergence rates obtained in [269] were suboptimal (with $\mathcal{O}(h)$ for the L^2-error for the velocity and $\mathcal{O}(h^{1/2})$ for the H^1-error for the velocity and L^2-error for the pressure with Taylor–Hood ($\mathbb{P}^2/\mathbb{P}^1$) elements) which was attributed to the Babuška paradox [12]. These initial estimates were later improved in the works by Bänsch and Deckelnick [17] and Knobloch [169] from $\mathcal{O}(h^{1/2})$ to $\mathcal{O}(h^{3/2})$ for the H^1-error and L^2-error for the velocity and pressure respectively, which can not be further improved for Taylor–Hood ($\mathbb{P}^2/\mathbb{P}^1$) elements owing to the approximation of Ω by a polygonal domain Ω_h as is demonstrated in, for instance, Strang and Fix [249]. A strong enforcement of the normal boundary condition (3.4) is also done in Behr [30], however, to take into account the issues arising from curved boundaries the normal at the nodes are calculated with consistent normals as suggested in Engelman *et al.* [106], as to overcome the Babuška paradox. Instead of modifying the function space of the velocity at the Navier boundary condition, a weak imposition with Lagrange multipliers was considered by Verfürth [272]. However, with the introduction of Lagrange multipliers the finite element approximation spaces have to be chosen carefully to satisfy the inf-sup condition. This is solved in [272] by enriching the velocity approximation space with bubble functions in the vicinity of the boundary Γ_G and in Verfürth [271] with residual boundary terms in a so-called stabilized Lagrange multiplier formulation. By employing this weak imposition, Verfürth was able to overcome the Babuška paradox. Instead of employing a Lagrange multiplier method, a penalty formulation was suggested by John [161] where the condition in normal direction is enforced by means of a penalty term. This suggested method was later used in the publications by John and Sahin [163] and John and Liakos [162] for turbulence modeling with LES.

A comparison between the approach with Lagrange multipliers [272] and a strong enforcement of the slip condition was done by Bänsch and Höhn [18], where they were more positively inclined to the use of a strong enforcement for the normal no-penetration constraint (3.4). However they mention that in the case of fictitious domain problems, the strong enforcement approach might be an unfeasible choice. More recently, weak enforcement techniques, i.e. the Lagrange multiplier methods suggested by Verfürth [271, 272] and the Nitsche's method, were investigated and compared by Urquiza *et al.* [267].

What all the methods mentioned above have in common is that they enforce the tangential part of the boundary condition (3.5) by substitution, i.e. the same approach as for a Neumann boundary condition. This leads to issues in the no-slip limit when Navier-slip is considered, as observed for instance by John [161]. In this section the imposition of the tangential direction will be investigated and a method suggested to create a formulation which permits both the Neumann ($\varepsilon \to \infty$) and Dirichlet ($\varepsilon \to 0$) limits. The formulation presented by Juntunen and Stenberg [166], which deals with the imposition of a Robin condition for the Poisson equation, will be used as inspiration in developing the formulation for the wall-tangential Robin condition of the GNBC.

3.2.1 Weak Form of the Navier–Stokes Equations with a General Navier Boundary

For the definition of the weak form, the same assumptions and notations for the spaces as is done in Section 2.1.2 is made here as well. Additionally, the following spaces are introduced,

$$\mathcal{V}_{\boldsymbol{g}}^{n} := \{\boldsymbol{u} \in [H^1(\Omega)]^d \mid \boldsymbol{u}\boldsymbol{P}^n = \boldsymbol{g}\boldsymbol{P}^n \text{ on } \Gamma_{\mathrm{G}} \wedge \boldsymbol{u} = \boldsymbol{g} \text{ on } \Gamma_{\mathrm{D}}\}, \tag{3.9}$$

$$RM(\Omega) := \left\{\boldsymbol{u}(\boldsymbol{x}) := \boldsymbol{c} + \boldsymbol{W}\boldsymbol{x},\ \boldsymbol{c} \in \mathbb{R}^d, \boldsymbol{W} \in S_d\ \ \forall\, \boldsymbol{x} \in \Omega\right\} \tag{3.10}$$

$$\mathcal{V}_{\boldsymbol{g}} := \begin{cases} \mathcal{V}_{\boldsymbol{g}}^{n} & \text{if } \Gamma_{\mathrm{G}}^{\varepsilon} \neq \emptyset \\ \mathcal{V}_{\boldsymbol{g}}^{n} \setminus RM(\Omega) & \text{if } \Gamma_{\mathrm{G}}^{\varepsilon} = \emptyset \end{cases} \tag{3.11}$$

$$\mathcal{Q} := \begin{cases} L^2(\Omega) & \text{if } \Gamma_{\mathrm{N}} \neq \emptyset \\ L_0^2(\Omega) & \text{if } \Gamma_{\mathrm{N}} = \emptyset \end{cases} \tag{3.12}$$

where S_d in (3.10) is the space of anti-symmetric $d \times d$ matrices.

Remark 3.1 (Restriction of velocity solution space $\mathcal{V}_{\boldsymbol{g}}$) *In (3.11) the solution space of the velocity is restricted to not include the set of rigid body motions if $\Gamma_{\mathrm{G}}^{\varepsilon} = \emptyset$. This approach is also pursued in Urquiza* et al. *[267], whereas in the publications by Verfürth [269, 271, 272] the space of symmetric rotations,*

$$\mathcal{R} := \operatorname{span}\left\{\boldsymbol{u}(\boldsymbol{x}) = \boldsymbol{\xi} \times \boldsymbol{x},\ \boldsymbol{\xi} \in \mathbb{R}^d,\ |\boldsymbol{\xi}| = 1,\ \boldsymbol{\xi} \text{ is an axis of symmetry of } \Omega\right\} \tag{3.13}$$

is removed from the velocity space instead. In the end, the restricted solution space $\mathcal{V}_{\boldsymbol{g}}$ will be the same regardless which approach is taken.

The weak form for the problem (3.1)–(3.5) is then defined as: Find the velocity and pressure field $(\boldsymbol{u}, p) \in \mathcal{V}_{\boldsymbol{g}} \times \mathcal{Q}$ such that

$$\begin{aligned}(\rho\frac{\partial \boldsymbol{u}}{\partial t}, \boldsymbol{v})_\Omega + (2\mu\boldsymbol{\epsilon}(\boldsymbol{u}), \boldsymbol{\epsilon}(\boldsymbol{v}))_\Omega + (\rho(\boldsymbol{u}\cdot\nabla)\boldsymbol{u}, \boldsymbol{v})_\Omega - (p, \nabla\cdot\boldsymbol{v})_\Omega + (q, \nabla\cdot\boldsymbol{u})_\Omega \\ - \langle(-p\boldsymbol{I} + 2\mu\boldsymbol{\epsilon}(\boldsymbol{u}))\cdot\boldsymbol{n}, \boldsymbol{v}\rangle_\Gamma = (\boldsymbol{f}, \boldsymbol{v})_\Omega \quad \forall\,(\boldsymbol{v}, q) \in \mathcal{V}_{\boldsymbol{0}} \times \mathcal{Q},\end{aligned} \tag{3.14}$$

where $\Gamma = \Gamma_{\mathrm{N}} \cup \Gamma_{\mathrm{G}}$.

3.2.2 Discretized Form for the Navier–Stokes Equations with a General Navier Boundary with CutFEM

Before discretizing the equations, it will be assumed that no approximation errors are introduced for the geometry, hence, $\Omega = \Omega_h$, $\Gamma = \Gamma_h$ and $\boldsymbol{n} = \boldsymbol{n}_h$ and the notations of these will be used interchangeably. The difficulties arising from these approximation errors will be treated in Chapter 4. For the formulation, it does not change much whether a CutFEM framework or not is pursued. Mainly the presence or absence of stabilization in the interface region makes the difference. Nevertheless, a CutFEM framework is presented here for the weak imposition of the boundary conditions as: find $U_h = (\boldsymbol{u}_h, p_h) \in \mathcal{W}_h$ such that for all $V_h = (\boldsymbol{u}_h, p_h) \in \mathcal{W}_h$

$$\mathcal{A}_h(U_h, V_h) + \mathcal{S}_h^*(U_h, V_h) + \mathcal{G}_h(U_h, V_h) + \mathcal{N}_h(U_h, V_h) = \mathcal{L}_h(V_h) + \mathcal{L}_h^{\mathcal{N}}(V_h) \tag{3.15}$$

where

$$\begin{aligned}
\mathcal{A}_h(U_h, V_h) =& (\rho \frac{\partial \boldsymbol{u}_h}{\partial t}, \boldsymbol{v}_h)_\Omega + (2\mu\boldsymbol{\epsilon}(\boldsymbol{u}_h), \boldsymbol{\epsilon}(\boldsymbol{v}_h))_\Omega + (\rho(\boldsymbol{u}_h \cdot \nabla)\boldsymbol{u}_h, \boldsymbol{v}_h)_\Omega \\
&- \langle(-p_h\boldsymbol{I} + 2\mu\boldsymbol{\epsilon}(\boldsymbol{u}_h)) \cdot \boldsymbol{n}, \boldsymbol{v}_h\rangle_\Gamma \\
&- (p_h, \nabla \cdot \boldsymbol{v}_h)_\Omega + (q_h, \nabla \cdot \boldsymbol{u}_h)_\Omega \qquad (3.16) \\
\mathcal{L}_h(V_h) =& (\boldsymbol{f}, \boldsymbol{v}_h)_\Omega \qquad (3.17) \\
\mathcal{L}_h^{\mathcal{N}}(V_h) =& \mathcal{L}_h^{\Gamma_\mathrm{N}}(V_h) + \mathcal{L}_h^{\Gamma_\mathrm{G},n}(V_h) + \mathcal{L}_h^{\Gamma_\mathrm{G},t}(V_h) \qquad (3.18) \\
\mathcal{N}_h(U_h, V_h) =& \mathcal{N}_h^{\Gamma_\mathrm{N}}(U_h, V_h) + \mathcal{N}_h^{\Gamma_\mathrm{G},n}(U_h, V_h) + \mathcal{N}_h^{\Gamma_\mathrm{G},t}(U_h, V_h) \qquad (3.19)
\end{aligned}$$

with the stabilization terms $\mathcal{S}_h^*(U_h, V_h)$ and $\mathcal{G}_h(U_h, V_h)$ defined as in Section 2.1.3 and Section 2.3.2.2 respectively. In Section 2.3.2 the spaces $\mathcal{V}_h$, $\mathcal{Q}_h$ and $\mathcal{W}_h = \mathcal{V}_h \times \mathcal{Q}_h$ were introduced, and are here briefly repeated to facilitate the reading of this chapter. The spaces $\mathcal{V}_h$ and $\mathcal{Q}_h$ are defined as

$$\mathcal{V}_h := [\mathcal{X}_h]^d, \quad \mathcal{Q}_h := [\mathcal{X}_h], \qquad (3.20)$$

where the shape function space $\mathcal{X}_h$ is defined as in (2.20) as

$$\mathcal{X}_h = \left\{ v_h \in C^0(\Omega_h) : v_h|_T \in \mathbb{V}^k(T) \; \forall \; T \in \mathcal{T}_h \right\}, \qquad (3.21)$$

where $\mathbb{V}^k(T)$ is a polynomial functions space on the element T in the active mesh $\mathcal{T}_h$. Left to define are the boundary terms $\mathcal{N}_h(U_h, V_h)$ and $\mathcal{L}_h^{\mathcal{N}}(V_h)$.

3.2.3 Imposition of the Neumann Condition on Γ_N

The final formulation for imposing a Neumann condition was already presented in (2.13), and as such is nothing new to the reader. However, to facilitate the understanding of the novel imposition of the general Navier condition, two points of view on how to reach this formulation is provided here. The first approach is to note that the boundary term $\langle(-p_h\boldsymbol{I} + 2\mu\boldsymbol{\epsilon}(\boldsymbol{u}_h)) \cdot \boldsymbol{n}, \boldsymbol{v}_h\rangle_\Gamma$ stemming from the integration by parts, also appears in the boundary condition (2.4). Consequently, the following equivalence can be drawn,

$$\langle(-p_h\boldsymbol{I} + 2\mu\boldsymbol{\epsilon}(\boldsymbol{u}_h)) \cdot \boldsymbol{n}, \boldsymbol{v}_h\rangle_{\Gamma_\mathrm{N}} = \langle \boldsymbol{h}, \boldsymbol{v}_h\rangle_{\Gamma_\mathrm{N}}. \qquad (3.22)$$

If this interpretation is pursued, the terms $\mathcal{N}_h^{\Gamma_\mathrm{N}}(U_h, V_h) = \mathcal{L}_h^{\Gamma_\mathrm{N}}(V_h) = 0$ and the so-called consistency term is just replaced by substitution. An alternative, but just as valid, interpretation is that the Neumann condition (2.4) is tested and added consistently to the equation in a weak sense. This is the case if the condition is tested with a test function $\boldsymbol{v}_h$ and added in the following way,

$$\mathcal{N}_h^{\Gamma_\mathrm{N}}(U_h, V_h) - \mathcal{L}_h^{\Gamma_\mathrm{N}}(V_h) = \langle(-p_h\boldsymbol{I} + 2\mu\boldsymbol{\epsilon}(\boldsymbol{u}_h)) \cdot \boldsymbol{n} - \boldsymbol{h}, \boldsymbol{v}_h\rangle_{\Gamma_\mathrm{N}}. \qquad (3.23)$$

Important to stress is that both of the above approaches, to impose a Neumann boundary condition, lead to the same formulation. The above method is the most common way of imposing a natural boundary condition and will be named as a *substitution method* in the following sections.

3.2.4 Imposition of the Dirichlet Condition on Γ_{G} in Normal Direction

In the wall-normal direction of the GNBC, a standard Dirichlet condition is imposed. Accordingly, the Nitsche's method introduced in Section 2.3.2.1, in the equations (2.80)–(2.81), can be applied here, with the condition constrained to only the normal part of the solution variables. This leads to the following addition to the weak form,

$$\begin{aligned}\mathcal{N}_h^{\Gamma_{\mathrm{G}},n}(U_h,V_h)-\mathcal{L}_h^{\Gamma_{\mathrm{G}},n}(V_h) =&\langle\frac{\rho\phi_u}{\gamma^n h}\mathscr{C}_{\Gamma_{\mathrm{G}}^n}(\boldsymbol{u}_h),\boldsymbol{v}_h\rangle_{\Gamma_{\mathrm{G}}}\\ &-\langle\mathscr{C}_{\Gamma_{\mathrm{G}}^n}(\boldsymbol{u}_h),\zeta_u 2\mu\boldsymbol{\epsilon}(\boldsymbol{v}_h)\boldsymbol{n}+q_h\boldsymbol{n}\rangle_{\Gamma_{\mathrm{G}}}\\ &-\langle(\rho\boldsymbol{u}_h\cdot\boldsymbol{n})\mathscr{C}_{\Gamma_{\mathrm{G}}^n}(\boldsymbol{u}_h),\boldsymbol{v}_h\rangle_{\Gamma_{\mathrm{in}}},\end{aligned}\tag{3.24}$$

where $\mathscr{C}_{\Gamma_{\mathrm{G}}^n}(\boldsymbol{u}_h)=(\boldsymbol{u}_h-\boldsymbol{g})\boldsymbol{P}^n$ is the condition (3.4) desired to have imposed in the normal direction, γ^n is the normal Nitsche penalty term, the term $\zeta_u\in\{-1,1\}$ determines whether the formulation is adjoint-consistent ($\zeta_u=1$) or adjoint-inconsistent ($\zeta_u=-1$) and the scaling ϕ_u is defined as in (2.82). Additionally, the inflow boundary Γ_{in}, i.e. when $\boldsymbol{u}_h\cdot\boldsymbol{n}<0$, will be from hereon assumed to only be limited to the pure Dirichlet part of the boundary, i.e. $\Gamma_{\mathrm{in}}\subseteq\Gamma_{\mathrm{D}}$ where $\Gamma_{\mathrm{D}}=\{\boldsymbol{x}\in\Gamma_{\mathrm{G}}\text{ with }\varepsilon=0\}$.

3.2.5 Imposition of the Robin Condition on Γ_{G} in Tangential Direction, by the Substitution Method

Now the wall-tangential Robin condition (3.5), containing both the derivative and the primary variable in the condition, will be considered. Primarily, attention to the split of the consistency term in a normal and tangential part is made. Splitting the consistency into its components leads to

$$\begin{aligned}\langle(-p_h\boldsymbol{I}+2\mu\boldsymbol{\epsilon}(\boldsymbol{u}_h))\cdot\boldsymbol{n},\boldsymbol{v}_h\rangle_{\Gamma} =&\langle((-p_h\boldsymbol{I}+2\mu\boldsymbol{\epsilon}(\boldsymbol{u}_h))\cdot\boldsymbol{n})\boldsymbol{P}^n,\boldsymbol{v}_h\rangle_{\Gamma}\\ &+\langle(2\mu\boldsymbol{\epsilon}(\boldsymbol{u}_h)\cdot\boldsymbol{n})\boldsymbol{P}^t,\boldsymbol{v}_h\rangle_{\Gamma}.\end{aligned}\tag{3.25}$$

Noticeable is the fact that the pressure disappears in the tangential direction. This is easily realizable from $(\boldsymbol{I}\boldsymbol{n})\boldsymbol{P}^t=\boldsymbol{n}(\boldsymbol{I}-\boldsymbol{n}\otimes\boldsymbol{n})=\boldsymbol{n}-\boldsymbol{n}=\boldsymbol{0}$. It immediately becomes apparent that a substitution method is valid here, as the consistency term in the tangential direction appears in the boundary condition (3.5) the following substitution can be undertaken,

$$\langle(2\mu\boldsymbol{\epsilon}(\boldsymbol{u}_h)\cdot\boldsymbol{n})\boldsymbol{P}^t,\boldsymbol{v}_h\rangle_{\Gamma_{\mathrm{G}}}=\langle\boldsymbol{h}\boldsymbol{P}^t-\frac{\mu}{\varepsilon}(\boldsymbol{u}_h-\boldsymbol{g})\boldsymbol{P}^t,\boldsymbol{v}_h\rangle_{\Gamma_{\mathrm{G}}}.\tag{3.26}$$

Consequently, this can also be written with the added terms of (3.18) and (3.19) as

$$\mathcal{N}_h^{\Gamma_{\mathrm{G}},t}(U_h,V_h)-\mathcal{L}_h^{\Gamma_{\mathrm{G}},t}(V_h)=\langle(2\mu\boldsymbol{\epsilon}(\boldsymbol{u}_h)\cdot\boldsymbol{n}-\boldsymbol{h})\boldsymbol{P}^t+\frac{\mu}{\varepsilon}(\boldsymbol{u}_h-\boldsymbol{g})\boldsymbol{P}^t,\boldsymbol{v}_h\rangle_{\Gamma_{\mathrm{G}}}.\tag{3.27}$$

These formulations lead to a way of imposing the wall-tangential condition of the general Navier condition.

Conditioning issues: A problem with the formulations (3.26) and (3.27) is apparent; the case of $\varepsilon \to 0$ is obviously not well defined. The case of $\varepsilon = 0$ could be covered by the classical Nitsche's method which boils down to a standard imposition of a Dirichlet condition. Nonetheless, conditioning issues are present for small slip lengths, thus making it difficult for iterative solvers to arrive at the solution. To demonstrate the ill-conditioning issue, a toy example of a Couette flow is given in the following Section 3.2.5.1.

3.2.5.1 Numerical Example: Couette Flow

A simple Couette flow can be setup to show the issues arising from the application of the substitution method to the general Navier condition.

An important assumption deriving the analytic solution of the Couette flow is that the pressure gradient is constant, and equals the prescribed body force, i.e. $\frac{\partial p}{\partial x} = f_x$, to keep the solution linear. The setup of the problem is depicted in Figure 3.3, where, as can be seen, Dirichlet conditions are set on the left and top boundaries. On the right boundary Γ_{N} a Neumann condition

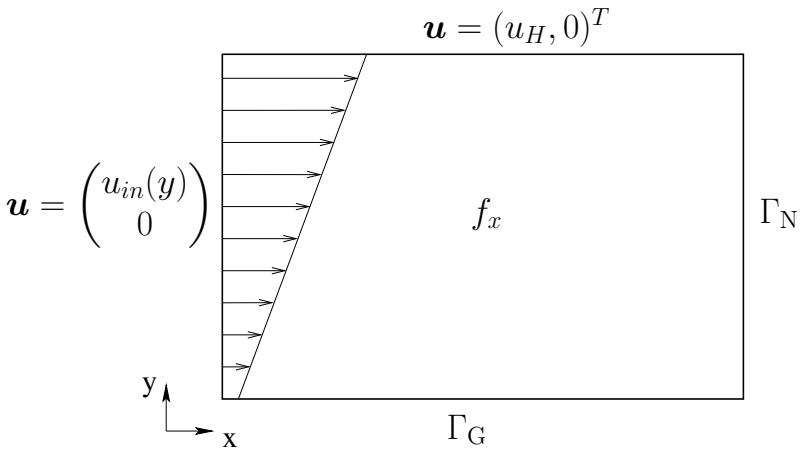

Figure 3.3: Setup for the Couette flow problem. On the top and left boundary, a constant velocity and the matching analytic velocity profile are prescribed. On the bottom boundary Γ_{G} the general Navier boundary is imposed and on the right boundary Γ_{N} a Neumann boundary with the fitting analytic traction is set.

is set with a prescribed traction $\boldsymbol{h}$ as

$$\boldsymbol{h} = \begin{pmatrix} -p_L \\ \mu \frac{\partial u_x}{\partial y} \end{pmatrix} = \begin{pmatrix} -p_L \\ \mu C_1 \end{pmatrix}$$

where p_L is the pressure prescribed at the boundary Γ_{N}. On the bottom boundary Γ_{G} a general Navier boundary is set as

$$\begin{pmatrix} -\varepsilon\mu \frac{\partial u_x}{\partial y} \\ u_y \end{pmatrix} = \begin{pmatrix} -\mu(u_x - u_0) + \varepsilon g_x \\ 0 \end{pmatrix}.$$

The analytic velocity and pressure are then given as

$$\boldsymbol{u} = \begin{pmatrix} C_1 y + C_2 \\ 0 \end{pmatrix}, \quad p = \frac{\partial p}{\partial x}(x - L) + p_L$$

where

$$C_1 = \frac{u_H - \frac{\varepsilon}{\mu}(g_x) - u_0}{(H+\varepsilon)}$$
$$C_2 = \frac{\varepsilon}{\mu}(g_x + \mu C_1) + u_0$$

In the ensuing simulations, the following parameters are fixed, $u_0 = 5$, $u_H = 53$, $g_x = 0.1$, $f_x = \frac{\partial p}{\partial x} = 10$, $H = L = 1.6$ (i.e. $\Omega_h = [0, 1.6] \times [0, 1.6]$) and $p_L = -4$. The mesh chosen for the system was a 16×16 partition of continuous bi-linear quadrilateral elements, and the Nitsche penalty parameter, for the imposition of the wall-normal Dirichlet condition, was set to $1/\gamma^n = 10.0$ for an adjoint-consistent ($\zeta_u = 1$) formulation. Furthermore, a residual based stabilization is chosen and no ghost penalty terms are necessary as a fitted mesh is used.

In the following example the condition number $\kappa(\boldsymbol{A})$ will be calculated for the converged Jacobian matrix of the system of equations $\boldsymbol{A}$ which normally for a given mesh size should remain constant. The Jacobian matrix is the variation of the residual R of the solution, i.e. $\boldsymbol{A} = \frac{\partial R(U_h^k, V_h)}{\partial U_h}$, which solving for the step $k+1$, depends on the previous step k. The condition number is defined as

$$\kappa(\boldsymbol{A}) = |\boldsymbol{A}||\boldsymbol{A}^{-1}|$$

with the matrix norm defined as $|\boldsymbol{A}| = \sup_{\boldsymbol{V} \in \mathbb{R}^n \setminus 0} |\boldsymbol{A} \cdot \boldsymbol{V}|/|\boldsymbol{V}|$, where $|\boldsymbol{V}|$ is the Euclidean norm. As was demonstrated by Juntunen and Stenberg [166], the substitution method for a Poisson equation with Robin boundary conditions, yields for the system matrix $\boldsymbol{A}$ (as the Poisson equation is linear system of equation) the following condition number,

$$\kappa(\boldsymbol{A}) = \mathcal{O}(h^{-2} + (\varepsilon h)^{-1}). \tag{3.28}$$

This trend seems to exists as well in the case for the Navier–Stokes equation as can be seen in Figure 3.4, where the condition number is evaluated for the converged Jacobian (i.e. the last iteration of the Newton iteration with a prescribed tolerance of 10^{-12}). For small ε a clear trend of a deteriorating condition number is visible. The contribution from the slip length starts dominating the system at different times for different dynamic viscosities, which is noticeable when comparing Figure 3.4a with $\nu = \mu/\rho = 10$ and Figure 3.4b with $\nu = \mu/\rho = 0.05$, where it becomes clear that small slip lengths start dominating the system earlier than for viscous dominated problems. Nevertheless, for non-linear systems determining where, and by how much, small slip lengths damages the system conditioning can be difficult to predict. As such, it would be beneficial with a formulation that can deal with the small ε limit, without causing conditioning problems.

3.2.6 Imposition of the Robin Condition on Γ_G in Tangential Direction, by means of the Nitsche's Method

Imposing a Robin condition for the Poisson problem faces the same issue as when the substitution method is applied in the case of the general Navier condition. For the Poisson problem a solution to the issues arising in the Dirichlet limit, was proposed by Juntunen and Stenberg [166]. In this publication both the Dirichlet and Neumann limits are well defined, and no

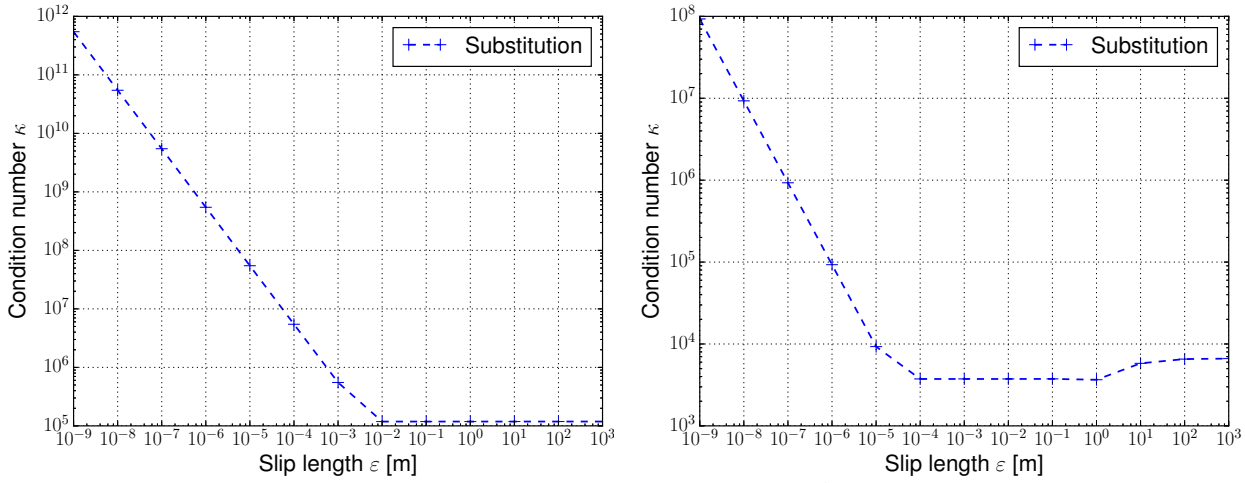

(a) $\rho = 0.1$, $\mu = 1.0$ (b) $\rho = 0.1$, $\mu = 0.005$

Figure 3.4: The sensitivity of the condition number for the Galerkin substitution with the choice of different slip lengths ε for the Couette flow problem.

ill conditioning occurs in neither limit. This method has since been applied to couple elliptic domains as in Annavarapu *et al.* [5] by imposing the Robin condition as an interface condition. A similar approach was pursued by Fernández and Landajuela [110] for a fluid-structure interaction coupling. Furthermore, Vergara [273] applied the method to impose defective boundary conditions for the Navier–Stokes equations.

The approach in [166] has much in common with how a Dirichlet condition is imposed by means of the Nitsche's method. It can be viewed as instead of taking the usual approach for Robin conditions, i.e. treating them as a Neumann condition, the condition is treated as one would a weak enforcement of a Dirichlet condition. Extending the approach to the Navier–Stokes equations the following addition of terms is made,

$$\begin{aligned}\mathcal{N}_h^{\Gamma_G,t}(U_h, V_h) - \mathcal{L}_h^{\Gamma_G,t}(V_h) =& \langle \frac{1}{\varepsilon + \gamma^t h} \mathscr{C}_{\Gamma_G^t}(\boldsymbol{u}_h), \boldsymbol{v}_h \rangle_{\Gamma_G} \\ &- \langle \frac{\gamma^t h}{\varepsilon + \gamma^t h} \mathscr{C}_{\Gamma_G^t}(\boldsymbol{u}_h), \zeta_u 2\boldsymbol{\epsilon}(\boldsymbol{v}_h)\boldsymbol{n} \rangle_{\Gamma_G}\end{aligned} \tag{3.29}$$

where

$$\mathscr{C}_{\Gamma_G^t}(\boldsymbol{u}_h) = (\varepsilon(2\mu\boldsymbol{\epsilon}(\boldsymbol{u})\boldsymbol{n} - \boldsymbol{h}) + \mu(\boldsymbol{u} - \boldsymbol{g}))\,\boldsymbol{P}^t \tag{3.30}$$

and the term $\zeta_u \in \{-1, 1\}$, is the same as introduced in Section 2.3.2.1, to prescribe either an adjoint-consistent $\zeta_u = 1$ or adjoint-inconsistent $\zeta_u = -1$ formulation. The omission of the testing with $q_h\boldsymbol{n}$ in comparison to (3.24) is explained by it not having any contribution in the tangential plane of the boundary condition. Furthermore, it is noticeable that the Nitsche penalty term is not scaled with any convective or reactive contribution. These scalings in the normal direction are detrimental in guaranteeing inf-sup stability, by contrast, they can be omitted in the tangential direction and the resulting formulation will still be inf-sup stable. Apart from demonstrating this in a rigorous mathematical way, which will be undertaken for the Oseen equation in Section 3.3, an interpretation of the physics can be done to understand the different scalings in normal and tangential directions. If the flow is strongly convection dominated, i.e. in

the Euler limit, or reaction dominated, i.e. in the Darcy limit, no tangential boundary condition on walls are to be imposed. Hence, in the limit of small viscosity, the imposition of the tangential condition disappears whereas the normal condition is still enforced as a result of the additional scaling added for these regimes. It is also apparent that the added terms are consistent. Given that when the boundary condition is fulfilled, $\mathscr{C}_{\Gamma_{\mathrm{G}}^t}(\boldsymbol{u}_h) = \mathbf{0}$, and consequently the added terms disappear.

Owing to the unusual scalings of the penalty and adjoint term, in the added terms (3.29), a short excursion in some important limiting cases of this formulation is conducted.

The Dirichlet limit, $[\varepsilon \to 0]$**:** By setting $\varepsilon = 0$, it can easily be seen that (3.29) reduces to

$$\mathscr{N}_h^{\Gamma_{\mathrm{G}},t}(U_h, V_h) - \mathscr{L}_h^{\Gamma_{\mathrm{G}},t}(V_h) = \langle \frac{\mu}{\gamma^t h}(\boldsymbol{u} - \boldsymbol{g})\boldsymbol{P}^t, \boldsymbol{v}_h \rangle_{\Gamma_{\mathrm{G}}} - \langle (\boldsymbol{u} - \boldsymbol{g})\boldsymbol{P}^t, \zeta_u \mu 2\boldsymbol{\epsilon}(\boldsymbol{v}_h)\boldsymbol{n} \rangle_{\Gamma_{\mathrm{G}}}, \quad (3.31)$$

which is nothing else than the standard terms added for an imposition of a Dirichlet condition by means of the Nitsche's method, as already dealt with in Section 2.3.2.1.

The Neumann limit, $[\varepsilon \to \infty \wedge \gamma^t h \ll \varepsilon]$**:** Taking the limit $\varepsilon \to \infty$ with a bounded penalty parameter γ^t, the following terms from (3.29) are added to the weak form,

$$\begin{aligned}\mathscr{N}_h^{\Gamma_{\mathrm{G}},t}(U_h, V_h) - \mathscr{L}_h^{\Gamma_{\mathrm{G}},t}(V_h) =& \langle (2\mu\boldsymbol{\epsilon}(\boldsymbol{u})\boldsymbol{n} - \boldsymbol{h})\boldsymbol{P}^t, \boldsymbol{v}_h \rangle_{\Gamma_{\mathrm{G}}} \\ &- \langle \gamma^t h(2\mu\boldsymbol{\epsilon}(\boldsymbol{u})\boldsymbol{n} - \boldsymbol{h})\boldsymbol{P}^t, \zeta_u 2\boldsymbol{\epsilon}(\boldsymbol{v}_h)\boldsymbol{n} \rangle_{\Gamma_{\mathrm{G}}}. \end{aligned} \quad (3.32)$$

On the first row in (3.32) the classical Neumann term emerges, where the condition is tested with the test function, just as was done in (3.27). Nonetheless, in this new formulation, an additional term appears on the second row which does not exist in the classical Galerkin substitution method. Noticeable is that this term is a consistent addition of the boundary condition, and as such does not violate the validity of the solution. Furthermore if $\gamma^t h \to 0$, i.e. when either the mesh is refined or when the tangential penalty parameter is small, goes to 0, and the standard Galerkin substitution approach is retained. The drawback of this imposition of a Neumann condition is, even though the stability properties (investigated in Section 3.3) of the suggested formulation postulates that for an adjoint-inconsistent formulation the choice of $0 \leq \gamma^t < \infty$ is permissible, In practice this is not realizable, as when γ^t becomes larger the discretized system of equations becomes increasingly ill-conditioned. Hence, in the Neumann limit the tangential parameter is effectively limited from above.

The Penalty-free limit, $[\gamma^t h \to \infty]$**:** Another interesting limit explored here is the penalty-free limit $\gamma^t \to \infty$, which yields the following terms,

$$\mathscr{N}_h^{\Gamma_{\mathrm{G}},t}(U_h, V_h) - \mathscr{L}_h^{\Gamma_{\mathrm{G}},t}(V_h) = -\langle (\varepsilon(2\mu\boldsymbol{\epsilon}(\boldsymbol{u})\boldsymbol{n} - \boldsymbol{h}) + \mu(\boldsymbol{u} - \boldsymbol{g}))\, \boldsymbol{P}^t, \zeta_u 2\boldsymbol{\epsilon}(\boldsymbol{v}_h)\boldsymbol{n} \rangle_{\Gamma_{\mathrm{G}}}. \quad (3.33)$$

This limit has been studied by Burman [50] and Boiveau and Burman [36] for the imposition of Dirichlet conditions, where it has been shown that adjoint-inconsistent $\zeta_u = -1$ formulations can be imposed without a penalty term, i.e. $\gamma \to \infty$. From the term (3.33), it is apparent that when ε becomes large, it will start dominating the conditioning of the system. Hence, as already observed in the previous paragraph, the penalty-free limit $\gamma^t \to \infty$ and Neumann limit

$\varepsilon \to \infty$ are not compatible. In this thesis, no stability arguments or deeper investigation will be undertaken for the penalty-free formulation, only the general feasibility of it is commented here.

The effects on the stability and a priori error estimates from the addition of the terms (3.24) and (3.29) will be further investigated for the linearized Navier–Stokes equation, i.e. the Oseen equation, in Section 3.3

Remark 3.2 *As the added boundary terms contain projection matrices, the necessary linearization to apply a Newton's method is not straightforward. Hence, the linearization of the terms are displayed in Appendix A to facilitate the implementation of these for the reader.*

3.2.6.1 Numerical Example: Couette Flow

The same toy example as conducted in Section 3.2.5.1 will be performed here as well for the imposition of the general Navier condition by means of the Nitsche's method. For the Nitsche terms, the wall-normal penalty parameter is kept as $1/\gamma^n = 10.0$ and the wall-tangential penalty parameter is chosen as $1/\gamma^t = 10.0$. As is done for the wall-normal terms, the wall-tangential imposition with the Nitsche's method is done with an adjoint-consistent formulation. It is clear

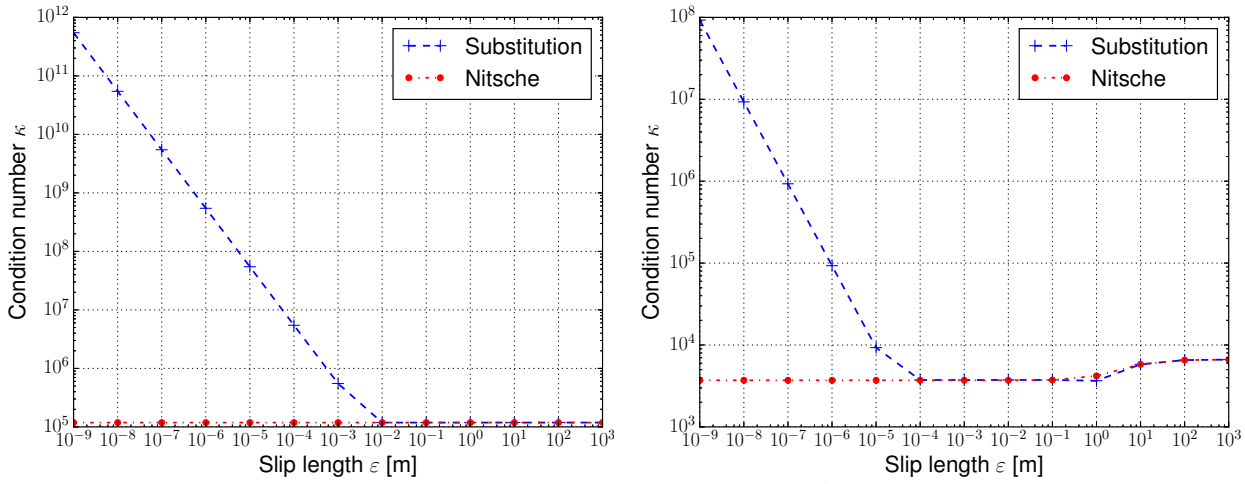

(a) $\rho = 0.1$, $\mu = 1.0$ (b) $\rho = 0.1$, $\mu = 0.005$

Figure 3.5: The sensitivity of the condition number for the Galerkin substitution and Nitsche's method with the choice of different slip lengths ε for the Couette flow problem.

in Figure 3.5 that with the new approach of imposing the tangential Robin condition (3.29) the condition number remains bounded in the small slip length limit and that for larger slip lengths it performs just as well as the substitution method. In the case of large dynamic viscosity as depicted in Figure 3.5a with $\nu = \mu/\rho = 10$ the condition number remains constant for all ε, and in the case of a smaller dynamic viscosity as shown in Figure 3.5b with $\nu = \mu/\rho = 0.05$ the proposed method provides bounded condition numbers. Only in the case of $\varepsilon = 1$ there is a slight deviation from the substitution method, but the limiting cases are overlapping. This deviation is not surprising as imposition of the boundary condition are different, and some variation of the condition number between the two is expected.

3.3 Analysis of the General Navier Boundary Condition for the Oseen Problem

In this section the linearized Navier–Stokes equation with general Navier boundary conditions will be analyzed. The reason why the linearized formulation is studied is in part due to the possibility to use techniques from functional analysis and linear functional theory, and in part that the iterative solving of the Navier–Stokes equations can be interpreted as solving a series of Oseen equation. Consequently, it has merit to investigate these sub-problems thoroughly.

The mathematical analysis conducted in this section was previously published in Winter *et al.* [279]. In particular Sections 3.3.2 – 3.3.6 will be presented with only minor modification – with most parts directly taken – from the aforementioned publication. Some of the more mathematical intricacies will be referred to the publication by Massing *et al.* [184] which deals with the same problem but for the Dirichlet case. This choice is done to facilitate the readability for an engineering audience and as such leave the most technical parts to the aforementioned publication. The focus here will be put on the most quintessential results of the analysis.

3.3.1 The Oseen Problem with General Navier Boundary Conditions

Given a domain $\Omega \subset \mathbb{R}^d$, $d \in \{2,3\}$, where Ω is either a bounded convex domain or a plane bounded domain with Lipschitz and piecewise C^2 boundary with convex angles. On this domain the non-linear Navier–Stokes equations (3.1)–(3.5) scaled with ρ^{-1} are considered. After applying a time discretization method and a linearization step, many solution algorithms of the Navier–Stokes equations can be reduced to solving a sequence of auxiliary Oseen type problems for the velocity field $\boldsymbol{u} : \Omega \to \mathbb{R}^d$ and the pressure field $p : \Omega \to \mathbb{R}$:

$$\sigma \boldsymbol{u} + \boldsymbol{\beta} \cdot \nabla \boldsymbol{u} - \nabla \cdot (2\nu \boldsymbol{\epsilon}(\boldsymbol{u})) + \nabla p = \boldsymbol{f} \quad \text{in } \Omega, \tag{3.34}$$

$$\nabla \cdot \boldsymbol{u} = 0 \quad \text{in } \Omega, \tag{3.35}$$

$$(\boldsymbol{u} - \boldsymbol{g})\, \boldsymbol{P}^n = \boldsymbol{0} \quad \text{on } \Gamma, \tag{3.36}$$

$$(\varepsilon(2\nu \boldsymbol{\epsilon}(\boldsymbol{u})\boldsymbol{n} - \boldsymbol{h}) + \nu(\boldsymbol{u} - \boldsymbol{g}))\, \boldsymbol{P}^t = \boldsymbol{0} \quad \text{on } \Gamma, \tag{3.37}$$

where $\boldsymbol{\epsilon}(\boldsymbol{u}) := \frac{1}{2}(\nabla \boldsymbol{u} + (\nabla \boldsymbol{u})^T)$ denotes the strain rate tensor, $\boldsymbol{\beta} \in [W^{1,\infty}(\Omega)]^d \cap H_0(\nabla\cdot;\Omega)$ the given divergence-free advective velocity field and $\boldsymbol{f} \in [L^2(\Omega)]^d$ the body force. The reactive term σ and the kinematic viscosity ν are assumed to be positive real-valued constants.

In the following, the space $W^{m,q}(\Omega)$, is a standard Sobolev space where $0 \leq m < \infty$ and $1 \leq q < \infty$, and the space $H^m(\Omega)$ is a subset of this space as $H^m(\Omega) = W^{m,2}(\Omega)$. Some properties of the functions and definitions already touched upon in Section 3.1 will be repeated here for completeness. For the boundary conditions (3.36)–(3.37) the prescribed velocity and traction are defined as

$$\boldsymbol{g} \in [H^{3/2}(\Gamma)]^d \qquad \text{and} \qquad \boldsymbol{h} \in [H^{1/2}(\Gamma)]^d, \tag{3.38}$$

and the normal and tangential projection matrices are construed from the outward pointing unit normal $\boldsymbol{n}$ of the boundary Γ as $\boldsymbol{P}^n := \boldsymbol{n} \otimes \boldsymbol{n}$ and $\boldsymbol{P}^t := \boldsymbol{I} - \boldsymbol{n} \otimes \boldsymbol{n}$, where $\boldsymbol{I}$ is the $d \times d$ identity matrix. Utilizing a non-negative slip length function $\varepsilon : \Gamma \to \mathbb{R}_0^+ \cup \{\infty\}$, the classical

Dirichlet boundary conditions can be recovered by setting $\varepsilon = 0$, which for $\nu > 0$ states that $\boldsymbol{u} = \boldsymbol{g}$ on $\Gamma_{\mathrm{D}} := \{\boldsymbol{x} \in \Gamma \text{ with } \varepsilon = 0\} \subseteq \Gamma$. By choosing $\varepsilon = \infty$ and $\boldsymbol{h} = \boldsymbol{0}$ the boundary condition reduces to a full-slip condition as the tangential velocity on Γ is not constrained anymore.

For the subsequent analysis some assumptions on the boundary sets are needed. The part of Γ with $0 \leq \varepsilon < \infty$ is denoted by Γ^{ε} and is assumed to be non-vanishing, i.e. $\mathrm{meas}(\Gamma^{\varepsilon}) > 0$, to avoid not well-posed pure slip-boundary problems, as discussed in Section 3.2.1. It is further assumed that the inflow boundary $\Gamma_{\mathrm{in}} := \{\boldsymbol{x} \in \Gamma \mid \boldsymbol{\beta} \cdot \boldsymbol{n} < 0\}$ is confined to the Dirichlet boundary, i.e. $\Gamma_{\mathrm{in}} \subseteq \Gamma_{\mathrm{D}}$.

3.3.2 Variational Formulation for the Oseen Equation

For completeness sake the functional spaces for the weak form of the Oseen equation will be repeated here, as they are, in essence, the same as introduced for the weak form of the Navier–Stokes equation with general Navier boundaries in Section 3.2.1,

$$\mathcal{V}_{\boldsymbol{g}} := \{\boldsymbol{u} \in [H^1(\Omega)]^d \mid (\boldsymbol{u} - \boldsymbol{g})\boldsymbol{P}^n = \boldsymbol{0} \text{ on } \Gamma \wedge \boldsymbol{u} = \boldsymbol{g} \text{ on } \Gamma_D\}, \tag{3.39}$$

$$\mathcal{V} := [H^1(\Omega)]^d \tag{3.40}$$

$$\mathcal{Q} := L^2_0(\Omega). \tag{3.41}$$

The corresponding weak formulation of the Oseen problem (3.34)–(3.37) is to find the velocity and the pressure field $(\boldsymbol{u}, p) \in \mathcal{V}_{\boldsymbol{g}} \times \mathcal{Q}$ such that

$$\begin{aligned} a(\boldsymbol{u}, \boldsymbol{v}) + b(p, \boldsymbol{v}) - b(q, \boldsymbol{u}) + \langle \frac{\nu}{\epsilon} \boldsymbol{u}\boldsymbol{P}^t, \boldsymbol{v} \rangle_{\Gamma} \\ = l(\boldsymbol{v}) + \langle (\boldsymbol{h} + \frac{\nu}{\epsilon}\boldsymbol{g})\boldsymbol{P}^t, \boldsymbol{v} \rangle_{\Gamma} \quad \forall\, (\boldsymbol{v}, q) \in \mathcal{V}_{\boldsymbol{0}} \times \mathcal{Q}, \end{aligned} \tag{3.42}$$

where

$$a(\boldsymbol{u}, \boldsymbol{v}) := (\sigma \boldsymbol{u}, \boldsymbol{v})_{\Omega} + (\boldsymbol{\beta} \cdot \nabla \boldsymbol{u}, \boldsymbol{v})_{\Omega} + (2\nu \boldsymbol{\epsilon}(\boldsymbol{u}), \boldsymbol{\epsilon}(\boldsymbol{v}))_{\Omega}, \tag{3.43}$$

$$b(p, \boldsymbol{v}) := -(p, \nabla \cdot \boldsymbol{v})_{\Omega}, \tag{3.44}$$

$$l(\boldsymbol{v}) := (\boldsymbol{f}, \boldsymbol{v})_{\Omega}. \tag{3.45}$$

For the well-posedness and solvability of the continuous Oseen problem (3.42), the interested reader is referred to, e.g. Girault and Raviart [127], Solonnikov [243] and in the case with general Navier boundary condition, to Verfürth [271].

3.3.3 A Stabilized Nitsche-type Cut Finite Element Method for the Oseen Problem

This section is devoted to introducing the necessary notation, formulation and stabilizations to undertake the proof of inf-sup stability and a priori error estimates for the discretized form of the Oseen equations. In the subsequent analysis the notation $a \lesssim b$ is used for $a \leq Cb$, where C is some generic positive constant that varies with the context it is used, but is always independent of the mesh size h and the intersection of the mesh $\mathcal{T}_h$ by Γ.

3.3.3.1 Computational Meshes and Cut Finite Element Spaces

The notation of Section 2.3.1.1 is here repeated, with some additional constraints on the computational mesh and the interface Γ. The sets introduced here are the same as introduced in the aforementioned section, however, as only one domain is considered the $+$ is omitted to shorten the notation, i.e. $\Omega = \Omega^+$ and $\Omega_h^* = \Omega_h^{+,*}$.

To simplify the analysis it is assumed that a sequence of quasi-uniform meshes $\widehat{\mathscr{T}}_h = \{T\}$, each consisting of shape-regular finite elements T with mesh size parameter h, cover the physical domain Ω. For each background mesh $\widehat{\mathscr{T}}_h$, the finite element solution is then approximated on an *active* part of the background mesh

$$\mathscr{T}_h := \{T \in \widehat{\mathscr{T}}_h : T \cap \Omega \neq \emptyset\}, \tag{3.46}$$

consisting of all elements in $\widehat{\mathscr{T}}_h$ which intersect the physical domain Ω. The possibly enlarged domain which is covered by the union of all elements $T \in \mathscr{T}_h$ is denoted by Ω_h^*. The subset of all elements, of the respective active mesh, which are located in the vicinity of the boundary Γ are denoted as

$$\mathscr{T}_\Gamma := \{T \in \mathscr{T}_h : T \cap \Gamma \neq \emptyset\}. \tag{3.47}$$

For the CIP and ghost penalty stabilizations the set of all facets is defined by $\mathscr{F}_h$. An important subset of $\mathscr{F}_h$ is the set of interior facets, which is the set of facets sharing two elements, denoted by T_F^+ and T_F^-, where both elements are in the active mesh, i.e. $T_F^+ \in \mathscr{T}_h$ and $T_F^- \in \mathscr{T}_h$. The notation $\mathscr{F}_\Gamma$ is used for the set of all interior facets belonging to elements intersected by the boundary Γ,

$$\mathscr{F}_\Gamma := \{F \in \mathscr{F}_i : \ T_F^+ \cap \Gamma \neq \emptyset \vee T_F^- \cap \Gamma \neq \emptyset\}. \tag{3.48}$$

Figure 2.7 summarizes the notation.

To carry out the subsequent numerical analysis, it is required that the interface is to be reasonably resolved by the mesh $\mathscr{T}_h$. Introducing first a the tubular region around a smooth surface Γ, which is defined as $U_\delta(\Gamma) = \{\boldsymbol{x} \in \mathbb{R}^d : \operatorname{dist}(\Gamma, \boldsymbol{x}) < \delta\}$. In this tubular region, there is a radius $\delta_0 > 0$ for which there exists a unique closest point projection $\mathfrak{p}(x)$, defined as

$$|\boldsymbol{x} - \mathfrak{p}(\boldsymbol{x})| = \operatorname{dist}(\Gamma, \boldsymbol{x}) \ \forall \boldsymbol{x} \in U_\delta(\Gamma).$$

For the following analysis it is assumed that this radius is larger than the mesh size, i.e. $\delta_0 > h$. In short, that the tubular region of the interface Γ needs to be larger than the mesh resolution.

Let $\mathscr{X}_h$ be the finite element spaces consisting of continuous piecewise polynomials (restricted to simplices, $\mathbb{P}^k$, in the following) of order k for a given mesh $\mathscr{T}_h$

$$\mathscr{X}_h = \left\{v_h \in C^0(\Omega_h^*) : v_h|_T \in \mathbb{P}^k(T) \, \forall \, T \in \mathscr{T}_h\right\}. \tag{3.49}$$

For the discrete cut finite element approximation of the solution to the Oseen problem, an equal-order interpolations for velocity and pressure are employed, where

$$\mathscr{V}_h = [\mathscr{X}_h]^d, \quad \mathscr{Q}_h = \mathscr{X}_h, \quad \mathscr{W}_h = \mathscr{V}_h \times \mathscr{Q}_h \tag{3.50}$$

is the discrete velocity space, the discrete pressure space and the total approximation space, respectively.

3.3.3.2 Weak Imposition of a Generalized Boundary Condition for the Oseen Equation

The weak form for a stabilized unfitted mesh approach of the imposition of a generalized Navier boundary conditions for the Oseen problem will be presented in this section. In the case when the slip length coefficient is sufficiently large, the tangential constraint (3.37) can be imposed by a Galerkin substitution method, just like it was done for the Navier–Stokes equation in Section 3.2.5. In the Oseen case this infers that the wall-tangential boundary term, stemming from the integration by parts of the momentum equation, can be rewritten for the discretized weak form as

$$-\langle(2\nu\boldsymbol{\epsilon}(\boldsymbol{u}_h)\boldsymbol{n})\boldsymbol{P}^t, \boldsymbol{v}_h\rangle_\Gamma = \langle(-\boldsymbol{h} + \varepsilon^{-1}\nu(\boldsymbol{u}-\boldsymbol{g}))\boldsymbol{P}^t, \boldsymbol{v}_h\rangle_\Gamma. \tag{3.51}$$

Such an imposition of the wall-tangential Robin condition provides a reasonable and stable method for large slip length coefficients ε. However, it is well known that for $\varepsilon \to 0$, i.e. when a Dirichlet condition is approached, the conditioning of the formulation deteriorates and, as a result, does not provide an accurate and stable formulation, see the results in Section 3.2.5 or the discussion in Juntunen and Stenberg [166]. Based on the work by Juntunen and Stenberg on the Poisson problem, a formulation will be proposed in the following, which overcomes this issue and provides stability, optimal *a priori* error estimates and a bounded conditioning with respect to small choices of $\varepsilon \in [0, \infty]$.

The unfitted Nitsche-type finite element formulation for the Oseen problem is given as: find $U_h = (\boldsymbol{u}_h, p_h) \in \mathcal{W}_h$ such that for all $V_h = (\boldsymbol{v}_h, q_h) \in \mathcal{W}_h$

$$A_h(U_h, V_h) + S_h(U_h, V_h) + G_h(U_h, V_h) = L_h(V_h), \tag{3.52}$$

where

$$A_h(U_h, V_h) := a_h(\boldsymbol{u}_h, \boldsymbol{v}_h) + b_h(p_h, \boldsymbol{v}_h) - b_h(q_h, \boldsymbol{u}_h), \tag{3.53}$$

with

$$a_h(\boldsymbol{u}_h, \boldsymbol{v}_h) := a(\boldsymbol{u}_h, \boldsymbol{v}_h) - \langle 2\nu\boldsymbol{\epsilon}(\boldsymbol{u}_h)\boldsymbol{n}, \boldsymbol{v}_h\rangle_\Gamma \tag{3.54}$$

$$- \zeta_u\langle \boldsymbol{u}_h\cdot\boldsymbol{n}, (2\nu\boldsymbol{\epsilon}(\boldsymbol{v}_h)\boldsymbol{n})\cdot\boldsymbol{n}\rangle_\Gamma + \langle \frac{\nu}{\gamma^n h}\boldsymbol{u}_h\cdot\boldsymbol{n}, \boldsymbol{v}_h\cdot\boldsymbol{n}\rangle_\Gamma \tag{3.55}$$

$$+ \langle \frac{\phi_u}{\gamma^n h}\boldsymbol{u}_h\cdot\boldsymbol{n}, \boldsymbol{v}_h\cdot\boldsymbol{n}\rangle_\Gamma - \langle (\boldsymbol{\beta}\cdot\boldsymbol{n})\boldsymbol{u}_h, \boldsymbol{v}_h\rangle_{\Gamma_{\text{in}}} \tag{3.56}$$

$$+ \langle \frac{1}{\varepsilon+\gamma^t h}\varepsilon(2\nu\boldsymbol{\epsilon}(\boldsymbol{u}_h)\boldsymbol{n})\boldsymbol{P}^t, \boldsymbol{v}_h\rangle_\Gamma + \langle \frac{1}{\varepsilon+\gamma^t h}\nu\boldsymbol{u}_h\boldsymbol{P}^t, \boldsymbol{v}_h\rangle_\Gamma \tag{3.57}$$

$$- \zeta_u\langle \frac{\gamma^t h}{\varepsilon+\gamma^t h}\varepsilon(2\nu\boldsymbol{\epsilon}(\boldsymbol{u}_h)\boldsymbol{n})\boldsymbol{P}^t, 2\boldsymbol{\epsilon}(\boldsymbol{v}_h)\boldsymbol{n}\rangle_\Gamma - \zeta_u\langle \frac{\gamma^t h}{\varepsilon+\gamma^t h}\nu\boldsymbol{u}_h\boldsymbol{P}^t, 2\boldsymbol{\epsilon}(\boldsymbol{v}_h)\boldsymbol{n}\rangle_\Gamma, \tag{3.58}$$

$$b_h(p_h, \boldsymbol{v}_h) := b(p_h, \boldsymbol{v}_h) + \langle p_h, \boldsymbol{v}_h\cdot\boldsymbol{n}\rangle_\Gamma, \tag{3.59}$$

$$L_h(V_h) := l(\boldsymbol{v}_h) \tag{3.60}$$

$$- \zeta_u\langle \boldsymbol{g}\cdot\boldsymbol{n}, (2\nu\boldsymbol{\epsilon}(\boldsymbol{v}_h)\boldsymbol{n})\cdot\boldsymbol{n}\rangle_\Gamma + \langle \frac{\nu}{\gamma^n h}\boldsymbol{g}\cdot\boldsymbol{n}, \boldsymbol{v}_h\cdot\boldsymbol{n}\rangle_\Gamma \tag{3.61}$$

$$- \langle \boldsymbol{g}\cdot\boldsymbol{n}, q_h\rangle_\Gamma + \langle \frac{\phi_u}{\gamma^n h}\boldsymbol{g}\cdot\boldsymbol{n}, \boldsymbol{v}_h\cdot\boldsymbol{n}\rangle_\Gamma - \langle (\boldsymbol{\beta}\cdot\boldsymbol{n})\boldsymbol{g}, \boldsymbol{v}_h\rangle_{\Gamma_{\text{in}}} \tag{3.62}$$

$$+ \langle \frac{1}{\varepsilon+\gamma^t h}\varepsilon\boldsymbol{h}\boldsymbol{P}^t, \boldsymbol{v}_h\rangle_\Gamma + \langle \frac{1}{\varepsilon+\gamma^t h}\nu\boldsymbol{g}\boldsymbol{P}^t, \boldsymbol{v}_h\rangle_\Gamma \tag{3.63}$$

$$- \zeta_u\langle \frac{\gamma^t h}{\varepsilon+\gamma^t h}\varepsilon\boldsymbol{h}\boldsymbol{P}^t, 2\boldsymbol{\epsilon}(\boldsymbol{v}_h)\boldsymbol{n}\rangle_\Gamma - \zeta_u\langle \frac{\gamma^t h}{\varepsilon+\gamma^t h}\nu\boldsymbol{g}\boldsymbol{P}^t, 2\boldsymbol{\epsilon}(\boldsymbol{v}_h)\boldsymbol{n}\rangle_\Gamma, \tag{3.64}$$

where $\phi_u : \Omega_h^* \to \mathbb{R}$ is defined on each element as

$$\phi_{u,T} := \nu + \|\boldsymbol{\beta}\|_{0,\infty,T} h + \sigma h^2. \tag{3.65}$$

The stabilization operators S_h, G_h are specified later in Section 3.3.3.3. Starting from the weak formulation (3.42), it can be seen that due to the weak imposition of the boundary condition, the standard consistency terms remain in the momentum equation (3.54) and (3.59). Equivalent to a Nitsche formulation for a pure Dirichlet boundary condition, these standard consistency terms on the boundary Γ are potential sources for instabilities and are analyzed further in Section 3.3.5 and 3.3.6. The constraints being imposed in wall-normal and wall-tangential directions, i.e. (3.36) and (3.37), are enforced by adding additional consistent boundary terms.

From the analysis it will become apparent that the formulations enjoy different stability properties depending on whether an adjoint consistent ($\zeta_u = 1$) or an adjoint inconsistent ($\zeta_u = -1$) formulation is chosen. For an adjoint consistent formulation a restriction on the penalty parameters are necessary to assure stability, i.e. $0 < \gamma^n, \gamma^t \leq C$, where the constant C depends on the shape and polynomial order of the chosen finite elements. Nonetheless, this formulation allows for the deduction of optimal convergence for the velocity L^2-error, as shown in Section 3.3.6. On the contrary, in the case of an adjoint in-consistent formulation, an improved inf-sup stability is enjoyed, which permits the choice of the penalty parameters to be $0 < \gamma^n, \gamma^t \leq \infty$. However, optimality for the velocity L^2-error is not guaranteed in this case anymore, and additionally, the choice of γ^t is effectively limited from above for large slip lengths owing to conditioning issues.

Remark 3.3 *For the analysis a continuous advective field $\boldsymbol{\beta}$ is utilized. Some assumptions on this field are necessary for the following analysis. Given a (Lipschitz)-continuous $\boldsymbol{\beta} \in [W^{1,\infty}(\Omega)]^d \subseteq [C^{0,1}(\Omega)]^d$, it is assumed that a piecewise constant approximation $\boldsymbol{\beta}_h^0 \in [\mathcal{X}_h^{\mathrm{dc},0}]^d$ satisfies*

$$\|\boldsymbol{\beta} - \boldsymbol{\beta}_h^0\|_{0,\infty,T} \lesssim h\|\boldsymbol{\beta}\|_{1,\infty,T} \quad \textit{and} \quad \|\boldsymbol{\beta}_h^0\|_{0,\infty,T} \lesssim \|\boldsymbol{\beta}\|_{0,\infty,T} \quad \forall\, T \in \mathcal{T}_h. \tag{3.66}$$

In the unfitted mesh case it is also assumed that there exists an extension $\boldsymbol{\beta}^* \in [W^{1,\infty}(\Omega^*)]^d$ from Ω to Ω^* satisfying $\|\boldsymbol{\beta}^*\|_{1,\infty,\Omega^*} \lesssim \|\boldsymbol{\beta}\|_{1,\infty,\Omega}$. Similar to the preceding works by Massing et al. *[184] and Burman* et al. *[63], it is assumed that the flow field $\boldsymbol{\beta}$ is sufficiently resolved by the mesh such that $\forall\, T \in \mathcal{T}_h$*

$$\|\boldsymbol{\beta}\|_{0,\infty,T'} \lesssim \|\boldsymbol{\beta}\|_{0,\infty,T} \lesssim \|\boldsymbol{\beta}\|_{0,\infty,T'} \quad \forall\, T' \in \omega(T), \tag{3.67}$$

where $\omega(T)$ denotes a local patch of elements neighboring T. As a result, the piecewise constant stabilization parameters are comparable locally in a neighborhood of elements, i.e.

$$\phi_T \sim \phi_{T'} \quad \forall T' \in \omega(T) \quad \textit{and} \quad \phi_F \sim \phi_T \quad \forall T \in \omega(F) \quad \textit{for } \phi \in \{\phi_u, \phi_\beta, \phi_p\}. \tag{3.68}$$

Remark 3.4 *For completeness sake, it is of importance to mention the connection between the reactive term σ and a temporal discretization, which can lead to problems in the small time-step limit for some formulations. As was already discussed in Massing* et al. *[184], the proposed formulation suffers from this drawback, owing to the scaling of ϕ_u, and should be further investigated if it can be alleviated in future research.*

3.3.3.3 Stabilization of the Discretized Equations

The stabilization of the weak form is the same as was introduced for the stabilization of the weak form of the Navier–Stokes equations. The domain stabilization term $S_h(U_h, V_h)$ is chosen as the CIP-stabilization introduced in Section 2.1.3.2, i.e.

$$S_h(U_h, V_h) = s_\beta(\boldsymbol{\beta}_h; \boldsymbol{u}_h, \boldsymbol{v}_h) + s_u(\boldsymbol{\beta}_h; \boldsymbol{u}_h, \boldsymbol{v}_h) + s_p(\boldsymbol{\beta}_h; p_h, q_h) \tag{3.69}$$

where s_β, s_u and s_p are defined in a similar fashion as (2.32)–(2.34), with the exception that the advective velocity is now given as $\boldsymbol{\beta}$ instead of $\boldsymbol{u}_h$ and a change in the scaling of the terms is made for the Oseen equation, resulting in

$$s_\beta(\boldsymbol{\beta}; \boldsymbol{u}_h, \boldsymbol{v}_h) := \gamma_\beta \sum_{F \in \mathcal{F}_i} \phi_{\beta,F} h \langle [\![\boldsymbol{\beta} \cdot \nabla \boldsymbol{u}_h]\!], [\![\boldsymbol{\beta} \cdot \nabla \boldsymbol{v}_h]\!] \rangle_F, \tag{3.70}$$

$$s_p(\boldsymbol{\beta}; p_h, q_h) := \gamma_p \sum_{F \in \mathcal{F}_i} \phi_{p,F} h \langle [\![\boldsymbol{n}_F \cdot \nabla p_h]\!], [\![\boldsymbol{n}_F \cdot \nabla q_h]\!] \rangle_F, \tag{3.71}$$

$$s_u(\boldsymbol{\beta}; \boldsymbol{u}_h, \boldsymbol{v}_h) := \gamma_u \sum_{F \in \mathcal{F}_i} \phi_{u,F} h \langle [\![\nabla \cdot \boldsymbol{u}_h]\!], [\![\nabla \cdot \boldsymbol{v}_h]\!] \rangle_F. \tag{3.72}$$

For the interface stabilization $G_h(U_h, V_h)$ the ghost penalty method, as introduced in Section 2.3.2.2, is employed, i.e.

$$G_h(U_h, V_h) = g_\sigma(\boldsymbol{u}_h, \boldsymbol{v}_h) + g_\nu(\boldsymbol{u}_h, \boldsymbol{v}_h) + g_\beta(\boldsymbol{\beta}; \boldsymbol{u}_h, \boldsymbol{v}_h) + g_u(\boldsymbol{\beta}; \boldsymbol{u}_h, \boldsymbol{v}_h) + g_p(\boldsymbol{\beta}; p_h, q_h) \tag{3.73}$$

where g_σ, g_ν, g_β, g_u and g_p are defined in a similar fashion as (2.85) – (2.89), and are repeated here for the Oseen case as,

$$g_\sigma(\boldsymbol{u}_h, \boldsymbol{v}_h) := \gamma_\sigma \sum_{F\in\mathscr{F}_\Gamma} \sum_{1\le j\le k} \sigma h^{2j+1} \langle [\![\partial_{\boldsymbol{n}}^j \boldsymbol{u}_h]\!], [\![\partial_{\boldsymbol{n}}^j \boldsymbol{v}_h]\!] \rangle_F, \tag{3.74}$$

$$g_\nu(\boldsymbol{u}_h, \boldsymbol{v}_h) := \gamma_\nu \sum_{F\in\mathscr{F}_\Gamma} \sum_{1\le j\le k} \nu h^{2j-1} \langle [\![\partial_{\boldsymbol{n}}^j \boldsymbol{u}_h]\!], [\![\partial_{\boldsymbol{n}}^j \boldsymbol{v}_h]\!] \rangle_F, \tag{3.75}$$

$$g_\beta(\boldsymbol{\beta}; \boldsymbol{u}_h, \boldsymbol{v}_h) := \gamma_\beta \sum_{F\in\mathscr{F}_\Gamma} \sum_{0\le j\le k-1} \phi_{\beta,F} h^{2j+1} \langle [\![\boldsymbol{\beta}\cdot\nabla\partial_{\boldsymbol{n}}^j \boldsymbol{u}_h]\!], [\![\boldsymbol{\beta}\cdot\nabla\partial_{\boldsymbol{n}}^j \boldsymbol{v}_h]\!] \rangle_F, \tag{3.76}$$

$$g_u(\boldsymbol{\beta}; \boldsymbol{u}_h, \boldsymbol{v}_h) := \gamma_u \sum_{F\in\mathscr{F}_\Gamma} \sum_{0\le j\le k-1} \phi_{u,F} h^{2j+1} \langle [\![\nabla\cdot\partial_{\boldsymbol{n}}^j \boldsymbol{u}_h]\!], [\![\nabla\cdot\partial_{\boldsymbol{n}}^j \boldsymbol{v}_h]\!] \rangle_F, \tag{3.77}$$

$$g_p(\boldsymbol{\beta}; p_h, q_h) := \gamma_p \sum_{F\in\mathscr{F}_\Gamma} \sum_{1\le j\le k} \phi_{p,F} h^{2j-1} \langle [\![\partial_{\boldsymbol{n}}^j p_h]\!], [\![\partial_{\boldsymbol{n}}^j q_h]\!] \rangle_F. \tag{3.78}$$

The scalings for the stabilization terms are defined as

$$\phi_{p,T} = \phi_{\beta,T} = h_T^2 \phi_{u,T}^{-1}, \tag{3.79}$$

where $\phi_{u,T}$ is defined in (3.65).

Remark 3.5 *In the stabilization operators s_β (3.70) and g_β (3.76) the advective velocity $\boldsymbol{\beta}$ can be replaced by a continuous interpolation $\boldsymbol{\beta}_h$, which satisfies the divergence-free constraint, i.e. $\nabla\cdot\boldsymbol{\beta}_h = 0$, and the assumptions specified in (3.66), without changing the results of the stability analysis and* a priori *estimates. An important connection to the Navier–Stokes case is the realization that while solving the non-linear system of equations, with for instance a Newton's method, the advective velocity $\boldsymbol{\beta}_h$ is the finite element approximation of $\boldsymbol{u}$ from a previous time or iteration step.*

Remark 3.6 *Given that there are a lot of terms to implement for the stabilization of the discretized equations, work has been done to simplify the formulation. In Burman [48], Braack* et al. *[40] and Schott [232] it is postulated that the CIP-stabilization terms s_β (3.70) and s_u (3.71) and the ghost penalty terms g_β (3.70) and g_u (3.71) can be replaced by a single operator,*

$$\overline{s}_\beta(\boldsymbol{\beta}; \boldsymbol{u}_h, \boldsymbol{v}_h) := \gamma_\beta \sum_{F\in\mathscr{F}_i} \overline{\phi}_\beta^{1,1} h \langle [\![\partial_{\boldsymbol{n}} \boldsymbol{u}_h]\!], [\![\partial_{\boldsymbol{n}} \boldsymbol{v}_h]\!] \rangle_F, \tag{3.80}$$

$$\overline{g}_\beta(\boldsymbol{\beta}; \boldsymbol{u}_h, \boldsymbol{v}_h) := \gamma_\beta \sum_{F\in\mathscr{F}_\Gamma} \sum_{1\le j\le k} \overline{\phi}_\beta^{j,k} h^{2j-1} \langle [\![\partial_{\boldsymbol{n}}^j \boldsymbol{u}_h]\!], [\![\partial_{\boldsymbol{n}}^j \boldsymbol{v}_h]\!] \rangle_F, \tag{3.81}$$

with

$$\overline{\phi}_\beta^{j,k} = \begin{cases} \gamma_\beta \phi_{\beta,F} ||\boldsymbol{\beta}||_{0,\infty,F}^2 + \gamma_u \phi_{u,F} & \text{for } j < k, \\ \gamma_\beta \phi_{\beta,F} ||\boldsymbol{\beta}\cdot\boldsymbol{n}_F||_{0,\infty,F}^2 + \gamma_u \phi_{u,F} & \text{for } j = k. \end{cases} \tag{3.82}$$

This reduces the effort of implementing the proposed stabilization terms, as now all the terms have the form of $\langle [\![\partial_{\boldsymbol{n}} \boldsymbol{u}_h]\!], [\![\partial_{\boldsymbol{n}} \boldsymbol{v}_h]\!] \rangle_F$ with different scalings. However, the simplification comes at the price of a slight over stabilization of the terms, in the form of additional (order preserving) cross-wind diffusion from employing $||\boldsymbol{\beta}||_{0,\infty,F}^2$ in $\overline{\phi}_\beta^{j,k}$. For a proof on this, see Lemma 3.9 in Schott [232].

3.3.3.4 Final Discrete Formulation and Norms

The full stabilized cut finite element method for the Oseen problem with generalized Navier boundary conditions then reads: find $U_h = (\boldsymbol{u}_h, p_h) \in \mathcal{W}_h$ such that for all $V_h = (\boldsymbol{v}_h, q_h) \in \mathcal{W}_h$

$$A_h(U_h, V_h) + S_h(U_h, V_h) + G_h(U_h, V_h) = L_h(V_h), \tag{3.83}$$

where A_h, L_h are the discrete operators including the weak constraint enforcement of the boundary conditions, defined in equations (3.53)–(3.64), $S_h(\cdot,\cdot)$ is the CIP operator to balance instabilities in the interior of the physical domain defined in equations (3.69)–(3.72) and $G_h(\cdot,\cdot)$ the ghost penalty operator, which extends stability control to the boundary zone when non-boundary-fitted meshes are used for the approximation and is defined in (3.73)–(3.78).

Inspired by the works of Massing *et al.* [184], on a related cut finite element method with Dirichlet boundary conditions, and the publication by Juntunen and Stenberg [166], on a Nitsche-type method for Robin-type constraints, the following (semi-)norms are introduced for the ensuing numerical analysis of (3.83). For functions $U = (\boldsymbol{u}, p)$ with $\boldsymbol{u} \in H^1(\Omega)$ and $p \in L^2(\Omega)$, the mesh-dependent energy norms related to the Nitsche-type formulation are defined as

$$\begin{aligned}|||\boldsymbol{u}|||^2 &:= \|\sigma^{\frac{1}{2}}\boldsymbol{u}\|_\Omega^2 + \|\nu^{\frac{1}{2}}\nabla\boldsymbol{u}\|_\Omega^2 + \|(\nu/(\gamma^n h))^{\frac{1}{2}}\boldsymbol{u}\cdot\boldsymbol{n}\|_\Gamma^2 + \|(\nu/(\varepsilon+\gamma^t h))^{\frac{1}{2}}\boldsymbol{u}\boldsymbol{P}^t\|_\Gamma^2 \\ &\quad + \||\boldsymbol{\beta}\cdot\boldsymbol{n}|^{\frac{1}{2}}\boldsymbol{u}\|_\Gamma^2 + \|(\phi_u/(\gamma^n h))^{\frac{1}{2}}\boldsymbol{u}\cdot\boldsymbol{n}\|_\Gamma^2, \end{aligned}\tag{3.84}$$

$$|||p|||_\phi^2 := \|\phi^{-\frac{1}{2}}p\|_\Omega^2. \tag{3.85}$$

Throughout the stability analysis control over discrete functions is required on unfitted meshes $\mathcal{T}_h$, which can be achieved thanks to the continuous interior and ghost penalty operators for the velocity and pressure. For discrete functions $\boldsymbol{u}_h \in \mathcal{V}_h \subset H^1(\mathcal{T}_h)$ and $p_h \in \mathcal{Q}_h \subset L^2(\mathcal{T}_h)$ the following norms are used

$$|||\boldsymbol{u}_h|||_h^2 := |||\boldsymbol{u}_h|||^2 + |\boldsymbol{u}_h|_h^2, \tag{3.86}$$

$$|||p_h|||_{h,\phi}^2 := |||p_h|||_\phi^2 + |p_h|_h^2, \tag{3.87}$$

with a piecewise constant scaling function ϕ and semi-norms which are defined by the stabilization operators

$$|\boldsymbol{u}_h|_h^2 := s_\beta(\boldsymbol{u}_h,\boldsymbol{u}_h) + s_u(\boldsymbol{u}_h,\boldsymbol{u}_h) + g_\sigma(\boldsymbol{u}_h,\boldsymbol{u}_h) + g_\nu(\boldsymbol{u}_h,\boldsymbol{u}_h) + g_\beta(\boldsymbol{u}_h,\boldsymbol{u}_h) + g_u(\boldsymbol{u}_h,\boldsymbol{u}_h), \tag{3.88}$$

$$|p_h|_h^2 := s_p(p_h,p_h) + g_p(p_h,p_h). \tag{3.89}$$

For the stability analysis the augmented natural energy norm for $U_h \in \mathcal{V}_h \times \mathcal{Q}_h$ is utilized

$$|||U_h|||_h^2 := |U_h|_h^2 + \|\phi_u^{\frac{1}{2}}\nabla\cdot\boldsymbol{u}_h\|_\Omega^2 + \frac{1}{1+\omega_h}\|\phi_\beta^{\frac{1}{2}}(\boldsymbol{\beta}\cdot\nabla\boldsymbol{u}_h + \nabla p_h)\|_\Omega^2 + \Phi\|p_h\|_\Omega^2, \tag{3.90}$$

and a semi-norm which is defined as

$$|U_h|_h^2 := |(\boldsymbol{u}_h, p_h)|_h^2 = |||\boldsymbol{u}_h|||_h^2 + |p_h|_h^2 = |||\boldsymbol{u}_h|||^2 + |\boldsymbol{u}_h|_h^2 + |p_h|_h^2, \tag{3.91}$$

with the non-dimensional scaling functions ω_h and Φ given as in Massing *et al.* [184] by

$$\omega_h := \frac{h^2|\boldsymbol{\beta}|_{1,\infty,\Omega}}{\nu + \sigma h^2}, \qquad \Phi^{-1} := \sigma C_P^2 + \|\boldsymbol{\beta}\|_{0,\infty,\Omega} C_P + \nu + \left(\frac{\|\boldsymbol{\beta}\|_{0,\infty,\Omega} C_P}{\sqrt{\nu + \sigma C_P^2}}\right)^2. \tag{3.92}$$

Note that it holds that $\Phi \lesssim \phi_u^{-1}$, this permits the creation of a lower bound of the locally scaled pressure norms. Moreover, C_P denotes the so-called Poincaré constant as defined in (3.101) in Section 3.3.4, which scales as the diameter of Ω.

For the *a priori* error analysis, additional control over boundary fluxes on Γ and the divergence of the velocity is desired. For this purpose, for sufficiently regular functions $U = (\boldsymbol{u}, p) \in H^2(\Omega) \times H^1(\Omega)$, the following norms are introduced

$$|||\boldsymbol{u}|||_*^2 := |||\boldsymbol{u}|||^2 + \|(\nu h)^{\frac{1}{2}} \nabla \boldsymbol{u} \cdot \boldsymbol{n}\|_\Gamma^2, \tag{3.93}$$

$$|||p|||_{*,\phi}^2 := |||p|||_\phi^2 + \|\phi^{-\frac{1}{2}} h^{\frac{1}{2}} p\|_\Gamma^2, \tag{3.94}$$

$$|||U|||_*^2 := |||\boldsymbol{u}|||_*^2 + \|\phi_u^{\frac{1}{2}} \nabla \cdot \boldsymbol{u}\|_\Omega^2 + |||p|||_{*,\Phi^{-1}}^2. \tag{3.95}$$

From the inverse estimate (3.99) (see Section 3.3.4) and the norm equivalences from Proposition 3.4, the discrete functions satisfy

$$|||\boldsymbol{u}_h|||_*^2 \lesssim |||\boldsymbol{u}_h|||^2 + g_\nu(\boldsymbol{u}_h, \boldsymbol{u}_h) \lesssim |||\boldsymbol{u}_h|||_h^2 \qquad \forall\, \boldsymbol{u}_h \in \mathcal{V}_h, \tag{3.96}$$

$$|||p_h|||_{*,\Phi^{-1}}^2 \lesssim |||p_h|||_{\Phi^{-1}}^2 + g_p(p_h, p_h) \lesssim |||p_h|||_{h,\Phi^{-1}}^2 \qquad \forall\, p_h \in \mathcal{Q}_h, \tag{3.97}$$

$$|||U_h|||_*^2 \lesssim |||U_h|||_h^2 \qquad \forall\, U_h \in \mathcal{W}_h. \tag{3.98}$$

3.3.4 Preliminary Estimates for the Analysis

In this section, the most important and useful estimates are collected, which will be used frequently throughout the stability and *a priori* error analysis of the proposed cut finite element method (3.83) in Section 3.3.5 and 3.3.6. First, the trace inequalities and inverse estimates are introduced and a comment on the Korn-type inequality for the strain-rate tensor in combination with Nitsche boundary terms to enforce a generalized Navier boundary condition is made. Next, suitable interpolation error estimates are introduced, which will be used to establish *a priori* error estimates. Finally, the role of the ghost penalty terms are addressed, and their effect of bounding norms in Ω_h^* with norms in Ω is demonstrated.

3.3.4.1 Useful Inequalities and Estimates

For discrete functions $v_h \in \mathcal{X}_h$ the following well-known generalized inverse and trace inequalities hold for elements T which are arbitrarily intersected by the boundary Γ:

$$\|D^j v_h\|_T + h^{\frac{1}{2}} \|\partial_{\boldsymbol{n}}^j v_h\|_{\partial T} + h^{\frac{1}{2}} \|\partial_{\boldsymbol{n}}^j v_h\|_{\Gamma \cap T} \lesssim h^{i-j} \|D^i v_h\|_T \quad \forall\, T \in \mathcal{T}_h, \quad 0 \leq i \leq j. \tag{3.99}$$

For functions $v \in H^1(\Omega_h^*)$, the following trace inequalities are valid

$$\|v\|_{\partial T} + \|v\|_{\Gamma \cap T} \lesssim h^{-1/2} \|v\|_T + h^{1/2} \|\nabla v\|_T \quad \forall\, T \in \mathcal{T}_h, \tag{3.100}$$

as shown in Hansbo and Hansbo [136] and Burman *et al.* [67]. Finally, assuming that $\mathrm{meas}(\Gamma^\varepsilon) > 0$, the generalized Poincaré inequality for $[H^1(\Omega)]^d$ functions with non-vanishing boundary trace from Brenner [43] is given as

$$\|\boldsymbol{v}\|_{0,\Omega} \lesssim C_P(\|\nabla \boldsymbol{v}\|_{0,\Omega} + \|\boldsymbol{v}\|_{\Gamma^\varepsilon}) \quad \forall\, \boldsymbol{v}_h \in [H^1(\Omega)]^d. \tag{3.101}$$

In the following, a generalized Korn-type inequality is presented and it is shown how to control the kernel of the strain-rate-deformation tensor $\boldsymbol{\epsilon}(\cdot)$ with the help of Nitsche-type penalty terms.

Proposition 3.1 *Let a semi-norm on $[H^1(\Omega)]^d$ be defined as $\|\boldsymbol{u}\|^2_{\Gamma^\varepsilon} := \int_{\Gamma^\varepsilon} \boldsymbol{u}^2 \,\mathrm{d}s$, where $\|\varepsilon\|_{\infty,\Gamma^\varepsilon} \leq c_\varepsilon < \infty$. Assuming that $\mathrm{meas}(\Gamma^\varepsilon) > 0$, then $\|\cdot\|_{\Gamma^\varepsilon}$ defines a norm on the space of rigid body motions*

$$RM(\Omega) := \{\boldsymbol{u} \in [H^1(\Omega)]^d \mid \boldsymbol{u}(\boldsymbol{x}) := \boldsymbol{c} + \boldsymbol{W}\boldsymbol{x},\ \boldsymbol{c} \in \mathbb{R}^d, \boldsymbol{W} \in S_d\, \forall\, \boldsymbol{x} \in \Omega\}, \tag{3.102}$$

where S_d is the space of anti-symmetric $d \times d$ matrices, i.e. $\boldsymbol{W} = -\boldsymbol{W}^T$. Note, that $RM(\Omega)$ is the kernel of the symmetric strain-rate-deformation tensor $\boldsymbol{\epsilon}(\cdot)$ in $[H^1(\Omega)]^d$ with $d \in \{2, 3\}$.

Proof. For a more explicit description of why $RM(\Omega)$ is the kernel of the tensor $\boldsymbol{\epsilon}(\cdot)$ in $[H^1(\Omega)]^d$, the reader is referred to, e.g. Mardal and Winther [183] or Brenner and Scott [45]. The claim regarding the norm property follows directly from the fact that $\mathrm{meas}(\Gamma^\varepsilon) > 0$ and from the uniqueness of the trivial solution $(\boldsymbol{c}, \boldsymbol{W}) = (\boldsymbol{0}, \boldsymbol{0}) \in \mathbb{R}^d \times S_d$ of the linear system $\boldsymbol{c} + \boldsymbol{W}\boldsymbol{x} = \boldsymbol{0}$ on Γ^ε.

□

Theorem 3.2 (Korn-type inequality) *Let $\mathrm{meas}(\Gamma^\varepsilon) > 0$ and $\|\cdot\|_{\Gamma^\varepsilon}$ be as defined in Proposition 3.1, then there exists a constant C_K such that*

$$\|\nabla \boldsymbol{u}\|_\Omega \leq \|\boldsymbol{u}\|_{1,\Omega} \leq C_K(\|\boldsymbol{\epsilon}(\boldsymbol{u})\|_\Omega + \|\boldsymbol{u}\|_{\Gamma^\varepsilon}) \quad \forall\, \boldsymbol{u} \in [H^1(\Omega)]^d. \tag{3.103}$$

Proof. The proof follows the technique proposed in Boiveau and Burman [36] and Brenner and Scott [45] for Korn-type inequalities and is therefore only sketched in the following. Let $[\hat{H}^1(\Omega)]^d := \{\boldsymbol{v} \in [H^1(\Omega)]^d : |\int_\Omega \nabla \times \boldsymbol{v}\,\mathrm{d}x| = 0 \wedge |\int_\Omega \boldsymbol{v}\,\mathrm{d}x| = 0\}$, then it holds $[H^1(\Omega)]^d = [\hat{H}^1(\Omega)]^d \oplus RM(\Omega)$ such that for each $\boldsymbol{u} \in [H^1(\Omega)]^d$ there exists a unique pair $(\boldsymbol{z}, \boldsymbol{w}) \in [\hat{H}^1(\Omega)]^d \oplus RM(\Omega)$ with $\boldsymbol{u} = \boldsymbol{z} + \boldsymbol{w}$ satisfying $\|\boldsymbol{z}\|_{1,\Omega} + \|\boldsymbol{w}\|_{1,\Omega} \lesssim \|\boldsymbol{u}\|_{1,\Omega}$ (open mapping theorem by Lax [175]). Following [36] the claim can be proven via contradiction. Assuming non-boundedness in (3.103), there exists a sequence $\{\boldsymbol{u}_n\} \subseteq [H^1(\Omega)]^d$ with $\|\boldsymbol{u}_n\|_{1,\Omega} = 1$ and $\|\boldsymbol{\epsilon}(\boldsymbol{u}_n)\|_\Omega + \|\boldsymbol{u}_n\|_{\Gamma^\varepsilon} < \frac{1}{n}$. Splitting $\boldsymbol{u}_n = \boldsymbol{z}_n + \boldsymbol{w}_n \in [\hat{H}^1(\Omega)]^d \oplus RM(\Omega)$ for each n it holds that $\|\boldsymbol{\epsilon}(\boldsymbol{z}_n)\|_\Omega = \|\boldsymbol{\epsilon}(\boldsymbol{u}_n)\|_\Omega < \frac{1}{n}$, since $\boldsymbol{\epsilon}(\boldsymbol{w}_n) = \boldsymbol{0}$. Applying the second Korn's inequality, see e.g. Brenner [44], the following relation is obtained

$$\|\boldsymbol{z}_n\|_{1,\Omega} \lesssim \|\boldsymbol{\epsilon}(\boldsymbol{z}_n)\|_\Omega + |\int_\Omega \nabla \times \boldsymbol{z}_n\,\mathrm{d}x| + |\int_\Omega \boldsymbol{z}_n\,\mathrm{d}x| = \|\boldsymbol{\epsilon}(\boldsymbol{z}_n)\|_\Omega \to 0 \text{ in } [H^1(\Omega)]^d. \tag{3.104}$$

Since $\boldsymbol{z}_n + \boldsymbol{w}_n$ is a bounded sequence and $RM(\Omega)$ is finite dimensional, $\{\boldsymbol{w}_n\}$ is a bounded sequence and as such there exists a convergent subsequence for which holds $\boldsymbol{u} = \lim_{n_k \to \infty} \boldsymbol{w}_{n_k}$ with $\boldsymbol{u} \in RM(\Omega)$ since $\lim_{n_k \to \infty} \boldsymbol{z}_{n_k} = \boldsymbol{0}$ in $[H^1(\Omega)]^d$. Note that by assumption $\|\boldsymbol{u}\|_{\Gamma^\varepsilon} = 0$ and $\|\boldsymbol{u}\|_{1,\Omega} = 1$. Since $\|\cdot\|_{\Gamma^\varepsilon}$ defines a norm on $RM(\Omega)$ whenever $\operatorname{meas}(\Gamma^\varepsilon) > 0$ (see Proposition 3.1), it follows that $\boldsymbol{u} = \boldsymbol{0} \in RM(\Omega)$ and therefore $\boldsymbol{u} = \boldsymbol{0} \in [H^1(\Omega)]^d$, which contradicts $\|\boldsymbol{u}\|_{1,\Omega} = 1$. As a result, the assumption of unboundedness of (3.103) is refuted, which proves the claim.

□

The subsequent corollary states that the Nitsche penalty terms occurring in the proposed Nitsche-type cut finite element formulation (3.83) are sufficient to control the rigid body motions in $[H^1(\Omega)]^d$, which remain undetermined by the strain-rate-deformation tensor $\boldsymbol{\epsilon}(\cdot)$.

Corollary 3.3 *Let the domain be bounded, i.e.* $\operatorname{diam}(\Omega) < \infty$*, the Nitsche penalty parameters* $\gamma^t, \gamma^n < \infty$ *and assume that normal and tangential velocities are constrained by Nitsche-type penalty terms on a non-vanishing part of the boundary* Γ^ε*, i.e.* $\operatorname{meas}(\Gamma^\varepsilon) > 0$*, then*

$$\|\nabla \boldsymbol{u}_h\|_\Omega^2 \leq \|\boldsymbol{u}_h\|_{1,\Omega}^2 \lesssim \|\boldsymbol{\epsilon}(\boldsymbol{u}_h)\|_\Omega^2 + \| (\gamma^n h)^{-\frac{1}{2}} \boldsymbol{u}_h \cdot \boldsymbol{n}\|_\Gamma^2 + \| \left(\varepsilon + \gamma^t h\right)^{-\frac{1}{2}} \boldsymbol{u}_h \boldsymbol{P}^t\|_{\Gamma^\varepsilon}^2. \quad (3.105)$$

Proof. The proof follows immediately from applying the Korn-type inequality deduced in Theorem 3.2, the definition of Γ^ϵ and the specified assumptions in the corollary

$$\begin{aligned}
&\|\boldsymbol{\epsilon}(\boldsymbol{u}_h)\|_\Omega^2 + \| (\gamma^n h)^{-\frac{1}{2}} \boldsymbol{u}_h \cdot \boldsymbol{n}\|_\Gamma^2 + \| \left(\varepsilon + \gamma^t h\right)^{-\frac{1}{2}} \boldsymbol{u}_h \boldsymbol{P}^t\|_{\Gamma^\varepsilon}^2 \\
&\quad \gtrsim \|\boldsymbol{\epsilon}(\boldsymbol{u}_h)\|_\Omega^2 + (\gamma^n \operatorname{diam}(\Omega))^{-1} \|\boldsymbol{u}_h \cdot \boldsymbol{n}\|_\Gamma^2 + (\|\varepsilon\|_{\infty,\Gamma^\varepsilon} + \gamma^t \operatorname{diam}(\Omega))^{-1} \|\boldsymbol{u}_h \boldsymbol{P}^t\|_{\Gamma^\varepsilon}^2 && (3.106) \\
&\quad \gtrsim \|\boldsymbol{\epsilon}(\boldsymbol{u}_h)\|_\Omega^2 + \|\boldsymbol{u}_h\|_{\Gamma^\varepsilon}^2 && (3.107) \\
&\quad \gtrsim \|\boldsymbol{u}_h\|_{1,\Omega}^2 \geq \|\nabla \boldsymbol{u}_h\|_\Omega^2. && (3.108)
\end{aligned}$$

□

3.3.4.2 Interpolation Operators

Since the finite element approximation space is defined on the enlarged domain Ω_h^*, a comment on the construction of an appropriate interpolation operator $L^2(\Omega) \to \mathscr{X}_h$ is made. From Stein [247] it is well known that for the Sobolev spaces $W^{m,q}(\Omega)$, $0 \leq m < \infty$, $1 \leq q \leq \infty$, a linear extension operator can be defined

$$E : W^{m,q}(\Omega) \to W^{m,q}(\Omega^*) \qquad \text{with} \qquad \|Ev\|_{m,q,\Omega^*} \lesssim \|v\|_{m,q,\Omega}, \quad (3.109)$$

where the following abbreviation for the extension is used $v^* := Ev$. Following the analysis provided by Massing *et al.* [184], let π_h denote the *Clément operator*, see for instance Ern and Guermond [108], then for $u \in H^s(\Omega)$ its "fictitious domain" extension is defined as $\pi_h^* : H^s(\Omega) \to \mathscr{X}_h$ by $\pi_h^* u := \pi_h(u^*)$. For some fixed Lipschitz-domain Ω^* satisfying $\Omega_h^* \subseteq \Omega^*$ for

$h \lesssim 1$, then the following interpolation estimates hold for functions $v \in H^r(\Omega^*)$ and its fictitious domain variant

$$\|v - \pi_h v\|_{s,T} \lesssim h^{t-s}|v|_{t,\omega(T)}, \quad 0 \leq s \leq t \leq m \quad \forall T \in \mathcal{T}_h, \tag{3.110}$$

$$\|v^* - \pi_h^* v\|_{s,\mathcal{T}_h} \lesssim h^{t-s}\|v\|_{t,\Omega}, \quad 0 \leq s \leq t \leq m, \tag{3.111}$$

owing to the boundedness of the extension operator (3.109), with $s, t \in \mathbb{N}$, $m = \min\{r, k+1\}$, k the interpolation order of $\mathcal{X}_h$ and $\omega(T)$ the set of elements in $\mathcal{T}_h$ sharing at least one vertex with T. Throughout the subsequent analysis $\boldsymbol{\pi}_h^*$ is employed for the Clément interpolant of vector-valued functions $\boldsymbol{v}$ and Π_h^* for functions in a product space.

3.3.4.3 The Bounding Effect of Ghost Penalties

Given that the primary variables are defined in Ω_h^* (which in most cases is a larger set than Ω), a connection of the norms defined on this domain and the physical domain Ω is necessary. In particular, it is important to ensure that norms defined in Ω_h^* can be bounded by terms defined in Ω to conduct the subsequent analysis. This connection can be made by utilizing ghost penalty terms, as is shown in the following Proposition 3.4.

Proposition 3.4 *Let Ω, Ω_h^* and $\mathcal{F}_\Gamma$ be defined as in Section 3.3.3.1 and the ghost penalty operators be given as in (3.74)–(3.78). Then for scalar functions $p_h \in \mathcal{Q}_h$ as well as for vector-valued equivalents $\boldsymbol{u}_h \in \mathcal{V}_h$ the following estimates hold*

$$\|\sigma^{\frac{1}{2}}\boldsymbol{u}_h\|_{\Omega_h^*}^2 \lesssim \|\sigma^{\frac{1}{2}}\boldsymbol{u}_h\|_\Omega^2 + g_\sigma(\boldsymbol{u}_h, \boldsymbol{u}_h) \lesssim \|\sigma^{\frac{1}{2}}\boldsymbol{u}_h\|_{\Omega_h^*}^2, \tag{3.112}$$

$$\|\nu^{\frac{1}{2}}\nabla\boldsymbol{u}_h\|_{\Omega_h^*}^2 \lesssim \|\nu^{\frac{1}{2}}\nabla\boldsymbol{u}_h\|_\Omega^2 + g_\nu(\boldsymbol{u}_h, \boldsymbol{u}_h) \lesssim \|\nu^{\frac{1}{2}}\nabla\boldsymbol{u}_h\|_{\Omega_h^*}^2. \tag{3.113}$$

Furthermore, let the scaling functions ϕ_β, ϕ_u and ϕ_p be defined as in (3.65) and (3.79) and let $\boldsymbol{\beta}_h^0 \in [\mathcal{X}_h^{\mathrm{dc},0}]^d$ be a piecewise constant approximation to $\boldsymbol{\beta}$ on $\mathcal{T}_h$, which satisfies the approximation properties specified in (3.66). Then the following estimates hold

$$\Phi\|p_h\|_{\Omega_h^*}^2 \lesssim \Phi\|p_h\|_\Omega^2 + g_p(p_h, p_h), \tag{3.114}$$

$$\|\phi_u^{\frac{1}{2}}\nabla\cdot\boldsymbol{u}_h\|_{\Omega_h^*}^2 \lesssim \|\phi_u^{\frac{1}{2}}\nabla\cdot\boldsymbol{u}_h\|_\Omega^2 + g_u(\boldsymbol{u}_h, \boldsymbol{u}_h), \tag{3.115}$$

$$\|\phi_\beta^{\frac{1}{2}}(\boldsymbol{\beta}_h^0 - \boldsymbol{\beta})\cdot\nabla\boldsymbol{u}_h\|_{\Omega_h^*}^2 \lesssim \omega_h\big(\|\nu^{\frac{1}{2}}\nabla\boldsymbol{u}_h\|_{\Omega_h^*}^2 + \|\sigma^{\frac{1}{2}}\boldsymbol{u}_h\|_{\Omega_h^*}^2\big), \tag{3.116}$$

$$\begin{aligned}\|\phi_\beta^{\frac{1}{2}}(\boldsymbol{\beta}_h^0\cdot\nabla\boldsymbol{u}_h + \nabla p_h)\|_{\Omega_h^*}^2 \lesssim{}& \|\phi_\beta^{\frac{1}{2}}(\boldsymbol{\beta}\cdot\nabla\boldsymbol{u}_h + \nabla p_h)\|_\Omega^2 + g_\beta(\boldsymbol{u}_h, \boldsymbol{u}_h) + g_p(p_h, p_h)\\ &+ \omega_h\big(\|\nu^{\frac{1}{2}}\nabla\boldsymbol{u}_h\|_{\Omega_h^*}^2 + \|\sigma^{\frac{1}{2}}\boldsymbol{u}_h\|_{\Omega_h^*}^2\big),\end{aligned} \tag{3.117}$$

Note that the hidden constants in (3.114)–(3.117) depend only on the shape-regularity and the polynomial order, but not on the mesh or the location of Γ within $\mathcal{T}_h$.

Proof. For detailed proofs of these estimates, the reader is referred to the preceding work by Massing *et al.* [184] (cf. Lemma 5.4, Corollary 5.5 and 5.7 and Lemma 5.8) and the references therein.

□

3.3.5 Stability and Continuity Properties

In this section the numerical analysis of the proposed cut finite element method (3.83) will be begun by demonstrating that the total bilinear form $A_h + S_h + G_h$ satisfies an inf-sup condition on the space $\mathcal{W}_h$ in a suitable energy norm $|||\cdot|||_h$. Emphasis is put on the fact that the inf-sup constant is independent on how the boundary intersects the underlying background mesh, as is essential in retaining a stable formulation in an unfitted mesh approach.

The approach pursued here is closely related to the analysis conducted by Massing *et al.* [184], and the main difference is in the treatment and analysis of the boundary terms for the weak enforcement of the general Navier boundary conditions. The major stability result relies on a modified coercivity estimate for the total bilinear form. Since fluid instabilities and the extension of the finite element method to unfitted meshes can be treated almost equivalently to [184], only the required statements from the latter publication will be recalled without presenting proofs.

The section is begun by deriving some important continuity estimates for parts of the stabilized form in Lemma 3.5, needed in the stability analysis and in the subsequent a priori estimate. Next, the coercivity estimate of the stabilized formulation with respect to the semi-norm $|U_h|_h$ on $\mathcal{W}_h$ is proven in Lemma 3.6. To conduct the ensuing inf-sup proof, control over three additional (semi-)norms

$$\|\phi_u^{\frac{1}{2}} \nabla \cdot \boldsymbol{u}_h\|_\Omega, \quad \|\phi_\beta^{\frac{1}{2}} (\boldsymbol{\beta} \cdot \nabla \boldsymbol{u}_h + \nabla p_h)\|_\Omega \quad \text{and} \quad \Phi^{\frac{1}{2}} \|p_h\|_\Omega, \tag{3.118}$$

is detrimental, this control is recovered in Lemmas 3.7, 3.8 and 3.10 with the help of CIP and ghost penalty stabilizations as introduced in Section 3.3.3.3 using techniques provided in Burman and Ern [52] and [184]. By combining the above mentioned estimates, a global inf-sup stability on $\mathcal{W}_h$ is shown in Theorem 3.11.

Lemma 3.5 (Continuity Estimates) *For an arbitrary choice of functions $\boldsymbol{u}, \boldsymbol{v} \in [H^2(\Omega)]^d$, $p \in H^1(\Omega)$ and discrete functions $\boldsymbol{u}_h, \boldsymbol{v}_h \in \mathcal{V}_h$, $p_h \in \mathcal{Q}_h$ the following continuity estimates hold provided that $\gamma^n, \gamma^t < \infty$*

$$a_h(\boldsymbol{u} + \boldsymbol{u}_h, \boldsymbol{v} + \boldsymbol{v}_h) - (\boldsymbol{\beta} \cdot \nabla(\boldsymbol{u} + \boldsymbol{u}_h), (\boldsymbol{v} + \boldsymbol{v}_h))_\Omega \lesssim |||\boldsymbol{u} + \boldsymbol{u}_h|||_* |||\boldsymbol{v} + \boldsymbol{v}_h|||_*, \tag{3.119}$$

$$a_h(\boldsymbol{u} + \boldsymbol{u}_h, \boldsymbol{v} + \boldsymbol{v}_h) + ((\boldsymbol{u} + \boldsymbol{u}_h), \boldsymbol{\beta} \cdot \nabla(\boldsymbol{v} + \boldsymbol{v}_h))_\Omega \lesssim |||\boldsymbol{u} + \boldsymbol{u}_h|||_* |||\boldsymbol{v} + \boldsymbol{v}_h|||_*, \tag{3.120}$$

$$a_h(\boldsymbol{u}_h, \boldsymbol{v}_h) - (\boldsymbol{\beta} \cdot \nabla \boldsymbol{u}_h, \boldsymbol{v}_h)_\Omega \gtrsim -|||\boldsymbol{u}_h|||_h |||\boldsymbol{v}_h|||_h, \tag{3.121}$$

$$a_h(\boldsymbol{u}_h, \boldsymbol{v}_h) + (\boldsymbol{u}_h, \boldsymbol{\beta} \cdot \nabla \boldsymbol{v}_h)_\Omega \gtrsim -|||\boldsymbol{u}_h|||_h |||\boldsymbol{v}_h|||_h, \tag{3.122}$$

$$|b_h(p + p_h, \boldsymbol{v} + \boldsymbol{v}_h)| \lesssim |||p + p_h|||_{*,\phi_u} (|||\boldsymbol{v} + \boldsymbol{v}_h|||_* + \|\phi_u^{\frac{1}{2}} \nabla \cdot (\boldsymbol{v} + \boldsymbol{v}_h)\|_\Omega), \tag{3.123}$$

$$|b_h(p + p_h, \boldsymbol{v}_h)| \lesssim |||p + p_h|||_{*,\phi_u} (|||\boldsymbol{v}_h|||_h + \|\phi_u^{\frac{1}{2}} \nabla \cdot \boldsymbol{v}_h\|_\Omega). \tag{3.124}$$

Proof. To start of, the continuity estimate for a_h with neglected advective bulk term as in (3.119) will be proven. The proof is straightforward as it follows directly from applying the Cauchy–Schwarz inequality for each term. For the bulk terms the following upper bounds can be made,

$$\begin{aligned} &|(\sigma(\boldsymbol{u} + \boldsymbol{u}_h), (\boldsymbol{v} + \boldsymbol{v}_h))_\Omega| + |(2\nu \boldsymbol{\epsilon}(\boldsymbol{u} + \boldsymbol{u}_h), \boldsymbol{\epsilon}(\boldsymbol{v} + \boldsymbol{v}_h))_\Omega| \\ &\quad \lesssim (\|\sigma^{\frac{1}{2}}(\boldsymbol{u} + \boldsymbol{u}_h)\|_\Omega + \|\nu^{\frac{1}{2}} \nabla(\boldsymbol{u} + \boldsymbol{u}_h)\|_\Omega)(\|\sigma^{\frac{1}{2}}(\boldsymbol{v} + \boldsymbol{v}_h)\|_\Omega + \|\nu^{\frac{1}{2}} \nabla(\boldsymbol{v} + \boldsymbol{v}_h)\|_\Omega) \quad (3.125) \\ &\quad \lesssim |||\boldsymbol{u} + \boldsymbol{u}_h|||_* |||\boldsymbol{v} + \boldsymbol{v}_h|||_*. \quad (3.126) \end{aligned}$$

It remains to estimate the boundary terms. By analogy, the estimate for all symmetric viscous and advective inflow Nitsche penalty terms follows directly from applying Cauchy–Schwarz inequality and the definition of $|||\cdot|||_*$. The non-symmetric boundary terms in a_h can be estimated as

$$
\begin{aligned}
&|\langle(\frac{\varepsilon}{\varepsilon+\gamma^t h}-1)(2\nu\boldsymbol{\epsilon}(\boldsymbol{u}+\boldsymbol{u}_h)\boldsymbol{n})\boldsymbol{P}^t,(\boldsymbol{v}+\boldsymbol{v}_h)\rangle_\Gamma| \\
&\quad= 2(\gamma^t)^{\frac{1}{2}}|\langle(\frac{\nu}{\varepsilon+\gamma^t h})((\gamma^t h)^{\frac{1}{2}}h^{\frac{1}{2}}\boldsymbol{\epsilon}(\boldsymbol{u}+\boldsymbol{u}_h)\boldsymbol{n})\boldsymbol{P}^t,(\boldsymbol{v}+\boldsymbol{v}_h)\rangle_\Gamma| && (3.127)\\
&\quad\lesssim 2(\gamma^t)^{\frac{1}{2}}||(\frac{\gamma^t h}{\varepsilon+\gamma^t h})^{\frac{1}{2}}(\nu h)^{\frac{1}{2}}(\nabla(\boldsymbol{u}+\boldsymbol{u}_h)\cdot\boldsymbol{n})||_\Gamma||(\frac{\nu}{\varepsilon+\gamma^t h})^{\frac{1}{2}}(\boldsymbol{v}+\boldsymbol{v}_h)\boldsymbol{P}^t||_\Gamma && (3.128)\\
&\quad\lesssim |||\boldsymbol{u}+\boldsymbol{u}_h|||_*|||\boldsymbol{v}+\boldsymbol{v}_h|||_*, && (3.129)
\end{aligned}
$$

which holds if $\gamma^t<\infty$, since $\frac{\gamma^t h}{\varepsilon+\gamma^t h}\leq 1$. Similarly, utilizing that $\frac{\gamma^t\varepsilon}{\varepsilon+\gamma^t h}\leq\gamma^t$ the following holds,

$$
\begin{aligned}
&|\zeta_u\langle\frac{\gamma^t h}{\varepsilon+\gamma^t h}\varepsilon(2\nu\boldsymbol{\epsilon}(\boldsymbol{u}+\boldsymbol{u}_h)\boldsymbol{n})\boldsymbol{P}^t,2\boldsymbol{\epsilon}(\boldsymbol{v}+\boldsymbol{v}_h)\boldsymbol{n}\rangle_\Gamma| \\
&\quad\lesssim 4(\frac{\gamma^t\varepsilon}{\varepsilon+\gamma^t h})||(\nu h)^{\frac{1}{2}}(\nabla(\boldsymbol{u}+\boldsymbol{u}_h)\cdot\boldsymbol{n})||_\Gamma||(\nu h)^{\frac{1}{2}}(\nabla(\boldsymbol{v}+\boldsymbol{v}_h)\cdot\boldsymbol{n})||_\Gamma && (3.130)\\
&\quad\lesssim \gamma^t|||\boldsymbol{u}+\boldsymbol{u}_h|||_*|||\boldsymbol{v}+\boldsymbol{v}_h|||_*. && (3.131)
\end{aligned}
$$

All remaining boundary terms in a_h can be estimated analogously, which yields

$$
|a_h(\boldsymbol{u}+\boldsymbol{u}_h,\boldsymbol{v}+\boldsymbol{v}_h)-(\boldsymbol{\beta}\cdot\nabla(\boldsymbol{u}+\boldsymbol{u}_h),(\boldsymbol{v}+\boldsymbol{v}_h))_\Omega|\lesssim|||\boldsymbol{u}+\boldsymbol{u}_h|||_*|||\boldsymbol{v}+\boldsymbol{v}_h|||_* \tag{3.132}
$$

and as a consequence (3.119). Estimate (3.120) can easily be deduced by integrating the advective bulk term by parts and applying the Cauchy–Schwarz inequality for the resulting boundary term

$$
\begin{aligned}
&|a_h(\boldsymbol{u}+\boldsymbol{u}_h,\boldsymbol{v}+\boldsymbol{v}_h)+((\boldsymbol{u}+\boldsymbol{u}_h),\boldsymbol{\beta}\cdot\nabla(\boldsymbol{v}+\boldsymbol{v}_h))_\Omega| \\
&\quad=|a_h(\boldsymbol{u}+\boldsymbol{u}_h,\boldsymbol{v}+\boldsymbol{v}_h)-(\boldsymbol{\beta}\cdot\nabla(\boldsymbol{u}+\boldsymbol{u}_h),(\boldsymbol{v}+\boldsymbol{v}_h))_\Omega+\langle(\boldsymbol{\beta}\cdot\boldsymbol{n})(\boldsymbol{u}+\boldsymbol{u}_h),(\boldsymbol{v}+\boldsymbol{v}_h)\rangle_\Gamma| && (3.133)\\
&\quad\lesssim|a_h(\boldsymbol{u}+\boldsymbol{u}_h,\boldsymbol{v}+\boldsymbol{v}_h)-(\boldsymbol{\beta}\cdot\nabla(\boldsymbol{u}+\boldsymbol{u}_h),(\boldsymbol{v}+\boldsymbol{v}_h))_\Omega|+|||\boldsymbol{u}+\boldsymbol{u}_h|||_*|||\boldsymbol{v}+\boldsymbol{v}_h|||_*. && (3.134)
\end{aligned}
$$

Setting $\boldsymbol{v}=\boldsymbol{u}=\boldsymbol{0}$ in (3.132) and (3.134) and applying relation (3.96), i.e. $|||\boldsymbol{v}_h|||_*\lesssim|||\boldsymbol{v}_h|||_h$, gives

$$
\begin{aligned}
|a_h(\boldsymbol{u}_h,\boldsymbol{v}_h)-(\boldsymbol{\beta}\cdot\nabla\boldsymbol{u}_h,\boldsymbol{v}_h)_\Omega|&\lesssim|||\boldsymbol{u}_h|||_h|||\boldsymbol{v}_h|||_h, && (3.135)\\
|a_h(\boldsymbol{u}_h,\boldsymbol{v}_h)+(\boldsymbol{u}_h,\boldsymbol{\beta}\cdot\nabla\boldsymbol{v}_h)_\Omega|&\lesssim|||\boldsymbol{u}_h|||_h|||\boldsymbol{v}_h|||_h, && (3.136)
\end{aligned}
$$

which leads to (3.121) and (3.122).

Similar estimates can be established for b_h by applying the Cauchy–Schwarz inequality

$$
\begin{aligned}
|b_h(p+p_h,&\boldsymbol{v}+\boldsymbol{v}_h)|\leq|(p+p_h,\nabla\cdot(\boldsymbol{v}+\boldsymbol{v}_h))_\Omega|+|\langle p+p_h,(\boldsymbol{v}+\boldsymbol{v}_h)\cdot\boldsymbol{n}\rangle_\Gamma| && (3.137)\\
&\lesssim\|\phi_u^{-\frac{1}{2}}(p+p_h)\|_\Omega(\|\phi_u^{\frac{1}{2}}\nabla\cdot(\boldsymbol{v}+\boldsymbol{v}_h)\|_\Omega+\|(\phi_u/h)^{\frac{1}{2}}(\boldsymbol{v}+\boldsymbol{v}_h)\cdot\boldsymbol{n}\|_\Gamma) \\
&\quad\|\phi_u^{-\frac{1}{2}}h^{\frac{1}{2}}(p+p_h)\|_\Gamma(\|\phi_u^{\frac{1}{2}}\nabla\cdot(\boldsymbol{v}+\boldsymbol{v}_h)\|_\Omega+\|(\phi_u/h)^{\frac{1}{2}}(\boldsymbol{v}+\boldsymbol{v}_h)\cdot\boldsymbol{n}\|_\Gamma) && (3.138)\\
&\lesssim|||p+p_h|||_{*,\phi_u}(|||\boldsymbol{v}+\boldsymbol{v}_h|||_*+\|\phi_u^{\frac{1}{2}}\nabla\cdot(\boldsymbol{v}+\boldsymbol{v}_h)\|_\Omega), && (3.139)
\end{aligned}
$$

which proves (3.123). Choosing $\boldsymbol{v} = \mathbf{0}$ and using (3.96) yields estimate (3.124).

□

The next lemma shows how the Nitsche-type boundary terms, which have been consistently added to enforce the general Navier boundary conditions, guarantee stability of the bilinear form with respect to a semi-norm on $\mathcal{W}_h$ and how ghost penalty terms extend stability to the enlarged domain Ω_h^*.

Lemma 3.6 (Coercivity estimate) *The stabilized cut finite element formulation is coercive, i.e.*

$$|U_h|_h^2 \lesssim A_h(U_h, U_h) + S_h(U_h, U_h) + G_h(U_h, U_h) \quad \forall\, U_h = (\boldsymbol{u}_h, p_h) \in \mathcal{W}_h \tag{3.140}$$

holds whenever the CIP and ghost penalty stability parameters $\gamma_\nu, \gamma_\sigma, \gamma_\beta, \gamma_u, \gamma_p$ are chosen large enough. For $\zeta_u = 1$, the Nitsche penalty parameters need to be chosen small enough, i.e. $0 < \gamma^n, \gamma^t \leq C < \infty$, where C depends on the shape and polynomial order of the elements (see inverse estimate (3.99)), however, it is independent of how the boundary intersects the element. By contrast, for $\zeta_u = -1$, the bilinear form is coercive for any choice $0 < \gamma^n, \gamma^t < \infty$. Note that $\operatorname{meas}(\Gamma^\varepsilon) > 0$ is assumed.

Proof. Starting from the definition of A_h, see (3.53), the following holds,

$$\begin{aligned}
A_h(U_h, U_h) = {} & \|\sigma^{\frac{1}{2}} \boldsymbol{u}_h\|_{0,\Omega}^2 + \|(2\nu)^{\frac{1}{2}} \boldsymbol{\epsilon}(\boldsymbol{u}_h)\|_{0,\Omega}^2 + (\boldsymbol{\beta} \cdot \nabla \boldsymbol{u}_h, \boldsymbol{u}_h)_\Omega + \| \left(\frac{\phi_u}{\gamma^n h} \right)^{\frac{1}{2}} \boldsymbol{u}_h \cdot \boldsymbol{n} \|_\Gamma^2 \\
& - \langle (\boldsymbol{\beta} \cdot \boldsymbol{n}) \boldsymbol{u}_h, \boldsymbol{u}_h \rangle_{\Gamma_{\text{in}}} + \| \left(\frac{\nu}{\gamma^n h} \right)^{\frac{1}{2}} \boldsymbol{u}_h \cdot \boldsymbol{n} \|_\Gamma^2 - (1 + \zeta_u) \langle (2\nu \boldsymbol{\epsilon}(\boldsymbol{u}_h) \boldsymbol{n}) \cdot \boldsymbol{n}, \boldsymbol{u}_h \cdot \boldsymbol{n} \rangle_\Gamma \\
& + \| \left(\frac{\nu}{\varepsilon + \gamma^t h} \right)^{\frac{1}{2}} \boldsymbol{u}_h \boldsymbol{P}^t \|_\Gamma^2 - (1 + \zeta_u) \langle \frac{\gamma^t h}{\varepsilon + \gamma^t h} 2\nu \boldsymbol{\epsilon}(\boldsymbol{u}_h) \boldsymbol{n}, \boldsymbol{u}_h \boldsymbol{P}^t \rangle_\Gamma \\
& - \zeta_u \| \left(\frac{4\gamma^t h \varepsilon}{\varepsilon + \gamma^t h} \right)^{\frac{1}{2}} \nu^{\frac{1}{2}} (\boldsymbol{\epsilon}(\boldsymbol{u}_h) \boldsymbol{n}) \boldsymbol{P}^t \|_\Gamma^2.
\end{aligned} \tag{3.141}$$

Integration by parts for the advective term together with continuity of $\boldsymbol{\beta}$ yields

$$(\boldsymbol{\beta} \cdot \nabla \boldsymbol{u}_h, \boldsymbol{u}_h)_\Omega = \frac{1}{2} \langle (\boldsymbol{\beta} \cdot \boldsymbol{n}) \boldsymbol{u}_h, \boldsymbol{u}_h \rangle_\Gamma - \frac{1}{2} ((\nabla \cdot \boldsymbol{\beta}) \boldsymbol{u}_h, \boldsymbol{u}_h)_\Omega. \tag{3.142}$$

Using the assumption $\nabla \cdot \boldsymbol{\beta} = 0$, with the help of the advective inflow control, i.e. $\boldsymbol{\beta} \cdot \boldsymbol{n} < 0$, imposed on $\Gamma_{\text{in}} \subseteq \Gamma_D \subseteq \Gamma$, the boundary control can be recovered on the entire boundary Γ as

$$\begin{aligned}
(\boldsymbol{\beta} \cdot \nabla \boldsymbol{u}_h, \boldsymbol{u}_h)_\Omega - \langle (\boldsymbol{\beta} \cdot \boldsymbol{n}) \boldsymbol{u}_h, \boldsymbol{u}_h \rangle_{\Gamma_{\text{in}}} &= \frac{1}{2} \langle (\boldsymbol{\beta} \cdot \boldsymbol{n}) \boldsymbol{u}_h, \boldsymbol{u}_h \rangle_\Gamma - \langle (\boldsymbol{\beta} \cdot \boldsymbol{n}) \boldsymbol{u}_h, \boldsymbol{u}_h \rangle_{\Gamma_{\text{in}}} \\
&= \frac{1}{2} \| |\boldsymbol{\beta} \cdot \boldsymbol{n}|^{\frac{1}{2}} \boldsymbol{u}_h \|_{0,\Gamma}^2.
\end{aligned} \tag{3.143}$$

For the viscous boundary terms, the following estimates can be established. The general idea is to bound the possible negative terms from above to cover the worst case scenario. By applying a

δ-scaled Cauchy–Schwarz inequality, a trace inequality (3.99) and the viscous norm equivalence from Proposition 3.4 for cut meshes, the following estimate can be established

$$
\begin{aligned}
&(1+\zeta_u)|\langle(2\nu\boldsymbol{\epsilon}(\boldsymbol{u}_h)\boldsymbol{n})\cdot\boldsymbol{n},\boldsymbol{u}_h\cdot\boldsymbol{n}\rangle_\Gamma| \\
&\quad\lesssim \frac{4}{2\delta_1}(1+\zeta_u)\gamma^n\|(\nu h)^{\frac{1}{2}}\boldsymbol{\epsilon}(\boldsymbol{u}_h)\boldsymbol{n}\|_\Gamma^2+\frac{\delta_1}{2}(1+\zeta_u)\|(\nu/(\gamma^n h))^{\frac{1}{2}}\boldsymbol{u}_h\cdot\boldsymbol{n}\|_\Gamma^2 \\
&\quad\lesssim \frac{4}{2\delta_1}(1+\zeta_u)\gamma^n\|\nu^{\frac{1}{2}}\nabla\boldsymbol{u}_h\|_{\Omega_h^*}+\frac{\delta_1}{2}(1+\zeta_u)\|(\nu/(\gamma^n h))^{\frac{1}{2}}\boldsymbol{u}_h\cdot\boldsymbol{n}\|_\Gamma^2 \\
&\quad\lesssim \frac{4}{2\delta_1}(1+\zeta_u)\gamma^n\big(\|\nu^{\frac{1}{2}}\nabla\boldsymbol{u}_h\|_\Omega^2+g_\nu(\boldsymbol{u}_h,\boldsymbol{u}_h)\big)+\frac{\delta_1}{2}(1+\zeta_u)\|(\nu/(\gamma^n h))^{\frac{1}{2}}\boldsymbol{u}_h\cdot\boldsymbol{n}\|_\Gamma^2. \qquad (3.144)
\end{aligned}
$$

By analogy, the following boundary term from (3.141) can be estimated as

$$
\begin{aligned}
&(1+\zeta_u)|\langle\frac{\gamma^t h}{\varepsilon+\gamma^t h}2\nu\boldsymbol{\epsilon}(\boldsymbol{u}_h)\boldsymbol{n},\boldsymbol{u}_h\boldsymbol{P}^t\rangle_\Gamma| \\
&\quad\lesssim \frac{4}{2\delta_2}(1+\zeta_u)\|(\nu(\gamma^t h)^2/(\varepsilon+\gamma^t h))^{\frac{1}{2}}\boldsymbol{\epsilon}(\boldsymbol{u}_h)\boldsymbol{n}\|_\Gamma^2+\frac{\delta_2}{2}(1+\zeta_u)\|(\nu/(\varepsilon+\gamma^t h))^{\frac{1}{2}}\boldsymbol{u}_h\boldsymbol{P}^t\|_\Gamma^2 \\
&\quad\lesssim \frac{4}{2\delta_2}(1+\zeta_u)\gamma^t(\gamma^t h)/(\varepsilon+\gamma^t h)\big(\|\nu^{\frac{1}{2}}\nabla\boldsymbol{u}_h\|_\Omega^2+g_\nu(\boldsymbol{u}_h,\boldsymbol{u}_h)\big) \\
&\qquad+\frac{\delta_2}{2}(1+\zeta_u)\|(\nu/(\varepsilon+\gamma^t h))^{\frac{1}{2}}\boldsymbol{u}_h\boldsymbol{P}^t\|_\Gamma^2. \qquad (3.145)
\end{aligned}
$$

The last term in (3.141) can be bounded by applying a trace inequality, such that

$$
\zeta_u\|\left(\frac{4\gamma^t h\varepsilon}{\varepsilon+\gamma^t h}\right)^{\frac{1}{2}}\nu^{\frac{1}{2}}(\boldsymbol{\epsilon}(\boldsymbol{u}_h)\boldsymbol{n})\boldsymbol{P}^t\|_\Gamma^2\lesssim 4\zeta_u\gamma^t\left(\frac{\varepsilon}{\varepsilon+\gamma^t h}\right)\big(\|\nu^{\frac{1}{2}}\nabla\boldsymbol{u}_h\|_\Omega^2+g_\nu(\boldsymbol{u}_h,\boldsymbol{u}_h)\big). \qquad (3.146)
$$

From the Corollary 3.3 a part of the remaining viscous terms in (3.141) can be estimated as

$$
\|\nu^{\frac{1}{2}}\boldsymbol{\epsilon}(\boldsymbol{u}_h)\|_\Omega^2+\frac{1}{2}\|\left(\frac{\nu}{\gamma^n h}\right)^{\frac{1}{2}}\boldsymbol{u}_h\cdot\boldsymbol{n}\|_\Gamma^2+\frac{1}{2}\|\left(\frac{\nu}{\varepsilon+\gamma^t h}\right)^{\frac{1}{2}}\boldsymbol{u}_h\boldsymbol{P}^t\|_{\Gamma^\varepsilon}^2\gtrsim\|\nu^{\frac{1}{2}}\nabla\boldsymbol{u}_h\|_\Omega^2, \qquad (3.147)
$$

and by combining the previous inequalities (3.141), (3.143), (3.144), (3.145), (3.146) with (3.106), the following estimate can be done

$$
\begin{aligned}
A_h(U_h,U_h)+g_\nu(\boldsymbol{u}_h,\boldsymbol{u}_h)\gtrsim\;&\|\sigma^{\frac{1}{2}}\boldsymbol{u}_h\|_{0,\Omega}^2+\frac{1}{2}\||\boldsymbol{\beta}\cdot\boldsymbol{n}|^{\frac{1}{2}}\boldsymbol{u}_h\|_{0,\Gamma}^2 \\
&+\left(1-\frac{4}{2\delta_1}(1+\zeta_u)\gamma^n\right)\left(\|\nu^{\frac{1}{2}}\nabla\boldsymbol{u}_h\|_{0,\Omega}^2+g_\nu(\boldsymbol{u}_h,\boldsymbol{u}_h)\right) \\
&+\left(-\frac{4}{2\delta_2}(1+\zeta_u)\gamma^t\left(\frac{\gamma^t h}{\varepsilon+\gamma^t h}\right)-4\zeta_u\gamma^t\left(\frac{\varepsilon}{\varepsilon+\gamma^t h}\right)\right)\left(\|\nu^{\frac{1}{2}}\nabla\boldsymbol{u}_h\|_{0,\Omega}^2+g_\nu(\boldsymbol{u}_h,\boldsymbol{u}_h)\right) \\
&+\left(\frac{1}{2}-\frac{\delta_1}{2}(1+\zeta_u)\right)\|(\nu/(\gamma^n h))^{\frac{1}{2}}\boldsymbol{u}_h\cdot\boldsymbol{n}\|_\Gamma^2 \\
&+\left(\frac{1}{2}-\frac{\delta_2}{2}(1+\zeta_u)\right)\|\left(\nu/(\varepsilon+\gamma^t h)\right)^{\frac{1}{2}}\boldsymbol{u}_h\boldsymbol{P}^t\|_\Gamma^2. \qquad (3.148)
\end{aligned}
$$

At this stage it is trivial to see that if an adjoint-inconsistent approach, i.e. $\zeta_u = -1$, is chosen, stability is guaranteed for any positive choice of $\gamma^n, \gamma^t < \infty$. As $(1+\zeta_u) = 0$ and, consequently, all contributions are positive in (3.148), which guarantees that the sum stays positive and can still be bounded from below by the semi-norm $|U_h|_h^2$.

More delicate is to show stability in the adjoint-consistent case, i.e. $\zeta_u = 1$, as it is apparent that for a careless choices of $\delta_1, \delta_2, \gamma^n$ or γ^t it can not be guaranteed that all contributions in (3.148) remain positive. Considering from here on the adjoint-consistent case, it is right away evident that from the last two rows an upper bound on $\delta_1, \delta_2 \leq c < 1/2$, is required. The second and third row can be combined and the scaling rewritten as

$$\begin{aligned}
&\left(1 - \frac{4}{2\delta_1}(1+\zeta_u)\gamma^n - \frac{4}{2\delta_2}(1+\zeta_u)\gamma^t\left(\frac{\gamma^t h}{\varepsilon+\gamma^t h}\right) - 4\zeta_u\gamma^t\left(\frac{\varepsilon}{\varepsilon+\gamma^t h}\right)\right) \\
&\quad = \frac{1}{\varepsilon+\gamma^t h}\left(\varepsilon + \gamma^t h - \frac{4}{\delta_1}\gamma^n\left(\varepsilon+\gamma^t h\right) - \frac{4}{\delta_2}\gamma^t(\gamma^t h) - 4\gamma^t\varepsilon\right) \\
&\quad = \frac{1}{\varepsilon+\gamma^t h}\left(\varepsilon\left[1 - \frac{4}{\delta_1}\gamma^n - 4\gamma^t\right] + \gamma^t h\left[1 - \frac{4}{\delta_1}\gamma^n - \frac{4}{\delta_2}\gamma^t\right]\right).
\end{aligned} \tag{3.149}$$

Choosing, for instance, $\delta_1 = \delta_2 = 1/4$, stability of the adjoint-consistent Nitsche-type method can be guaranteed by bounding the stabilization parameters γ^n, γ^t by $\gamma^n \leq \delta_1/8 = 1/32$ and $\gamma^t \leq \delta_2/8 = 1/32$. Note that the parameters also need to be lower bounded, i.e. $\gamma^n, \gamma^t > 0$, not to lose contributions of the bulk measures contained in the energy-type semi-norm $|U_h|_h$ and to prevent ill-conditioning. Finally, the claim (3.140) follows by adding all other stabilization terms in S_h and G_h, not already included in the analysis.

□

The next three Lemmas are recalled from the work by Massing *et al.* [184] and show how the CIP, the ghost penalty and the Nitsche-related stabilization terms can be used to recover the missing velocity and pressure semi-norm parts which are included in $|||V_h|||_h$.

First, control over the incompressibility constraint is recovered with the help of the stabilization terms s_u and g_u. This is required for low Reynolds-numbers when the viscous H^1-semi-norm control $\|\nu^{\frac{1}{2}}\boldsymbol{\epsilon}(\boldsymbol{u}_h)\|_\Omega$ vanishes.

Lemma 3.7 *There is a constant $c_1 > 0$ such that for each $\boldsymbol{u}_h \in \mathcal{V}_h$ there exists a $q_h \in \mathcal{Q}_h$ satisfying*

$$-b_h(q_h, \boldsymbol{u}_h) \gtrsim \|\phi_u^{\frac{1}{2}}\nabla\cdot\boldsymbol{u}_h\|_\Omega^2 - c_1\Big(s_u(\boldsymbol{u}_h,\boldsymbol{u}_h) + g_u(\boldsymbol{u}_h,\boldsymbol{u}_h) + \|h^{-\frac{1}{2}}\phi_u^{\frac{1}{2}}\boldsymbol{u}_h\cdot\boldsymbol{n}\|_\Gamma^2\Big) \tag{3.150}$$

and the stability estimate

$$|||q_h|||_{h,\phi}^2 = \|\phi^{-\frac{1}{2}}q_h\|_\Omega^2 + |q_h|_h^2 \lesssim \|\phi_u^{\frac{1}{2}}\nabla\cdot\boldsymbol{u}_h\|_{\mathcal{T}_h}^2 \lesssim \|\phi_u^{\frac{1}{2}}\nabla\cdot\boldsymbol{u}_h\|_\Omega^2 + g_u(\boldsymbol{u}_h,\boldsymbol{u}_h) \tag{3.151}$$

with $\phi \in \{\phi_u, \Phi^{-1}\}$ whenever the CIP and ghost penalty parameter γ_u is chosen sufficiently large.

Proof. A detailed proof can be found in Massing *et al.* [184] (cf. Lemma 6.3).

□

The next lemma shows how additional control over a mixed semi-norm of the form $\|\phi_\beta^{\frac{1}{2}}(\boldsymbol{\beta}\cdot\nabla\boldsymbol{u}_h+\nabla p_h)\|_\Omega^2$ can be recovered with the help of the CIP stabilizations s_β, s_p and the ghost penalty stabilizations.

Lemma 3.8 *There is a constant $c_2>0$ such that for each $U_h=(\boldsymbol{u}_h,p_h)\in\mathcal{W}_h$ a $\boldsymbol{v}_h\in V_h$ can be constructed, satisfying*

$$\begin{aligned}(\boldsymbol{\beta}\cdot\nabla\boldsymbol{u}_h+\nabla p_h,\boldsymbol{v}_h)_\Omega &\gtrsim \|\phi_\beta^{\frac{1}{2}}(\boldsymbol{\beta}\cdot\nabla\boldsymbol{u}_h+\nabla p_h)\|_\Omega^2 - c_2(s_\beta(\boldsymbol{u}_h,\boldsymbol{u}_h)+s_p(p_h,p_h)\\ &\quad+\omega_h\|\nu^{\frac{1}{2}}\nabla\boldsymbol{u}_h\|_{\Omega_h^*}^2+\|\sigma^{\frac{1}{2}}\boldsymbol{u}_h\|_{\Omega_h^*}^2) \qquad (3.152)\\ &\gtrsim \|\phi_\beta^{\frac{1}{2}}(\boldsymbol{\beta}\cdot\nabla\boldsymbol{u}_h+\nabla p_h)\|_\Omega^2 - c_2(1+\omega_h)|U_h|_h^2 \qquad (3.153)\end{aligned}$$

and the stability estimate

$$\begin{aligned}&\|h^{-\frac{1}{2}}\phi_u^{\frac{1}{2}}\boldsymbol{v}_h\cdot\boldsymbol{n}\|_\Gamma^2+|||\boldsymbol{v}_h|||_h^2+\|\phi_\beta^{\frac{1}{2}}\boldsymbol{\beta}\cdot\nabla\boldsymbol{v}_h\|_\Omega^2+\|\phi_u^{\frac{1}{2}}\nabla\cdot\boldsymbol{v}_h\|_\Omega^2\\ &\qquad\lesssim \|\phi_\beta^{\frac{1}{2}}(\boldsymbol{\beta}_h\cdot\nabla\boldsymbol{u}_h+\nabla p_h)\|_{\mathcal{T}_h}^2 \qquad (3.154)\\ &\qquad\lesssim \|\phi_\beta^{\frac{1}{2}}(\boldsymbol{\beta}\cdot\nabla\boldsymbol{u}_h+\nabla p_h)\|_\Omega^2+(1+\omega_h)|U_h|_h^2, \qquad (3.155)\end{aligned}$$

whenever the stability parameters $\gamma_\beta,\gamma_p,\gamma_\nu,\gamma_\sigma$ are chosen sufficiently large and the Nitsche penalty parameter γ^n is chosen sufficiently small.

Proof. A detailed proof of this estimate has been presented in Massing *et al.* [184] (cf. Lemma 6.4).

□

Next, two estimates from [184] are recalled which will be useful in deriving the final stability estimate in Theorem 3.11.

Lemma 3.9 *Let $\boldsymbol{u}_h,\boldsymbol{v}_h\in\mathcal{V}_h$, then the following estimates hold*

$$\begin{aligned}&|||\boldsymbol{v}_h|||_h^2+(1+\omega_h)^{-1}\|\phi_\beta^{\frac{1}{2}}\boldsymbol{\beta}\cdot\nabla\boldsymbol{v}_h\|_\Omega^2+\|\phi_u^{\frac{1}{2}}\nabla\cdot\boldsymbol{v}_h\|_\Omega^2\\ &\qquad\lesssim |||\boldsymbol{v}_h|||_h^2+\big(\nu+\|\boldsymbol{\beta}\|_{0,\infty,\Omega}h+\sigma C_P^2\big)|||\nabla\boldsymbol{v}_h|||_{\mathcal{T}_h}^2 \qquad (3.156)\\ &\qquad\lesssim \big(\nu+\|\boldsymbol{\beta}\|_{0,\infty,\Omega}h+\sigma C_P^2\big)\big(\|\nabla\boldsymbol{v}_h\|_{\mathcal{T}_h}^2+\|h^{-\frac{1}{2}}\boldsymbol{v}_h\|_\Gamma^2\big) \qquad (3.157)\\ &\qquad\lesssim \Phi^{-1}\big(\|\nabla\boldsymbol{v}_h\|_{\mathcal{T}_h}^2+\|h^{-\frac{1}{2}}\boldsymbol{v}_h\|_\Gamma^2\big), \qquad (3.158)\end{aligned}$$

$$|(\boldsymbol{u}_h,\boldsymbol{\beta}\cdot\nabla\boldsymbol{v}_h)_\Omega|\lesssim|||\boldsymbol{u}_h|||_h\frac{\|\boldsymbol{\beta}\|_{0,\infty,\Omega}C_P}{\sqrt{\nu+\sigma C_P^2}}\|\nabla\boldsymbol{v}_h\|_\Omega\lesssim|||\boldsymbol{u}_h|||_h\Phi^{-\frac{1}{2}}\|\nabla\boldsymbol{v}_h\|_\Omega. \qquad (3.159)$$

Proof. A detailed proof can be found in Massing *et al.* [184] (cf. Lemma 6.5).

□

Finally, a stabilized inf-sup condition for the operator $b_h(p_h, \boldsymbol{v}_h)$ holds, provided that the pressure stabilization operator s_p is added, which gives the desired L^2-pressure norm control.

Lemma 3.10 *There is a constant $c_3 > 0$ such that for each pressure $p_h \in \mathcal{Q}_h$ there exists a velocity field $\boldsymbol{v}_h \in \mathcal{V}_h$ satisfying*

$$b_h(p_h, \boldsymbol{v}_h) \gtrsim \Phi \|p_h\|_\Omega^2 - c_3 s_p(p_h, p_h) \tag{3.160}$$

and the stability estimate

$$\begin{aligned} |||\boldsymbol{v}_h|||_h^2 + (1+\omega_h)^{-1}\|\phi_\beta^{\frac{1}{2}}\boldsymbol{\beta}\cdot\nabla\boldsymbol{v}_h\|_\Omega^2 + \|\phi_u^{\frac{1}{2}}\nabla\cdot\boldsymbol{v}_h\|_\Omega^2 &\lesssim \Phi^{-1}(\|\nabla\boldsymbol{v}_h\|_{\mathcal{T}_h}^2 + \|h^{-\frac{1}{2}}\boldsymbol{v}_h\|_\Gamma^2) \\ &\lesssim \Phi\|p_h\|_\Omega^2 + g_p(p_h, p_h), \end{aligned} \tag{3.161}$$

whenever the stability parameters $\gamma_\nu, \gamma_\sigma, \gamma_\beta, \gamma_u, \gamma_p$ are chosen large enough.

Proof. A detailed proof of this modified inf-sup condition has been presented in Massing *et al.* [184] (cf. Lemma 6.6).

□

Collecting the previous Lemmas, the final inf-sup stability estimate of the stabilized cut finite element method $A_h + S_h + G_h$, see (3.83), can be stated with respect to the energy norm (3.90)

$$|||U_h|||_h^2 := |U_h|_h^2 + \|\phi_u^{\frac{1}{2}}\nabla\cdot\boldsymbol{u}_h\|_\Omega^2 + \frac{1}{1+\omega_h}\|\phi_\beta^{\frac{1}{2}}(\boldsymbol{\beta}\cdot\nabla\boldsymbol{u}_h + \nabla p_h)\|_\Omega^2 + \Phi\|p_h\|_\Omega^2.$$

The subsequent theorem ensures existence and uniqueness of a discrete velocity and pressure solution.

Theorem 3.11 *Let $U_h = (\boldsymbol{u}_h, p_h) \in \mathcal{W}_h$. Then, under the assumptions of Lemma 3.6 on the Nitsche penalty parameter γ^t depending on $\zeta_u \in \{-1, 1\}$, on γ^n being sufficiently small as stated in Lemmas 3.6 and 3.8 and that CIP and ghost penalty stability parameters $\gamma_\nu, \gamma_\sigma, \gamma_\beta, \gamma_u, \gamma_p$ are chosen large enough (see Lemmas 3.6–3.10), the cut finite element method (3.83) is inf-sup stable*

$$|||U_h|||_h \lesssim \sup_{V_h \in \mathcal{W}_h \setminus \{0\}} \frac{A_h(U_h, V_h) + S_h(U_h, V_h) + G_h(U_h, V_h)}{|||V_h|||_h}. \tag{3.162}$$

Note that the hidden stability constant is independent of the mesh size h, the slip length coefficient $\varepsilon \in [0, \infty]$ and in case of unfitted meshes independent of the position of the boundary relative to the background mesh.

Proof. Since the proof follows the procedure proposed by Massing *et al.* [184], the major steps

are only sketched in the following. For a given $U_h \in \mathcal{W}_h$, a test function $V_h \in \mathcal{W}_h$ based on estimates derived in Lemmas 3.6, 3.7, 3.8 and 3.10 is constructed.

Step 1. Choosing the test function $V_h^1 := (\mathbf{0}, q_h^1)$ with q_h^1 from Lemma 3.7 to recover control over the divergence and utilizing its stability bounds (3.150) and (3.151) the following holds true

$$
\begin{aligned}
(A_h + S_h + G_h)(U_h, V_h^1) &= -b_h(q_h^1, \boldsymbol{u}_h) + s_p(p_h, q_h^1) + g_p(p_h, q_h^1) && (3.163)\\
&\gtrsim \|\phi_u^{\frac{1}{2}} \nabla \cdot \boldsymbol{u}_h\|_\Omega^2 - c_1\big(s_u(\boldsymbol{u}_h, \boldsymbol{u}_h) + g_u(\boldsymbol{u}_h, \boldsymbol{u}_h) + \|h^{-\frac{1}{2}} \phi_u^{\frac{1}{2}} \boldsymbol{u}_h \cdot \boldsymbol{n}\|_\Gamma^2\big) \\
&\quad - \delta^{-1}\big(s_p(p_h, p_h) + g_p(p_h, p_h)\big) - \delta\big(s_p(q_h^1, q_h^1) + g_p(q_h^1, q_h^1)\big) && (3.164)\\
&\gtrsim \|\phi_u^{\frac{1}{2}} \nabla \cdot \boldsymbol{u}_h\|_\Omega^2 - c_1\big(|\boldsymbol{u}_h|_h^2 + \|h^{-\frac{1}{2}} \phi_u^{\frac{1}{2}} \boldsymbol{u}_h \cdot \boldsymbol{n}\|_\Gamma^2\big) \\
&\quad - \delta^{-1}|p_h|_h^2 - \delta \|\phi_u^{\frac{1}{2}} \nabla \cdot \boldsymbol{u}_h\|_{\mathcal{T}_h}^2 && (3.165)\\
&\gtrsim (1-\delta)\|\phi_u^{\frac{1}{2}} \nabla \cdot \boldsymbol{u}_h\|_\Omega^2 - C_1(\delta)|U_h|_h^2 && (3.166)
\end{aligned}
$$

for any positive $\gamma^n \leq C < \infty$. This shows the need for the boundary-normal Nitsche penalty term at Γ for convective and reactive dominant flows as well as the need for the pressure and divergence CIP and ghost penalty terms.

Step 2. Inserting $V_h^2 := (\boldsymbol{v}_h^2, 0)$ with $\boldsymbol{v}_h^2$, from Lemma 3.8 into the formulation $A_h + S_h + G_h$, followed by applying the continuity estimate (3.121) for a_h and the stability bounds (3.153) and (3.155) yields the following

$$
\begin{aligned}
(A_h + S_h + G_h)(U_h, V_h^2) &= a_h(\boldsymbol{u}_h, \boldsymbol{v}_h^2) + b_h(p_h, \boldsymbol{v}_h^2) + (S_h + G_h)(U_h, V_h^2) && (3.167)\\
&\gtrsim -\delta^{-1}|||\boldsymbol{u}_h|||_h^2 - \delta|||\boldsymbol{v}_h^2|||_h^2 \\
&\quad + \|\phi_\beta^{\frac{1}{2}}(\boldsymbol{\beta} \cdot \nabla \boldsymbol{u}_h + \nabla p_h)\|_\Omega^2 - c_2(1+\omega_h)|U_h|_h^2 && (3.168)\\
&\gtrsim (1-\delta)\|\phi_\beta^{\frac{1}{2}}(\boldsymbol{\beta} \cdot \nabla \boldsymbol{u}_h + \nabla p_h)\|_\Omega^2 - C_2(\delta)(1+\omega_h)|U_h|_h^2. && (3.169)
\end{aligned}
$$

Step 3. The L^2-pressure norm term can be constructed by testing with $V_h^3 := (\boldsymbol{v}_h^3, 0)$, where $\boldsymbol{v}_h^3$ is now chosen as in Lemma 3.10. Utilizing the continuity estimate (3.122) for a_h and making use of the estimates (3.158), (3.159), and the stability bound (3.161) for the chosen test function permits the deduction that

$$
\begin{aligned}
(A_h + S_h + G_h)(U_h, V_h^3) &= a_h(\boldsymbol{u}_h, \boldsymbol{v}_h^3) + b_h(p_h, \boldsymbol{v}_h^3) + (S_h + G_h)(U_h, V_h^3) && (3.170)\\
&\gtrsim -|||\boldsymbol{u}_h|||_h |||\boldsymbol{v}_h^3|||_h - (\boldsymbol{u}_h, \boldsymbol{\beta} \cdot \nabla \boldsymbol{v}_h^3)_\Omega + \Phi\|p_h\|_\Omega^2 - c_3 s_p(p_h, p_h) && (3.171)\\
&\gtrsim -\delta^{-1}|||\boldsymbol{u}_h|||_h^2 - \delta\Phi^{-1}(\|\nabla \boldsymbol{v}_h^3\|_{\mathcal{T}_h}^2 + \|h^{-\frac{1}{2}} \boldsymbol{v}_h^3\|_\Gamma^2) \\
&\quad - \delta^{-1}|||\boldsymbol{u}_h|||_h^2 - \delta\Phi^{-1}\|\nabla \boldsymbol{v}_h^3\|_\Omega^2 + \Phi\|p_h\|_\Omega^2 - c_3 s_p(p_h, p_h) && (3.172)\\
&\gtrsim (1-2\delta)\Phi\|p_h\|_\Omega^2 - 2\delta^{-1}|||\boldsymbol{u}_h|||_h^2 - c_3 s_p(p_h, p_h) - 2\delta g_p(p_h, p_h) && (3.173)\\
&\gtrsim \Phi\|p_h\|_\Omega^2 - C_3(\delta)|U_h|_h^2. && (3.174)
\end{aligned}
$$

Step 4. From the coercivity estimate in Lemma 3.6 the positive semi-norm term $|U_h|_h$ is obtained with the choice $V_h^4 := U_h$

$$A_h(U_h, V_h^4) + S_h(U_h, V_h^4) + G_h(U_h, V_h^4) \gtrsim |U_h|_h^2. \tag{3.175}$$

Step 5. It remains to combine Step 1–4 by choosing δ sufficiently small and defining the final test function

$$V_h^5 := \eta(V_h^1 + (1+\omega_h)^{-1}V_h^2 + V_h^3) + V_h^4 \tag{3.176}$$

for a given U_h. Choosing $\eta > 0$ sufficiently small for some $2\eta \sim (C_1(\delta) + C_2(\delta) + C_3(\delta))^{-1}$ allows for the possibility to gain control over all desired norm parts in $|||U_h|||_h$ and at the same time to absorb the defective $|U_h|_h$-contribution, which stems from testing with V_h^1, V_h^2, V_h^3. Consequently,

$$\begin{aligned}(A_h + S_h + G_h)(U_h, V_h^5) &\gtrsim (1 - \eta(C_1(\delta) + C_2(\delta) + C_3(\delta)))|U_h|_h^2 \\ &\quad + \eta\left(\|\phi_u^{\frac{1}{2}}\nabla\cdot\boldsymbol{u}_h\|_\Omega^2 + \frac{1}{1+\omega_h}\|\phi_\beta^{\frac{1}{2}}(\boldsymbol{\beta}\cdot\nabla\boldsymbol{u}_h + \nabla p_h)\|_\Omega^2 + \Phi\|p_h\|_\Omega^2\right) \\ &\gtrsim |||U_h|||_h^2. \end{aligned} \tag{3.177}$$

The inf-sup stability estimate can be concluded as

$$(A_h + S_h + G_h)(U_h, V_h^5) \gtrsim |||U_h|||_h |||V_h^5|||_h, \tag{3.178}$$

after dividing by $|||V_h^5|||_h$ and choosing the supremum over $V_h \in \mathcal{W}_h\backslash\{0\}$. To conclude the proof, it remains to prove that $|||V_h^5|||_h \lesssim |||U_h|||_h$. Note that

$$|||V_h^5|||_h \leq |||U_h|||_h + \eta|||V_h^1|||_h + \frac{\eta}{1+\omega_h}|||V_h^2|||_h + \eta|||V_h^3|||_h. \tag{3.179}$$

Thanks to the stability estimate (3.155) and norm definitions (3.90) and (3.91) it holds that

$$|||V_h^2|||_h^2 = |||\boldsymbol{v}_h^2|||_h^2 + g_p(0,0) + s_p(0,0) + (1+\omega_h)^{-1}\|\phi_\beta^{\frac{1}{2}}\boldsymbol{\beta}\cdot\nabla\boldsymbol{v}_h^2\|_\Omega^2 + \|\phi_u^{\frac{1}{2}}\nabla\cdot\boldsymbol{v}_h^2\|_\Omega^2 \tag{3.180}$$

$$\lesssim (1 + (1+\omega_h)^{-1})(\|\phi_\beta^{\frac{1}{2}}(\boldsymbol{\beta}\cdot\nabla\boldsymbol{u}_h + \nabla p_h)\|_\Omega^2 + (1+\omega_h)|U_h|_h^2) \tag{3.181}$$

$$\lesssim (1+\omega_h)|||U_h|||_h^2. \tag{3.182}$$

Similarly, the stability bound (3.151) for q_h^1 implies that

$$|||V_h^1|||_h^2 = \Phi\|q_h^1\|_\Omega^2 + |q_h^1|_h^2 \lesssim |||U_h|||_h^2 \tag{3.183}$$

and from (3.161) it is obtained that

$$|||V_h^3|||_h^2 = |||\boldsymbol{v}_h^3|||_h^2 + (1+\omega_h)^{-1}\|\phi_\beta^{\frac{1}{2}}\boldsymbol{\beta}\cdot\nabla\boldsymbol{v}_h^3\|_\Omega^2 + \|\phi_u^{\frac{1}{2}}\nabla\cdot\boldsymbol{v}_h^3\|_\Omega^2 \lesssim |||U_h|||_h^2. \tag{3.184}$$

As a result it holds

$$|||V_h^5|||_h \lesssim (1 + \eta + \eta(1+\omega_h)^{-\frac{1}{2}} + \eta)|||U_h|||_h \lesssim |||U_h|||_h, \tag{3.185}$$

which concludes the proof.

□

3.3.6 A Priori Error Estimates

This section is devoted to the *a priori* error analysis of the proposed cut finite element method. In Theorem 3.15 an energy-norm error estimate is derived for the discrete velocity and pressure solution. Thereafter in Theorem 3.16, a standard duality technique to establish optimal error convergence in the velocity L^2-norm for viscous dominating flow is conducted for the adjoint-consistent formulation

3.3.6.1 Consistency and Interpolation Error Estimates

First it is shown that the discrete formulation (3.83) satisfies a weakened form of the Galerkin orthogonality.

Lemma 3.12 (Weakened Galerkin Orthogonality) *Assume that the solution $U = (\boldsymbol{u}, p)$ of the formulation (3.34)–(3.37) is sufficiently regular, i.e. in $[H^2(\Omega)]^d \times H^1(\Omega)$, and let $U_h = (\boldsymbol{u}_h, p_h) \in \mathcal{V}_h \times \mathcal{Q}_h$ be the cut finite element solution to the discrete weak formulation (3.83). Then, the error $U - U_h$ satisfies a weak Galerkin orthogonality property*

$$A_h(U - U_h, V_h) = S_h(U_h, V_h) + G_h(U_h, V_h) \quad \forall\, V_h \in \mathcal{V}_h \times \mathcal{Q}_h. \tag{3.186}$$

Proof. The proof follows standard techniques. Multiplying the problem formulation (3.34)–(3.35) with test functions $V_h = (\boldsymbol{v}_h, q_h) \in \mathcal{V}_h \times \mathcal{Q}_h$, integrating over Ω, performing integration by parts and using the fact that all additional Nitsche-related terms vanish for U satisfying the boundary condition, yields

$$\mathbf{I} = A_h(U, V_h) - L_h(V_h) = 0 \qquad \forall\, V_h \in \mathcal{V}_h \times \mathcal{Q}_h, \tag{3.187}$$

$$\mathbf{II} = A_h(U_h, V_h) + S_h(U_h, V_h) + G_h(U_h, V_h) - L_h(V_h) = 0 \quad \forall\, V_h \in \mathcal{V}_h \times \mathcal{Q}_h, \tag{3.188}$$

where the last equation holds for the discrete solution $U_h \in \mathcal{V}_h \times \mathcal{Q}_h$. The combination $\mathbf{I} - \mathbf{II}$ yields the claim.

□

The following Lemma recalls the well known weak consistency property of continuous interior penalty and ghost penalty stabilization operators S_h, G_h, and as such they do not deteriorate the optimality of the proposed cut finite element scheme.

Lemma 3.13 (Weak Consistency) *For all functions $(\boldsymbol{u}, p) \in [H^r(\Omega)]^d \times H^s(\Omega)$ there holds*

$$\begin{aligned} S_h(\Pi_h^* U, \Pi_h^* U) + G_h(\Pi_h^* U, \Pi_h^* U) \lesssim\ & (\nu + \|\boldsymbol{\beta}\|_{0,\infty,\Omega} h + \sigma h^2) h^{2r_u - 2} \|\boldsymbol{u}\|^2_{r_u,\Omega} \\ & + \max_{T \in \mathcal{T}_h} \left\{ (\nu + \|\boldsymbol{\beta}\|_{0,\infty,T} h + \sigma h^2)^{-1} \right\} h^{2s_p} \|p\|^2_{s_p,\Omega}, \end{aligned} \tag{3.189}$$

where k is the polynomial degree of the respective Clément interpolants $\Pi_h^* U = (\boldsymbol{\pi}_h^* \boldsymbol{u}, \pi_h^* p)$ for the velocity and pressure and $r_u := \min\{r, k+1\}$ and $s_p := \min\{s, k+1\}$.

Proof. A detailed proof of the weak consistency of the proposed continuous interior penalty and ghost penalty operators S_h and G_h has been given in [184] (see Lemma 7.2) and the references therein. □

The next Lemma ensures that the interpolation error between a continuous solution and its Clément interpolation converges with optimal rates.

Lemma 3.14 (Interpolation Estimates) *Assume that* $(\boldsymbol{u}, p) \in [H^r(\Omega)]^d \times H^s(\Omega)$ *and let* $r_u := \min\{r, k+1\} \geq 2$, $s_p := \min\{s, k+1\} \geq 1$ *where* k *is the polynomial degree of the approximation spaces for the velocity and pressure. Then*

$$|||\boldsymbol{u} - \boldsymbol{\pi}_h^* \boldsymbol{u}|||_* + \|\phi_u^{\frac{1}{2}} \nabla \cdot (\boldsymbol{u} - \boldsymbol{\pi}_h^* \boldsymbol{u})\|_\Omega \lesssim (\nu + \|\boldsymbol{\beta}\|_{0,\infty,\Omega} h + \sigma h^2)^{\frac{1}{2}} h^{r_u - 1} \|\boldsymbol{u}\|_{r_u,\Omega}, \tag{3.190}$$

$$|||p - \pi_h^* p|||_{*,\phi} \lesssim \max_{T \in \mathcal{T}_h} \left\{ (\nu + \|\boldsymbol{\beta}\|_{0,\infty,T} h + \sigma h^2)^{-1} \right\}^{\frac{1}{2}} h^{s_p} \|p\|_{s_p,\Omega} \tag{3.191}$$

with $\phi \in \{\phi_u, \Phi^{-1}\}$ *in the pressure estimate.*

Proof. The proof follows the techniques proposed in [184] (see Lemma 7.3). By applying the interpolation estimate (3.111), the viscous, the reactive and the divergence bulk error measures can be estimated as

$$\begin{aligned} \|\nu^{\frac{1}{2}} \nabla (\boldsymbol{u}^* - \boldsymbol{\pi}_h^* \boldsymbol{u})\|_\Omega^2 + \|\sigma^{\frac{1}{2}} (\boldsymbol{u}^* - \boldsymbol{\pi}_h^* \boldsymbol{u})\|_\Omega^2 + \|\phi_u^{\frac{1}{2}} \nabla \cdot (\boldsymbol{u}^* - \boldsymbol{\pi}_h^* \boldsymbol{u})\|_\Omega^2 \\ \lesssim (\nu + \|\boldsymbol{\beta}\|_{0,\infty,\Omega} h + \sigma h^2) h^{2(r_u - 1)} \|\boldsymbol{u}\|_{r_u,\Omega}^2 \end{aligned} \tag{3.192}$$

and similarly for the pressure

$$\begin{aligned} \|\phi_u^{-\frac{1}{2}} (p^* - \pi_h^* p)\|_\Omega^2 &\lesssim \sum_{T \in \mathcal{T}_h} (\nu + \|\boldsymbol{\beta}\|_{0,\infty,T} h + \sigma h^2)^{-1} h^{2 s_p} \|p^*\|_{s_p,\omega(T)}^2 \\ &\lesssim \max_{T \in \mathcal{T}_h} \left\{ (\nu + \|\boldsymbol{\beta}\|_{0,\infty,T} h + \sigma h^2)^{-1} \right\} h^{2 s_p} \|p\|_{s_p,\Omega}^2. \end{aligned} \tag{3.193}$$

Considering the normal and tangential boundary semi-norms with $\gamma^t, \gamma^n \geq c > 0$ and $\varepsilon \geq 0$, the claim follows by combining the interpolation estimate (3.111), the trace inequality (3.100) and the definition of the scaling function ϕ_u such that

$$\|((\nu + \phi_u)/(\gamma^n h))^{\frac{1}{2}} (\boldsymbol{u}^* - \boldsymbol{\pi}_h^* \boldsymbol{u}) \boldsymbol{P}^n\|_\Gamma^2 \lesssim \|((\nu + \phi_u)/h)^{\frac{1}{2}} (\boldsymbol{u}^* - \boldsymbol{\pi}_h^* \boldsymbol{u})\|_\Gamma^2 \tag{3.194}$$

$$\lesssim (\nu + \|\boldsymbol{\beta}\|_{0,\infty,\Omega} h + \sigma h^2) \big(h^{-2} \|\boldsymbol{u}^* - \boldsymbol{\pi}_h^* \boldsymbol{u}\|_{\mathcal{T}_h}^2 + \|\nabla (\boldsymbol{u}^* - \boldsymbol{\pi}_h^* \boldsymbol{u})\|_{\mathcal{T}_h}^2 \big) \tag{3.195}$$

$$\lesssim (\nu + \|\boldsymbol{\beta}\|_{0,\infty,\Omega} h + \sigma h^2) h^{2(r_u - 1)} \|\boldsymbol{u}\|_{r_u,\Omega}^2, \tag{3.196}$$

$$\|(\nu/(\varepsilon + \gamma^t h))^{\frac{1}{2}} (\boldsymbol{u}^* - \boldsymbol{\pi}_h^* \boldsymbol{u}) \boldsymbol{P}^t\|_\Gamma^2 \lesssim \|(\nu/h)^{\frac{1}{2}} (\boldsymbol{u}^* - \boldsymbol{\pi}_h^* \boldsymbol{u})\|_\Gamma^2 \tag{3.197}$$

$$\lesssim \nu \big(h^{-2} \|\boldsymbol{u}^* - \boldsymbol{\pi}_h^* \boldsymbol{u}\|_{\mathcal{T}_h}^2 + \|\nabla (\boldsymbol{u}^* - \boldsymbol{\pi}_h^* \boldsymbol{u})\|_{\mathcal{T}_h}^2 \big) \tag{3.198}$$

$$\lesssim \nu h^{2(r_u - 1)} \|\boldsymbol{u}\|_{r_u,\Omega}^2. \tag{3.199}$$

The remaining boundary terms can be estimated in a similar fashion,

$$\begin{aligned}
\||\boldsymbol{\beta}\cdot\boldsymbol{n}|^{\frac{1}{2}}(\boldsymbol{u}^*-\boldsymbol{\pi}_h^*\boldsymbol{u})\|_\Gamma^2 &\lesssim \|\boldsymbol{\beta}\|_{0,\infty,\Omega}(h^{-1}\|\boldsymbol{u}^*-\boldsymbol{\pi}_h^*\boldsymbol{u}\|_{\mathcal{T}_h}^2+h\|\nabla(\boldsymbol{u}^*-\boldsymbol{\pi}_h^*\boldsymbol{u})\|_{\mathcal{T}_h}^2)\\
&\lesssim (\|\boldsymbol{\beta}\|_{0,\infty,\Omega}h)h^{2(r_u-1)}\|\boldsymbol{u}\|_{r_u,\Omega}^2, \qquad (3.200)\\
\|(\nu h)^{\frac{1}{2}}\nabla(\boldsymbol{u}^*-\boldsymbol{\pi}_h^*\boldsymbol{u})\cdot\boldsymbol{n}\|_\Gamma^2 &\lesssim \nu\|\nabla(\boldsymbol{u}^*-\boldsymbol{\pi}_h^*\boldsymbol{u})\|_{\mathcal{T}_h}^2+\nu h^2\|D^2(\boldsymbol{u}^*-\boldsymbol{\pi}_h^*\boldsymbol{u})\|_{\mathcal{T}_h}^2\\
&\lesssim \nu h^{2(r_u-1)}\|\boldsymbol{u}\|_{r_u,\Omega}^2, \qquad (3.201)\\
\|\phi_u^{-\frac{1}{2}}h^{\frac{1}{2}}(p^*-\pi_h^*p)\|_\Gamma^2 &\lesssim \|\phi_u^{-\frac{1}{2}}(p^*-\pi_h^*p)\|_{\mathcal{T}_h}^2+h^2\|\phi_u^{-\frac{1}{2}}\nabla(p^*-\pi_h^*p)\|_{\mathcal{T}_h}^2\\
&\lesssim \max_{T\in\mathcal{T}_h}\left\{\phi_u^{-1}\right\}h^{2s_p}\|p\|_{s_p,\Omega}^2. \qquad (3.202)
\end{aligned}$$

Collecting all estimates and noting that $\Phi\lesssim\phi_u^{-1}$ yields the claim.

□

3.3.6.2 A Priori Error Estimates

In the ensuing section, the main *a priori* estimate for the velocity and pressure errors with respect to a natural energy norm is stated.

Theorem 3.15 (Energy norm error estimate) *Assume that the continuous solution of the Oseen problem (3.34)–(3.37) resides in $U=(\boldsymbol{u},p)\in[H^r(\Omega)]^d\times H^s(\Omega)$ and let $U_h=(\boldsymbol{u}_h,p_h)\in\mathcal{V}_h\times\mathcal{Q}_h$ be the discrete solution of problem (3.83). Let the energy type norm be defined as in (3.95), then*

$$\begin{aligned}
|||U-U_h|||_* \lesssim{}& (1+\omega_h)^{\frac{1}{2}}\left(\nu+\|\boldsymbol{\beta}\|_{0,\infty,\Omega}h+\sigma h^2\right)^{\frac{1}{2}}h^{r_u-1}\|\boldsymbol{u}\|_{r_u,\Omega}\\
&+\max_{T\in\mathcal{T}_h}\left\{(\nu+\|\boldsymbol{\beta}\|_{0,\infty,\Omega}h+\sigma h^2)^{-1}\right\}^{\frac{1}{2}}h^{s_p}\|p\|_{s_p,\Omega}, \qquad (3.203)
\end{aligned}$$

where $r_u:=\min\{r,k+1\}\geq 2$ and $s_p:=\min\{s,k+1\}\geq 1$. Note that the hidden constants are independent of h, are bounded with respect to the slip length coefficient $\varepsilon\in[0,\infty]$ and, owing to the ghost penalty stabilization terms G_h, independent of how the boundary intersects the mesh $\mathcal{T}_h$. The (hidden) scaling functions ω_h,Φ are as defined in (3.92).

Proof. Starting off, the total discretization error is split into a discrete error and an interpolation part by applying (3.98) and the norm definitions in Section 3.3.3.4

$$|||U-U_h|||_*\lesssim|||U-\Pi_h^*U|||_*+|||\Pi_h^*U-U_h|||_*\lesssim|||U-\Pi_h^*U|||_*+|||\Pi_h^*U-U_h|||_h. \qquad (3.204)$$

As the term $|||U-\Pi_h^*U|||_*$ is readily estimated from the interpolation estimates (3.190) and (3.191), accordingly, only the discrete error $|||\Pi_h^*U-U_h|||_h$ needs to be considered from here on. From the inf-sup condition (3.162) there exists a $|||V_h|||_h=1$ such that

$$\begin{aligned}
|||\Pi_h^*U-U_h|||_h &\lesssim A_h(\Pi_h^*U-U_h,V_h)+S_h(\Pi_h^*U-U_h,V_h)+G_h(\Pi_h^*U-U_h,V_h) \qquad (3.205)\\
&= A_h(\Pi_h^*U-U,V_h)+S_h(\Pi_h^*U,V_h)+G_h(\Pi_h^*U,V_h), \qquad (3.206)
\end{aligned}$$

where the last step follows from applying the weak Galerkin orthogonality (3.186). By applying a Cauchy–Schwarz inequality on the stabilization terms $S_h(\Pi_h^* U, V_h)$ and $G_h(\Pi_h^* U, V_h)$ and utilizing the results from Lemma 3.13 the following estimate can be made for the stabilization terms

$$S_h(\Pi_h^* U, V_h) + G_h(\Pi_h^* U, V_h) \lesssim (\nu + \|\boldsymbol{\beta}\|_{0,\infty,\Omega} h + \sigma h^2)^{\frac{1}{2}} h^{r_u - 1} \|\boldsymbol{u}\|_{r_u,\Omega} + \max_{T \in \mathcal{T}_h} \left\{ (\nu + \|\boldsymbol{\beta}\|_{0,\infty,T} h + \sigma h^2)^{-1} \right\}^{\frac{1}{2}} h^{s_p} \|p\|_{s_p,\Omega}. \quad (3.207)$$

The term $A_h(\Pi_h^* U - U, V_h)$ can be estimated by integrating $b_h(q_h, \boldsymbol{\pi}_h^* \boldsymbol{u} - \boldsymbol{u})$ by parts and applying the continuity estimates (3.120) and (3.124) to $a_h(\boldsymbol{\pi}_h^* \boldsymbol{u} - \boldsymbol{u}, \boldsymbol{v}_h)$ and $b_h(\pi_h^* p - p, \boldsymbol{v}_h)$ respectively, such that

$$\begin{aligned} A_h(\Pi_h^* U - U, V_h) &= a_h(\boldsymbol{\pi}_h^* \boldsymbol{u} - \boldsymbol{u}, \boldsymbol{v}_h) + b_h(\pi_h^* p - p, \boldsymbol{v}_h) - b_h(q_h, \boldsymbol{\pi}_h^* \boldsymbol{u} - \boldsymbol{u}) && (3.208) \\ &\lesssim |||\boldsymbol{\pi}_h^* \boldsymbol{u} - \boldsymbol{u}|||_* |||\boldsymbol{v}_h|||_h - (\boldsymbol{\pi}_h^* \boldsymbol{u} - \boldsymbol{u}, \boldsymbol{\beta} \cdot \nabla \boldsymbol{v}_h)_\Omega \\ &\quad + |||\pi_h^* p - p|||_{*,\phi_u} (|||\boldsymbol{v}_h|||_h + \|\phi_u^{\frac{1}{2}} \nabla \cdot \boldsymbol{v}_h\|_\Omega) - (\boldsymbol{\pi}_h^* \boldsymbol{u} - \boldsymbol{u}, \nabla q_h)_\Omega && (3.209) \\ &\lesssim (|||\boldsymbol{\pi}_h^* \boldsymbol{u} - \boldsymbol{u}|||_* + |||\pi_h^* p - p|||_{*,\phi_u})(|||\boldsymbol{v}_h|||_h + \|\phi_u^{\frac{1}{2}} \nabla \cdot \boldsymbol{v}_h\|_\Omega) \\ &\quad - (\boldsymbol{\pi}_h^* \boldsymbol{u} - \boldsymbol{u}, \boldsymbol{\beta} \cdot \nabla \boldsymbol{v}_h + \nabla q_h)_\Omega. && (3.210) \end{aligned}$$

Thanks to the interpolation estimate Lemma 3.14 and keeping in mind that $|||\boldsymbol{v}_h|||_h + \|\phi_u^{\frac{1}{2}} \nabla \cdot \boldsymbol{v}_h\|_\Omega \lesssim |||V_h|||_h = 1$, it only remains to estimate the last term. Its estimate follows readily from applying a Cauchy–Schwarz inequality, using (3.110) and the definition of ϕ_β to arrive at

$$\begin{aligned} &|(\boldsymbol{\pi}_h^* \boldsymbol{u} - \boldsymbol{u}, \boldsymbol{\beta} \cdot \nabla \boldsymbol{v}_h + \nabla q_h)| \\ &\quad \lesssim (1 + \omega_h)^{\frac{1}{2}} \|\phi_\beta^{-\frac{1}{2}} (\boldsymbol{\pi}_h^* \boldsymbol{u} - \boldsymbol{u})\|_\Omega \cdot (1 + \omega_h)^{-\frac{1}{2}} \|\phi_\beta^{\frac{1}{2}} (\boldsymbol{\beta} \cdot \nabla \boldsymbol{v}_h + \nabla q_h)\|_\Omega && (3.211) \\ &\quad \lesssim (1 + \omega_h)^{\frac{1}{2}} (\nu + \|\boldsymbol{\beta}\|_{0,\infty,\Omega} h + \sigma h^2)^{\frac{1}{2}} h^{r_u - 1} \|\boldsymbol{u}\|_{r_u,\Omega} |||V_h|||_h, && (3.212) \end{aligned}$$

which concludes the proof of the *a priori* error estimate (3.203).

□

3.3.6.3 L^2-Optimal Estimate for Flows with Large Viscosity

As the observant reader might have noticed, in the viscous limit the energy norm (3.203) yields a suboptimal convergence of $\|\boldsymbol{u}^* - \boldsymbol{u}_h\|_\Omega \leq \mathcal{O}(h^k)$. As such, in the final part of this section on a priori error estimates, an optimal L^2-error estimate for the velocity of an adjoint-consistent ($\zeta_u = 1$) formulation for viscous dominated flows will be deduced. For the subsequent analysis viscous dominated flow is assumed, and as such

$$\nu \geq \|\boldsymbol{\beta}\|_{0,\infty,T} h_T + \sigma h_T^2 \quad \forall T \in \mathcal{T}_h. \quad (3.213)$$

The proof follows the standard Aubin–Nitsche duality argument, see e.g. Aubin [8] and Nitsche [205], and requires the established optimal energy-type error estimate from Theorem 3.15. A similar estimate for the Oseen problem has been derived for boundary-fitted meshes by Burman

et al. [63]. The first step for this method is to start from the dual problem of the Oseen equation (3.34)–(3.37), that is: find the adjoint velocity and pressure pair $(\boldsymbol{w}, r)$ such that

$$\sigma \boldsymbol{w} + (-\boldsymbol{\beta}) \cdot \nabla \boldsymbol{w} - \nabla \cdot (2\nu \boldsymbol{\epsilon}(\boldsymbol{w})) + \nabla(-r) = \tilde{\boldsymbol{f}} \quad \text{in } \Omega, \tag{3.214}$$

$$\nabla \cdot \boldsymbol{w} = 0 \quad \text{in } \Omega, \tag{3.215}$$

$$\boldsymbol{w}\boldsymbol{P}^n = \boldsymbol{0} \quad \text{on } \Gamma, \tag{3.216}$$

$$(\varepsilon 2\nu \boldsymbol{\epsilon}(\boldsymbol{w})\boldsymbol{n} + (\nu + \varepsilon \boldsymbol{\beta} \cdot \boldsymbol{n})\boldsymbol{w})\, \boldsymbol{P}^t = \boldsymbol{0} \quad \text{on } \Gamma. \tag{3.217}$$

Additional elliptic regularity on the solution and that it belongs to $(\boldsymbol{w}, r) \in [H^2(\Omega)]^d \times H^1(\Omega)$ is assumed, so that it satisfies

$$\nu \|\boldsymbol{w}\|_{2,\Omega} + \|r\|_{1,\Omega} \leq C \|\tilde{\boldsymbol{f}}\|_{0,\Omega}, \tag{3.218}$$

provided that the boundaries are sufficiently smooth, see e.g. Girault and Raviart [127], Temam [261] or Amrouche and Girault [4]. Note that due to the homogeneous boundary conditions in (3.216)–(3.217) the estimate (3.218) is independent of the boundary data. However, the dimensionless constant C may depend on the physical parameters $\nu, \sigma, \boldsymbol{\beta}$ and the domain Ω. By choosing $\tilde{\boldsymbol{f}} = \boldsymbol{u} - \boldsymbol{u}_h \in L^2(\Omega)$ as the right hand side of the dual momentum equation, the desired error quantity bounds the dual solution $(\boldsymbol{w}, r)$ in (3.218).

A peculiarity of the dual problem (3.216)–(3.217) is the fact that the dual advective velocity is set as the negative advective velocity field of the primal problem. As a result, inflow and outflow parts of the boundary of the primal and dual problems swap. Similarly, the dual pressure solution r changes the sign compared to the pressure solution p of the primal problem. For further explanations on the dual problem, see e.g. the textbook by Quarteroni [216].

In the following it will be assumed that $\boldsymbol{\beta} \cdot \boldsymbol{n} = 0$ on $\Gamma \setminus \Gamma_{\mathrm{D}}$, which simplifies (3.217). This assumption is for one motivated by the physics, as the general Navier boundary condition finds its use mainly for modeling slip at non-penetrable walls, i.e. $\boldsymbol{u} \cdot \boldsymbol{n} = 0$ on Γ. Apart of this, it is also an issue in the following analysis as the Aubin–Nitsche argument breaks down with the introduced asymmetry caused by permitting inflow at general Navier boundaries. Concretely, this problem arises from the integration by parts of the convective term and in the addition of consistent Nitsche terms for the boundary condition (3.217). A different approach to prove an optimal L^2-estimate would need to be opted for if the possibility of inflow is wished to be considered, see Remark 3.7 for a short discussion on the problematic terms.

Theorem 3.16 (Velocity L^2-error estimate) *Let $U = (\boldsymbol{u}, p) \in [H^r(\Omega)]^d \times H^s(\Omega)$ be the continuous solution to the Oseen problem (3.34)–(3.37) and $U_h = (\boldsymbol{u}_h, p_h) \in \mathcal{V}_h \times \mathcal{Q}_h$ be the discrete solution of the problem (3.83). Under previously specified assumptions, for an adjoint-consistent Nitsche-type formulation ($\zeta_u = 1$) the following holds,*

$$\|\boldsymbol{u} - \boldsymbol{u}_h\|_{0,\Omega} \lesssim h^{r_u} \|\boldsymbol{u}\|_{r_u,\Omega} + h^{s_p+1} \nu^{-1} \|p\|_{s_p,\Omega}, \tag{3.219}$$

provided that viscous forces dominate the flow as assumed in (3.213) with $r_u := \min\{r, k+1\}$ and $s_p := \min\{s, k+1\}$. Note that the hidden constant is independent of h and independent of how the boundary intersects the mesh $\mathcal{T}_h$. However, the constant depends on the physical parameters.

Proof. As the desired velocity L^2-error $\|\boldsymbol{u}-\boldsymbol{u}_h\|_{0,\Omega}$ is needed to be estimated, the choice of $\tilde{\boldsymbol{f}}=\boldsymbol{u}-\boldsymbol{u}_h$ is made as the right hand side of the dual momentum equation (3.214). Next (3.214)–(3.215) are multiplied with test functions $\boldsymbol{v}:=\boldsymbol{u}-\boldsymbol{u}_h$ and $-q:=-(p-p_h)$, respectively. After integrating by parts, using $\nabla\cdot\boldsymbol{\beta}=0$ and the relation

$$\langle((-\boldsymbol{\beta})\cdot\boldsymbol{n})\boldsymbol{w},\boldsymbol{v}\rangle_\Gamma=\boldsymbol{0} \tag{3.220}$$

as $\boldsymbol{w}=\boldsymbol{0}$ on Γ_{D} and $\boldsymbol{\beta}\cdot\boldsymbol{n}=0$ on $\Gamma\setminus\Gamma_{\mathrm{D}}$, the following is obtained

$$\begin{aligned}\|\boldsymbol{u}-\boldsymbol{u}_h\|_{0,\Omega}^2 &= (\sigma\boldsymbol{w},\boldsymbol{v})_\Omega+((-\boldsymbol{\beta})\cdot\nabla\boldsymbol{w},\boldsymbol{v})_\Omega-(\nabla\cdot(2\nu\boldsymbol{\epsilon}(\boldsymbol{w})),\boldsymbol{v})_\Omega\\ &\quad+(\nabla(-r),\boldsymbol{v})_\Omega-(\nabla\cdot\boldsymbol{w},q)_\Omega &(3.221)\\ &=(\sigma\boldsymbol{w},\boldsymbol{v})_\Omega+(\boldsymbol{w},\boldsymbol{\beta}\cdot\nabla\boldsymbol{v})_\Omega+(\boldsymbol{\epsilon}(\boldsymbol{w}),2\nu\boldsymbol{\epsilon}(\boldsymbol{v}))_\Omega-\langle2\nu\boldsymbol{\epsilon}(\boldsymbol{w})\boldsymbol{n},\boldsymbol{v}\rangle_\Gamma\\ &\quad+(r,\nabla\cdot\boldsymbol{v})_\Omega-\langle r,\boldsymbol{v}\cdot\boldsymbol{n}\rangle_\Gamma-(\nabla\cdot\boldsymbol{w},q)_\Omega &(3.222)\\ &=a(\boldsymbol{v},\boldsymbol{w})-\langle2\nu\boldsymbol{\epsilon}(\boldsymbol{w})\boldsymbol{n},\boldsymbol{v}\rangle_\Gamma-b_h(r,\boldsymbol{v})+b(q,\boldsymbol{w}). &(3.223)\end{aligned}$$

Using the boundary conditions for the normal and tangential directions (3.216)–(3.217), with the assumption that $\boldsymbol{\beta}\cdot\boldsymbol{n}=0$ on $\Gamma\setminus\Gamma_{\mathrm{D}}$, the boundary conditions then reduce to $\boldsymbol{w}\cdot\boldsymbol{n}=0$ in the wall-normal direction on Γ and $(\varepsilon(2\nu\boldsymbol{\epsilon}(\boldsymbol{w})\boldsymbol{n})+\nu\boldsymbol{w})\boldsymbol{P}^t=\boldsymbol{0}$ in the wall-tangential direction on Γ. Accordingly, the following terms can be added consistently to (3.223)

$$\begin{aligned}0&=\langle\boldsymbol{w}\cdot\boldsymbol{n},q\rangle_\Gamma-\zeta_u\langle\boldsymbol{w}\cdot\boldsymbol{n},(2\nu\boldsymbol{\epsilon}(\boldsymbol{v})\boldsymbol{n})\cdot\boldsymbol{n}\rangle_\Gamma+\langle\frac{\nu}{\gamma^n h}\boldsymbol{w}\cdot\boldsymbol{n},\boldsymbol{v}\cdot\boldsymbol{n}\rangle_\Gamma+\langle\frac{\phi_u}{\gamma^n h}\boldsymbol{w}\cdot\boldsymbol{n},\boldsymbol{v}\cdot\boldsymbol{n}\rangle_\Gamma\\ &=\quad I\qquad\qquad+II\qquad\qquad+III\qquad\qquad+IV, &(3.224)\\ 0&=\langle\frac{1}{\varepsilon+\gamma^t h}(\varepsilon(2\nu\boldsymbol{\epsilon}(\boldsymbol{w})\boldsymbol{n})+\nu\boldsymbol{w})\boldsymbol{P}^t,\boldsymbol{v}\rangle_\Gamma-\zeta_u\langle\frac{\gamma^t h}{\varepsilon+\gamma^t h}(\varepsilon(2\nu\boldsymbol{\epsilon}(\boldsymbol{w})\boldsymbol{n})+\nu\boldsymbol{w})\boldsymbol{P}^t,2\boldsymbol{\epsilon}(\boldsymbol{v})\boldsymbol{n}\rangle_\Gamma\\ &=\qquad\qquad V\quad+VI\qquad\qquad\qquad\qquad+VII\quad+VIII. &(3.225)\end{aligned}$$

Important to note is that these terms are added to impose the boundary conditions in the same way for the dual problem as they were in the primal problem. It is immediately apparent that in (3.223) the simplification $b(q,\boldsymbol{w})+I=b_h(q,\boldsymbol{w})$ can be made. The viscous term can be split into its directional parts such that

$$-\langle2\nu\boldsymbol{\epsilon}(\boldsymbol{w})\boldsymbol{n},\boldsymbol{v}\rangle_\Gamma+V=-\langle(2\nu\boldsymbol{\epsilon}(\boldsymbol{w})\boldsymbol{n})\cdot\boldsymbol{n},\boldsymbol{v}\cdot\boldsymbol{n}\rangle_\Gamma-\langle\frac{\gamma^t h}{\varepsilon+\gamma^t h}(2\nu\boldsymbol{\epsilon}(\boldsymbol{w})\boldsymbol{n})\boldsymbol{P}^t,\boldsymbol{v}\rangle_\Gamma \tag{3.226}$$

and

$$\begin{aligned}II+VIII&=-\zeta_u\langle\boldsymbol{w}\cdot\boldsymbol{n},(2\nu\boldsymbol{\epsilon}(\boldsymbol{v})\boldsymbol{n})\cdot\boldsymbol{n}\rangle_\Gamma-\zeta_u\langle\frac{(\varepsilon+\gamma^t h)-\varepsilon}{\varepsilon+\gamma^t h}\nu\boldsymbol{w}\boldsymbol{P}^t,2\boldsymbol{\epsilon}(\boldsymbol{v})\boldsymbol{n}\rangle_\Gamma\\ &=-\zeta_u\langle\boldsymbol{w},2\nu\boldsymbol{\epsilon}(\boldsymbol{v})\boldsymbol{n}\rangle_\Gamma+\zeta_u\langle\frac{\varepsilon}{\varepsilon+\gamma^t h}\nu\boldsymbol{w}\boldsymbol{P}^t,2\boldsymbol{\epsilon}(\boldsymbol{v})\boldsymbol{n}\rangle_\Gamma. &(3.227)\end{aligned}$$

Collecting all terms from (3.223)–(3.227), yields the following,

$$a(\boldsymbol{v},\boldsymbol{w}) - \langle 2\nu\boldsymbol{\epsilon}(\boldsymbol{w})\boldsymbol{n},\boldsymbol{v}\rangle_\Gamma + II + III + IV + V + VI + VII + VIII \tag{3.228}$$

$$= a(\boldsymbol{v},\boldsymbol{w}) - \zeta_u\langle \boldsymbol{w}, 2\nu\boldsymbol{\epsilon}(\boldsymbol{v})\boldsymbol{n}\rangle_\Gamma \tag{3.229}$$

$$- \langle (2\nu\boldsymbol{\epsilon}(\boldsymbol{w})\boldsymbol{n})\cdot\boldsymbol{n}, \boldsymbol{v}\cdot\boldsymbol{n}\rangle_\Gamma + \langle \frac{\nu}{\gamma^n h}\boldsymbol{w}\cdot\boldsymbol{n}, \boldsymbol{v}\cdot\boldsymbol{n}\rangle_\Gamma \tag{3.230}$$

$$+ \langle \frac{\phi_u}{\gamma^n h}\boldsymbol{w}\cdot\boldsymbol{n}, \boldsymbol{v}\cdot\boldsymbol{n}\rangle_\Gamma \tag{3.231}$$

$$+ \zeta_u\langle \frac{\varepsilon}{\varepsilon+\gamma^t h}\boldsymbol{w}, (2\nu\boldsymbol{\epsilon}(\boldsymbol{v})\boldsymbol{n})\boldsymbol{P}^t\rangle_\Gamma + \langle \frac{1}{\varepsilon+\gamma^t h}\boldsymbol{w}, \nu\boldsymbol{v}\boldsymbol{P}^t\rangle_\Gamma \tag{3.232}$$

$$- \zeta_u\langle \frac{\gamma^t h}{\varepsilon+\gamma^t h}2\boldsymbol{\epsilon}(\boldsymbol{w})\boldsymbol{n}, \varepsilon 2\nu\boldsymbol{\epsilon}(\boldsymbol{v})\boldsymbol{n}\rangle_\Gamma - \langle \frac{\gamma^t h}{\varepsilon+\gamma^t h}2\boldsymbol{\epsilon}(\boldsymbol{w})\boldsymbol{n}, \nu\boldsymbol{v}\boldsymbol{P}^t\rangle_\Gamma. \tag{3.233}$$

Given that $\boldsymbol{w} = \boldsymbol{0}$ on $\Gamma_{\text{in}} \subset \Gamma_{\text{D}}$, i.e $\langle(\boldsymbol{\beta}\cdot\boldsymbol{n})\boldsymbol{w},\boldsymbol{v}\rangle_{\Gamma_{\text{in}}} = 0$, and $\zeta_u = 1$, i.e. an adjoint-consistent formulation, it is clear that the formulations (3.229)–(3.233) and (3.54)–(3.58) are identical, and hence,

$$a(\boldsymbol{v},\boldsymbol{w}) - \langle 2\nu\boldsymbol{\epsilon}(\boldsymbol{w})\boldsymbol{n},\boldsymbol{v}\rangle_\Gamma + II + III + IV + V + VI + VII + VIII = a_h(\boldsymbol{v},\boldsymbol{w}). \tag{3.234}$$

It is important to stress that (3.234) would not hold true for an adjoint-inconsistent formulation as ζ_u appears on different terms in the primal and adjoint problem.

Defining $W := (\boldsymbol{w}, r)$, the L^2-error can now be expressed as

$$\|\boldsymbol{u}-\boldsymbol{u}_h\|_{0,\Omega}^2 = a_h(\boldsymbol{u}-\boldsymbol{u}_h,\boldsymbol{w}) + b_h(p-p_h,\boldsymbol{w}) - b_h(r,\boldsymbol{u}-\boldsymbol{u}_h) = A_h(U-U_h,W), \tag{3.235}$$

i.e. it can be expressed in terms of the discrete bilinear operator (3.53) associated to the primal problem (3.34)–(3.37), where the sufficiently smooth solution W of the dual problem now takes the role of the test function.

Note that under the assumption of dominating viscous forces (3.213), it holds for the advective term occurring in the continuity estimate of a_h in (3.119) that

$$|(\boldsymbol{\beta}\cdot\nabla(\boldsymbol{u}-\boldsymbol{u}_h),\boldsymbol{w}-\boldsymbol{\pi}_h^*\boldsymbol{w})_\Omega|$$

$$\lesssim \nu^{-\frac{1}{2}}\|\nu^{\frac{1}{2}}\nabla(\boldsymbol{u}-\boldsymbol{u}_h)\|_\Omega \max_{T\in\mathcal{T}_h}\{\underbrace{\left(\frac{\|\boldsymbol{\beta}\|_{0,\infty,T}h}{\nu}\right)}_{\lesssim 1}\}\cdot\nu h^{-1}\|\boldsymbol{w}-\boldsymbol{\pi}_h^*\boldsymbol{w}\|_\Omega \tag{3.236}$$

$$\lesssim \nu^{-\frac{1}{2}}|||\boldsymbol{u}-\boldsymbol{u}_h|||\cdot h\nu\|\boldsymbol{w}\|_{2,\Omega}, \tag{3.237}$$

where the interpolation estimate (3.111) for the Clément interpolant was used in the last step. The L^2-velocity error can then be further estimated by using the weak Galerkin orthogonality from Lemma 3.12 with $\Pi_h^* W \in \mathcal{V}_h \times \mathcal{Q}_h$, the continuity of a_h, b_h provided in Lemma 3.5 (equations (3.119) and (3.123)) and by applying a Cauchy–Schwarz inequality to the remaining

stabilization operators

$$\|\boldsymbol{u}-\boldsymbol{u}_h\|_{0,\Omega}^2 = A_h(U-U_h, W-\Pi_h^* W) + S_h(U_h,\Pi_h^* W) + G_h(U_h,\Pi_h^* W)) \tag{3.238}$$

$$= a_h(\boldsymbol{u}-\boldsymbol{u}_h, \boldsymbol{w}-\boldsymbol{\pi}_h^*\boldsymbol{w}) + b_h(p-p_h, \boldsymbol{w}-\boldsymbol{\pi}_h^*\boldsymbol{w}) - b_h(r-\pi_h^* r, \boldsymbol{u}-\boldsymbol{u}_h) + (S_h+G_h)(U_h,\Pi_h^* W) \tag{3.239}$$

$$\lesssim |||\boldsymbol{u}-\boldsymbol{u}_h|||_* |||\boldsymbol{w}-\boldsymbol{\pi}_h^*\boldsymbol{w}|||_* + |(\boldsymbol{\beta}\cdot\nabla(\boldsymbol{u}-\boldsymbol{u}_h), \boldsymbol{w}-\boldsymbol{\pi}_h^*\boldsymbol{w})_\Omega| + |||U-U_h|||_* |||r-\pi_h^* r|||_{*,\phi_u} + |||p-p_h|||_{*,\Phi^{-1}} (\nu\Phi)^{-\frac{1}{2}} (\|\nu^{\frac{1}{2}}\nabla(\boldsymbol{w}-\boldsymbol{\pi}_h^*\boldsymbol{w})\|_\Omega + \|(\nu/h)^{\frac{1}{2}}(\boldsymbol{w}-\boldsymbol{\pi}_h^*\boldsymbol{w})\cdot\boldsymbol{n}\|_\Gamma) + (S_h+G_h)(U_h,U_h)^{\frac{1}{2}} \cdot (S_h+G_h)(\Pi_h^* W,\Pi_h^* W)^{\frac{1}{2}} \tag{3.240}$$

$$\lesssim |||U-U_h|||_* \cdot (|||\boldsymbol{w}-\boldsymbol{\pi}_h^*\boldsymbol{w}|||_* + |||r-\pi_h^* r|||_{*,\phi_u}) + (S_h+G_h)(U_h,U_h)^{\frac{1}{2}} \cdot (S_h+G_h)(\Pi_h^* W,\Pi_h^* W)^{\frac{1}{2}} \tag{3.241}$$

$$\lesssim \nu^{-\frac{1}{2}} \Big(|||U-U_h|||_* + (S_h+G_h)(U_h-\Pi_h^* U, U_h-\Pi_h^* U)^{\frac{1}{2}} + (S_h+G_h)(\Pi_h^* U,\Pi_h^* U)^{\frac{1}{2}} \Big) \cdot \nu^{\frac{1}{2}} \Big(|||\boldsymbol{w}-\boldsymbol{\pi}_h^*\boldsymbol{w}|||_* + |||r-\pi_h^* r|||_{*,\phi_u} + (S_h+G_h)(\Pi_h^* W,\Pi_h^* W)^{\frac{1}{2}} \Big) \tag{3.242}$$

$$\lesssim \nu^{-\frac{1}{2}} \Big(|||U-U_h|||_* + |||U_h-\Pi_h^* U|||_h + (S_h+G_h)(\Pi_h^* U,\Pi_h^* U)^{\frac{1}{2}} \Big) \tag{3.243}$$

$$\cdot\, h(\nu\|\boldsymbol{w}\|_{2,\Omega} + \|r\|_{1,\Omega}) \tag{3.244}$$

$$\lesssim (1+\omega_h)^{\frac{1}{2}} \nu^{-\frac{1}{2}} (\nu^{\frac{1}{2}} h^{r_u-1}\|\boldsymbol{u}\|_{r_u,\Omega} + \nu^{-\frac{1}{2}} h^{s_p}\|p\|_{s_p,\Omega}) \cdot h \cdot \|\boldsymbol{u}-\boldsymbol{u}_h\|_{0,\Omega} \tag{3.245}$$

$$\lesssim (h^{r_u}\|\boldsymbol{u}\|_{r_u,\Omega} + h^{s_p+1}\nu^{-1}\|p\|_{s_p,\Omega}) \cdot \|\boldsymbol{u}-\boldsymbol{u}_h\|_{0,\Omega}. \tag{3.246}$$

In line (3.244) the energy-norm *a priori* error estimate from Theorem 3.15 is used in (3.203) and (3.205) for $(\boldsymbol{u},p) \in [H^{r_u}(\Omega)]^d \times H^{s_p}(\Omega)$ under the assumption of dominant viscous effects (3.213). Note that for $\phi \in \{\phi_u, \Phi^{-1}\}$ it holds that $\nu/\phi \lesssim 1$. Thanks to the interpolation estimate Lemma 3.14, in (3.244) the desired additional power of h for $(\boldsymbol{w},r) \in [H^2(\Omega)]^d \times H^1(\Omega)$ is gained by estimating

$$\nu^{\frac{1}{2}}(|||\boldsymbol{w}-\boldsymbol{\pi}_h^*\boldsymbol{w}|||_* + |||r-\pi_h^* r|||_{*,\phi} + (S_h+G_h)(\Pi_h^* W,\Pi_h^* W)^{\frac{1}{2}}) \tag{3.247}$$

$$\lesssim \nu^{\frac{1}{2}} h(\nu^{\frac{1}{2}}\|\boldsymbol{w}\|_{2,\Omega} + \nu^{-\frac{1}{2}}\|r\|_{1,\Omega}) \lesssim h\|\boldsymbol{u}-\boldsymbol{u}_h\|_{0,\Omega}, \tag{3.248}$$

together with the boundedness (3.218) of the solution to the dual problem (3.214)–(3.217). Note that for S_h and G_h the weak consistency estimates from Lemma 3.13 hold. Finally, the claim follows after dividing by $\|\boldsymbol{u}-\boldsymbol{u}_h\|_{0,\Omega}$ in (3.246).

□

Remark 3.7 *If the assumption $\boldsymbol{\beta}\cdot\boldsymbol{n} \neq 0$ on $\Gamma \setminus \Gamma_D$ does not hold true. The following terms would need to be added in* (3.225)*,*

$$\ldots + \langle \frac{1}{\varepsilon+\gamma^t h}(\varepsilon\boldsymbol{\beta}\cdot\boldsymbol{n})\boldsymbol{w}\boldsymbol{P}^t, \boldsymbol{v}\rangle_\Gamma - \zeta_u \langle \frac{\gamma^t h}{\varepsilon+\gamma^t h}(\varepsilon\boldsymbol{\beta}\cdot\boldsymbol{n})\boldsymbol{w}\boldsymbol{P}^t, 2\boldsymbol{\epsilon}(\boldsymbol{v})\boldsymbol{n}\rangle_\Gamma. \tag{3.249}$$

These terms can not be rewritten in a clever way to conduct the crucial step (3.234) of the Aubin–Nitsche argument. Hence, a different approach would be needed to be taken without the aforementioned assumption.

3.3.7 Numerical Validation

The error estimates derived in the *a priori* error analysis, as summarized in the Theorems 3.15 and 3.16, are here validated by the results of a 2D box-flow case. The same case as in Winter *et al.* [279] will be considered here.

The stabilization parameters employed in the following simulations are taken by large from Massing *et al.* [184] and Schott and Wall [229] and are repeated here for completeness. The CIP-stabilization terms (3.70)–(3.72) are set as $\gamma_\beta = \gamma_p = 0.01$ and $\gamma_u = 0.05\gamma_\beta$, as suggested by Burman [48]. For the convective, pressure and velocity ghost penalty stabilizations (3.76)–(3.78) the same parameters are used as for the CIP-stabilization. In the case of the viscous (3.75) and (pseudo-) reactive (3.74) ghost penalty a value of $\gamma_\nu = 0.05$ and $\gamma_\sigma = 0.005$ is prescribed, respectively. The second order terms of the ghost penalties (i.e. for $j = 2$ in the equations (3.74), (3.75) and (3.78) and $j = 1$ in (3.76) and (3.77)) are scaled by 0.05 in comparison to the first order terms, as without this scaling too strong enforcement of these terms were observed, ruining the solution. Higher order terms of the ghost penalties, i.e. $j > 2$, are neglected in the following, as their influence on the solution and stability is negligible for linear and quadratic elements. Note that for simulations with higher-order approximations, i.e. $k > 1$, the simplified variant $\overline{g}_\beta$ (3.81) for the convective and divergence ghost penalty terms g_β, g_u (see (3.76) and (3.77)) and $\overline{s}_\beta$ (3.80) for the related continuous interior penalty stabilizations s_β, s_u (see (3.70) and (3.71)) are used.

The different flow regimes appearing in $\phi_u, \phi_\beta, \phi_p$ (see (3.65) and (3.79)) are weighted as $\nu + c_u(\|\boldsymbol{\beta}\|_{0,\infty,T}h) + c_\sigma(\sigma h^2)$, where the constants are given as $c_u = 1/6$ and $c_\sigma = 1/12$ as suggested in Schott *et al.* [230]. If nothing else is mentioned, then the simulations are conducted with an adjoint-consistent Nitsche's method (i.e. $\zeta_u = 1$) and with penalty parameters of $1/\gamma^n = 1/\gamma^t = 10.0$. As there is a need to integrate cut elements of non-regular shapes, standard integration rules can not be applied. To overcome this issue, the integration rules proposed by Sudhakar *et al.* [254] are used.

All simulations presented in this publication have been performed using the parallel finite element software environment "Bavarian Advanced Computational Initiative" (BACI), see the technical report by Wall *et al.* [277].

3.3.7.1 Problem Setup – 2D Box Flow

The following numerical example is inspired from the example done for Stokes flow by Urquiza *et al.* [267], but made more complex as in the aforementioned publication a second order velocity solution could depict the analytic solution. In addition the pressure was chosen as a constant zero field, which can lead to super convergent behavior of the pressure. In the following, the technique of manufactured solutions will be used to create the example. A criteria on the choice of a suitable velocity field is that it needs to be divergence-free ($\nabla \cdot \boldsymbol{u} = 0$), additionally to this a pressure field is chosen and when put into the Oseen equations with $\boldsymbol{\beta} = \boldsymbol{u}$, they generate an associated volumetric body force $\boldsymbol{f}$. By imposing appropriate boundary conditions

and providing an appropriate volumetric body force, the solution is known and error studies can be conducted for the example. The domain Ω used here is a square $\{(x, y), -1 < x < 1, -1 < y < 1\}$ and the solution of the velocity $\boldsymbol{u} = (u_1, u_2)$ and pressure p are chosen as

$$u_1(x, y) = 0.75y^3(1 - x^4) + 1.25y(1 - x^2), \tag{3.250}$$
$$u_2(x, y) = -0.75x^3(1 - y^4) - 1.25x(1 - y^2), \tag{3.251}$$
$$p(x, y) = \left(\sum_{i=0}^{2} \frac{(3x)^{2i+1}}{(2i+1)!}\right)\left(\sum_{j=0}^{3} \frac{(3y)^{2j}}{(2j)!}\right), \tag{3.252}$$

and visualized in Figure 3.6 The geometry here is chosen such that there is no geometric approximation error by the meshes, this avoids issues stemming from the Babuška paradox [12]. Issues arising when geometric approximation errors are present will be investigated in Chapter 4.

From simple derivation, it can be seen that the analytical velocity field ($\boldsymbol{u} = (u_1, u_2)$) is divergence-free. The volume force field $\boldsymbol{f}$ is chosen such that from the chosen fields (3.250)–(3.252), the Oseen equations (3.34)–(3.35) are still satisfied. This gives the following volume force field $\boldsymbol{f} = (f_1, f_2)$,

$$\begin{aligned}
f_1 =& -\nu\left(-9.0x^2y^3 + 4.5y\left(-x^4+1\right) - 2.5y\right) \\
&+ \sigma\left(0.75y^3\left(-x^4+1\right) + 1.25y\left(-x^2+1\right)\right) \\
&+ \left(-3.0x^3y^3 - 2.5xy\right)\left(0.75y^3\left(-x^4+1\right) + 1.25y\left(-x^2+1\right)\right) \\
&+ \left(-0.75x^3\left(-y^4+1\right) - 1.25x\left(-y^2+1\right)\right)\left(-1.25x^2 + 2.25y^2\left(-x^4+1\right) + 1.25\right) \\
&+ \left(\sum_{i=0}^{2} \frac{(3x)^{2i}}{(2i)!}\right)\left(\sum_{j=0}^{3} \frac{(3y)^{2j}}{(2j)!}\right) \\
f_2 =& -\nu\left(9.0x^3y^2 - 4.5x\left(-y^4+1\right) + 2.5x\right) \\
&+ \sigma\left(-0.75x^3\left(-y^4+1\right) - 1.25x\left(-y^2+1\right)\right) \\
&+ \left(3.0x^3y^3 + 2.5xy\right)\left(-0.75x^3\left(-y^4+1\right) - 1.25x\left(-y^2+1\right)\right) \\
&+ \left(0.75y^3\left(-x^4+1\right) + 1.25y\left(-x^2+1\right)\right)\left(-2.25x^2\left(-y^4+1\right) + 1.25y^2 - 1.25\right) \\
&+ \left(\sum_{i=0}^{2} \frac{(3x)^{2i+1}}{(2i+1)!}\right)\left(\sum_{j=1}^{3} \frac{(3y)^{2j-1}}{(2j-1)!}\right).
\end{aligned} \tag{3.253}$$

When the discrete case is considered, a nodal interpolation of the continuous counterpart is used for the force field $\boldsymbol{f}_h$ and the advective velocity $\boldsymbol{\beta}_h$. This interpolation can lead to the effect that the discrete advective field $\boldsymbol{\beta}_h$ is not pointwise divergence-free anymore. This type of discrepancy has been reported by Massing *et al.* [184] and Burman and Fernández [54] to cause deteriorating pressure L^2-error convergence for large reactive terms σ. Furthermore, if a non-viscous dominated case is to be considered, the reactive term σ is required to be large enough to guarantee coercivity. If a too small σ is chosen, it can lead to convergence issues. In the following numerical example, the flow is viscous dominated, and hence, no convergence issues of this form were observed.

The boundary conditions applied on the boundary Γ is the general Navier boundary for the Oseen problem, as given in (3.36)–(3.37). For the boundary terms, the prescribed velocity is set

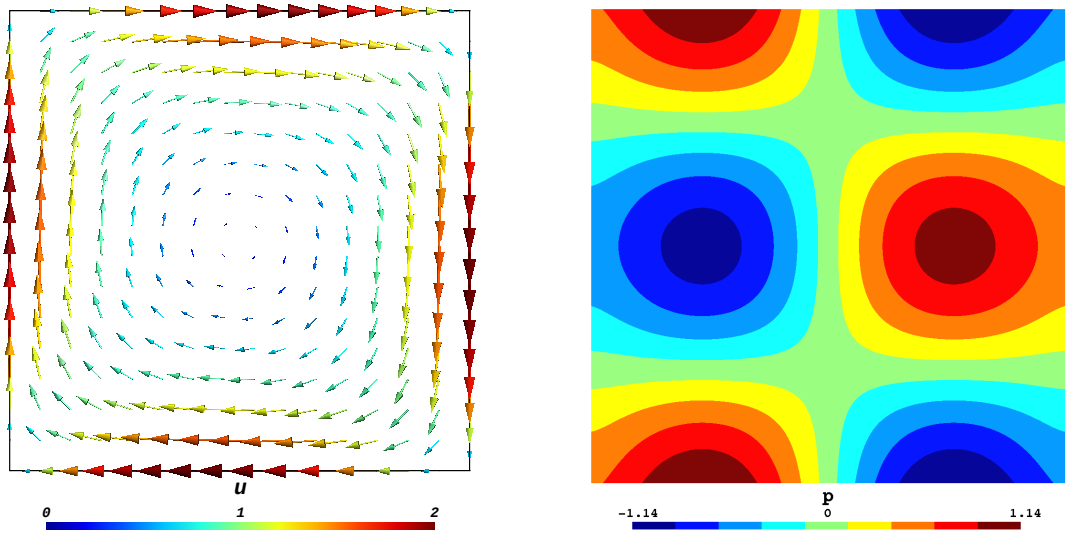

Figure 3.6: The analytic velocity (left) and pressure (right) solution to the two-dimensional box-flow problem. The figures are taken from Winter *et al.* [279].

as the analytic velocity, i.e. $\boldsymbol{g} = \boldsymbol{u}$, and the prescribed traction is calculated from the analytic velocity as $\boldsymbol{h} = 2\nu\boldsymbol{\epsilon}(\boldsymbol{u})$. With this choice of $\boldsymbol{g}$ and $\boldsymbol{h}$, the solution of the system of equations is independent of the choice of the slip length ε. An important observation is the fact that $\boldsymbol{u}\boldsymbol{P}^n = \boldsymbol{0}$ on Γ, which adheres to the assumptions from the analysis. The imposition of the boundary condition on Γ is done by means of the method (3.83), as introduced in Section 3.3.3.2.

In the following simulations, a background mesh $\widehat{\mathcal{T}}_h$ is chosen which covers a rectangular domain $[-1.6, 1.6]^2$. This background mesh is, if nothing else is mentioned, rotated by the angle $\theta = 0.25\pi$ around the origin to ensure a non-trivial computational mesh $\mathcal{T}_h$, see Figure 3.7. It consists of a partition of equally sized triangles with mesh size $h = 3.2/N$, where h denotes the short length of the triangles. The triangle elements will either be linear $\mathbb{P}^1$ or quadratic $\mathbb{P}^2$ equal order approximations for velocity and pressure, i.e. $\mathcal{V}_h^k \times \mathcal{Q}_h^k$ where $k \in \{1, 2\}$. This choice of elements stands in contrast with the publication Winter *et al.* [279], where bi-linear $\mathbb{Q}^1$ or bi-quadratic $\mathbb{Q}^2$ elements were chosen for the numerical analysis.

The parameters for the Oseen problem are chosen for this example as $\nu = 1.0$ and $\sigma = 1.0$. This choice of parameters leads to a viscous-dominated problem. If one is interested in the non-viscous case, that is for small ν, the tangential components will disappear from the formulation, as these scale with ν, and hence, the same formulation as presented and studied in Massing *et al.* [184] is retained. Owing to this fact, this numerical study will be focused on investigating viscous flow. Given the absence of Neumann boundaries for this setup, the pressure is only defined up to a constant. To filter out the constant pressure mode, the additional condition that $\int_\Omega p_h dx = 0$ is imposed during the solution process.

3.3.7.2 Mesh Refinement Study

To corroborate the results from the *a priori* error analysis, a mesh refinement study is undertaken for both linear and quadratic elements. For the linear elements $\mathbb{P}^1$, a series of mesh sizes are

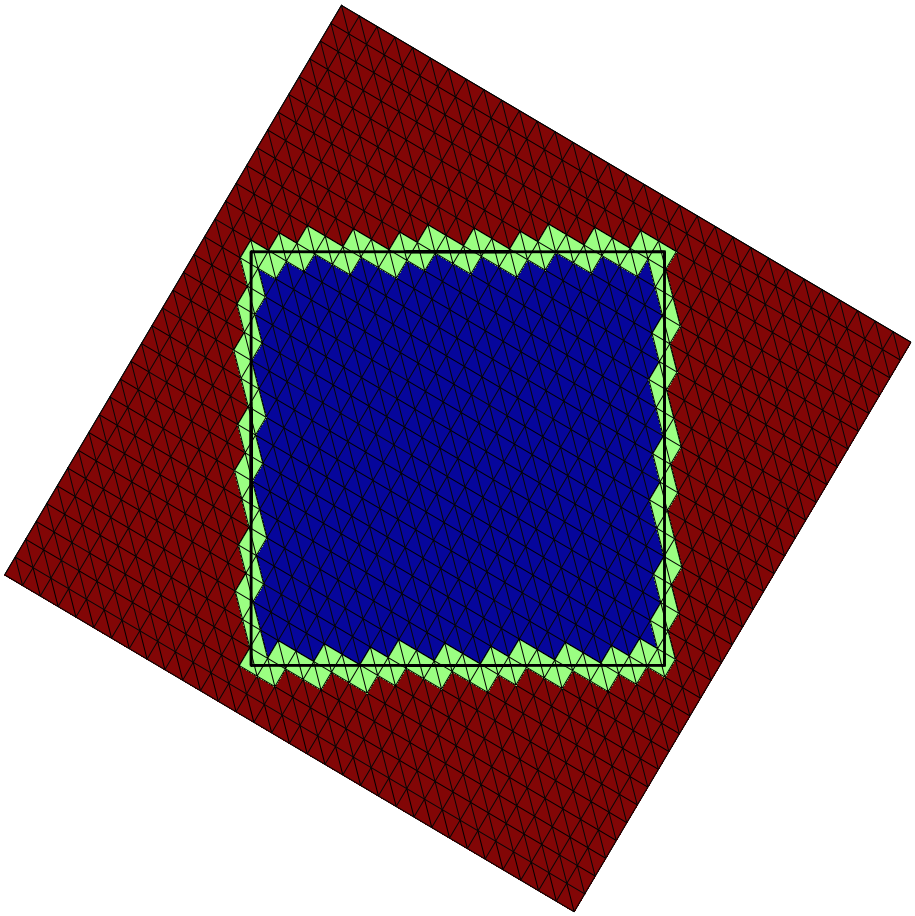

Figure 3.7: This figure shows the background mesh $\widehat{\mathcal{T}}_h$ rotated at 0.17 radians. The active computational mesh $\mathcal{T}_h$ is covered by the green and blue domains. In the green domain, the elements are cut and ghost penalties are applied on their facets. The red domain indicates the inactive part of the background mesh.

chosen with $N \in [8; 512]$, whereas for the quadratic $\mathbb{P}^2$ elements $N \in [8; 256]$ is chosen. The robustness of the proposed method is demonstrated by undertaking the convergence study for a choice of three different slip lengths, $\varepsilon \in [10^{-10}; 1.0; 10^{10}]$.

The L^2-errors of $\boldsymbol{u}_h$, $\nabla \boldsymbol{u}_h$ and p_h are presented in Figure 3.8 for the linear $\mathbb{P}^1$ approximations evaluated in Ω and on Γ. From the convergence plots, it can be verified that the optimal convergence $\mathcal{O}(h^2)$ for the velocity L^2-error is retained, as predicted in Theorem 3.16, irregardless of the choice of ε. The pressure error in the domain converges faster than the predicted $\mathcal{O}(h)$ from theory (see Theorem 3.15), however, on the boundary the predicted order of $\mathcal{O}(h)$ can be observed. Consequently, the enhanced convergence of the pressure in the domain can be suspected to stem from the fact that it has not yet reached the asymptotic region. Finally, the velocity gradient error behaves as expected, with a first order convergence, as predicted from theory. Additionally, the recorded errors remain of comparable size throughout the mesh refinement for the different choices of slip lengths.

The same error norms used in the linear case are employed as well for the quadratic $\mathbb{P}^2$ elements case, of which the results can be seen in Figure 3.9. The results demonstrate the expected behavior, and similar conclusions can be drawn as in the case for linear elements. For

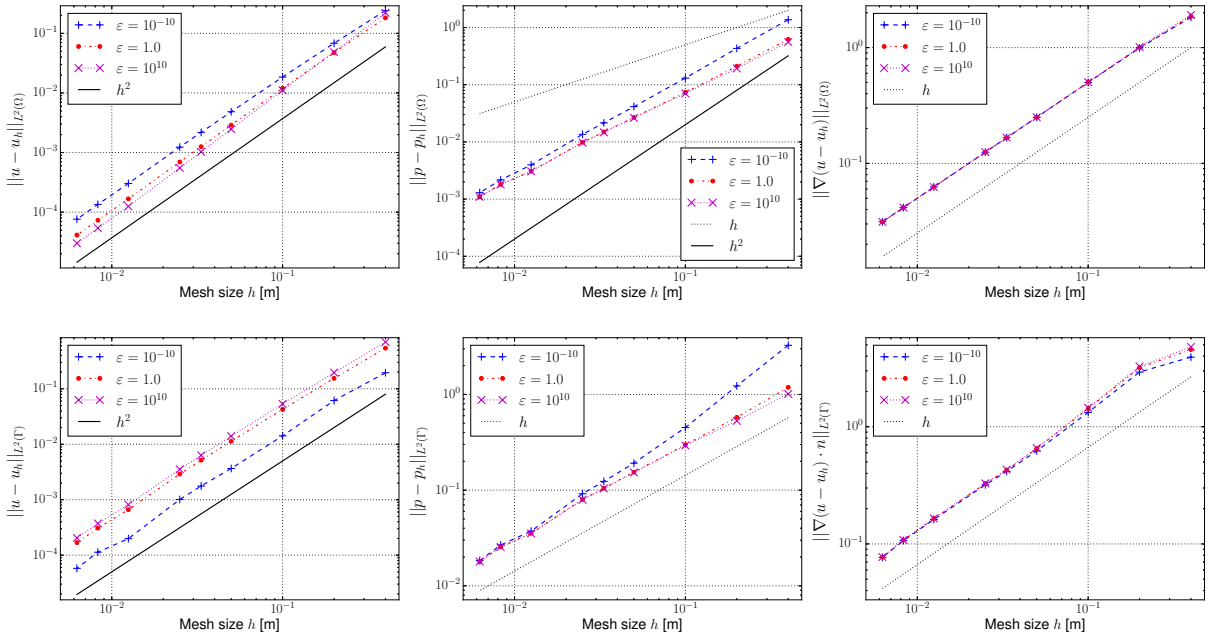

Figure 3.8: Error convergence study for an adjoint-consistent Nitsche's method with $\mathbb{P}^1$ elements: bulk errors (top row) and boundary errors (bottom row) for velocity, pressure and velocity gradient (from left to right).

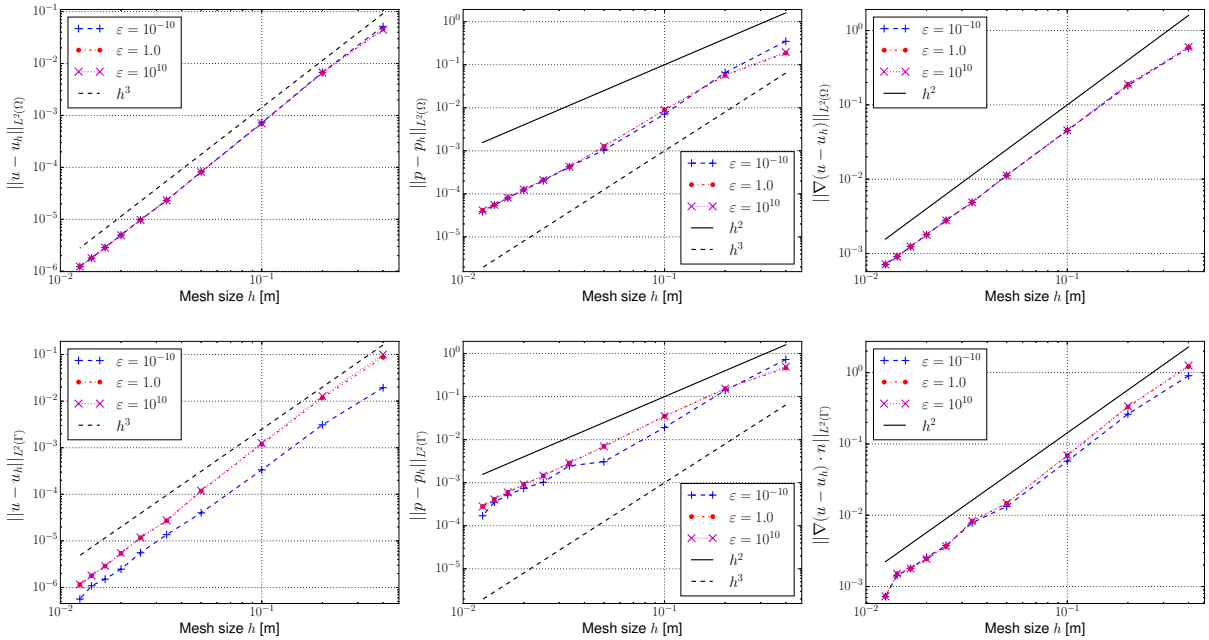

Figure 3.9: Error convergence study for an adjoint-consistent Nitsche's method with $\mathbb{P}^2$ elements: bulk errors (top row) and boundary errors (bottom row) for velocity, pressure and velocity gradient (from left to right).

the velocity L^2-error optimal convergence $\mathcal{O}(h^3)$ is observed, and for the pressure and velocity gradient at least $\mathcal{O}(h^2)$ order of convergence is retained. Moreover, this convergence is observed irregardless of the choice of ε.

3.3.7.3 Nitsche Stabilization Parameter Study

As the Nitsche parameter has a large effect on the stability of the proposed method, a sensitivity study is carried out to investigate how the solution behaves for different choices of the parameter. In the following, the sensitivity study is conducted for an adjoint-consistent formulation with linear $\mathbb{P}^1$ elements, whereas for the adjoint-inconsistent configuration, both linear $\mathbb{P}^1$ and quadratic $\mathbb{P}^2$ elements are investigated. A fixed mesh size is used for this sensitivity study, and the finest grid size is employed here, i.e. $N = 512$ for the linear elements and $N = 256$. In the analysis the normal γ^n and tangential γ^t stabilization parameters were introduced as distinct separate entities. In the following sensitivity study, however, they are varied at the same time and the stabilization parameter is chosen as, $\gamma = \gamma^t = \gamma^n$. The study is carried out, as was also done in the mesh convergence case, with a choice of three different slip lengths $\varepsilon = \{10^{-10}; 1.0; 10^{10}\}$.

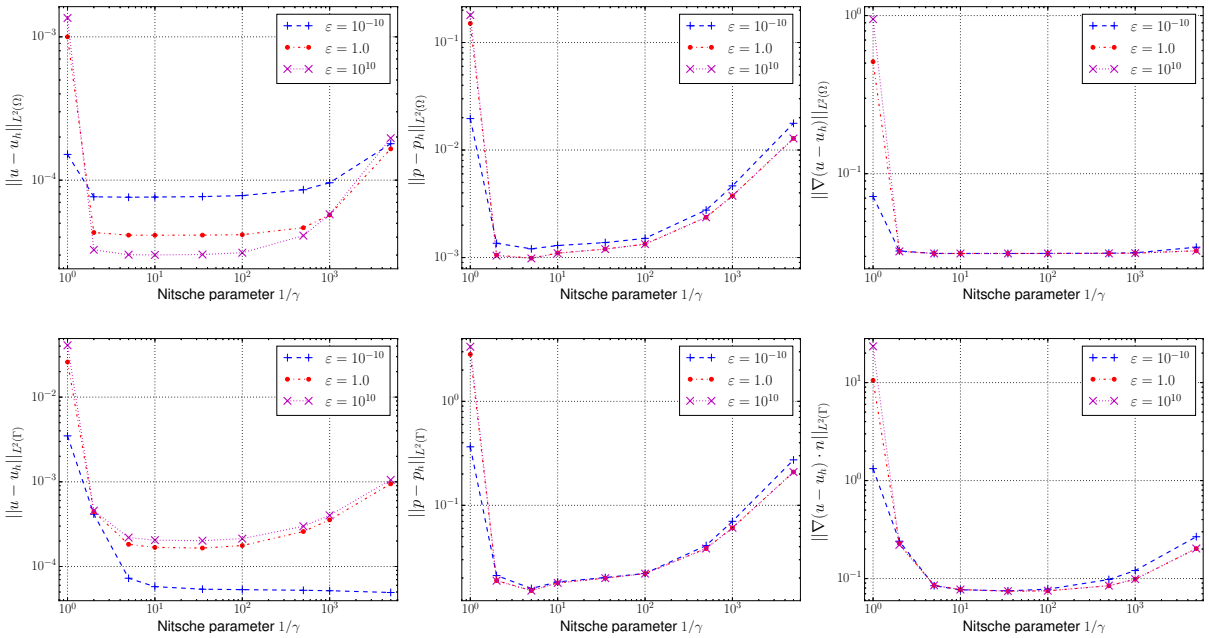

Figure 3.10: Nitsche stabilization parameter sensitivity study for an adjoint-consistent Nitsche's method with $\mathbb{P}^1$ elements: bulk errors (top row) and boundary errors (bottom row) for velocity, pressure and velocity gradient (from left to right).

The sensitivity study for the adjoint-consistent formulation ($\zeta_u = 1$) is demonstrated in Figure 3.10. As is expected, given the results from the inf-sup stability analysis in Section 3.3.5, the error diverges as $1/\gamma$ becomes too small. In the case for linear triangular elements and this problem setup, the stability limit can be said to be reached around $1/\gamma \approx 1.0$. This stands in good agreement to the results observed in Winter *et al.* [279], where for bi-linear quadratic elements a limit of $1/\gamma \approx 4.0$ was observed. Another interesting observation is the different behavior of the velocity error at the interface for different choices of ε. For all the norms and slip lengths, the error increases when the Nitsche parameter $1/\gamma$ increases, except in the case of the velocity interface error for the choice of $\varepsilon = 10^{-10}$. This peculiarity can be explained from the fact that in the case of larger slip lengths when the penalty $1/\gamma$ increases, the normal condition is enforced more strongly than the tangential condition. This can be motivated from taking a look

at the $\varepsilon \to \infty$ limit demonstrated in (3.32). A larger choice of $1/\gamma$ will thus lead to a smaller contribution of the tangential term, and hence, as the normal penalty term becomes larger, it starts to dominate. By contrast, when the slip length is small, the velocity boundary condition is imposed in both the normal and tangential direction, and consequently, the boundary condition of the velocity will become more strongly enforced with increasing $1/\gamma$. However, this only holds true for the velocity at the boundary, the gradient and pressure are both effected negatively from an increased Nitsche penalty parameter.

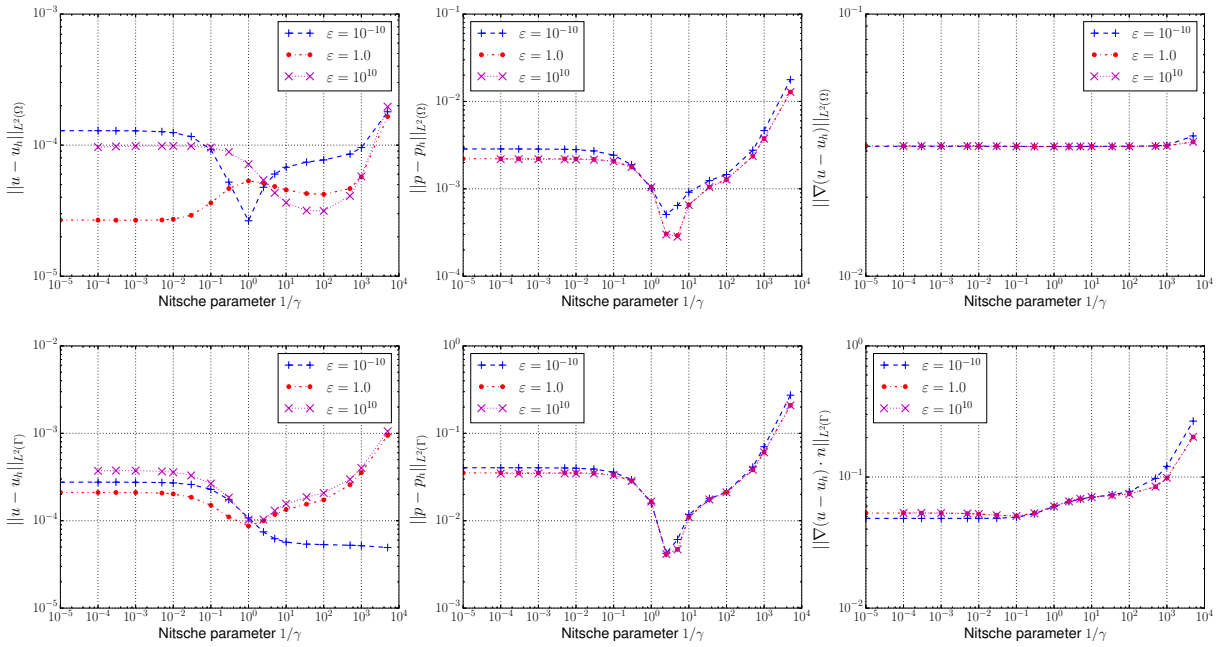

Figure 3.11: Nitsche stabilization parameter sensitivity study for an adjoint-inconsistent Nitsche's method with $\mathbb{P}^1$ elements: bulk errors (top row) and boundary errors (bottom row) for velocity, pressure and velocity gradient (from left to right).

As it was verified in the previous paragraph, the adjoint-consistent ($\zeta_u = 1$) formulation has stability issues when the Nitsche penalty parameter $1/\gamma$ becomes small. From the stability analysis, the adjoint-inconsistent ($\zeta_u = -1$) formulation enjoys a much larger stability region ($0 < 1/\gamma < \infty$) for the Nitsche penalty parameter. However, as was demonstrated in (3.33), the combination of a small $1/\gamma^t$ and a large ε leads to conditioning issues. These properties of the proposed formulation can be seen in Figure 3.11 for linear elements and in Figure 3.12 for quadratic elements. As when a slip length of $\varepsilon = 10^{10}$ is considered, it is noticeable that for both linear and quadratic elements, the employed linear solver does not converge, and hence no solution is obtained. This occurs for both the linear and quadratic case at $1/\gamma < 10^{-4}$. For other choices of slip length, i.e. $\varepsilon = 1.0$ or $\varepsilon = 10^{-10}$, the error remains stable also for smaller choices of $1/\gamma$, corroborating the results from theory which states that $1/\gamma > 0$ is a sufficient choice for stability. A difference between the linear and the quadratic case, is that in the quadratic case the error remains stable longer before a large stabilization parameter $1/\gamma$ effects the attained solution negatively.

In the publication by Winter *et al.* [279] a clear minimum was found for the bi-linear $\mathbb{Q}^1$ and bi-quadratic $\mathbb{Q}^2$ elements for the choice of $1/\gamma \approx 10$. In the case with linear $\mathbb{P}^1$ and quadratic $\mathbb{P}^2$

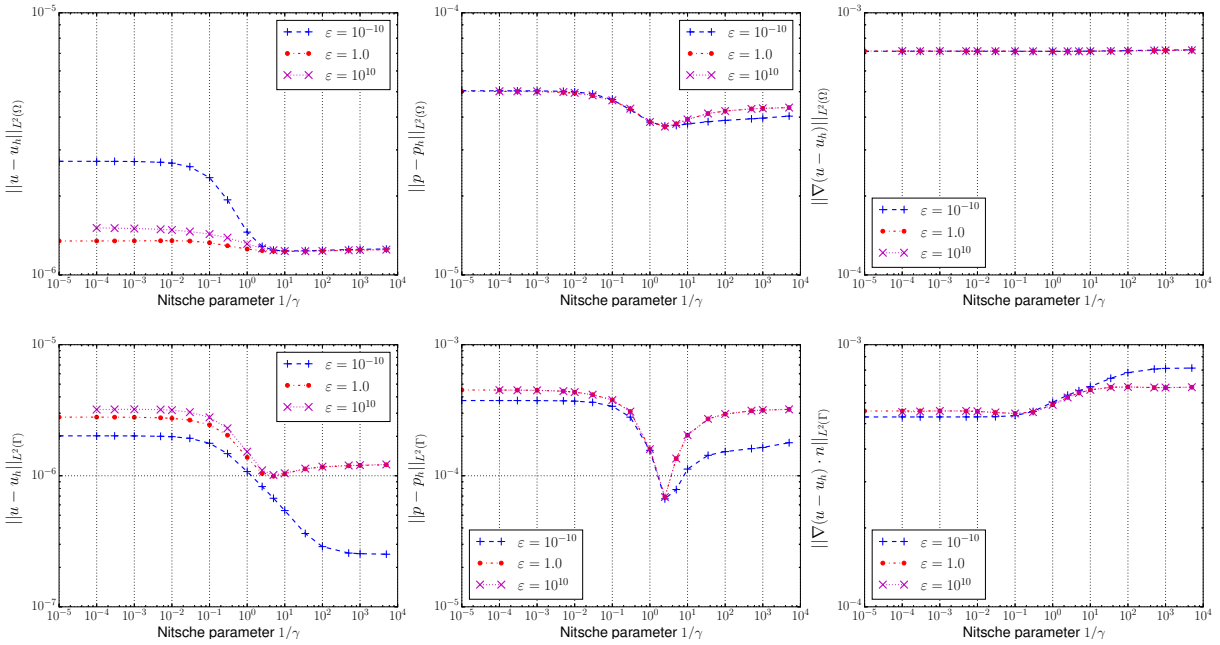

Figure 3.12: Nitsche stabilization parameter sensitivity study for an adjoint-inconsistent Nitsche's method with $\mathbb{P}^2$ elements: bulk errors (top row) and boundary errors (bottom row) for velocity, pressure and velocity gradient (from left to right).

elements, a clear minimum is not as easily established. For the adjoint-inconsistent formulation a minimum in the pressure error is retained for $1/\gamma \approx 3.0$. However, for the adjoint-consistent case a more sensible choice would seem to be around $1/\gamma \approx 10.0$. Nevertheless, the proposed range in [279] and Schott and Wall [229] of $1/\gamma \in (10, 50)$ is assessed from the results here to still be a reasonable choice for the Nitsche penalty parameter.

3.3.7.4 Slip Length Sensitivity Study

As was discussed in Section 3.2.5, conditioning issues of the discretized system occurs for small ε. To demonstrate the robustness of the proposed method, errors are evaluated for a fixed background mesh, consisting of $\mathbb{P}^1$ elements, and the slip length is varied in a series of $\varepsilon \in [10^{-10}, 10^{10}]$ and compared to the substitution method of imposing the general Navier condition. As can be seen in Figure 3.13, when the imposition is done with the Nitsche's method the error remains bounded and approaches an asymptotic value once either the Dirichlet or Neumann dominated region is reached. This is not the case for the substitution method as it is evident from Figure 3.13 that no asymptotic value is approached in the Dirichlet limit ($\varepsilon \to 0$), which is predicted in the numerical analysis. This divergent substitution method starts producing noticeably larger errors at around $\varepsilon < 10^{-5}$, which is in good agreement with what was observed for bi-linear elements in Winter *et al.* [279]. As the slip length is decreased furthermore the error grows consecutively worse until the chosen linear solver cannot solve the system of equations for $\varepsilon < 10^{-7}$. Also notable is the fact that for large slip lengths, i.e. $\varepsilon \to \infty$, the errors between the two methods are of comparable size, and hence, the additional terms in (3.32) do not deteriorate the error.

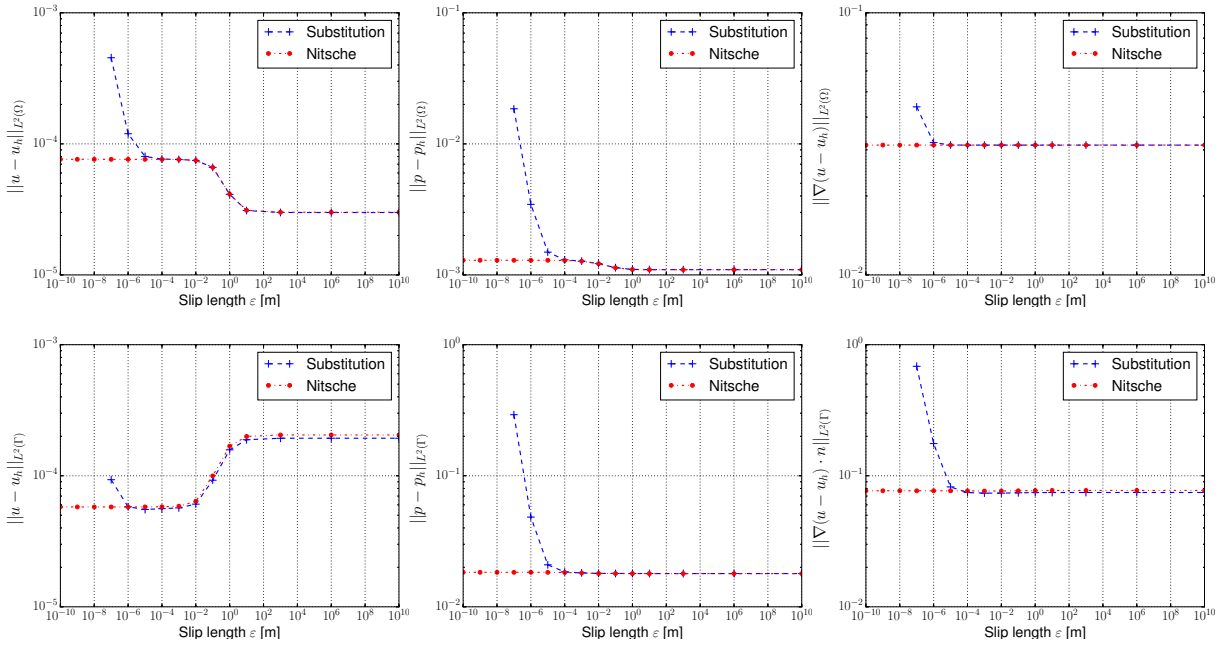

Figure 3.13: Slip length parameter study for an adjoint-consistent Nitsche's method with $\mathbb{P}^1$ elements: bulk errors (top row) and boundary errors (bottom row) for velocity, pressure and velocity gradient (from left to right).

3.3.7.5 Rotation of Background Mesh Sensitivity Study

As a cut finite element method is utilized, i.e. an unfitted mesh approach is pursued, an important measure to investigate is how sensitive the solution is to perturbations of the mesh. To examine this, the rotation of the mesh is here varied for $\theta \in [0, 0.5\pi]$. In Figure 3.14, the sensitivity of a mesh with $N = 512$ is analyzed for different degrees of rotation. First thing to note is that for a rotation of $\theta = 0$ and $\theta = 0.5\pi$ the error is the same, as these configurations are identical. Another important observation is that even though the error can differ between different rotations of the mesh, in the end all errors are bounded and only vary slightly. This stems from the stabilizing effect of the ghost penalties. That some variations in the errors from the rotations are expected is clear from the fact that the computational mesh $\mathcal{T}_h$ will change in size for different rotations. This will lead to different amounts of faces which need to be stabilized with the ghost penalties. As a consequence, the contribution of these terms will change depending on the configuration, and this will slightly so change the size of the contribution these terms have in the discretized system of equations. Moreover, the approximation space can also end up in a more or less advantageous position, depending at what angle the background mesh is. For instance the mesh might be cut in a more or less beneficial way of handling corners, and hence variations in the observed error can also be explained in part from this.

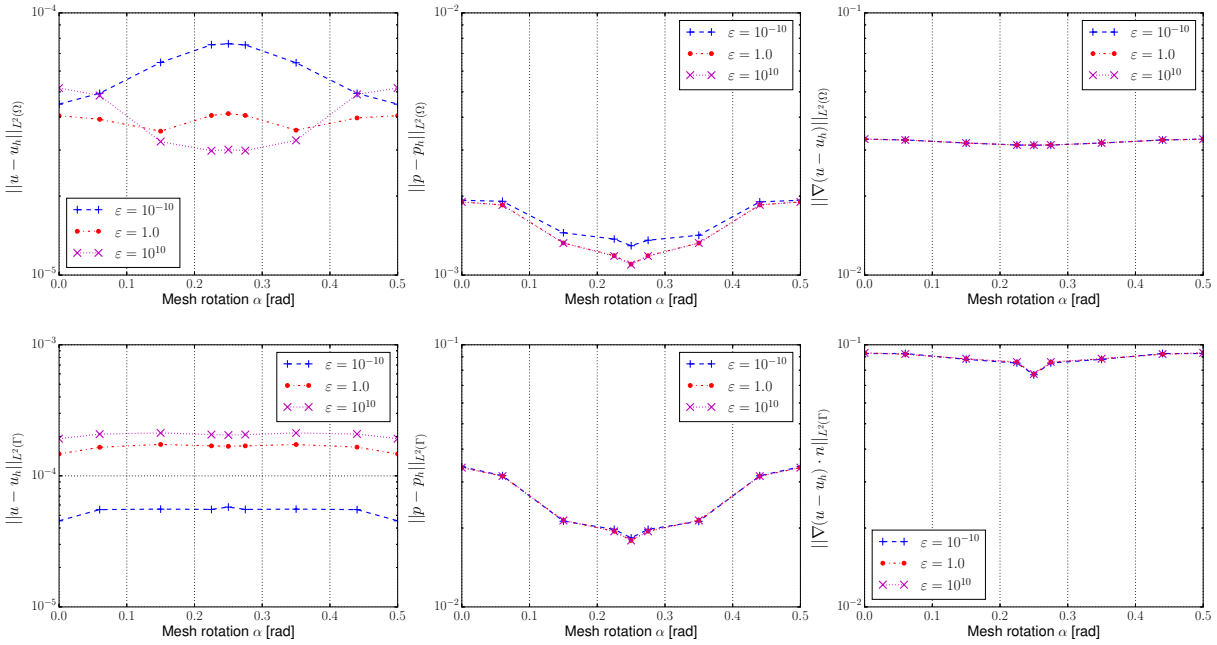

Figure 3.14: Sensitivity study on the rotation of the background mesh for an adjoint-consistent Nitsche's method with $\mathbb{P}^1$ elements: bulk errors (top row) and boundary errors (bottom row) for velocity, pressure and velocity gradient (from left to right).

Chapter 4

The General Navier Boundary Condition on Approximated Geometries

In the previous Chapter 3, a thorough analysis of the formulation for the Navier–Stokes equation and a mathematical analysis for its linearized form were conducted. Nonetheless, throughout the aforementioned chapter, an assumption on the absence of variational crimes was made. A variational crime can be summed up by the simple fact that the discrete functional space $\mathcal{W}_h$ is not necessarily a subset of the continuous functional space $\mathcal{W}$, i.e. $\mathcal{W}_h \nsubseteq \mathcal{W}$. In the textbooks by Strang and Fix [249] and Brenner and Scott [45], three types of variational crimes are identified:

a) The fact that the integrals of the weak form are only evaluated approximately by numerical quadrature.

b) The approximated domain Ω_h does not coincide with the physical domain Ω. This is for instance the case when a non-polygonal domain is approximated by a polygonal one.

c) Non-conforming elements are employed for the discretization. An example of this is the use of elements for the Stokes or Navier–Stokes equations, which do not satisfy C^0 continuity.

This chapter will be dealing with the presence of the case b), i.e. when a geometrical error exists and the domains Ω and Ω_h do not coincide. This case always occurs in a sense with the way the CutFEM is utilized in this thesis, as the domain Ω is approximated by a piecewise linear approximation. For the general Navier boundary condition, the geometrical approximation error takes shape in two distinct forms.

First, the choice of the discretized normal vector $\boldsymbol{n}_h$ on the boundary Γ_h influences the solution. If a piecewise constant normal $\boldsymbol{n}_h$ is chosen, which arises as a natural choice for a polygonal domain, convergence errors become apparent. This issue of convergence is normally attributed to the so-called *Babuška paradox*, described first in the publication by Babuška [12]. The implications of the Babuška paradox are investigated in Section 4.1 in the frame of a CutFEM. Section 4.1 also introduces a creation of a smoothed normal field by means of a level-set function. This smoothing is demonstrated to have a detrimental effect on the convergence of the solution. Moreover, the quality of the approximate normal vector on the boundary Γ_h is related

to the quality of the solution, and it is postulated that the normal needs to converge with at least the same order as the velocity if optimal order of convergence is to be achieved.

Second, the fact that the approximated domain Ω_h and physical domain Ω do not coincide, also implies that the approximated boundary Γ_h and physical boundary Γ do neither. This begs the question, what boundary condition is to be enforced on Γ_h to guarantee that the solution in Ω_h converges with the desired order to the physical one? A solution to this problem was suggested by Bramble *et al.* [42], where they used Taylor expansions to connect the condition on Γ_h with Γ. In their publication, they demonstrated the improved effect in the context of a Poisson equation on a fitted mesh. Recently, this idea was applied to the CutFEM by Burman *et al.* [66], also for the Poisson equation. Based on the aforementioned works, in Section 4.2 a novel approach for imposing a GNBC with the CutFEM for second order elements, retaining optimal order of convergence, is presented. Given that the GNBC contains a standard Dirichlet condition, in the case of $\varepsilon = 0$, the proposed formulation is also valid for this simpler case as well.

In contrast to the thorough mathematical analysis of the Oseen equation in Section 3.3, this chapter will be dealing primarily with the Navier–Stokes equations. Hence, heuristic arguments will be made and motivated by numerical examples with accompanying convergence studies, which is done without diving too deep into the mathematical intricacies.

4.1 Geometrical Error Introduced by an Approximated Normal Vector

In this section, it will be assumed that the only geometrical approximation error stems from the normal approximation, i.e. $\boldsymbol{n}_h \neq \boldsymbol{n}$. Or that at least the geometrical error stemming from the non-coinciding domains $\Omega_h \neq \Omega$, converges with sufficient order to not affect the order of convergence for bi-linear $\mathbb{Q}^1$ elements.

The discrete formulation for the Navier–Stokes equations with a general Navier boundary condition was presented in (3.15), and is reproduced here for the convenience of the reader. On the domain Ω_h with the boundary $\Gamma_h = \Gamma_{\mathrm{G},h} \cup \Gamma_{\mathrm{N},h}$, find $U_h = (\boldsymbol{u}_h, p_h) \in \mathcal{W}_h$ such that for all $V_h = (\boldsymbol{v}_h, q_h) \in \mathcal{W}_h$

$$\mathcal{A}_h(U_h, V_h) + \mathcal{S}_h^*(U_h, V_h) + \mathcal{G}_h(U_h, V_h) + \mathcal{N}_h(U_h, V_h) = \mathcal{L}_h(V_h) + \mathcal{L}_h^{\mathcal{N}}(V_h) \tag{4.1}$$

where

$$\begin{aligned}
\mathcal{A}_h(U_h, V_h) =& (\rho \frac{\partial \boldsymbol{u}_h}{\partial t}, \boldsymbol{v}_h)_{\Omega_h} + (2\mu\boldsymbol{\epsilon}(\boldsymbol{u}_h), \boldsymbol{\epsilon}(\boldsymbol{v}_h))_{\Omega_h} + (\rho(\boldsymbol{u}_h \cdot \nabla)\boldsymbol{u}_h, \boldsymbol{v}_h)_{\Omega_h} \\
&- \langle(-p_h\boldsymbol{I} + 2\mu\boldsymbol{\epsilon}(\boldsymbol{u}_h)) \cdot \boldsymbol{n}_h, \boldsymbol{v}_h\rangle_{\Gamma_h} \\
&- (p_h, \nabla \cdot \boldsymbol{v}_h)_{\Omega_h} + (q_h, \nabla \cdot \boldsymbol{u}_h)_{\Omega_h} && (4.2)\\
\mathcal{L}_h(V_h) =& (\boldsymbol{f}, \boldsymbol{v}_h)_{\Omega_h} && (4.3)\\
\mathcal{L}_h^{\mathcal{N}}(V_h) =& \mathcal{L}_h^{\Gamma_{\mathrm{N}}}(V_h) + \mathcal{L}_h^{\Gamma_{\mathrm{G}},n}(V_h) + \mathcal{L}_h^{\Gamma_{\mathrm{G}},t}(V_h) && (4.4)\\
\mathcal{N}_h(U_h, V_h) =& \mathcal{N}_h^{\Gamma_{\mathrm{N}}}(U_h, V_h) + \mathcal{N}_h^{\Gamma_{\mathrm{G}},n}(U_h, V_h) + \mathcal{N}_h^{\Gamma_{\mathrm{G}},t}(U_h, V_h) && (4.5)
\end{aligned}$$

with the stabilization terms $\mathcal{S}_h^*(U_h, V_h)$ and $\mathcal{G}_h(U_h, V_h)$ defined as in Section 2.1.3 and Section 2.3.2.2, respectively. The product space is defined as $\mathcal{W}_h = \mathcal{V}_h \times \mathcal{Q}_h$, and its constituent spaces are given as

$$\mathcal{V}_h := [\mathcal{X}_h]^d, \tag{4.6}$$

$$\mathcal{Q}_h := \begin{cases} \mathcal{X}_h & \text{if } \Gamma_{\mathrm{N}} \neq \emptyset \\ \mathcal{X}_h \cap L_0^2(\Omega_h) & \text{if } \Gamma_{\mathrm{N}} = \emptyset. \end{cases} \tag{4.7}$$

The shape function space $\mathcal{X}_h$ is defined as in (2.20) as

$$\mathcal{X}_h = \left\{ v_h \in C^0(\Omega_h) : v_h|_T \in \mathbb{V}^k(T) \; \forall \; T \in \mathcal{T}_h \right\}, \tag{4.8}$$

where $\mathbb{V}^k(T)$ is a polynomial functions space on the element T in the active mesh $\mathcal{T}_h$. In this chapter $\mathbb{V}^k(T)$ will be chosen as rectangular $\mathbb{Q}^1$ or $\mathbb{Q}^2$ elements. The boundary terms are defined as

$$\mathcal{N}_h^{\Gamma_{\mathrm{N}}}(U_h, V_h) - \mathcal{L}_h^{\Gamma_{\mathrm{N}}}(V_h) = \langle (-p_h \boldsymbol{I} + 2\mu\boldsymbol{\epsilon}(\boldsymbol{u}_h)) \cdot \boldsymbol{n}_h - \boldsymbol{h}, \boldsymbol{v}_h \rangle_{\Gamma_{\mathrm{N},h}}, \tag{4.9}$$

$$\begin{aligned} \mathcal{N}_h^{\Gamma_{\mathrm{G}},n}(U_h, V_h) - \mathcal{L}_h^{\Gamma_{\mathrm{G}},n}(V_h) =& \langle \frac{\rho\phi_u}{\gamma^n h} \mathcal{C}_{\Gamma_{\mathrm{G}}^n}(\boldsymbol{u}_h), \boldsymbol{v}_h \rangle_{\Gamma_{\mathrm{G},h}} \\ & - \langle \mathcal{C}_{\Gamma_{\mathrm{G}}^n}(\boldsymbol{u}_h), \zeta_u 2\mu\boldsymbol{\epsilon}(\boldsymbol{v}_h)\boldsymbol{n}_h + q_h \boldsymbol{n}_h \rangle_{\Gamma_{\mathrm{G},h}} \end{aligned} \tag{4.10}$$

$$\begin{aligned} \mathcal{N}_h^{\Gamma_{\mathrm{G}},t}(U_h, V_h) - \mathcal{L}_h^{\Gamma_{\mathrm{G}},t}(V_h) =& \langle \frac{1}{\varepsilon + \gamma^t h} \mathcal{C}_{\Gamma_{\mathrm{G}}^t}(\boldsymbol{u}_h), \boldsymbol{v}_h \rangle_{\Gamma_{\mathrm{G},h}} \\ & - \langle \frac{\gamma^t h}{\varepsilon + \gamma^t h} \mathcal{C}_{\Gamma_{\mathrm{G}}^t}(\boldsymbol{u}_h), \zeta_u 2\boldsymbol{\epsilon}(\boldsymbol{v}_h)\boldsymbol{n}_h \rangle_{\Gamma_{\mathrm{G},h}}, \end{aligned} \tag{4.11}$$

where the condition operators are defined as

$$\mathcal{C}_{\Gamma_{\mathrm{G}}^n}(\boldsymbol{u}_h) = (\boldsymbol{u}_h - \boldsymbol{g})\boldsymbol{P}^n \tag{4.12}$$

$$\mathcal{C}_{\Gamma_{\mathrm{G}}^t}(\boldsymbol{u}_h) = (\varepsilon(2\mu\boldsymbol{\epsilon}(\boldsymbol{u}_h)\boldsymbol{n}_h - \boldsymbol{h}) + \mu(\boldsymbol{u}_h - \boldsymbol{g}))\,\boldsymbol{P}^t. \tag{4.13}$$

The projection matrices are, if nothing else is mentioned, constructed as $\boldsymbol{P}^n = \boldsymbol{n}_h \otimes \boldsymbol{n}_h$ and $\boldsymbol{P}^t = \boldsymbol{I} - \boldsymbol{P}^n$.

In the case when Dirichlet conditions are imposed, i.e. $\varepsilon = 0$, the choice of a piecewise constant normal $\boldsymbol{n}_h$ on Γ_h does not introduce problems when imposing the boundary condition, as the normal does not appear in the condition $\boldsymbol{u} = \boldsymbol{g}$ on Γ_{D}. On the contrary, for a general Navier boundary condition, the split into a Dirichlet condition in normal direction and Robin condition in tangential direction introduces a dependency on the quality of approximation of the normal vector on the boundary. In Verfürth [270] it is shown that the Stokes equation with a Navier slip boundary condition, reduces in the two dimensional case to a simply supported plate with Poisson ratio zero,

$$\begin{aligned} \Delta^2 z &= \frac{\partial f_2}{\partial x} - \frac{\partial f_1}{\partial y} \text{ in } \Omega, \\ z &= \Delta z - \kappa \frac{\partial z}{\partial \boldsymbol{n}} \text{ on } \Gamma, \end{aligned} \tag{4.14}$$

where the velocity is given as $\boldsymbol{u} = \left(\frac{\partial z}{\partial y}, -\frac{\partial z}{\partial x}\right)^T$ and κ is the curvature of the boundary Γ, i.e. $\kappa = \nabla \cdot \boldsymbol{n}$. Now, as is highlighted in Liakos [180], when a polygonal domain is considered, the normal on the boundary is piecewise constant. This leads to a curvature which is piecewise zero, and consequently the equation (4.14) is not approximated correctly. This fact, is how the Babuška paradox [12] appears when general Navier boundary conditions are considered. An alternative view on this paradox is made apparent from Figure 4.1, where the creation of a normal and tangential space on a polygonal domain is depicted. Here it is clear that at the intersection between two boundary segments (in Figure 4.1 denoted as node **A**) the creation of an unique normal space $\boldsymbol{P}^n$ is not well-defined. For a strong imposition of the boundary, this begs the question, what normal vector to use to create the projection vectors $\boldsymbol{P}^n$ and $\boldsymbol{P}^t$ at the node **A**? To resolve this ambiguity in the choice of normal vector, Engelman *et al.* [106] proposed

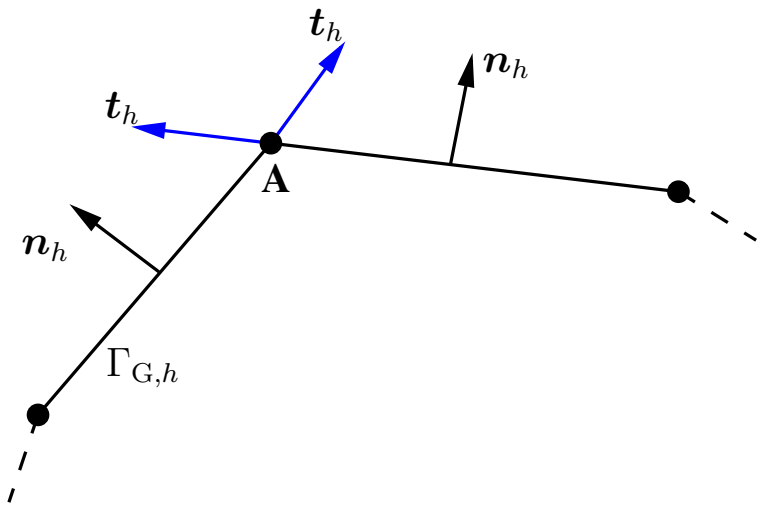

Figure 4.1: An illustration of the tangential $\boldsymbol{t}_h$ and normal $\boldsymbol{n}_h$ vectors at a node **A** on a polygonal boundary $\Gamma_{\mathrm{G},h}$. It is apparent that the normal and tangential spaces between the segments of the polygon are discontinuous, thus making the choice of projection space at **A** undefined.

a method to create normals at the nodes of the mesh which adhere to the conservation of mass equation in a weak sense, i.e. $\int_{\Gamma_h} \boldsymbol{u}_h \cdot \boldsymbol{n}_h d\Gamma_h = 0$. This method was later improved by Behr [30], where a different approach to creating the nodal vectors was proposed, resulting in smaller spurious currents for free surface flows in circular vessels.

Instead of imposing the boundary condition in a strong sense, a weak formulation can be pursued in its stead to overcome the Babuška paradox. The first attempts to do this was conducted with Lagrange multipliers. In Verfürth [272] this was done using Lagrange multipliers stabilized by enriching the velocity approximation space in the vicinity of the boundary, and in Verfürth [271] with Lagrange multipliers stabilized with residual boundary terms. The two aforementioned Lagrange multiplier approaches were compared in a recent publication by Urquiza *et al.* [267] to a Nitsche enforcement of the wall-normal no-penetration condition for the Stokes equation. This publication conducts convergence studies to verify the theoretical findings from the numerical analysis of these methods. In particular, the case with curved boundaries, and their approximation with polygonal domains is studied. Optimal order of convergence in the

usual norms were obtained for the stabilized Lagrange multiplier method with equal-order $\mathbb{P}^1$ elements and a $\mathbb{P}^0$ discontinuous Lagrange multiplier function space, whereas with Taylor–Hood ($\mathbb{P}^2/\mathbb{P}^1$) elements suboptimal convergence was obtained in the usual norms. In the case of the Nitsche's method, equal-order $\mathbb{P}^1$ elements with a small penalty parameters $1/\gamma^n$ gave the best results (i.e. convergence of order $\mathcal{O}(h)$ in the usual norms), whereas other combinations did not result in optimal convergence.

The results obtained in [267] for the Nitsche's method indicate a serious problem of convergence in the case of curved domains, as not only small penalty parameter values should lead to optimal order of convergence. Given that the wall-normal no-penetration boundary condition (4.12) is employed in this thesis in a similar fashion as in the aforementioned publication, the question arises if a practical solution to improve the convergence of the solution exists?

Proposition 4.1 *Starting with an obvious problem arising from using the normal $\boldsymbol{n}_h$ from an polygonal approximation of a curved domain, is the fact that it is piecewise constant. As indicated in Liakos [180], such a normal has zero divergence almost everywhere on the surface, and accordingly, no curvature in (4.14). A remedy to this, is to create a continuous normal field on the surface Γ_h. A possible way to do this, when the domain is defined implicitly by a level-set function, is to smooth the gradients $\nabla\phi_h$ of the underlying level-set field. The relation*

$$\boldsymbol{n} = \frac{\nabla\phi}{|\nabla\phi|} \tag{4.15}$$

can then be used to create a continuous normal field on Γ_h. One of the smoothing techniques introduced in Section 2.2.1.4, can be applied for this purpose.

Proposition 4.2 *Another indicator that the normal used for the projections $\boldsymbol{P}^n$ and $\boldsymbol{P}^t$ needs to be improved can be derived from the a priori error estimate in Theorem 3.15. The energy norm used there contains the terms $\|\boldsymbol{u}\cdot\boldsymbol{n}\|_\Gamma$. Now, if a perturbation is introduced in the normal for the discretized form, $\boldsymbol{n}_h$, the difference to the exact solution would be*

$$\begin{aligned}\|\boldsymbol{u}\cdot\boldsymbol{n} - \boldsymbol{u}_h\cdot\boldsymbol{n}_h\|_\Gamma &\leq \|\boldsymbol{u}\cdot\boldsymbol{n} - \boldsymbol{u}\cdot\boldsymbol{n}_h\|_\Gamma + \|\boldsymbol{u}\cdot\boldsymbol{n}_h - \boldsymbol{u}_h\cdot\boldsymbol{n}_h\|_\Gamma \\ &\leq \|\boldsymbol{u}\|_\Gamma\|\boldsymbol{n}-\boldsymbol{n}_h\|_\Gamma + \|(\boldsymbol{u}-\boldsymbol{u}_h)\cdot\boldsymbol{n}_h\|_\Gamma.\end{aligned} \tag{4.16}$$

Hence, from this heuristic derivation, it is clear that if an error in the normal is introduced, it would be expected that problems arise if $\|\boldsymbol{n}-\boldsymbol{n}_h\|_\Gamma$ does not converge with a sufficiently high order of convergence.

Given the above postulates on the properties of a smoothed/continuous normal vector $\widetilde{\boldsymbol{n}_h}$ on Γ_h, a study on the effectiveness of the normal smoothing is conducted. For this purpose a Taylor–Couette problem with general Navier boundary conditions is constructed in the following Section 4.1.1 and the comparison between a smoothed normal $\widetilde{\boldsymbol{n}_h}$ to the standard piecewise constant $\boldsymbol{n}_h$ is made.

The computations in the following are carried out with the formulation presented in (4.1). Modifications to this formulation are only due to the different projection matrices $\boldsymbol{P}^n$ and $\boldsymbol{P}^t$ employed in the condition operators $\mathscr{C}_{\Gamma_{\mathrm{G}}^n}$ and $\mathscr{C}_{\Gamma_{\mathrm{G}}^t}$ appearing in (4.10)– (4.11).

4.1.1 The Taylor–Couette Flow Problem with General Navier Boundaries

To analyze the effects of geometrical approximation errors, a suitable example needs to be construed. For this purpose, two-dimensional Taylor–Couette flow is chosen. As the physical domain Ω consists of the enclosed area between two circles, it has a convex outer interface and a concave inner boundary. For the piecewise linear approximation of this domain, this entails that close to the concave surface parts of Ω_h will lie outside of Ω and the other way around in the vicinity of the convex surface, thus covering both possible cases. The normal of the boundary Γ can be expressed by an analytic expression given that the boundaries of the physical domain are circles. Hence, the error of the normal compared to the approximated boundaries can be estimated. Moreover, the analytic solution of the flow is non-trivial and is, as such, suitable for convergence studies.

Given that this example forms the basis of the analysis for studying geometrical errors in this chapter, a derivation of the solution is made here to facilitate the understanding of the problem. Additionally, the Taylor–Couette flow is seldomly encountered with general Navier boundaries, hence the analytic solution might not be as readily available as in the case of Dirichlet boundaries.

The analytic solution to a two dimensional flow is given here for a flow between two rotating cylinders. As the flow is rotational, the solution will be construed in polar coordinates, i.e.

$$\boldsymbol{u} = (u_r, u_\theta)^T .$$

The flow is assumed to be axisymmetrical, hence $u_r = 0$ and $\frac{\partial u_\theta}{\partial \theta} = 0$. The domain Ω is confined by an inner cylinder with radius r_i and boundary Γ_i and an outer cylinder with radius r_o and boundary Γ_o, as demonstrated in Figure 4.2. Both the inner and outer cylinder are prescribed general Navier boundary conditions. However, it is assumed that $\varepsilon = \infty$ does not occur on Γ_i and Γ_o at the same time. This is to avoid ill-posed problems with full slip boundaries on an enclosed domain with symmetries. Given these assumptions, the following simplified system of equations of the Navier–Stokes equations are retained,

$$\rho \frac{u_\theta^2}{r} = \frac{\partial p}{\partial r}, \tag{4.17}$$

$$\frac{u_\theta}{r} = \frac{1}{r}\frac{\partial}{\partial r}\left(r \frac{\partial u_\theta}{\partial r}\right) \text{ in } \Omega. \tag{4.18}$$

From the geometry it can be deduced that $\boldsymbol{n}_{\Gamma_i} = -\boldsymbol{e}_r$ and $\boldsymbol{n}_{\Gamma_o} = \boldsymbol{e}_r$. The projection onto the tangential plane can be written as $\boldsymbol{P}^t = \boldsymbol{e}_\theta \otimes \boldsymbol{e}_\theta$. Where $\boldsymbol{e}_r$ and $\boldsymbol{e}_\theta$ are the unit vector in radial and in angular direction, respectively. The boundary condition of the outer cylinder is prescribed as

$$\begin{aligned} \varepsilon \left(\boldsymbol{\sigma} \cdot \boldsymbol{e}_r\right) \cdot \boldsymbol{e}_\theta + \mu u_\theta &= \mu g_{\theta,o} + \varepsilon h_{\theta,i} \\ u_r &= 0 \text{ on } \Gamma_o, \end{aligned} \tag{4.19}$$

and for the inner cylinder

$$\begin{aligned} \varepsilon \left(\boldsymbol{\sigma} \cdot (-\boldsymbol{e}_r)\right) \cdot \boldsymbol{e}_\theta + \mu u_\theta &= \mu g_{\theta,i} + \varepsilon h_{\theta,o} \\ u_r &= 0 \text{ on } \Gamma_i. \end{aligned} \tag{4.20}$$

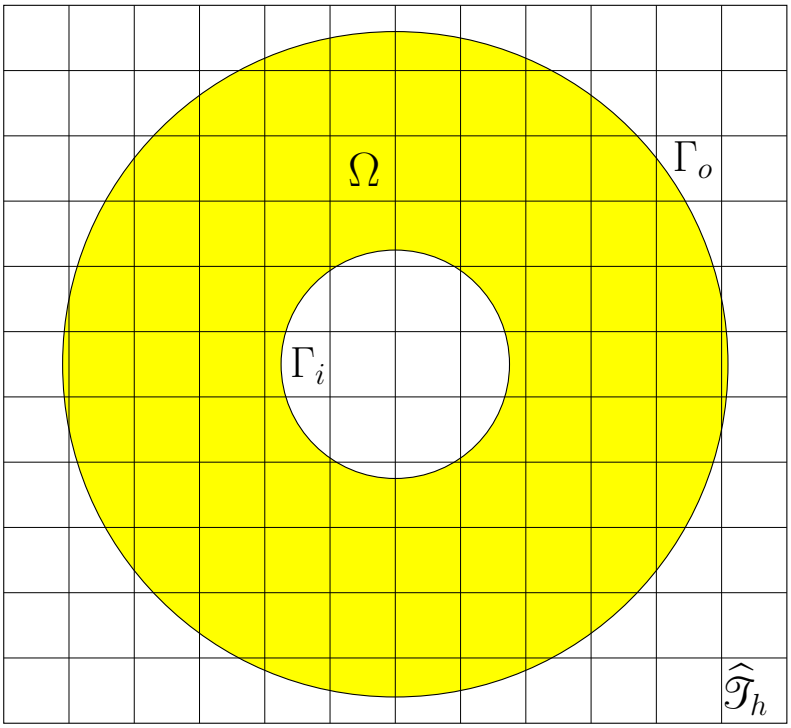

Figure 4.2: Computational domain for the Taylor–Couette simulation. The yellow area defines the physical domain Ω, with the inner boundary Γ_i and outer boundary Γ_o. The black grid represents the computational mesh $\widehat{\mathcal{T}}_h$.

The stress tensor is defined in polar coordinates as

$$\boldsymbol{\sigma} = \begin{pmatrix} -p + 2\mu\frac{\partial u_r}{\partial r} & \mu\left(r\frac{\partial}{\partial r}\left(\frac{u_\theta}{r}\right) + \frac{1}{r}\frac{\partial u_r}{\partial \theta}\right) \\ \mu\left(r\frac{\partial}{\partial r}\left(\frac{u_\theta}{r}\right) + \frac{1}{r}\frac{\partial u_r}{\partial \theta}\right) & -p + 2\mu\left(\frac{1}{r}\frac{\partial u_\theta}{\partial \theta} + \frac{u_r}{r}\right) \end{pmatrix} \tag{4.21}$$

and the traction on the boundary is accordingly defined as

$$\boldsymbol{\sigma}\cdot\boldsymbol{e}_r = \left(-p + 2\mu\frac{\partial u_r}{\partial r}\right)\boldsymbol{e}_r + \left(\mu r\frac{\partial}{\partial r}\left(\frac{u_\theta}{r}\right) + \frac{\mu}{r}\frac{\partial u_r}{\partial \theta}\right)\boldsymbol{e}_\theta. \tag{4.22}$$

In the tangential direction on Γ this reduces to (including the assumption of rotational symmetry)

$$(\boldsymbol{\sigma}\cdot\boldsymbol{n}_r)\cdot\boldsymbol{e}_\theta = \mu r\frac{\partial}{\partial r}\left(\frac{u_\theta}{r}\right). \tag{4.23}$$

The equation (4.18) is expanded and yields,

$$r^2\frac{\partial^2 u_\theta}{\partial r^2} + r\frac{\partial u_\theta}{\partial r} - u_\theta = 0. \tag{4.24}$$

A solution of the form $u_\theta = r^\gamma$ is sought, and the following solution is found,

$$u_\theta(r) = Ar + \frac{B}{r} \tag{4.25}$$

$$p(r) = \frac{1}{\rho}\left(\frac{A^2r^2}{2} + 2AB\log(r) - \frac{B^2}{2r^2} + C\right) \tag{4.26}$$

To find the constants A and B, the boundary conditions need to be imposed on the solution. Defining the following parameters to shorten notation,

$$\begin{pmatrix} a_{11} & a_{12} \\ a_{21} & a_{22}. \end{pmatrix} = \begin{pmatrix} \mu r_i & -\varepsilon_i \mu \frac{-2}{r_i^2} + \frac{\mu}{r_i} \\ \mu r_o & \varepsilon_o \mu \frac{-2}{r_o^2} + \frac{\mu}{r_o} \end{pmatrix} \tag{4.27}$$

$$\begin{pmatrix} b_i \\ b_o \end{pmatrix} = \begin{pmatrix} \mu g_{\theta,i} + \varepsilon_i h_{\theta,i} \\ \mu g_{\theta,o} + \varepsilon_o h_{\theta,o} \end{pmatrix}. \tag{4.28}$$

The following linear system of equations

$$\begin{aligned} a_{11}A + a_{12}B &= b_i \\ a_{21}A + a_{22}B &= b_o, \end{aligned} \tag{4.29}$$

can be postulated to obtain the parameters A and B, such that the boundary conditions are satisfied. Finally, the constant C needs to be specified, as the pressure solution is only determined upto a constant. In the following, the mean pressure over the domain is assumed to be zero, i.e. $\int_\Omega p = 0$. From this the constants can be calculated as

$$\begin{aligned} A &= \frac{b_i a_{22} - a_{12} b_o}{a_{11}a_{22} - a_{12}a_{21}} \\ B &= \frac{b_o a_{11} - a_{21} b_i}{a_{11}a_{22} - a_{12}a_{21}} \\ C &= \frac{-\left[A^2 r^4/8 + 2ABr^2\left(\log(r)/2 - 1/4\right) - B^2 \log(r)/2\right]_{r_1}^{r_2}}{r_2^2/2 - r_1^2/2}. \end{aligned} \tag{4.30}$$

As the analytic solution is derived in polar coordinates, the transformation into a Cartesian coordinate system, where the CutFEM will be applied, is necessary. The relation is the following, where $r = \sqrt{x^2 + y^2}$,

$$\boldsymbol{u} = \begin{pmatrix} u_x \\ u_y \end{pmatrix} = \begin{pmatrix} \cos(\theta)u_r - \sin(\theta)u_\theta \\ \sin(\theta)u_r + \cos(\theta)u_\theta \end{pmatrix} = \begin{pmatrix} -u_\theta \frac{y}{r} \\ u_\theta \frac{x}{r} \end{pmatrix}, \tag{4.31}$$

with the pressure being trivial to calculate from the definition of r in Cartesian coordinates.

Choice of parameters for the numerical analysis In the following studies, the viscosity and density are chosen as $\rho = 1.0$ [kg/m^3] and $\mu = 1.0$ [kg/(s $\cdot$ m)] respectively. The radius of the inner cylinder is chosen as $r_i = 0.19$ [m] and the outer one as $r_o = 0.49$ [m]. On the boundaries the velocity and traction on the inner cylinder Γ_i are given as $g_{\theta,i} = -0.19$ [m/s] and $h_{\theta,i} = -2.5$ [N/m^2], whereas for the outer cylinder Γ_o it is chosen as $g_{\theta,o} = 0.49$ [m/s] and $h_{\theta,o} = 0.5$ [N/m^2]. In the following, the approach is to set one cylinder as a pure Dirichlet problem (i.e. $\varepsilon = 0$) and vary the slip length on the other. In Figure 4.3, the constants A, B and C are demonstrated for this setup with varying ε [m], where Figure 4.3a has $\varepsilon_o = 0$ and varying ε_i and Figure 4.3b with the opposite configuration. From the figures, it becomes clear that there are two constant regions and one transitional region. To conduct a thorough study of this problem, the slip lengths will be chosen such that all these regions are covered. As such, the following six different combinations will be considered:

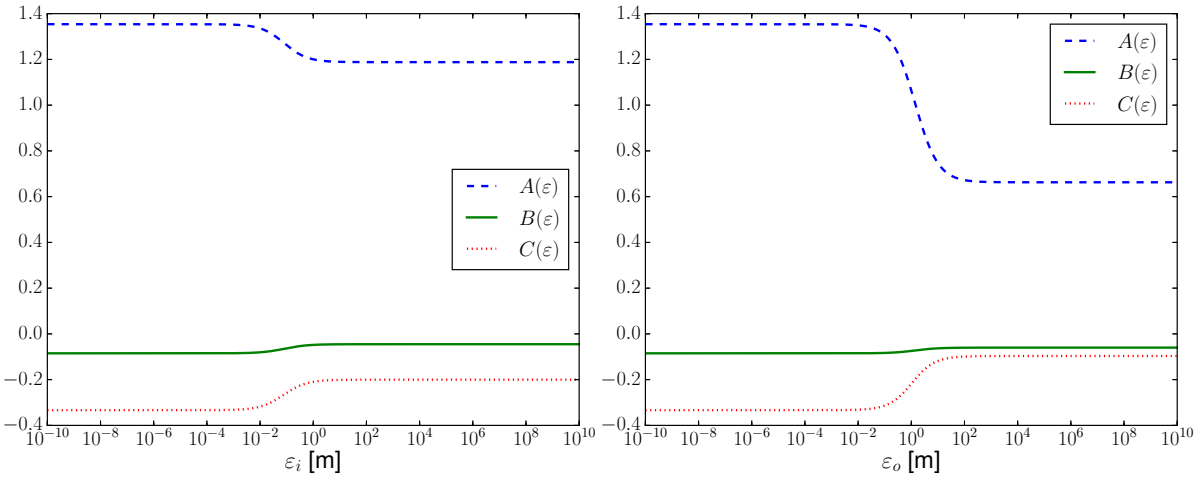

(a) $\varepsilon_o = 0$ (b) $\varepsilon_i = 0$

Figure 4.3: Variations of the constants A, B and C, depending on ε.

- *Case Inner*:
  $\varepsilon_i = \{\ 10^{-10}\ ,\ 0.082\ ,\ 10^{10}\ \}$
  $\varepsilon_o = 0.0$

- *Case Outer*:
  $\varepsilon_i = 0.0$
  $\varepsilon_o = \{\ 10^{-10}\ ,\ 1.42\ ,\ 10^{10}\ \}.$

The value of the slip length in the transition region is chosen at the point where $\frac{dA}{d\varepsilon}$ is the largest, hence $\varepsilon_i = 0.082$ and $\varepsilon_o = 1.42$. The velocity and pressure solution, in polar coordinates, for *Case Inner* is given in Figure 4.4 and for *Case Outer* in Figure 4.5. A two-dimensional

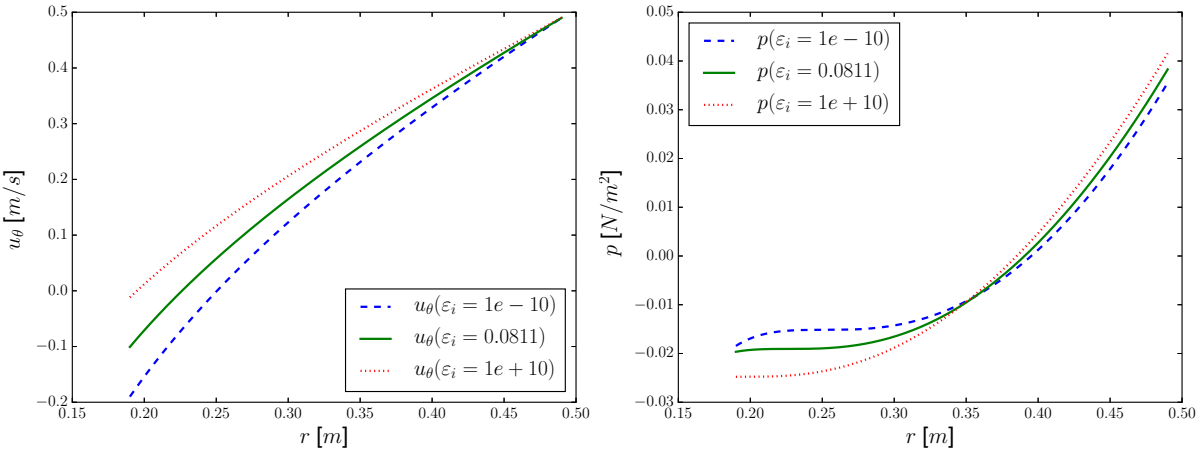

Figure 4.4: Axisymmetric analytic solution of the Taylor–Couette problem, when *Case Inner* is considered.

depiction of the solution for the case of $\varepsilon_i = 0.0$ and $\varepsilon_i = 10^{-10}$ is also illustrated in Figure 4.6.

Imposition of boundary values on the approximated boundary Γ_h As the boundary values $\boldsymbol{g}$ and $\boldsymbol{h}$ are defined on either Γ_i or Γ_o and not on the approximated boundaries $\Gamma_{i,h}$ or $\Gamma_{o,h}$, extensions to these need to be created. Accordingly, the following extensions of the boundary

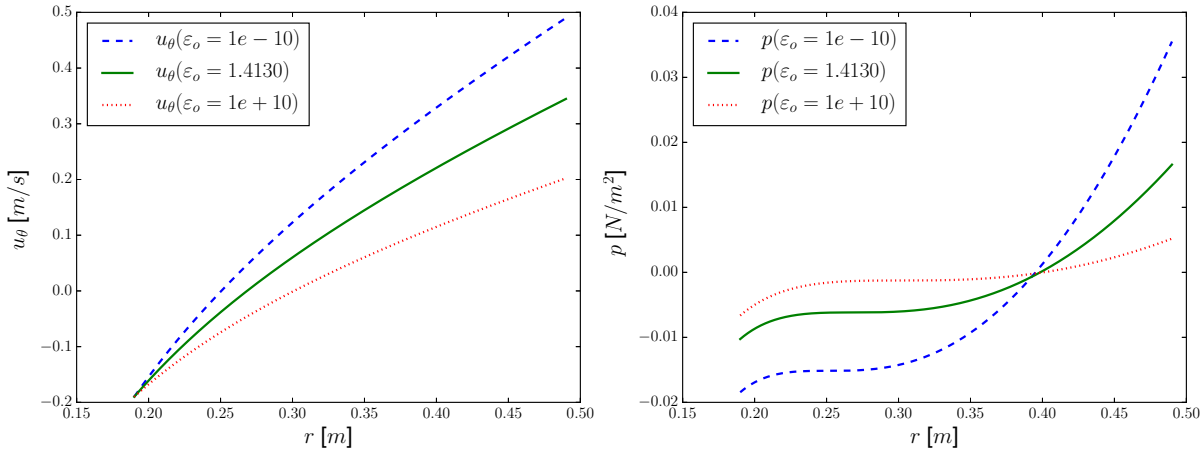

Figure 4.5: Axisymmetric analytic solution of the Taylor–Couette problem, when *Case Outer* is considered.

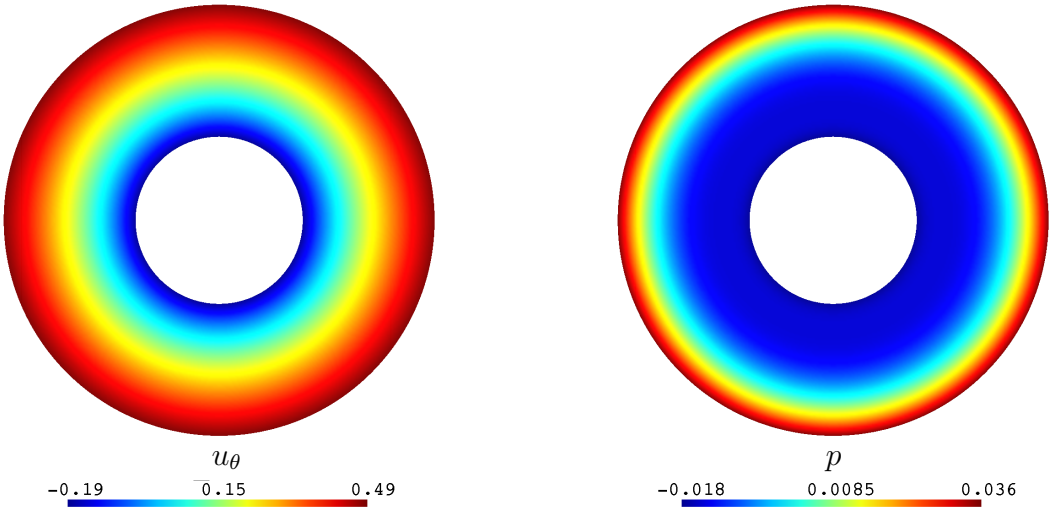

Figure 4.6: Analytic solution on the domain Ω, depicted for u_θ on the left and the pressure p on the right.

values are introduced

$$\boldsymbol{g}_i(\boldsymbol{x}) = \frac{g_{\theta,i}}{r_i}\begin{pmatrix}-y\\ x\end{pmatrix}, \qquad \boldsymbol{g}_o(\boldsymbol{x}) = \frac{g_{\theta,o}}{r_o}\begin{pmatrix}-y\\ x\end{pmatrix} \tag{4.32}$$

$$\boldsymbol{h}_i(\boldsymbol{x}) = \frac{h_{\theta,i}}{r_i}\begin{pmatrix}-y\\ x\end{pmatrix}, \qquad \boldsymbol{h}_o(\boldsymbol{x}) = \frac{h_{\theta,o}}{r_o}\begin{pmatrix}-y\\ x\end{pmatrix}. \tag{4.33}$$

This is one possible choice of constructing the extension. Another possibility would be to divide the vectors by r instead of r_i or r_o. Nonetheless, this choice provided good results in the subsequent numerical examples, hence it is deemed a reasonable choice. Another quantity of interest on the boundary Γ_h is the analytic normal vector on the surfaces Γ_i and Γ_o. A similar

extension as done for the boundary values $\boldsymbol{g}$ and $\boldsymbol{h}$ is construed as well for the analytic normal,

$$\boldsymbol{n}(\boldsymbol{x}) = \begin{cases} \frac{1}{r}\begin{pmatrix} x \\ y \end{pmatrix} & \text{if} \quad \boldsymbol{x} \in \Gamma_{o,h} \\ -\frac{1}{r}\begin{pmatrix} x \\ y \end{pmatrix} & \text{if} \quad \boldsymbol{x} \in \Gamma_{i,h}. \end{cases} \tag{4.34}$$

Defining the computational domain by a level-set function The domain is defined by the combination of the following two level-set functions,

$$\begin{aligned} \phi_i(\boldsymbol{x}) &= \sqrt{x^2 + y^2} - r_i, \quad \forall \ \boldsymbol{x} \in \mathbb{R}^2, \\ \phi_o(\boldsymbol{x}) &= \sqrt{x^2 + y^2} - r_o, \quad \forall \ \boldsymbol{x} \in \mathbb{R}^2. \end{aligned} \tag{4.35}$$

The zero iso-contour of the level-set function ϕ_i defines the inner cylinder with radius r_i, and correspondingly the zero iso-contour of the level-set function ϕ_o defines the outer cylinder. The combination of the two is made in the following fashion

$$\phi(\boldsymbol{x}) = \begin{cases} \phi_i(\boldsymbol{x}) & \text{if} \quad |\phi_i| \leq |\phi_o| \\ \phi_o(\boldsymbol{x}) & \text{if} \quad |\phi_o| < |\phi_i|, \end{cases} \tag{4.36}$$

which delivers the desired level-set function describing the space between two cylinders. For a more comprehensive exposition on the combination of level-set functions to create geometrical shapes, the dissertation by Schott [232] provides a nice variety of examples. This constructed level-set field is then projected by a nodal projection onto the background mesh and the cut of this mesh is carried out as explained in Section 2.2.1.1.

Stabilization of the discretized weak form In the subsequent numerical studies, the background mesh $\widehat{\mathcal{T}}_h$ is chosen as a rectangular domain $[-0.5, 0.5]^2$ [m]^2. It consists of $N \times N$ equally sized square elements with bi-linear $\mathbb{Q}^1$ or bi-quadratic $\mathbb{Q}^2$, equal-order, element approximation for velocity and pressure. Given the nature of an equal-order finite element discretization, stabilization terms needs to be added to obtain a stable formulation. The domain stabilization is done for this example with CIP-stabilization, as explained in Section 2.1.3.2. To stabilize the instabilities arising from cutting the background mesh, ghost penalty stabilization terms are introduced as shown in Section 2.3.2.2. The constants for the stabilization terms are chosen the same way as for the 2D Box Flow problem in Section 3.3.7. That is, $\gamma_\beta = \gamma_p = 0.01$, $\gamma_u = 0.05\gamma_\beta$, $\gamma_\nu = 0.05$ and $\gamma_\sigma = 0.005$ for the first order ghost penalty terms and the second order terms are scaled with 0.05 to their first order counter parts. The ghost penalty terms for the Navier–Stokes equation were introduced in (2.85)–(2.89). Higher order terms than second order are omitted, with the same reasoning as in the publication by Winter *et al.* [279]. For the CIP-stabilization terms (2.32)–(2.34) a similar approach is taken as for the Oseen equation, with $\phi_u, \phi_\beta, \phi_p$ (see (2.36) and (2.37)) weighted as $\nu + c_u(\|\boldsymbol{u}_h\|_{0,\infty,T} h) + c_\sigma(\sigma h^2)$, where the constants are given as $c_u = 1/6$ and $c_\sigma = 1/12$ as suggested in Schott *et al.* [230]. Additionally, the simplified implementation for higher order approximations, i.e. $k > 1$, of the ghost penalty $\overline{g}_\beta$ and CIP term $\overline{s}_\beta$ are employed, as discussed in Remark 3.6.

Numerical integration Given that the CutFEM will be utilized in the following examples, the need arises to integrate cut elements of non-regular shapes. As the standard integration rules are not applicable, the non-regular shapes are decomposed into triangles for which the integration rules are well defined (also known as *tessellation*). See Section 2.3.2.3, for a short discussion on the possible ways of carrying out the numerical integration for cut elements.

The mesh refinement convergence studies If nothing else is mentioned, the following simulations are conducted with an adjoint-inconsistent ($\zeta_u = -1$) Nitsche's method, with the penalty parameter $1/\gamma^t = 1/\gamma^n = 5.0$. The mesh sizes used for the convergence studies are 8×8 - 650×650 for bi-linear $\mathbb{Q}^1$ elements and 8×8 - 192×192 for bi-quadratic $\mathbb{Q}^2$ elements. The norms are evaluated on the computational domain Ω_h and the interface error is evaluated on the joint boundary $\Gamma_h = \Gamma_{i,h} \cup \Gamma_{o,h}$.

4.1.1.1 Convergence Behavior of a Piecewise Constant Normal

To start with, a naive approach is pursued where a piecewise constant normal is employed at the boundaries of the cylinders. This is to observe the ensuing convergence and to attain a point of reference for different approaches. Hence, the projection matrix is chosen as

$$\boldsymbol{P}^n = \boldsymbol{n}_h \otimes \boldsymbol{n}_h$$

where the normal $\boldsymbol{n}_h$ is taken from the piecewise linear approximated boundary Γ_h. For this choice of normal the ensuing convergence behavior for meshes consisting of $\mathbb{Q}^1$ elements is depicted in Figure 4.7.

As can be seen in the aforementioned figure, for the choice of a small slip length $\varepsilon_i = 10^{-10}$ or $\varepsilon_o = 10^{-10}$, which corresponds to a de facto Dirichlet condition on both the inner and outer cylinder, optimal order of convergence is observed. That is, $\mathcal{O}(h^2)$ order of convergence for the velocity and at least $\mathcal{O}(h)$ for the pressure and velocity gradient. Everything being the same, when the slip length is increased, a loss of convergence is noticeable for the primary variables $\boldsymbol{u}_h$ and p_h. For the velocity, instead of a second order convergence, now only a first order $\mathcal{O}(h)$ convergence is observable. Moreover, for the velocity gradient the expected order of convergence is observed in the domain, however, on the boundary a constant error can be seen. This loss of convergence also occurs for the pressure which now seems to have a constant error and is not converging at all anymore. Another interesting observation, is the fact that for the velocity error, a larger ε results in a higher base error. A possible motivation to this is that the tangential contribution, mitigating the effects of the normal error, becomes smaller as the slip length increases.

The aforementioned loss of convergence is expected, given the nature of the Babuška paradox. The Proposition 4.1 predicts this loss of convergence if $\|\boldsymbol{n} - \boldsymbol{n}_h\|_\Gamma$ is converging with less than the expected convergence of $\|\boldsymbol{u} - \boldsymbol{u}_h\|_\Gamma$. The convergence of the discrete normal $\boldsymbol{n}_h$ on Γ_h is depicted in Figure 4.8. In this figure it is clear that a linear convergence, is received in the L^2-norm over the interface. Hence, it can be postulated that to achieve optimal order of convergence, the normal vector should converge with at least $\mathcal{O}(h^2)$.

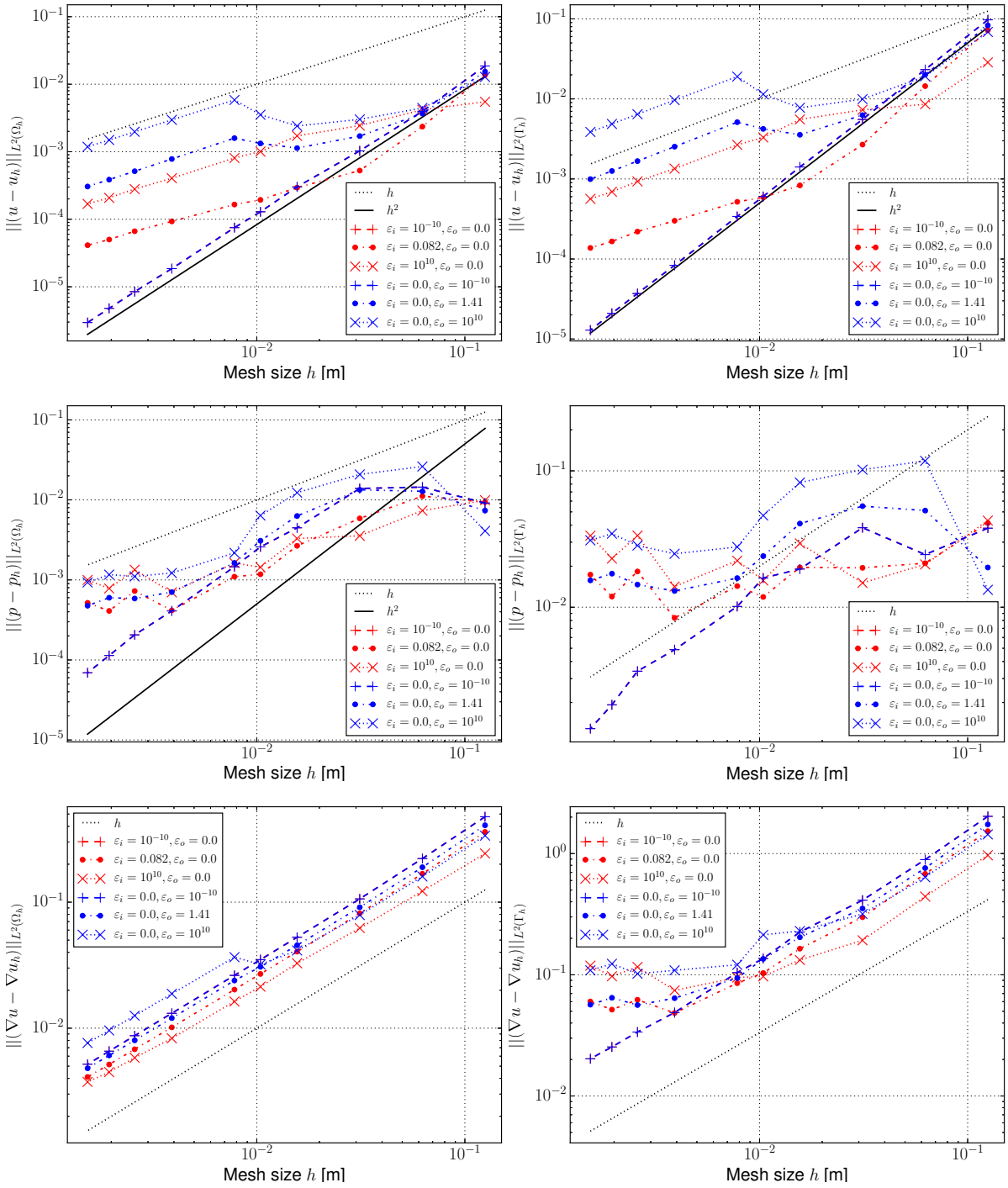

Figure 4.7: Error convergence study for an adjoint-inconsistent Nitsche's method with $\mathbb{Q}^1$ elements and a piecewise constant normal $\boldsymbol{n}_h$ on the boundary: bulk errors (left column) and boundary errors (right column) for velocity, pressure and velocity gradient (from top to bottom).

4.1.1.2 Convergence Behavior of a Smoothed Normal

The suspicion of the previous Section 4.1.1.1 is that owing to the linear convergence of the normal on the boundary, the primary variables lose an order of convergence. To verify this,

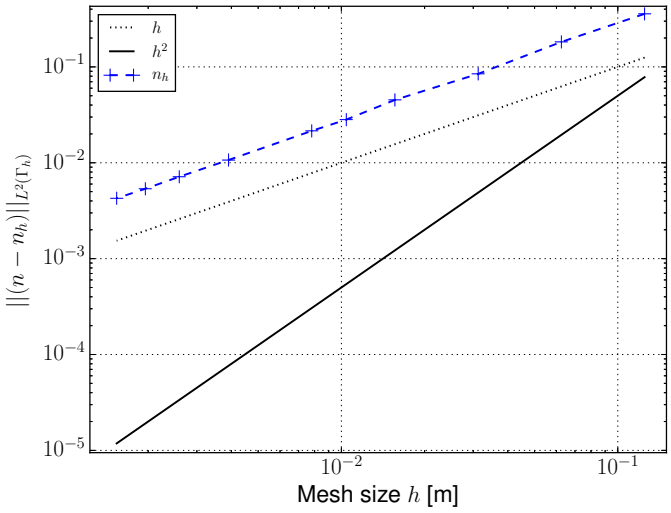

Figure 4.8: Error convergence study for the piecewise constant normal $\boldsymbol{n}_h$ evaluated on the cut interface Γ_h.

instead of employing the piecewise constant normal at the interface $\Gamma_h = \Gamma_{o,h} \cup \Gamma_{i,h}$, a smoothed normal from the level-set is employed in its stead. The smoothing of the normal is done here by means of a L^2-projection of the level-set gradient, where

$$\widetilde{\boldsymbol{n}}_h = \frac{\widetilde{\nabla \phi_h}(\boldsymbol{x})}{|\widetilde{\nabla \phi_h}(\boldsymbol{x})|} \tag{4.37}$$

is the smoothed normal, and the smoothed gradient field $\widetilde{\nabla \phi_h}$ is created as explained in Section 2.2.1.4. Consequently, the projection normal is then given as

$$\boldsymbol{P}^n = \widetilde{\boldsymbol{n}}_h \otimes \widetilde{\boldsymbol{n}}_h. \tag{4.38}$$

The improved convergence is evident from the results in Figure 4.9. The expected optimal order of convergence for the velocity and its gradient is recognized and the pressure attains at least a first order convergence. Nonetheless, a peculiarity in the convergence of the velocity is noticeable at around $h \approx 10^{-2}$, where for *Case Outer* a small region does not converge with the correct order, and the error might even increase to the next point as is the case for $\varepsilon_o = 10^{10}$. Possible explanations to this can stem from the cut configuration of the outer cylinder, or that the formulation had not yet reached its asymptotic limit. Furthermore, it is important to stress that optimal convergence is observed with the prescribed settings for the studied range of element sizes, which does not guarantee the continued observed asymptotic convergence. However, the attained results demonstrate an improved convergence in comparison to the piecewise constant normal case and indicate that the switch to the smoothed normal should resolve the convergence issues.

The explanation given in Proposition 4.1 seems to hold merit as in Figure 4.10 a convergence of $\mathcal{O}(h^2)$ is attained for the normal $\widetilde{n}_h$ on the interface Γ_h. This was postulated to be a necessary requirement to reach optimal order of convergence, which the observed results verify. Given that a smoothed normal $\widetilde{\boldsymbol{n}}_h$ is used here from a level-set function which is projected onto a bi-linear $\mathbb{Q}^1$ mesh, it is not guaranteed that the smoothed normal will converge with the same order as the interpolation of the level-set ϕ_h. In fact, the observed super-convergence of the smoothed

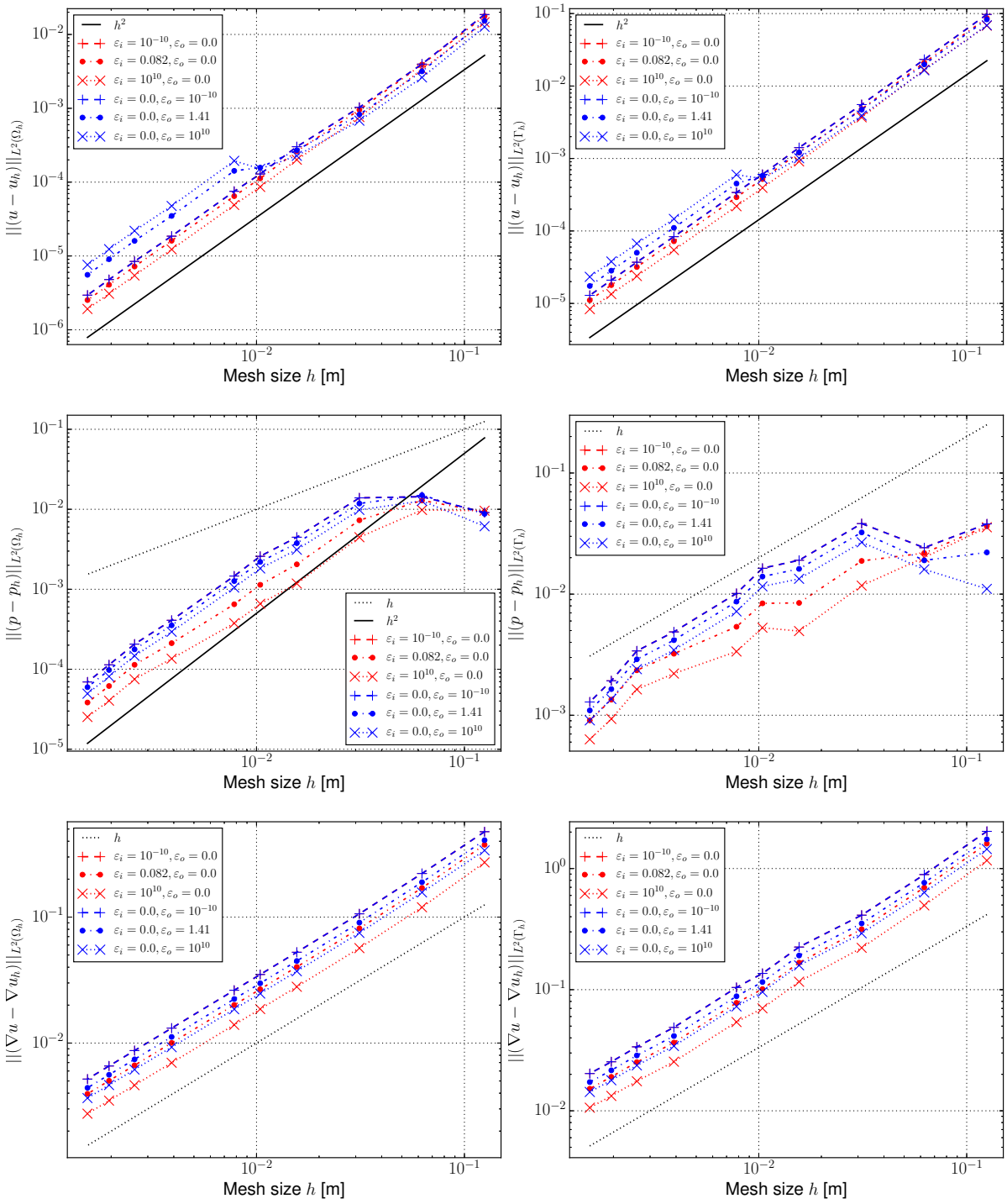

Figure 4.9: Error convergence study for an adjoint-inconsistent Nitsche's method with $\mathbb{Q}^1$ elements and a smoothed normal $\widetilde{\boldsymbol{n}}_h$ on the boundary: bulk errors (left column) and boundary errors (right column) for velocity, pressure and velocity gradient (from top to bottom).

normal for this example is an exception, rather than the norm. This fact will become apparent in the subsequent Section 4.2 which deals with higher order elements.

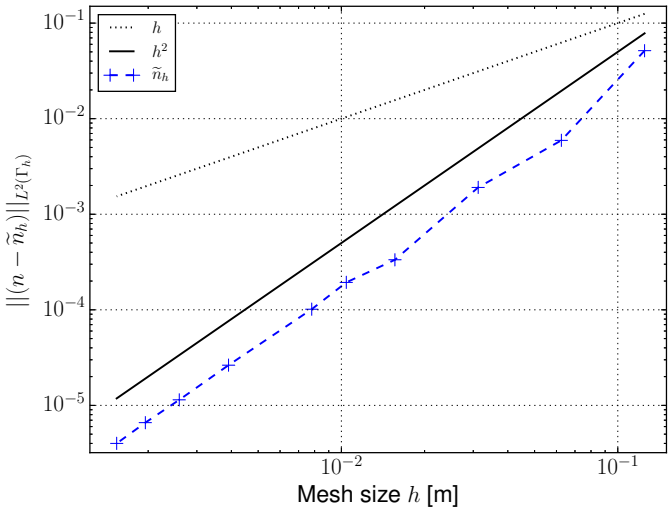

Figure 4.10: Error convergence study for the smoothed normal $\widetilde{\boldsymbol{n}}_h$ created from the L^2-projection of the gradient of the level-set ϕ_h, which is discretized by a mesh of $\mathbb{Q}^1$ elements.

For completeness sake, it should be mentioned that the author of this thesis also conducted studies with a residual-based stabilization (as compared to a CIP-stabilization) for the above mentioned problem and was able to still attain optimal order of convergence for the smoothed normal case.

4.1.2 Moving Rotating Torus

To demonstrate the validity of the proposed method for more complex situations, a challenging three dimensional problem is attempted. The problem that will be considered here is construed from a moving rotating torus in a rectangular channel with the measurements $[-1.0, 1.0] \times [-1.0, 1.0] \times [-1.0, 3.0]$ $[\mathrm{m}]^3$. The torus is given a major radius of $r_{\mathrm{maj}} = 0.5$ $[\mathrm{m}]$ and a minor radius of $r_{\mathrm{min}} = 0.2$ $[\mathrm{m}]$. The orientation of the torus is determined by the vector $\boldsymbol{r}_0^{\mathrm{torus}}$, which determines its local z-axis. In this example it coincides with the translation vector and is defined as

$$\boldsymbol{r}_0^{\mathrm{torus}} = \boldsymbol{r}^{\mathrm{trans}} = \boldsymbol{e}_z = (0, 0, 1)^T.$$

The center of the torus is moved in the following fashion in space,

$$\boldsymbol{x}^{\mathrm{center}}(t) = -\frac{L_d}{2}\cos(\psi_d t)\boldsymbol{r}^{\mathrm{trans}},$$

and accordingly, its velocity is readily attained by a simple derivation to be

$$\boldsymbol{u}^{\mathrm{center}}(t) = \frac{L_d}{2}\psi_d \sin(\psi_d t)\mathbf{r}^{\mathrm{trans}}.$$

The parameters for this example are chosen as $L_d = 2.0$ $[\mathrm{m}]$ and $\psi_d = 0.6$ $[1/\mathrm{s}]$, which implies that $\boldsymbol{x}^{\mathrm{center}}(0) = (0, 0, 0)^T$ and the time for the torus to return to its initial position is $T^{\mathrm{cycle}} \approx 10.47$ $[\mathrm{s}]$. For the rotational vector, the following is prescribed,

$$\boldsymbol{r}^{\mathrm{rot}} = (0, 0, 1)^T \tag{4.39}$$

$$\boldsymbol{\omega}^{\mathrm{torus}} = 2.0\pi\Omega^{\mathrm{rev}}(t)\boldsymbol{r}^{\mathrm{rot}} \tag{4.40}$$

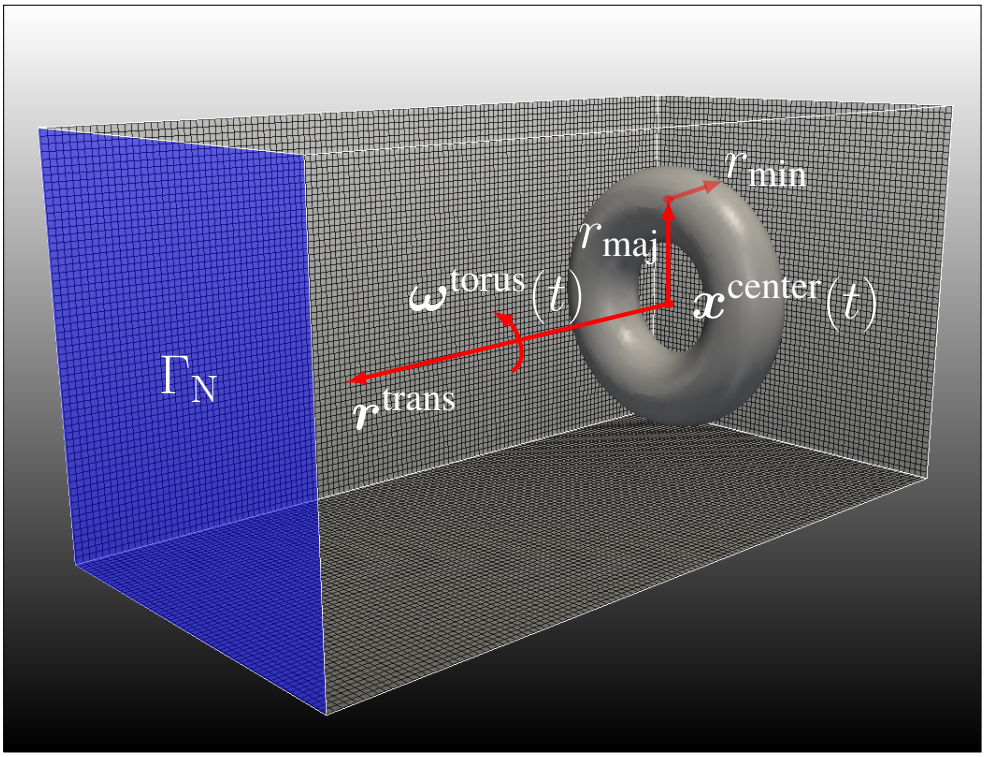

Figure 4.11: Setup for the moving rotating torus example. The wall highlighted in blue is given a Neumann boundary Γ_{N} whereas the other boundaries of the rectangular channel are set as full slip Γ_{slip} boundaries. The torus moves along the z-axis and also rotates around this axis (defined by the rotation vector $\boldsymbol{\omega}^{\text{torus}}$). It is defined by its center $\boldsymbol{x}_{\text{center}}$, the major radius r_{maj}, the minor radius r_{min} and its orientation $\boldsymbol{r}_0^{\text{torus}}$, which coincides with the translation vector $\boldsymbol{r}^{\text{trans}}$ in this example.

with

$$\Omega^{\text{rev}}(t) = \begin{cases} \frac{0.095}{2}(1 - \cos(\frac{\pi t}{T_{\text{ramp}}})) & \forall t < T_{\text{ramp}} \\ 0.095 & \forall t \geq T_{\text{ramp}} \end{cases} \tag{4.41}$$

where Ω^{rev} has the dimension $[\text{s}^{-1}]$ and $T_{\text{ramp}} = 0.05$ [s] is set in this example.

Given that $\boldsymbol{\omega}^{\text{torus}}$ and $\boldsymbol{r}_0^{\text{torus}}$ are parallel in this example, the torus only rotates around its own axis, hence $\boldsymbol{r}^{\text{torus}} = \boldsymbol{r}_0^{\text{torus}}$. For completeness sake, it should be mentioned that this is not a necessary condition. If the aforementioned vectors are not parallel, Rodrigues formula [223] can be applied to compute the new torus vector after the rotation has been applied as

$$\boldsymbol{r}^{\text{torus}}(t) = \boldsymbol{r}_0^{\text{torus}} \cos\theta + (\mathbf{r}^{\text{rot}} \times \boldsymbol{r}_0^{\text{torus}}) \sin\theta + \mathbf{r}^{\text{rot}}(\mathbf{r}^{\text{rot}} \cdot \boldsymbol{r}_0^{\text{torus}})(1 - \cos\theta) \tag{4.42}$$

where $\theta(t) = 2.0\pi\Omega^{\text{rev}}t$. The rotational contribution to the velocity is given from

$$\boldsymbol{u}^{\text{rot}}(\boldsymbol{x}, t) = \boldsymbol{\omega}^{\text{torus}} \times (\boldsymbol{x} - \boldsymbol{x}^{\text{center}}(t))$$

where $\boldsymbol{x}$ lies on the surface of the torus, i.e. $\boldsymbol{x} \in \Gamma^{\text{torus}}$.

In this example the torus is specified implicitly by a level-set field. As the torus moves over time, the level-set field needs to be able to depict this motion. To define this, the following

vectors are introduced,

$$\boldsymbol{r}^{\text{orto}}(\boldsymbol{x},t) = [(\boldsymbol{x} - \boldsymbol{x}^{\text{center}}(t)) \cdot \boldsymbol{r}^{\text{torus}}(t)]\, \boldsymbol{r}^{\text{torus}}(t) \tag{4.43}$$

$$\boldsymbol{r}^{\text{base}}(\boldsymbol{x},t) = (\boldsymbol{x} - \boldsymbol{x}^{\text{center}}(t)) - \boldsymbol{r}^{\text{orto}}(\boldsymbol{x},t). \tag{4.44}$$

The level-set field for the moving rotating torus can then be defined as

$$\phi(\boldsymbol{x},t) = \sqrt{(|\boldsymbol{r}^{\text{base}}(\boldsymbol{x},t)| - r_{\text{maj}})^2 + |\boldsymbol{r}^{\text{orto}}(\boldsymbol{x},t)|^2} - r_{\text{min}}. \tag{4.45}$$

The velocities enforced on the surface of the torus Γ^{torus} are constructed from the translational and rotational velocities as

$$\boldsymbol{g}(\boldsymbol{x},t) = \boldsymbol{u}^{\text{center}}(t) + \boldsymbol{u}^{\text{rot}}(\boldsymbol{x},t) \quad \text{for} \quad \boldsymbol{x} \in \Gamma^{\text{torus}}. \tag{4.46}$$

As a general Navier condition is imposed on the surface of the torus Γ^{torus}, a traction $\boldsymbol{h}$ is also required to be set. This traction is chosen to be zero, i.e. $\boldsymbol{h} = \boldsymbol{0}$, thus making the condition on the surface effectively a Navier slip condition. For an illustration on the above introduced vectors and the zero iso-contour of the level-set at time $t = 0$, see Figure 4.11. In the same figure, the Neumann boundary Γ_{N} is clearly defined as the plane $[-1,1] \times [-1,1] \times \{3\}$ of the rectangular channel. The traction of the Neumann boundary is set as $\boldsymbol{h} = \boldsymbol{0}$, i.e. a no-traction condition. The rest of the channel walls are given a full slip boundary Γ_{slip}, which is prescribed by means of the substitution method. The slip length of the torus is varied in its radial direction in the following fashion

$$\varepsilon(\boldsymbol{x},t) = e^{-100(|\boldsymbol{r}^{\text{base}}(\boldsymbol{x},t)| - r_{\text{maj}})}. \tag{4.47}$$

This implies that at the innermost radius of the torus (i.e. $r_{\text{maj}} - r_{\text{min}}$), the slip length is $\varepsilon \approx 10^9$ [m] and at the outermost radius (i.e. $r_{\text{maj}} + r_{\text{min}}$), $\varepsilon \approx 10^{-8}$ [m]. Hence, on the outermost parts of the torus no-slip will be imposed, whereas in the inner parts a full slip condition is imposed. In between these two parts, an exponential transition made. It is apparent from the start that this choice of slip length would be impossible to enforce with the standard substitution method, given the low slip length. By contrast, the method introduced in Section 3.3, has no problem imposing this condition, as will be seen in the subsequent results.

To compare the results obtained with the Navier slip boundary, the same simulation is conducted as well for a pure no-slip boundary. From this, the results can be compared and the feasibility of the Navier slip solution can be related to the more well-known solution with the no-slip condition. To distinguish between the two cases, the one with varying slip length will be from hereon denoted as the **Navier slip case** and the no-slip as the **no-slip case**. The properties of the fluid is chosen as $\mu = 0.002$ [kg/(s · m)] and $\rho = 1.0$ [kg/m^3] and the simulation is run in the time interval $t \in [0, 11]$ [s]. The normal of the boundary of the torus is given from a smoothed level-set gradient field, which is created from the L^2-projection of the gradients. For the computational mesh a $[60 \times 60 \times 120]$ uniform partition into equal-order $\mathbb{Q}^1$ tri-linear elements is done. In the domain the discretized weak form is stabilized with a residual based stabilization (see Section 2.1.3.1) and the instabilities arising from the cut is taken care of by the addition of ghost penalty stabilization terms (see Section 2.3.2.2). For the time integration a backward Euler scheme is used (i.e. a one-step theta scheme with $\Theta = 1$), as explained in Section 2.3.3, with a time step size of $\Delta t = 0.01$. For the imposition of the boundary condition, an adjoint-consistent formulation is employed with Nitsche penalty parameters of $1/\gamma^t = 1/\gamma^n = 35$. In

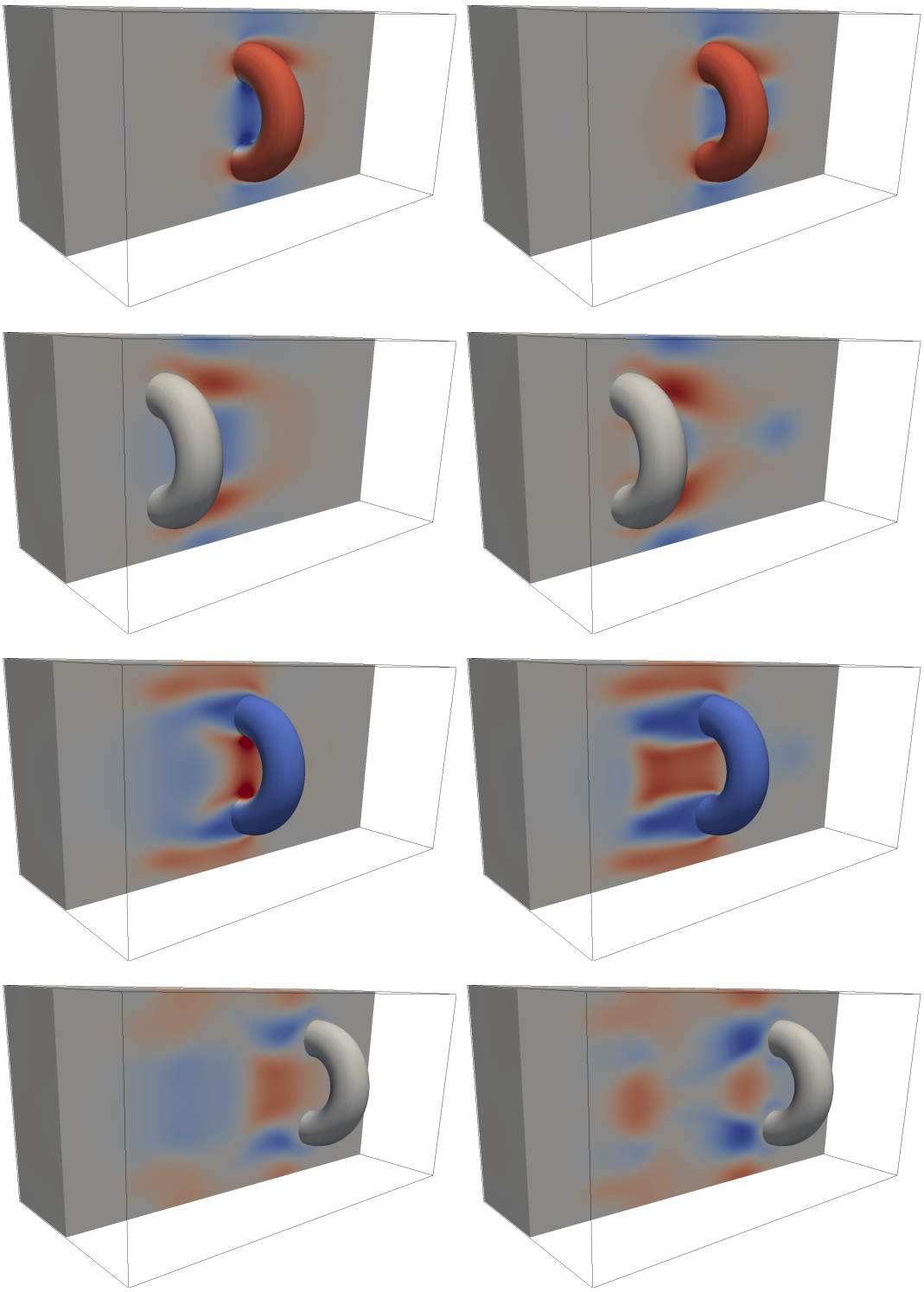

Figure 4.12: The z-component of the velocity u_z is illustrated in this figure. On the left the configuration with a Navier-slip condition is presented, whereas on the right a full no-slip condition is illustrated. Higher velocities are shown as red and lower as blue (the velocity color scale is $[-0.8, 0.8]$). The results are shown at the times $t = \{2.62, 5.24, 7.85, 10.47\}$ with time increasing from top to bottom.

the following, the dimensions of quantities will be dropped to shorten the text. If nothing else is mentioned, standard SI-units are implied.

A first quantity of interest, which is easily verifiable whether the Navier slip case has the desired effect, is to look at the velocity in z-direction, i.e. u_z. In Figure 4.12 the mid-cross section of the channel is shown and u_z is depicted at four times, $t = \{2.62, 5.24, 7.85, 10.47\}$. These times are chosen at important points in the trajectory of the torus. At $t \approx 2.62$ the torus passes through the middle of the channel, with its highest translational velocity in its path, this occurs again at $t \approx 7.85$ however on its path back to the starting position. The time $t \approx 5.24$ is the turning point of the tours at $(0, 0, 2)$, respectively $t \approx 10.47$ is the turning point at $(0, 0, 0)$. Hence, four times have been elected which illustrates the flow at important points in the trajectory of the torus. In the aforementioned figure, the time is increased from top to bottom, i.e. the first row contains the results for $t = 2.62$ and the last for $t = 10.47$. The figures on the left depict the case with Navier slip, whereas on the right no-slip is depicted. Here it is immediately apparent that in the inner of the torus, the flow slips along the torus for the Navier slip case whereas in the no-slip case it sticks to the torus making a boundary layer visible in the inner of the torus. This observed difference between the no-slip and Navier slip case is the a priori expected behavior. As another verification the flow around the outside of the torus is similar in both the Navier slip and the no-slip case, as they should be, given that both are in practice no-slip conditions at the outer rim of the torus. At $t = 5.24$, i.e. on the second row, the flow which is dragged with the torus in the no-slip case is notably larger than in the Navier slip case. Also velocities further back in the channel can be observed which are not present in the Navier slip case. Given that there is more drag in the no-slip case, the flow created by the torus should affect a larger volume of the flow in the channel, which is also observed. In the case of $t = 7.85$ similar observations as for $t = 2.62$ can be made, i.e. the flow slips through the torus and sticks on the outside in the Navier slip case, whereas it always sticks in the no-slip case. At this time it is also clear that there is more flow through the torus in the Navier slip case compared to the no-slip case, which is logical given that there is little resistance for the flow to pass through the inner of the torus, and hence the flow will chose this path of least resistance. At the final time $t = 10.47$, it is apparent that the that the no-slip configuration has a larger effect on the flow profile further back in the channel, which was also observed at the time $t = 5.24$.

Continuing with a view on the velocity tangential to the trajectory of the torus, construed as

$$\boldsymbol{u}_\theta = \left(\boldsymbol{I} - \frac{(\boldsymbol{x} - \boldsymbol{x}^{\text{center}}) \otimes (\boldsymbol{x} - \boldsymbol{x}^{\text{center}})}{|\boldsymbol{x} - \boldsymbol{x}^{\text{center}}|^2} \right) (\boldsymbol{I} - \boldsymbol{r}^{\text{torus}} \otimes \boldsymbol{r}^{\text{torus}}) \boldsymbol{u}, \tag{4.48}$$

where $u_\theta = |\boldsymbol{u}_\theta|$. This velocity gives a good measure how well the Navier slip case works for the imposed rotation Ω^{rev} on the torus. The results are given in Figure 4.13 and are structured in the same fashion as in Figure 4.12, that is $t = 2.62$ on the top row with increasing time to the bottom row of $t = 10.47$ and the Navier slip case on the left and the no-slip case on the right. On the first row, i.e. at $t = 2.62$, the most apparent observation is the fact that, as the torus itself is also colored with the color of u_θ, the rotational velocity in the inner of the torus is noticeably higher for the no-slip case. At $t = 5.24$ it can be observed that the rotational velocity is observably larger in the wake over which the inner of the torus has passed in the no-slip case, compared to the Navier slip case. In the Navier slip case there has been virtually no creation of velocity in the tangential direction from the inner part of the torus. In the subsequent row, for $t = 7.85$, the Navier slip case has some observable velocities also in the wake of the inner part of the torus. In

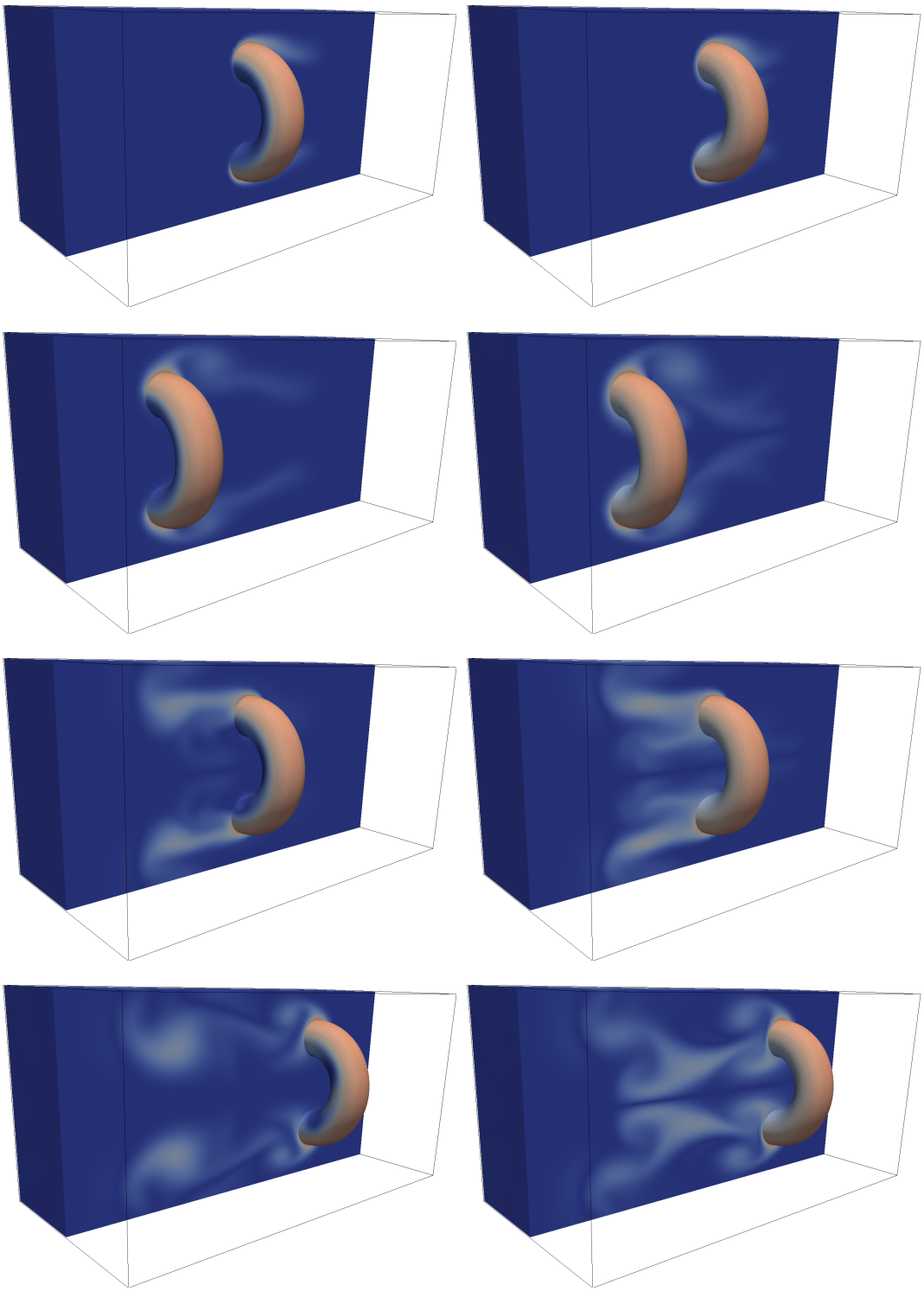

Figure 4.13: Rotational velocity u_θ around the z-axis. On the left the configuration with a Navier-slip condition is presented, whereas on the right a full no-slip condition is illustrated. Higher velocities are shown as red and lower as blue (the velocity color scale is $[0, 0.6]$). The results are shown at the times $t = \{2.62, 5.24, 7.85, 10.47\}$ with time increasing from top to bottom.

comparison to the no-slip case, these velocities are indeed much smaller, but nevertheless, still present. A reasonable explanation to this could be that when the torus starts returning towards its initial position it crosses through its own wake. Owing to this, it creates vortices, which also appears in the Navier slip case. By extension, a similar explanation of the tangential velocity profile can be given for $t = 10.47$. At this time some tangential velocity can be seen as having been produced from the inner of the torus in the Navier slip case, but in no way comparable with the no-slip case. Qualitatively, the findings from observing the tangential velocity validates that the imposition of the Navier condition has the desired effect.

Given that the set-up of the simulation is rather convection dominated, taking $L = r_{\text{maj}} + r_{\text{min}}$ and $U_{max} \approx 0.6$ this gives a Reynolds number of $\text{Re} \approx 400$. This is arguably not sufficient for fully turbulent flow, but still has regimes dominated by convection. Given this, to visualize the flow in three dimensions, the Q-criterion described in Hunt *et al.* [152] can be employed. It is calculated by

$$Q = \frac{1}{2}\left(\boldsymbol{\Omega} : \boldsymbol{\Omega} - \boldsymbol{\epsilon} : \boldsymbol{\epsilon}\right) \tag{4.49}$$

with $\boldsymbol{\Omega} = 1/2\left(\nabla \boldsymbol{u} - (\nabla \boldsymbol{u})^T\right)$. The physical representation of this criterion is that eddies can be defined as regions where $Q > 0$. In Figure 4.14 the iso-contour of $Q = 0.15$ is illustrated for the times $t = \{2.62, 5.24, 7.85, 10.47\}$. In accordance with what was observed in regards to the fluid sticking to the torus in the previous results for u_z and u_θ, it would be expected here that eddies are being created mainly from no-slip boundaries, and that no, or only little, production of eddies is to be expected for slip boundaries. This hypothesis is readily verified from the results at $t = 2.62$ and $t = 5.24$, found on the first and second rows of Figure 4.14, respectively. Here eddies are created from the outer boundary of the torus (i.e. the no-slip part) whereas only in the no-slip case are eddies produced from the inner boundary of the torus. When the torus returns to its initial position, depicted at times $t = 7.85$ and $t = 10.47$, the eddies become more complex and chaotic, demonstrating the complexity of the flow. Here again the most important observation comes from the fact that there is a clear absence of eddies in the middle of the channel for the Navier slip case, whereas in the no-slip case eddies are also present in the middle of the channel. This observation supports the initial assumption of the shape of the flow.

To further analyze the solution, a snap shot of the Navier slip case at $t = 2.62$ is given in Figure 4.15 with $u_z, \boldsymbol{u}_\theta$ and p depicted on the surface. From these three snapshots, the effect of the imposed slip in the inner of the torus is apparent. In the upper left image, the velocity in z-direction u_z is depicted. It shows that in the inner of the torus the flow does not stick but rather glides through, with a higher speed than the speed with which the fluid is dragged along the outer borders of the torus. Similar observations for the rotational velocity $\boldsymbol{u}_\theta$ can be made from the upper right figure. It can be seen here that in the inner of the torus, the rotational motion does not effect the flow, as its rotational velocity is close to zero. A somewhat more interesting observation can be found for the pressure on the torus, depicted in the lower left image. The pressure on the surface orthogonal to the flow has the highest pressure as it has to push the fluid in front of it, whereas lower pressures are observed in the inner and outer surfaces of the torus. The fact that the inner of the torus experiences a smaller pressure than that at the outer radius can be explained by a simple Bernoulli argument that a higher velocity magnitude results in a larger pressure drop. This explanation is in good agreement with the observed velocities u_z and $\boldsymbol{u}_\theta$ on the surface of the torus.

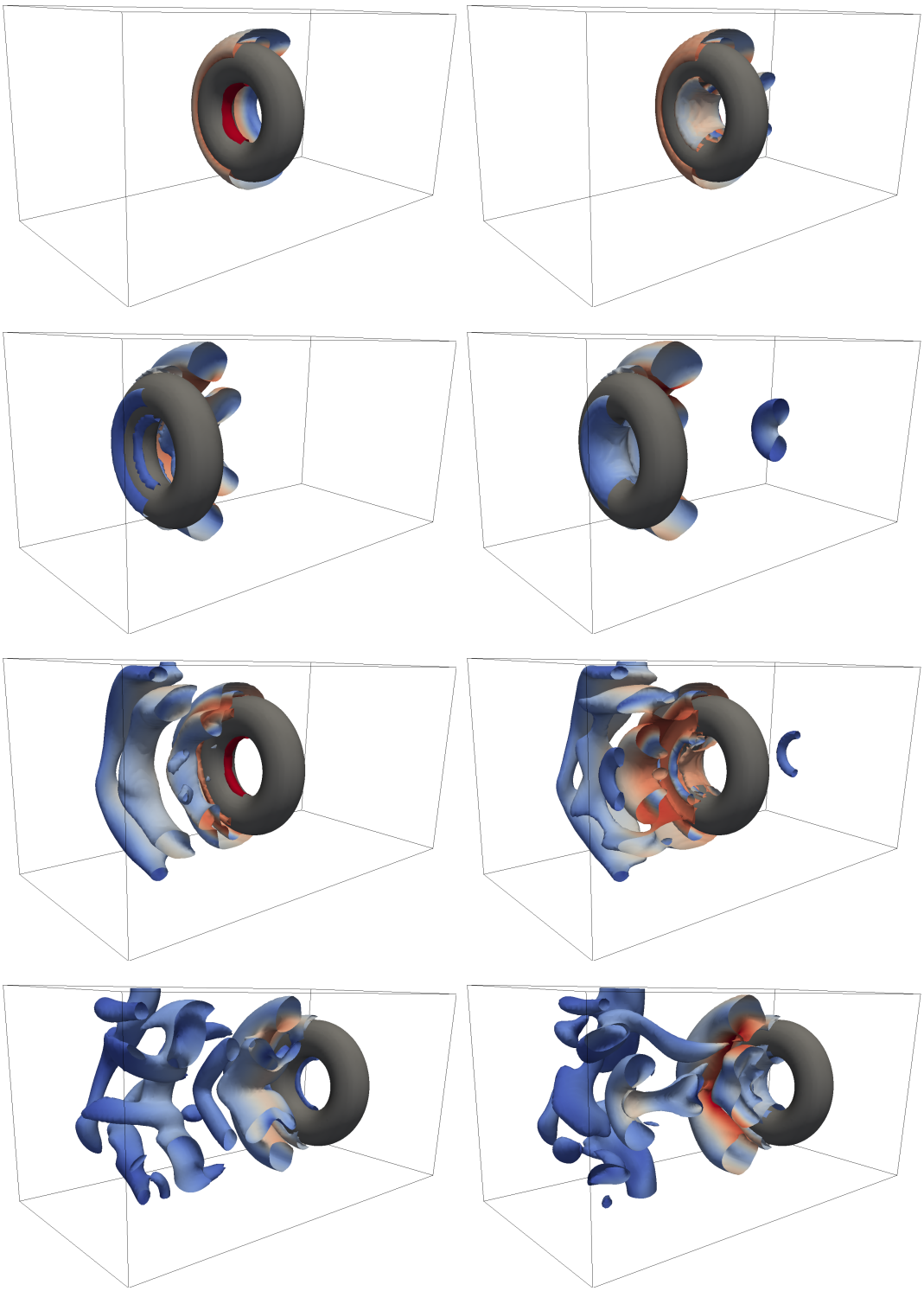

Figure 4.14: Eddies visualized by the Q-criterion, with iso-contours of $Q = 0.15$, for the torus with Navier slip condition on the left and no-slip on the right. The iso-contours are colored by the velocity magnitude $|\boldsymbol{u}_h|$, with higher velocities shown as red and lower as blue (the velocity color scale is $[0, 0.8]$). The results are shown at the times $t = \{2.62, 5.24, 7.85, 10.47\}$ with time increasing from top to bottom.

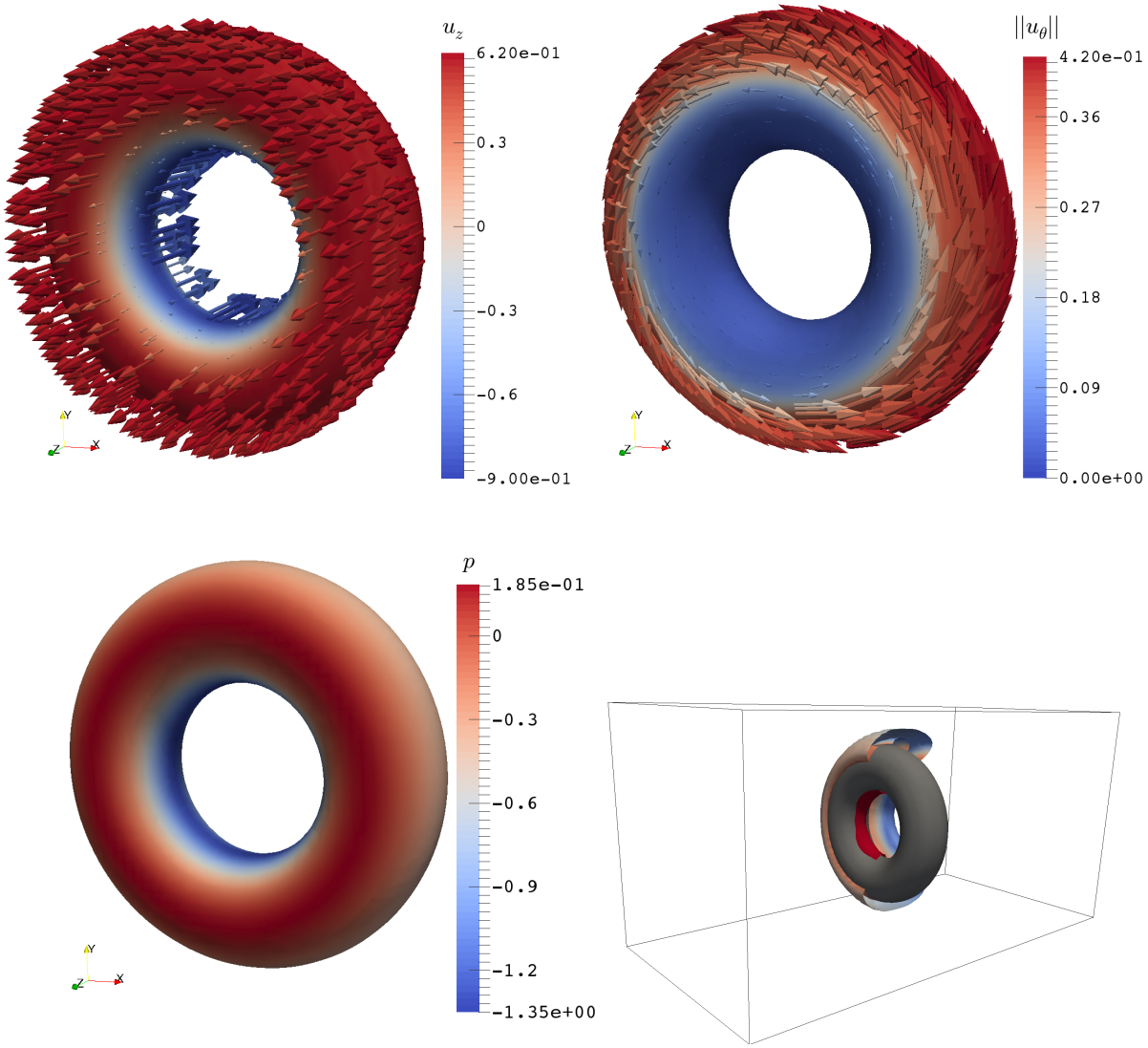

Figure 4.15: The velocities and pressure on the torus are demonstrated here for $t = 2.62$. This is when the torus is in the middle of the channel, and hence has its highest velocity in z-direction of $u_z = 0.6$. In the upper left picture the velocity in z-direction is shown and in the upper right the rotational velocity u_θ. On the bottom row the pressure distribution on the torus is shown on the left and the state of the flow in the channel is demonstrated by the picture of the Q-criterion (reproduced from the top left image in Figure 4.14), shown on the right.

Finally, to quantify the results, the velocity in z-direction, u_z, and the pressure are evaluated at two points over time. The two points are chosen in the middle of the trajectory of the torus, i.e. at $z = 1$. Both of the points are fixed in the middle of the width of the channel, i.e. $x = 0$. Hence, only the "height" of the point is varied. One of the points is left in the very middle of the channel, that is $\boldsymbol{x} = (0, 0, 1)$, thus the midpoint of the torus passes over this point twice, at the times $t = 2.62$ and 7.85. The second point is put higher up in the channel, in between the outer radius of the torus (at $y = 0.7$) and the wall (at $y = 1.0$), at $\boldsymbol{x} = (0, 0.85, 1)$. The solutions for the no-slip and Navier slip cases are then compared, and the results are depicted in Figure 4.16

for $\boldsymbol{x} = (0, 0, 1)$ and Figure 4.17 for $\boldsymbol{x} = (0, 0.85, 1)$. In the figures, the no-slip case is described as **Dirichlet** whereas the Navier Slip case is named as **Navslip**.

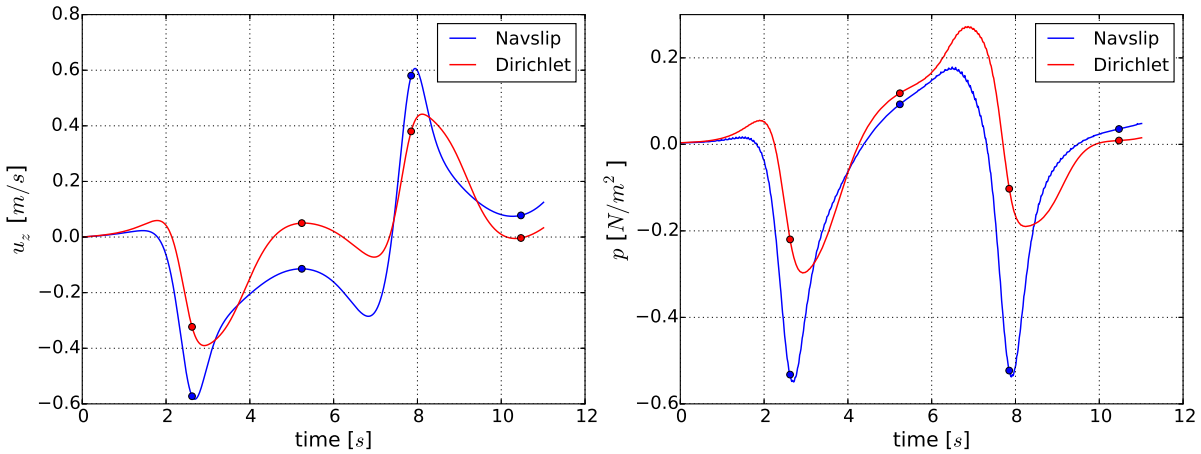

(a) Velocity in z-direction over time.

(b) Pressure over time.

Figure 4.16: Velocity in z-direction and pressure evaluated over time on the midpoint of the rectangular channel (i.e. $\boldsymbol{x} = (0, 0, 1)$). The points in the plot indicate the times $t = \{2.62, 5.25, 7.85, 10.47\}$.

Starting with the point $\boldsymbol{x} = (0, 0, 1)$, the velocity in z-direction is shown in Figure 4.16a. First thing to notice is that the torus pushes more fluid in front of it in the no-slip case, than in the Navier slip case for the initial times $0 \leq t \leq 2$, which is quite natural considering the additional traction applied on the fluid in the no-slip case from the torus. When the torus starts passing over the point at $2 \leq t \leq 4$, instead of pushing the fluid away, it is forced to stream through the torus to allow the torus to pass. Here the Navier slip case has a noticeably larger absolute velocity, i.e. more fluid streams through the inner of the torus than in the no-slip case. This is a sensible result given the lower friction in the Navier slip case. Continuing to the region in which the torus turns around, i.e. $4 \leq t \leq 6.5$, the magnitude of the velocity decreases in both the cases. In the Navier slip case, the velocity does not dissipate as much as in the no-slip case, which might be explained by the fact that the reduced traction does not exert the same pull on the fluid once the torus has passed over it. For the last part, the torus crosses over the point anew, here again an initial push is identifiable in front of the torus at $t \approx 7$, and then a sharp increase in the velocity to permit the fluid to stream through the torus. As was the case for the first passage over the point, the Navier slip case exhibits a larger absolute velocity here as well. The pressure solution is displayed in Figure 4.16b and corroborates the findings of the velocity solution. As is expected, when the torus approaches the point of measurement, an increase in pressure is observed as fluid is pushed out of the way, as can be seen at times $t \approx 2$ and $t \approx 6.5$. A stark drop in the pressure is noticeable when the torus traverses over the point of measurement, i.e. at times $t \approx 2.62$ and $t \approx 7.85$. This can be motivated by a simple Bernoulli argument, where given that the velocity increases here a drop in pressure is expected.

Now on to the results for the outer point $\boldsymbol{x} = (0, 0.85, 1)$. An important difference to the aforementioned point of measurement $\boldsymbol{x} = (0, 0, 1)$, is that for both the no-slip case and Navier slip case the outer part of the torus is virtually no-slip. Hence, similar behavior for the two cases is to be expected at this point of measurement. This is also apparent from the plots in Figure 4.17,

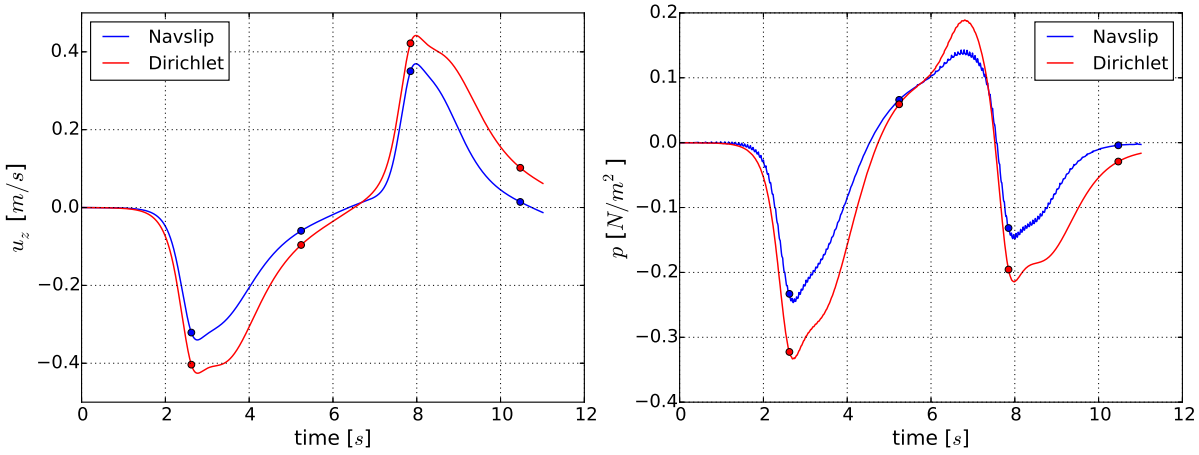

(a) Velocity in z-direction over time.

(b) Pressure over time.

Figure 4.17: Velocity in z-direction and pressure evaluated over time on the point located between the top of the channel and the torus (i.e. $\boldsymbol{x} = (0, 0.85, 1)$). The points in the plot indicate the times $t = \{2.62, 5.25, 7.85, 10.47\}$

where the results display similar behavior with only different scaling. Starting with the velocity in z-direction, as displayed in Figure 4.17a, it is apparent that the torus does not push the fluid onward in the initial phase of $0 \leq t \leq 2$, as was observed in Figure 4.16a. A likely explanation to this is the surrounding slip walls of the channel. Next, the magnitude of the velocity increases to displace fluid in the way of the torus. What is noticeable here is the fact that the no-slip case has a greater velocity than the Navier slip case. This is quite reasonable given that in the Navier slip case more of the fluid will flow through the inner part of the torus as this way has less resistance than in the no-slip case. Consequently, less fluid will take the path on the outer side of the torus in the Navier slip case compared to the no-slip case, and as such the speed of the flow is larger in the no-slip case for the times $t = 2.62$ and $t = 7.85$. With the increase in velocity at these points in time, a corresponding drop in pressure is observed in Figure 4.17b. An interesting observation which can be seen in the pressure solution is the push exerted by the torus on the fluid at around $t = 6.5$, which is not present in the first traversal of this measurement point at $t \approx 2$. This increase in pressure is not readily seen in the velocity solution, but the velocity remains small until the noticeable pressure drop occurs at $t \approx 7$, which can be connected to the behavior of the pressure solution.

In conclusion, the results obtained indicate that the proposed method produces good and robust results. Furthermore, compared to a no-slip solution, the differences observed are reasonable and can be explained from the premise of the difference in boundary conditions.

4.2 Geometric Error Introduced by Approximation of the Domain

In the previous Section 4.1, the importance of the quality of the approximated normal compared to the exact normal was demonstrated. However, the second problem identified in the

introduction of this Chapter, i.e. the error introduced by $\Omega_h \neq \Omega$, was not addressed. Even though this domain approximation error was present in the convergence study of Section 4.1.1, it did not affect the order of convergence. Hence, as is common for linear elements, for a sufficiently resolved discretized domain of polygonal shape, this domain approximation error can be neglected as it converges with the same order as the primary variables. Nevertheless, this problem becomes acutely present when higher-order meshes are considered, as this domain approximation error will start to dominate at some point and remove the benefits of using higher-order elements in the first place.

The benefits of using higher-order elements are apparent from their increased convergence rates, but also the fact that in certain cases they are faster than low-order methods as investigated by, for instance, Huerta *et al.* [147]. However, the mesh generation for curved domains pose a challenge when higher order methods are employed. In the publication by Ruiz-Gironés *et al.* [225], two requirements are noted to be of importance for the mesh generation. First, no inverted elements are allowed to be present in the mesh, as these will ruin the conditioning of the discretized system. Secondly, the geometric error introduced by the approximation of the physical domain needs to be bounded and converge with the correct order under mesh refinement. Recently a plethora of publications to construe higher-order meshes with cruved domain boundaries have been published. Apart from the already mentioned [225], Toulorge *et al.* [265], Fortunato and Persson [116] and Moxey *et al.* [198] have made contributions in this field in recent years.

Given the issues with creating curved meshes, methods have been developed to retain a discretized polygonal domain Ω_h and extend the solutions of this domain onto the physical domain and its boundary. Two notable approaches can be identified in the literature. The method first introduced, was by Bramble *et al.* [42] for the Poisson equation, and the method was later extended by Dupont [102] to include parabolic equations. In these publications, higher order convergence is retained by employing a closest point mapping to the exact boundary and extending the solution to the boundary by means of a Taylor expansion. A drawback of this method is the requirement, that the distance between Γ and Γ_h needs to be of the order h^2. This requirement was relaxed by the proposed method of Cockburn *et al.* [75], which only requires the distance between Γ and Γ_h to be of order h to still retain the desired order of convergence. This method has later been improved and analyzed in the subsequent publications by Cockburn and Solano [73, 74] and Cockburn *et al.* [76]. The drawback of using this method is the necessity of evaluating path integrals from the discretized surface Γ_h to the true surface Γ, making this method intrinsically more complex than the proposed method by Bramble *et al.* [42].

Unfitted mesh methods struggle with the same issue as their fitted mesh counterparts. That is, guaranteeing that the geometric error introduced from the approximation of the physical domain does not dominate the solution. Different ways of circumventing this issue can be found in the literature. In Dréau *et al.* [98] the cut elements are constructed from an isosurface of a level-set and the approximated boundary is refined linearly within a element up to a certain user defined limit. A different approach is pursued by Cheng and Fries [69] where the division of the cut element into volume cells permits the volume cells to have one curved side to better approximate the curved interface. A recently proposed approach by Lehrenfeld [178] suggests that instead of adapting the volume cells of the cut elements individually, the background mesh is instead mapped to provide higher order approximation of the boundary. Lastly, a method building on the work of Bramble *et al.* [42] was recently published by Burman *et al.* [66]. In it, a piecewise

linear cut of the background mesh is still conducted and instead, the terms added in the weak imposition of the boundary condition are modified.

In this thesis, the approach by Burman *et al.* [66] will be pursued to attain optimal convergence for second order elements for fictitious domain problems with the general Navier boundary condition on curved domains. The choice of using the boundary value correction is mainly motivated by the simplicity of the implementation, as the method only necessitates the addition of terms evaluated on the boundary Γ_h. Hence, no existing algorithm for the decomposition of cut elements into volume cells needs to be adapted, neither does a transformation of the background mesh need to be carried out.

In Section 4.2.1 the extension of the method by Burman *et al.* [66] from the Poisson equation with Dirichlet boundary conditions to the Navier–Stokes equation with general Navier boundaries is presented. Following this, the method is verified by employing this method to the Taylor–Couette example introduced in Section 4.1.1.

4.2.1 Boundary Value Expansion by means of Taylor Expansion

As mentioned in the preamble to this Section, the logical extension to the Navier–Stokes equations with general Navier condition from the method introduced for the Poisson equation by Burman *et al.* [66], and later analyzed for the adjoint-inconsistent case by Boiveau *et al.* [37], will be presented here. A derivation of the proposed method is shown, but rigorous proofs are omitted and instead the method is motivated by a convergence study of the already introduced Taylor–Couette flow problem with general Navier boundary conditions in Section 4.1.1.

First a tubular region $U_\delta(\Gamma)$ needs to be defined around the interface Γ. A signed distance function, ϕ is defined as positive on the inside of the domain Ω and negative on the outside. The tubular domain can then be defined as

$$U_\delta(\Gamma) = \left\{ \boldsymbol{x} \in \mathbb{R}^d : |\phi(x)| < \delta \right\}. \tag{4.50}$$

Now consider a constant $\delta_0 > 0$ such that the closest point mapping $\mathfrak{p}(\boldsymbol{x}) : U_{\delta_0}(\Gamma) \to \Gamma$ is well defined and that the identity

$$\mathfrak{p}(\boldsymbol{x}) = \boldsymbol{x} + \phi(\boldsymbol{x})\boldsymbol{n}(\mathfrak{p}(\boldsymbol{x})) \tag{4.51}$$

holds, where $\boldsymbol{n}$ is the exterior unit normal on Γ. It is assumed that δ_0 is chosen small enough, such that the projection $\mathfrak{p}(\boldsymbol{x})$ is a bijection. The polygonal domain Ω_h, with boundary Γ_h, is defined by the the zero level-set of the nodal interpolant ϕ_h of ϕ and its construction is described in Section 2.2.1.1.

Now, the question arises how the projection between the two surfaces should be construed? In the publication by Burman *et al.* [66] two possible paths can be pursued. These choices for the projection are illustrated in Figure 4.18. Either the projection is carried out by using the normal vector $\boldsymbol{n}_h$ stemming from the boundary Γ_h of the polygonal approximation Ω_h. This projection can be written as

$$\mathfrak{p}_{\boldsymbol{n}_h}(\boldsymbol{x}) = \boldsymbol{x} + d_{\boldsymbol{n}_h}(\boldsymbol{x})\boldsymbol{n}_h(\boldsymbol{x}) \tag{4.52}$$

where the distance $d_{\boldsymbol{n}_h}$ has to be calculated by some iterative process to find where the extension from the approximated boundary Γ_h intersects the true boundary Γ. The second option is to

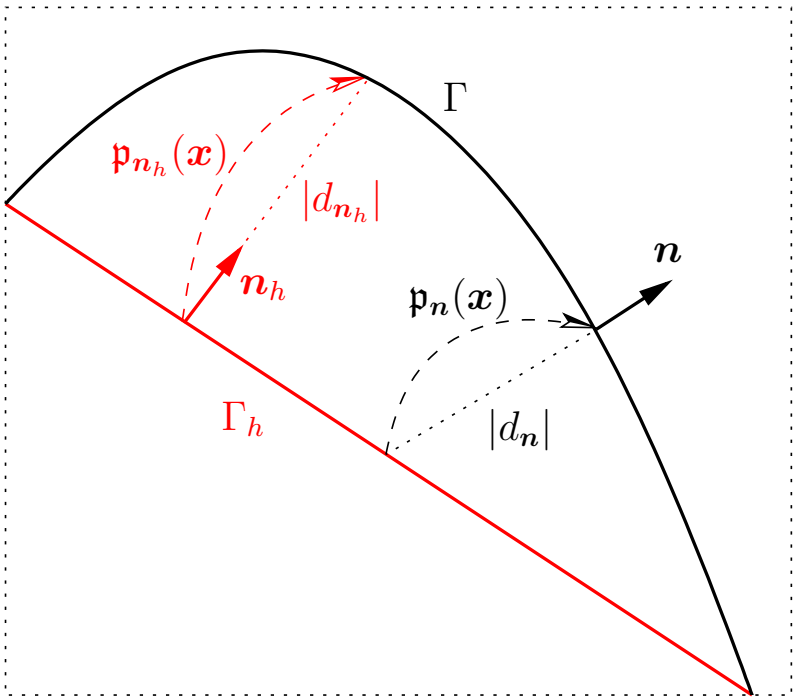

Figure 4.18: A visualization of the two possible ways of creating the projection as described in Burman *et al.* [66]. In red, the projection $\mathfrak{p}_{\boldsymbol{n}_h}$ is created from the normal vector $\boldsymbol{n}_h$ of the piecewise linear interface Γ_h. The second option is depicted in black, where the projection $\mathfrak{p}_{\boldsymbol{n}}$ is constructed from the normal $\boldsymbol{n}$ of the interface Γ.

employ the normal vector $\boldsymbol{n}$ on the true boundary Γ to create the projection. This leads to the following formula for the projection,

$$\mathfrak{p}_{\boldsymbol{n}}(\boldsymbol{x}) = \boldsymbol{x} + d_{\boldsymbol{n}}(\boldsymbol{x})\boldsymbol{n}(\mathfrak{p}_{\boldsymbol{n}}(\boldsymbol{x})) \tag{4.53}$$

with $d_{\boldsymbol{n}}(\boldsymbol{x}) = \phi(\boldsymbol{x})$, which is the same projection as introduced for the tubular region in (4.51). To calculate $\mathfrak{p}_{\boldsymbol{n}}(\boldsymbol{x})$, a nonlinear system needs to be solved as $\boldsymbol{n}(\mathfrak{p}_{\boldsymbol{n}}(\boldsymbol{x}))$ and $d_{\boldsymbol{n}}(\boldsymbol{x})$ have to be sought by an iterative process. As such, in this thesis an approximation to this second projection is suggested as

$$\mathfrak{p}_{\boldsymbol{n}}(\boldsymbol{x}) \approx \mathfrak{p}_{\phi_h}(\boldsymbol{x}) = \boldsymbol{x} - \phi_h(\boldsymbol{x})\frac{\widetilde{\nabla\phi_h}(\boldsymbol{x})}{|\widetilde{\nabla\phi_h}(\boldsymbol{x})|}, \tag{4.54}$$

where ϕ_h is the level-set value and $\widetilde{\nabla\phi_h}$ its smoothed gradient at $\boldsymbol{x}$. Given that the assumptions made in Ω_h are the same as in Burman *et al.* [66], the distance of the projections can be taken from the aforementioned publication as

$$\delta_h = \|d_{\boldsymbol{n}}\|_{L^\infty(\Gamma_h)} \leq \|d_{\boldsymbol{n}_h}\|_{L^\infty(\Gamma_h)} \lesssim h^2, \tag{4.55}$$

and the error of the normal as

$$\|\boldsymbol{n}_h(\boldsymbol{x}) - \boldsymbol{n}(\mathfrak{p}(\boldsymbol{x}))\|_{L^\infty(\Gamma_h)} \lesssim h. \tag{4.56}$$

This first order convergence of the normal as suggested in [66], was also observed in Section 4.1.1.1 for the Taylor–Couette problem with the choice of a piecewise constant normal vector.

Assuming that suitable extensions of the body force $\boldsymbol{f} \in [L^2(\Omega \cup \Omega_h)]^d$ and primary variables $\boldsymbol{u} \in [H^1(\Omega \cup \Omega_h)]^d$ and $p \in L^2(\Omega \cup \Omega_h)$ exist in the tubular region $U_{\delta_0}(\Gamma)$. The weak form of the Navier–Stokes equations can be rewritten as

$$\begin{aligned}
&(\rho\frac{\partial \boldsymbol{u}}{\partial t}, \boldsymbol{v})_{\Omega_h} + (2\mu\boldsymbol{\epsilon}(\boldsymbol{u}), \boldsymbol{\epsilon}(\boldsymbol{v}))_{\Omega_h} + (\rho(\boldsymbol{u}\cdot\nabla)\boldsymbol{u}, \boldsymbol{v})_{\Omega_h} - (p, \nabla\cdot\boldsymbol{v})_{\Omega_h} + (q, \nabla\cdot\boldsymbol{u})_{\Omega_h} \\
&\quad -(\rho\frac{\partial \boldsymbol{u}}{\partial t} - \nabla\cdot(2\mu\boldsymbol{\epsilon}(\boldsymbol{u})) + \rho(\boldsymbol{u}\cdot\nabla)\boldsymbol{u} + \nabla p - \boldsymbol{f}, \boldsymbol{v})_{\Omega_h\setminus\Omega} - (q, \nabla\cdot\boldsymbol{u})_{\Omega_h\setminus\Omega} \\
&\qquad - \langle(-p\boldsymbol{I} + 2\mu\boldsymbol{\epsilon}(\boldsymbol{u}))\cdot\boldsymbol{n}, \boldsymbol{v}\rangle_{\Gamma_h} = (\boldsymbol{f}, \boldsymbol{v})_{\Omega_h}.
\end{aligned} \tag{4.57}$$

This weak form is the same as the already well known weak form of the Navier–Stokes equations, apart from the addition of the terms of the form $(\cdot,\cdot)_{\Omega_h\setminus\Omega}$. These are parts of Ω_h which lies outside of Ω, and hence, suitable extensions of the primary variables are needed here to guarantee that the solution in Ω converges to the correct solution.

Assuming that the boundary condition imposed on Γ is a general Navier condition, and that $\mathrm{meas}(\Gamma^\varepsilon) > 0$. The proposed Nitsche's method, imposing the general Navier condition, is applied here to impose the boundary condition on the discrete boundary Γ_h. However, the difference here is that instead of imposing the primary variables on the discrete boundary Γ_h, the condition is projected onto the true boundary Γ. As such, the following formulation takes shape,

$$\begin{aligned}
&(\rho\frac{\partial \boldsymbol{u}}{\partial t}, \boldsymbol{v})_{\Omega_h} + (2\mu\boldsymbol{\epsilon}(\boldsymbol{u}), \boldsymbol{\epsilon}(\boldsymbol{v}))_{\Omega_h} + (\rho(\boldsymbol{u}\cdot\nabla)\boldsymbol{u}, \boldsymbol{v})_{\Omega_h} - (p, \nabla\cdot\boldsymbol{v})_{\Omega_h} + (q, \nabla\cdot\boldsymbol{u})_{\Omega_h} \\
&\quad - (\rho\frac{\partial \boldsymbol{u}}{\partial t} - \nabla\cdot(2\mu\boldsymbol{\epsilon}(\boldsymbol{u})) + \rho(\boldsymbol{u}\cdot\nabla)\boldsymbol{u} + \nabla p - \boldsymbol{f}, \boldsymbol{v})_{\Omega_h\setminus\Omega} - (q, \nabla\cdot\boldsymbol{u})_{\Omega_h\setminus\Omega} \\
&\quad + \langle\frac{\rho\phi_u}{\gamma^n h}\mathscr{C}_{\Gamma^n}(\boldsymbol{u}, \mathfrak{p}_{\boldsymbol{n}}), \boldsymbol{v}\rangle_{\Gamma_h} - \langle\mathscr{C}_{\Gamma^n}(\boldsymbol{u}, \mathfrak{p}_{\boldsymbol{n}}), \zeta_u 2\mu\boldsymbol{\epsilon}(\boldsymbol{v})\boldsymbol{n}_h + q\boldsymbol{n}_h\rangle_{\Gamma_h} \\
&\quad + \langle\frac{1}{\varepsilon\circ\mathfrak{p}_{\boldsymbol{n}} + \gamma^t h}\mathscr{C}_{\Gamma^t}(\boldsymbol{u}, \mathfrak{p}_{\boldsymbol{n}}), \boldsymbol{v}\rangle_{\Gamma_h} - \langle\frac{\gamma^t h}{\varepsilon\circ\mathfrak{p}_{\boldsymbol{n}} + \gamma^t h}\mathscr{C}_{\Gamma^t}(\boldsymbol{u}, \mathfrak{p}_{\boldsymbol{n}}), \zeta_u 2\boldsymbol{\epsilon}(\boldsymbol{v})\boldsymbol{n}_h\rangle_{\Gamma_h} \\
&\quad - \langle(-p\boldsymbol{I} + 2\mu\boldsymbol{\epsilon}(\boldsymbol{u}))\cdot\boldsymbol{n}_h, \boldsymbol{v}\rangle_{\Gamma_h} = (\boldsymbol{f}, \boldsymbol{v})_{\Omega_h}.
\end{aligned} \tag{4.58}$$

The added terms in line three and four of (4.58), are almost identical to the ones added when no geometric approximation error was present in Section 3.2. However, a difference is noticeable in what conditions are imposed. The normal and tangential condition are defined as

$$\mathscr{C}_{\Gamma^n}(\boldsymbol{u}, \mathfrak{p}_{\boldsymbol{n}}) = \mu(\boldsymbol{u} - \boldsymbol{g})\circ\mathfrak{p}_{\boldsymbol{n}}(\boldsymbol{P}^n\circ\mathfrak{p}_{\boldsymbol{n}}) \tag{4.59}$$

$$\mathscr{C}_{\Gamma^t}(\boldsymbol{u}, \mathfrak{p}_{\boldsymbol{n}}) = (\varepsilon(2\mu\boldsymbol{\epsilon}(\boldsymbol{u})\boldsymbol{n} - \boldsymbol{h}) + \mu(\boldsymbol{u} - \boldsymbol{g}))\circ\mathfrak{p}_{\boldsymbol{n}}(\boldsymbol{P}^t\circ\mathfrak{p}_{\boldsymbol{n}}). \tag{4.60}$$

The boundary terms, such as $\boldsymbol{g}$, $\boldsymbol{h}$, ε, $\boldsymbol{n}$, $\boldsymbol{P}^n$ and $\boldsymbol{P}^t$ are all defined on Γ, and hence the projection onto this surface gives well defined values. In contrast, the terms $\boldsymbol{u}\circ\mathfrak{p}_{\boldsymbol{n}}(\boldsymbol{x})$ and $2\mu\boldsymbol{\epsilon}(\boldsymbol{u})\circ\mathfrak{p}_{\boldsymbol{n}}(\boldsymbol{x})$ are not known on the boundary Γ, as they exist in Ω_h and not Ω. As suggested in [66], a Taylor expansion can be carried out in the direction of the projection from Γ_h to Γ to obtain the values

on Γ. Accordingly, the following approximations are construed,

$$\boldsymbol{u} \circ \mathfrak{p}_{\boldsymbol{n}}(\boldsymbol{x}) \approx T^{\boldsymbol{n}}_{m,k}(\boldsymbol{u})(\boldsymbol{x}) = \sum_{i=m}^{k} \frac{D^j_{\boldsymbol{n}} \boldsymbol{u}(\boldsymbol{x})}{j!} d^j_{\boldsymbol{n}}(\boldsymbol{x}), \tag{4.61}$$

where $D^j_{\boldsymbol{n}}$ is the jth partial derivative in the direction of the normal $\boldsymbol{n}$. The approximated boundary condition terms can be reformulated as

$$\mathscr{C}^{T_k}_{\Gamma^n}(\boldsymbol{u}, \mathfrak{p}_{\boldsymbol{n}}) = \mu \left[T^{\boldsymbol{n}}_{0,k}(\boldsymbol{u}) - \boldsymbol{g} \circ \mathfrak{p}_{\boldsymbol{n}}\right] (\boldsymbol{P}^n \circ \mathfrak{p}_{\boldsymbol{n}}) \tag{4.62}$$

$$\mathscr{C}^{T_k}_{\Gamma^t}(\boldsymbol{u}, \mathfrak{p}_{\boldsymbol{n}}) = \left[\varepsilon \circ \mathfrak{p}_{\boldsymbol{n}}(2\mu T^{\boldsymbol{n}}_{0,k}(\boldsymbol{\epsilon}(\boldsymbol{u}))\boldsymbol{n} \circ \mathfrak{p}_{\boldsymbol{n}} - \boldsymbol{h} \circ \mathfrak{p}_{\boldsymbol{n}}) + \mu(T_{0,k}(\boldsymbol{u}) - \boldsymbol{g} \circ \mathfrak{p}_{\boldsymbol{n}})\right] (\boldsymbol{P}^t \circ \mathfrak{p}_{\boldsymbol{n}}), \tag{4.63}$$

which can be evaluated on Γ_h. Defining $U = (\boldsymbol{u}, p)$ and $V = (\boldsymbol{v}, q)$, it is possible to rewrite the weak form as

$$\mathscr{A}_h(U, V) - \mathscr{B}(U, V) + \mathscr{N}^k_h(U, V) + \mathscr{B}^{\mathscr{N}}_h(U, V) = \mathscr{L}_h(V), \tag{4.64}$$

where

$$\begin{aligned}\mathscr{A}_h(U, V) &= (\rho \frac{\partial \boldsymbol{u}}{\partial t}, \boldsymbol{v})_{\Omega_h} + (2\mu\boldsymbol{\epsilon}(\boldsymbol{u}), \boldsymbol{\epsilon}(\boldsymbol{v}))_{\Omega_h} + (\rho(\boldsymbol{u} \cdot \nabla)\boldsymbol{u}, \boldsymbol{v})_{\Omega_h} - (p, \nabla \cdot \boldsymbol{v})_{\Omega_h} \\ &\quad + (q, \nabla \cdot \boldsymbol{u})_{\Omega_h} - \langle(-p\boldsymbol{I} + 2\mu\boldsymbol{\epsilon}(\boldsymbol{u})) \cdot \boldsymbol{n}_h, \boldsymbol{v}\rangle_{\Gamma_h} \end{aligned} \tag{4.65}$$

$$\mathscr{B}(U, V) = (\rho \frac{\partial \boldsymbol{u}}{\partial t} - \nabla \cdot (2\mu\boldsymbol{\epsilon}(\boldsymbol{u})) + \rho(\boldsymbol{u} \cdot \nabla)\boldsymbol{u} + \nabla p - \boldsymbol{f}, \boldsymbol{v})_{\Omega_h \setminus \Omega} + (q, \nabla \cdot \boldsymbol{u})_{\Omega_h \setminus \Omega} \tag{4.66}$$

$$\begin{aligned}\mathscr{N}^k_h(U, V) &= \langle \frac{\rho\phi_u}{\gamma^n h} \mathscr{C}^{T_k}_{\Gamma^n}(\boldsymbol{u}, \mathfrak{p}_{\boldsymbol{n}}), \boldsymbol{v}\rangle_{\Gamma_h} - \langle \mathscr{C}^{T_k}_{\Gamma^n}(\boldsymbol{u}, \mathfrak{p}_{\boldsymbol{n}}), \zeta_u 2\mu\boldsymbol{\epsilon}(\boldsymbol{v})\boldsymbol{n}_h + q\boldsymbol{n}_h\rangle_{\Gamma_h} \\ &\quad + \langle \frac{1}{(\varepsilon \circ \mathfrak{p}_{\boldsymbol{n}}) + \gamma^t h} \mathscr{C}^{T_k}_{\Gamma^t}(\boldsymbol{u}, \mathfrak{p}_{\boldsymbol{n}}), \boldsymbol{v}\rangle_{\Gamma_h} - \langle \frac{\gamma^t h}{(\varepsilon \circ \mathfrak{p}_{\boldsymbol{n}}) + \gamma^t h} \mathscr{C}^{T_k}_{\Gamma^t}(\boldsymbol{u}, \mathfrak{p}_{\boldsymbol{n}}), \zeta_u 2\boldsymbol{\epsilon}(\boldsymbol{v})\boldsymbol{n}_h\rangle_{\Gamma_h} \end{aligned} \tag{4.67}$$

$$\begin{aligned}\mathscr{B}^{\mathscr{N}^k}_h(U, V) &= \langle \frac{\rho\phi_u}{\gamma^n h} \left[\mathscr{C}_{\Gamma^n}(\boldsymbol{u}, \mathfrak{p}_{\boldsymbol{n}}) - \mathscr{C}^{T_k}_{\Gamma^n}(\boldsymbol{u}, \mathfrak{p}_{\boldsymbol{n}})\right], \boldsymbol{v}\rangle_{\Gamma_h} \\ &\quad - \langle \left[\mathscr{C}_{\Gamma^n}(\boldsymbol{u}, \mathfrak{p}_{\boldsymbol{n}}) - \mathscr{C}^{T_k}_{\Gamma^n}(\boldsymbol{u}, \mathfrak{p}_{\boldsymbol{n}})\right], \zeta_u 2\mu\boldsymbol{\epsilon}(\boldsymbol{v})\boldsymbol{n}_h + q\boldsymbol{n}_h\rangle_{\Gamma_h} \\ &\quad + \langle \frac{1}{(\varepsilon \circ \mathfrak{p}_{\boldsymbol{n}}) + \gamma^t h} \left[\mathscr{C}_{\Gamma^t}(\boldsymbol{u}, \mathfrak{p}_{\boldsymbol{n}}) - \mathscr{C}^{T_k}_{\Gamma^t}(\boldsymbol{u}, \mathfrak{p}_{\boldsymbol{n}})\right], \boldsymbol{v}\rangle_{\Gamma_h} \\ &\quad - \langle \frac{\gamma^t h}{(\varepsilon \circ \mathfrak{p}_{\boldsymbol{n}}) + \gamma^t h} \left[\mathscr{C}_{\Gamma^t}(\boldsymbol{u}, \mathfrak{p}_{\boldsymbol{n}}) - \mathscr{C}^{T_k}_{\Gamma^t}(\boldsymbol{u}, \mathfrak{p}_{\boldsymbol{n}})\right], \zeta_u 2\boldsymbol{\epsilon}(\boldsymbol{v})\boldsymbol{n}_h\rangle_{\Gamma_h} \end{aligned} \tag{4.68}$$

$$\mathscr{L}_h(V) = (\boldsymbol{f}, \boldsymbol{v})_{\Omega_h}. \tag{4.69}$$

These terms can be explained in a simple manner. In the domain the term $\mathscr{A}(U, V)$ describes the weak form on the approximated domain Ω_h, $\mathscr{B}(U, V)$ is the error introduced if the approximated domain Ω_h lies outside of Ω and $\mathscr{L}_h(V)$ is the body force acting on the approximated domain. On the boundary, $\mathscr{N}^k_h(U, V)$ defines the imposition of the approximated boundary condition with the Taylor expansion of order k and $\mathscr{B}^{\mathscr{N}^k}_h(U, V)$ is the error the Taylor expansion introduces.

Finally, the discretized weak form of a stabilized unfitted finite element method is attained when the terms $\mathscr{B}$ and $\mathscr{B}^{\mathscr{N}^k}_h$ are dropped. The effect of these terms will not be further investigated

here, but rather assumed that the error introduced from these terms does not dominate the solution for a sufficiently high choice of k for the Taylor expansion. The interested reader is directed to the publication by [66] for a thorough proof on the Poisson equation. The discretized weak form can then be formulated as: find $U_h = (\boldsymbol{u}_h, p_h) \in \mathcal{W}_h$ such that for all $V_h = (\boldsymbol{v}_h, q_h) \in \mathcal{W}_h$ it holds

$$\mathcal{A}(U_h, V_h) + \mathcal{S}_h^*(U_h, V_h) + \mathcal{G}_h^*(U_h, V_h) + \mathcal{N}_h^k(U_h, V_h) = \mathcal{L}_h(V_h), \tag{4.70}$$

where $\mathcal{S}_h^*(U_h, V_h)$ is the stabilization in the domain, i.e. residual based or interior penalty (see Section 2.1.3), and $\mathcal{G}_h^*(U_h, V_h)$ are the ghost penalty terms stabilizing pathological cut cases (see Section 2.3.2.2).

Remark 4.1 *In the publication by Burman* et al. *[66], for the discretized weak form of the Poisson equation the equivalent terms to $\mathcal{B}(U, V)$ and $\mathcal{B}_h^{\mathcal{N}^k}(U, V)$ are omitted and error estimates created to ensure that no loss of convergence occurs. The error estimates for these two terms can not be transferred directly from the Poisson equation to the Navier–Stokes equation, but can give an indication what is to be expected from these terms in the viscous dominated regime. In the aforementioned publication, the equivalent of $\mathcal{B}(U, V)$ for the Poisson problem is estimated to converge with $h^{1/2}\delta_h^{l+1}$ in the energy norm and $\delta_h^{l+3/2}$ in the L^2-norm. The exponent l is determined by the regularity of the problem, in the case of the Poisson equation this comes down to in what space the right hand side resides in for sufficiently smooth domains, i.e. $f \in H^l$. Similarly, the equivalent boundary term to $\mathcal{B}_h^{\mathcal{N}^k}(U, V)$ in the Poisson equation was estimated to converge with $h^{-1/2}\delta_h^{k+1}$ in the energy norm and δ_h^{k+1} in the L^2-norm, where k is the highest order term added from the Taylor expansion $T_{0,k}^{\boldsymbol{n}}$.*

Remark 4.2 *An indication that the presented method is sensible, is the fact that when $k = 0$, i.e. only the zeroth order term in the Taylor expansion is imposed, the standard formulation of a Nitsche boundary condition is retained.*

4.2.2 Second Order Approximation for the Taylor–Couette Flow Problem

To verify the feasibility of this boundary correction method for the general Navier condition in a CutFEM framework, the Taylor–Couette example from Section 4.1.1 is revisited. This example is of particular interest for this higher order case as the domain is convex, i.e. the term $\mathcal{B}$ is not zero by default. In the following, results for second order bi-quadratic $\mathbb{Q}^2$ elements will be presented. From Remark 4.1 it was found that if $\delta_h \sim h^2$, only a first order Taylor expansion is needed to attain optimal order of convergence for the Poisson problem. Hence, taking this result as a guideline, only a first order Taylor expansion will be considered in the following. For the convenience of the reader the first order expansion is shown here,

$$T_{0,1}^{\boldsymbol{n}}(\boldsymbol{u})(\boldsymbol{x}) = u_i(\boldsymbol{x}) + \frac{\partial u_i(\boldsymbol{x})}{\partial x_j} n_j(\boldsymbol{x}) d_{\boldsymbol{n}}(\boldsymbol{x}) \tag{4.71}$$

$$T_{0,1}^{\boldsymbol{n}}(2\boldsymbol{\epsilon}(\boldsymbol{u}))(\boldsymbol{x}) = \left(\frac{\partial u_i(\boldsymbol{x})}{\partial x_j} + \frac{\partial u_j(\boldsymbol{x})}{\partial x_i}\right) + \left(\frac{\partial^2 u_i(\boldsymbol{x})}{\partial x_j \partial x_k} + \frac{\partial^2 u_j(\boldsymbol{x})}{\partial x_i \partial x_k}\right) n_k d_{\boldsymbol{n}}(\boldsymbol{x}), \tag{4.72}$$

where indices are summed in accordance with Einstein notation.

To attain a point of reference, in Figure 4.19 the result when a zeroth-order Taylor expansion term is imposed and no projection is chosen, i.e. $\mathfrak{p}_{\boldsymbol{n}}(\boldsymbol{x}) = \boldsymbol{x}$, is depicted. As the issues stemming from a piecewise constant normal were already studied in Section 4.1.1 a smoothed projection matrix is chosen right from the start, i.e.

$$\boldsymbol{P}^n = \widetilde{\boldsymbol{n}_h} \otimes \widetilde{\boldsymbol{n}_h}, \tag{4.73}$$

constructed by a L^2-projection of the level-set gradient. From Figure 4.19, it is immediately apparent that the convergence of the velocity $\boldsymbol{u}_h$ is only $\mathcal{O}(h^2)$, as can be seen in the top left image for the error in the domain, which is less than what optimally should be attainable with $\mathcal{O}(h^3)$. Additionally, the interface errors of the pressure and velocity gradient seem to also have issues converging with optimal order in the asymptotic limit, as seen on the right side of the second and third row of the Figure, respectively. Relating the attained results to the analysis of the Poisson problem in Remark 4.1, the L^2-error estimate obtained in the publication [66] predicts (given $\delta_h \lesssim h^2$) that the primary variable converges with h^2 without correction terms. Furthermore, it is predicted that in the energy norm only a $h^{1.5}$ convergence should be obtained instead of the optimal order h^2. In the case of the L^2-error of the velocity, the predictions of the analysis of the Poisson problem can be applied to the Navier–Stokes problem as well, as the reduction to h^2 can be observed. However, for the energy norm, it is not as apparent that it loses half an order of convergence, even though the interface norms of the pressure and velocity gradient show tendencies towards this.

Given the way the smoothing of the projection matrices is done with a L^2-projection of the level-set gradient, the error of the smoothed normal vector on the interface Γ_h is depicted in Figure 4.20. In this Figure, it is clear, that even though ϕ_h now has a higher order approximation with $\mathbb{Q}^2$ than in the linear case of Section 4.1.1.2, the L^2-projection still only delivers a convergence with $\mathcal{O}(h^2)$. As such, it can be concluded that in the linear case, a super convergence of the normal vector was observed. Furthermore, as this normal vector has lower order of convergence than the optimal order of $\boldsymbol{u}_h$, it would be expected from the results in Section 4.1, that this error, at some point, will also affect the convergence.

To compare the results obtained without any projection or additional Taylor expansion terms, a simulation is carried out with a projection of the boundary values with $\mathfrak{p}_{\phi_h}$ and the Taylor expansion with

$$T^{\phi_h}_{m,k}(\boldsymbol{u})(\boldsymbol{x}) = \sum_{i=m}^{k} \frac{D^j_{\boldsymbol{n}_{\phi_h}} \boldsymbol{u}(\boldsymbol{x})}{j!} \phi_h^j(\boldsymbol{x}), \tag{4.74}$$

where $m = 0$ and $k = 1$ with the normal $\boldsymbol{n}_{\phi_h}$ defined as

$$\boldsymbol{n}_{\phi_h} = \frac{\widetilde{\nabla \phi_h}}{|\widetilde{\nabla \phi_h}|}.$$

Herein $\widetilde{\nabla \phi_h}$ is the L^2-projected gradient of the discretized level-set function ϕ_h, which is construed in the same way as $\widetilde{\boldsymbol{n}_h}$ is. Hence, the Taylor expansion is executed in the same way as the projection $\mathfrak{p}_{\phi_h}$, as to stay consistent. The smoothed projection matrix $\boldsymbol{P}^n = \widetilde{\boldsymbol{n}_h} \otimes \widetilde{\boldsymbol{n}_h}$ is still employed in the following (even though it exhibits suboptimal order of convergence) to

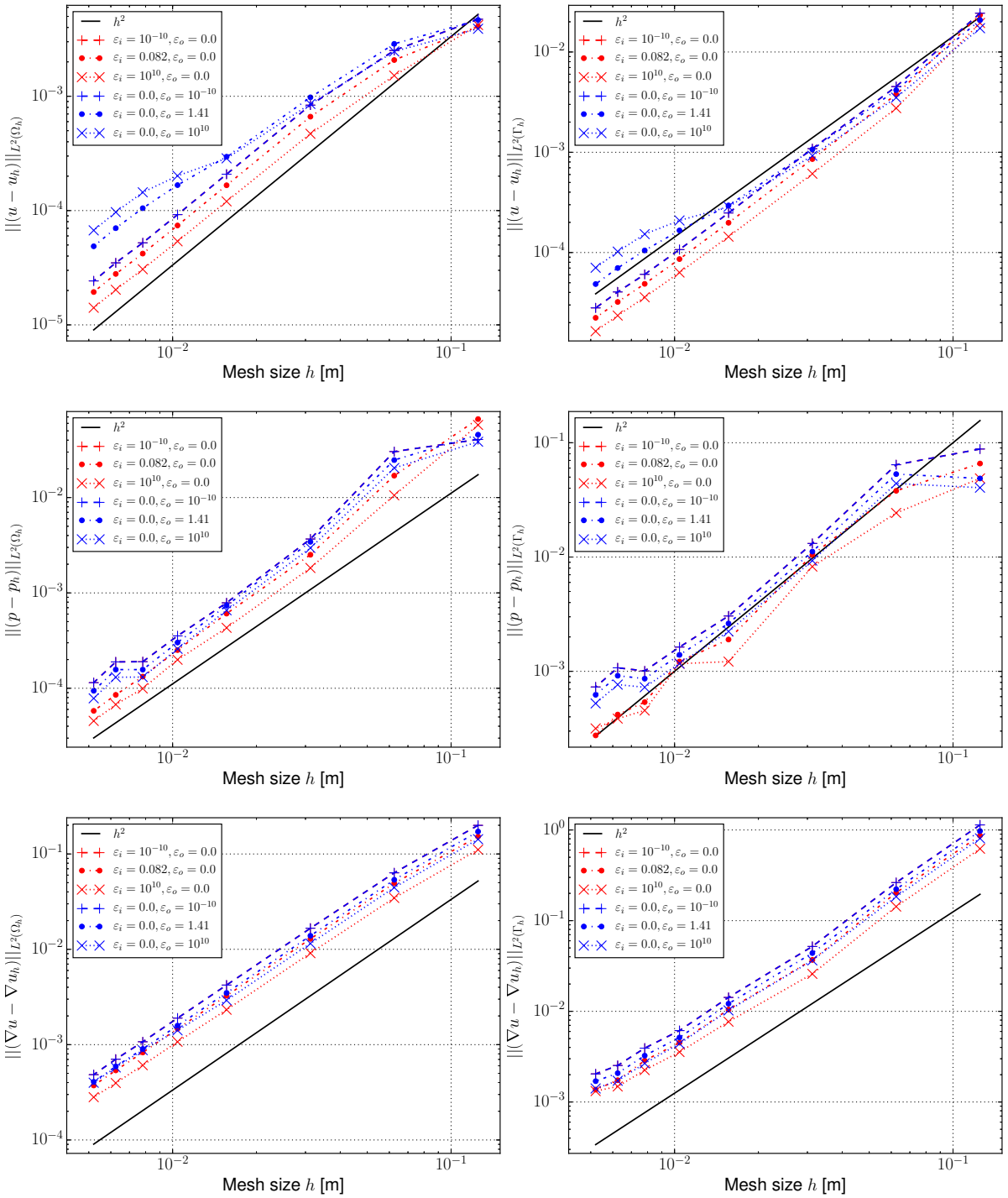

Figure 4.19: Error convergence study for an adjoint-inconsistent Nitsche's method with $\mathbb{Q}^2$ elements, a smoothed normal $\widetilde{\boldsymbol{n}}_h$ on the boundary and no projection or higher order Taylor expansion terms, i.e. $\mathfrak{p}_{\mathbf{0}}(\boldsymbol{x}) = \boldsymbol{x}$ and $T^{\boldsymbol{n}}_{0,0}$ is employed. Bulk errors (left column) and boundary errors (right column) for velocity, pressure and velocity gradient (from top to bottom).

demonstrate the improvement stemming from the projection $\mathfrak{p}_{\phi_h}$ and the addition of additional Taylor expansion terms.

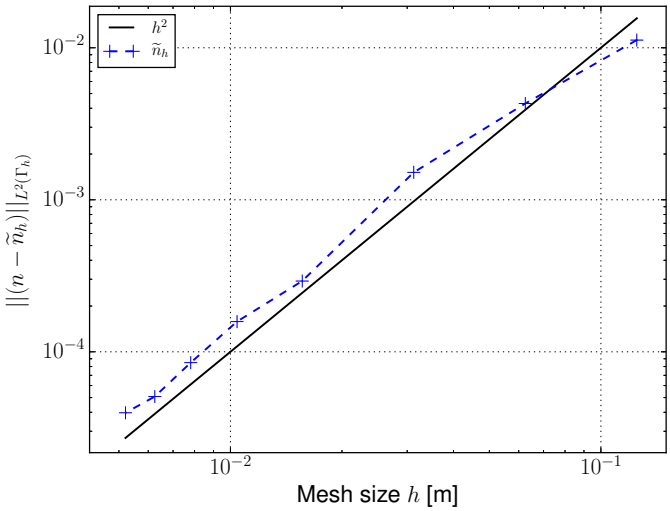

Figure 4.20: Error convergence study for the smoothed normal $\widetilde{\boldsymbol{n}}$ created from the L^2-projection of the gradient of ϕ_h, which is approximated by $\mathbb{Q}^2$ elements.

In Figure 4.21 the results of the changed projection $\mathfrak{p}_{\phi_h}$ and the addition of first order Taylor expansion terms is noticeable. What immediately catches the eye, is the fact that in the domain Ω_h the velocity converges with the order h^3 now instead of h^2, as seen in the top left image of the figure. Also noticeable is that the pressure, in comparison to Figure 4.19, is not as sensitive to the cut configuration and has less fluctuations, as seen in the mid left row of Figure 4.21. The gradient of the velocity is not influenced particularly from the aforementioned changes, at least not in a way which can be detected from the depicted graphs. Nonetheless, it is apparent that the velocity and its gradient in the case of changing slip length on the inner cylinder starts to deviate from the optimal convergence of h^3 in the asymptotic limit, as can be seen in the top right and lower right subfigures of Figure 4.21. In particular the case with $\varepsilon_i = 10^{10}$ and $\varepsilon_o = 0$ starts deviating before the others. This behavior could be explained by the error introduced from the projection matrix. Given that the curvature of the inner cylinder is larger than on the outer one, the approximated normal error would be expected to be larger here as well.

As is suspected above, the approximation of $\boldsymbol{P}^n$ and $\boldsymbol{P}^t$ might lie at the root of the deteriorating convergence for the velocity and its gradient on the interface. To test this, the approximation of the projection matrices need to be improved. Either the underlying order of the elements for the level-set ϕ_h needs to be increased, or a better approximation of $\boldsymbol{n}$ needs to be provided. In this case the latter is chosen to demonstrate the effect of the quality of the projection matrix. The normal of choice for this will be the analytic normal $\boldsymbol{n}(\boldsymbol{x})$ as introduced in (4.34). This choice of normal for the projection matrices is obviously not an available choice for most simulations. Nevertheless, by removing this source of error, insight can be gained in the importance of this term. As such, the results of this choice are demonstrated in Figure 4.22. From this Figure, it is clearly visible that the solution with $\varepsilon_i = 10^{10}$ and $\varepsilon_o = 0$ has improved and is now converging without losing its order of convergence for the velocity and its gradient on the the interface Γ_h. This result strongly supports the claim on the importance of the quality of the approximation for the projection matrices $\boldsymbol{P}^n$ and $\boldsymbol{P}^t$. It also gives further proof to the hypothesis that the normal used for the creation of these projection matrices should converge with at least the desired order of the velocity $\boldsymbol{u}_h$, if optimal order of convergence is to be achieved when the boundary condition

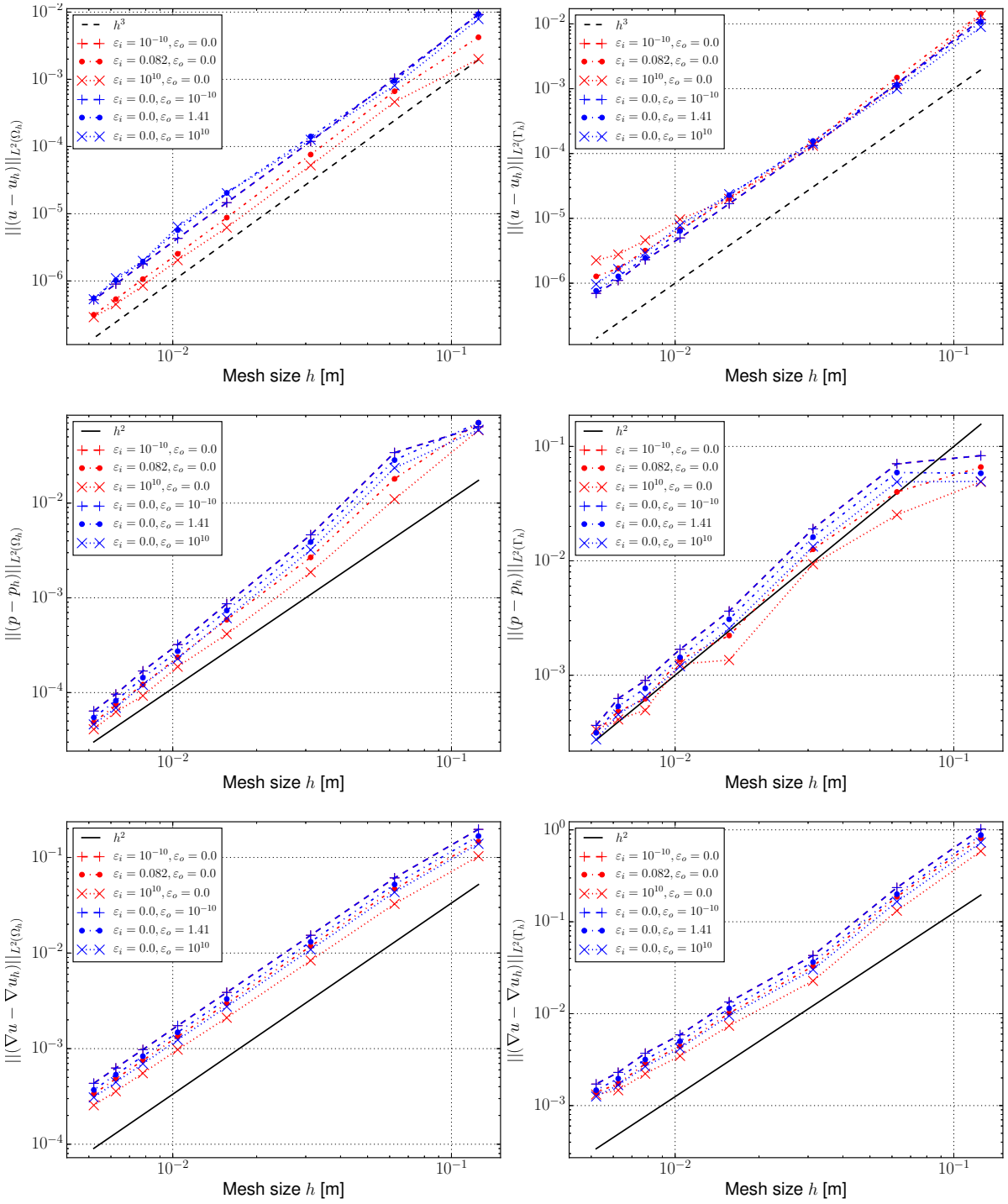

Figure 4.21: Error convergence study for an adjoint-inconsistent Nitsche's method with $\mathbb{Q}^2$ elements, a smoothed normal $\widetilde{\boldsymbol{n}}_h$ on the boundary Γ_h, a projection of the boundary values with $\mathfrak{p}_{\phi_h}$ and first order Taylor expansion employed, i.e. $T^{\phi_h}_{0,1}(\boldsymbol{u})$ and $T^{\phi_h}_{0,1}(\boldsymbol{\epsilon}(\boldsymbol{u}))$ on the boundary Γ_h. Bulk errors (left column) and boundary errors (right column) for velocity, pressure and velocity gradient (from top to bottom).

is imposed by the Nitsche's method for the GNBC. Furthermore, when higher order elements

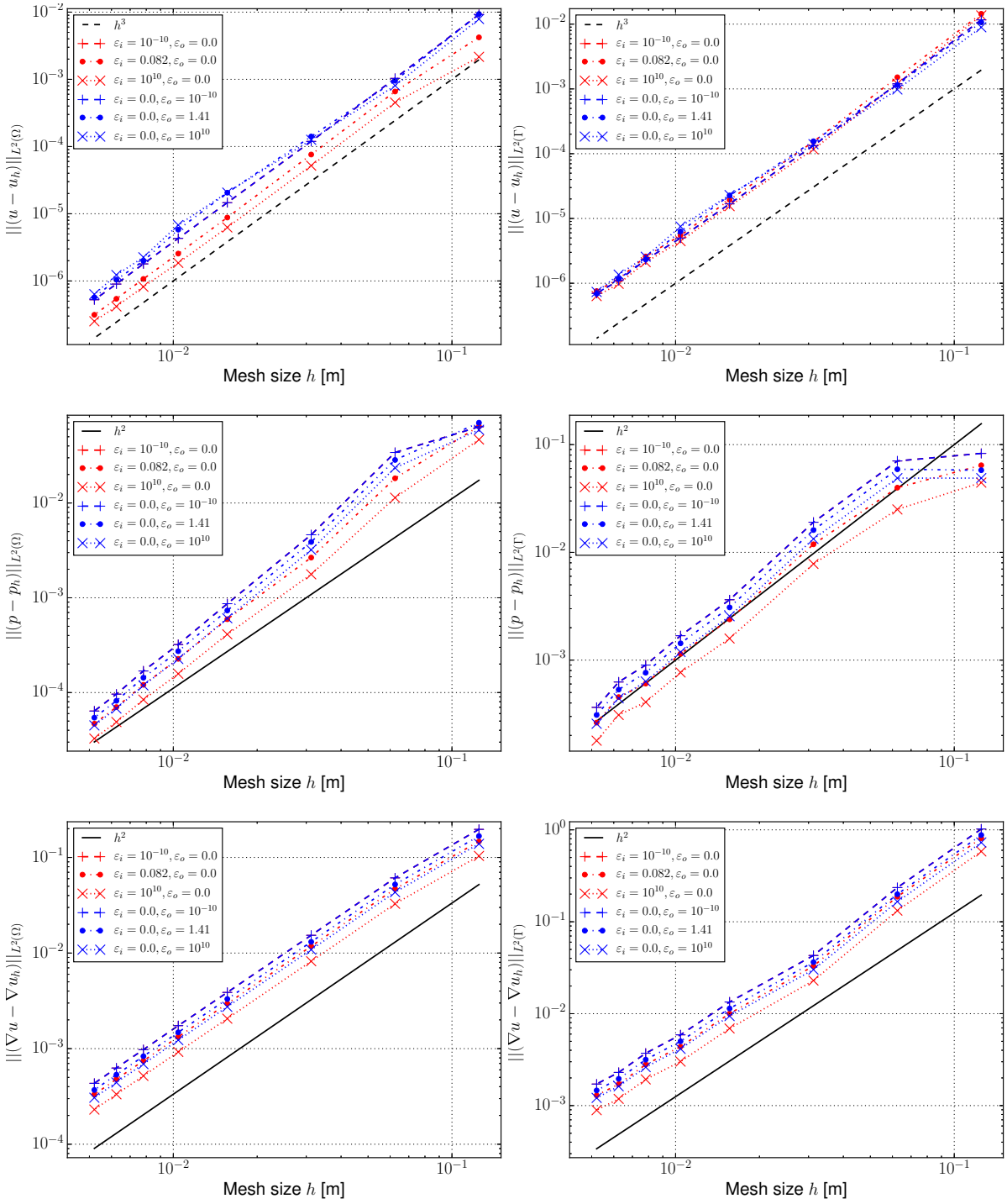

Figure 4.22: Error convergence study for an adjoint-inconsistent Nitsche's method with $\mathbb{Q}^2$ elements, the analytic normal $\boldsymbol{n}$ on the boundary Γ_h, a projection of the boundary values with $\mathfrak{p}_{\phi_h}$ and first order Taylor expansion employed, i.e. $T^{\phi_h}_{0,1}(\boldsymbol{u})$ and $T^{\phi_h}_{0,1}(\boldsymbol{\epsilon}(\boldsymbol{u}))$ on the boundary Γ_h. Bulk errors (left column) and boundary errors (right column) for velocity, pressure and velocity gradient (from top to bottom).

are utilized it is also verified that, at least for quadratic elements, some form of boundary value

correction needs to be carried out to ensure that the errors stemming from $\mathscr{B}$ and $\mathscr{B}_h^{\mathcal{N}^k}$ are not dominating the error of the weak form. In the observed case with bi-quadratic elements, the projection with $\mathfrak{p}_{\phi_h}$ and a Taylor expansion carried out with $\boldsymbol{n}_{\phi_h}$ was deemed sufficient to keep the optimal order of convergence. Nonetheless, more investigation into the behavior of this formulation for higher than second order elements is necessary in future research.

Chapter 5

Towards a Computational Model for Wetting Processes with the General Navier Condition

As was already mentioned in the introduction of the General Navier boundary condition (see Section 3.1), one of the places it comes up in physical models is for wetting processes. This phenomenon will be further investigated in this chapter, and in particular into how a general Navier slip method can be applied in the case of multiphase flow systems with Moving Contact Lines (MCL). These systems appear in a plethora of different applications and phenomena important for both industrial applications as well as natural processes. One example is droplet impact with spreading and splashing phenomena which can be encountered in technical applications such as ink-jet printing, fire suppression by sprinklers and internal combustion engines, to name a few; a review article on these phenomena was done by Yarin [280]. Another area of importance lies in microfluidics, where applications can be found in, for instance, drug screening, thermal management of semiconductors and forensic analysis, see Darhuber and Troian [81] for an overview on this topic. Furthermore, in heat exchange systems and in cooling of high-energy density electronic components the presence of nucleate boiling makes these type of systems also contain moving contact lines, as bubbles form on the solid surface. A review on nucleate boiling can be found in Dhir [89]. One final example where the presence of moving contact lines is important is multiphase flow in porous media, as the length scale of the cavities make surface tension forces important; for more information on this topic, see the review article by Adler and Brenner [2].

The physics and physical modeling regarding the motion of contact lines are still a topic of debate in the scientific community, as stressed in the review article by Sui *et al.* [257] and the article by Kirkinis and Davis [168]. The chapter starts by giving a short review of the physics of capillary systems with contact lines in Section 5.1. The static and dynamic cases are presented, and arguments are given why the modeling of dynamic wetting processes is still a topic under investigation. In Section 5.2 existing numerical approaches are briefly reviewed and a sharp interface model is chosen to implement a novel localized slip method with the general Navier boundary condition in a CutFEM framework. The weak form and its associated discretized form are presented in the subsequent subsections. To conclude the chapter, two numerical examples are conducted in Section 5.3. First, a simulation of a static droplet with large contrast in material parameters is carried out. Error studies for this example investigate the most promising approach

regarding the imposition of surface tension forces and smoothing of level-set gradients. The section is finalized with a dynamic droplet spreading to highlight the strengths and shortcomings of the proposed method.

5.1 Physics and Modeling of Wetting Processes

First of all, modeling a fluid is modeling the motion of its molecules at its core. Approaches where the molecules are modeled to determine the motion of a fluid have been used to better understand moving contact lines in for instance, Koplik *et al.* [170], Koplik *et al.* [171] and Thompson and Robbins [264]. The drawback of these simulations is the fact that they are restricted to systems of approximately two orders of magnitude larger than the molecular length scale, as highlighted in Sui *et al.* [257]. To be able to conduct simulations of sizes larger than this, the standard approach is to apply the continuum hypothesis, which assumes that a fluid behaves as a continuum. For liquids at ambient conditions the continuum hypothesis already holds at length scales of 10 nanometers, as reported in Tryggvason *et al.* [266]. Furthermore, in molecular dynamics simulations, Koplik *et al.* [170] were able to recreate Poiseuille flow with a channel containing a couple of hundred molecules.

5.1.1 Treatment of the Interface between Two Immiscible Fluids

Given that two-phase flow is considered here, the thickness of the interface between the two phases is also a length which becomes important to consider. In Figure 5.1 the issue where to set the interface between two immiscible fluids, depicted as a positive Ω^+ and a negative Ω^- fluid phase, is illustrated. Two possible paths can be pursued. One path is to model the

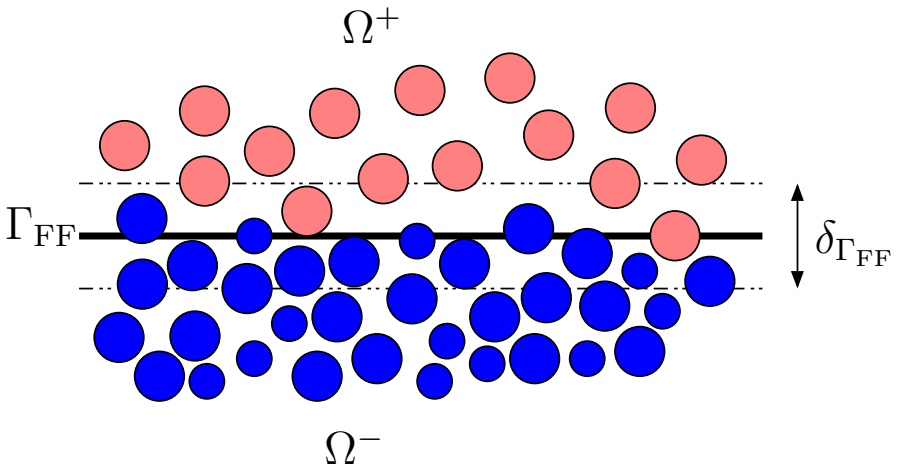

Figure 5.1: Visualization of the roughness, $\delta_{\Gamma_{\mathrm{FF}}}$, of an interface, Γ_{FF}, between two immiscible fluids, where the phases are given as a positive Ω^+ and negative Ω^- fluid phase.

interface with a finite thickness $\delta_{\Gamma_{\mathrm{FF}}}$, as first proposed in the phase field model by Korteweg [172]. The other possibility is to model this interfacial region as a two-dimensional dividing surface Γ_{FF}. In the case of the dividing surface, to take effects from the interfacial region into

consideration, *excess* quantities are introduced (such as mass and energy) to the surface Γ_{FF}. For the excess mass density a *surface* mass density $\rho^{\Gamma_{\mathrm{FF}}}$ is introduced. If this quantity is assumed as $\rho^{\Gamma_{\mathrm{FF}}} = 0$, a *clean interface model* is employed. This clean interface model is used in most sharp interface models without the presence of tensides, as reported by Groß and Reusken [133]. Nonetheless, other models which take into consideration interface formation processes, do not make this assumption such as the model proposed by Shikhmurzaev [240].

When modeling a fluid with the continuum hypothesis, intermolecular forces are usually neglected inside the fluid. Nevertheless, these forces can not be neglected in the interfacial region between two immiscible fluids. The following explanations of surface tension and contact lines are taken from the text book by Lautrup [174]. On a molecular scale, the surface tension force stems from the fact that on both sides of the interface there exist different molecules, and they have different attractive properties (van der Waals forces). Thus surface tension is a force stemming inherently from molecular interaction. The transition layer between two materials (not necessarily fluids) on a macroscopic scale is viewed as a thin sheet, and in the continuum limit appears as a surface. This surface can, nonetheless, posses macroscopic properties such as a surface energy. The *surface energy* per unit area $[\mathrm{J/m^2}]$ is equivalent to a force per unit length $[\mathrm{N/m}]$ and is referred to as a *surface tension*. However, this equivalency has been disputed in for instance Finn [113, 114], where it is argued that the perspective of surface energy density is the only correct one. In this thesis, the expressions will be used interchangeably, as is done in the majority of publications on this topic, and will be denoted as σ. Another important observation on surface energy density is that it is positive for non-mixable fluids. A possible interpretation on the process of dissolving two solvable fluids is that the interface between the two fluids has a negative surface energy, and hence tries to maximize the area between the fluids.

5.1.2 Importance of Capillary Effects and the Bond Number

When modeling physical systems, it is important to keep in mind when an effect dominates and when it is negligible. Capillary effects, stemming from the surface tension, are no exception. For a two-phase flow system, there are four forces which influence the system: capillary forces, body forces, inertial forces and viscous forces. Normally either one or two of these forces are dominating the system and the others can be neglected, as emphasized by Dodge [92]. Assuming a system at rest, only gravitational (i.e., body forces) or capillary forces will be dominating the system. The force which is dominating the system can be be determined by the Bond number, defined as

$$\mathrm{Bo} = \frac{\Delta\rho g L^2}{\sigma} \sim \frac{\textit{body forces}}{\textit{surface tension}}.$$

where g is the gravitational acceleration, $\Delta\rho = |\rho^+ - \rho^-|$ the difference in density between the two fluids and L the characteristic length of the system. From this dimensionless number, it can be inferred at what length scale capillary forces start to dominate. This length scale is usually called the capillary length, and is given as

$$l_\sigma = \sqrt{\frac{\sigma}{\Delta\rho g}}.$$

For a common air-water system, a capillary length of about 2.7 [mm] is obtained. Hence, if the modeled system is much larger than this capillary length, capillary effects can be neglected, as

is stressed in De Gennes *et al.* [85]. Consequently, if for instance the motion of a swimming pool or a harbor is to be modeled, capillary effects will not effect the outcome of the solution by much. In contrast, when modeling the motion of a water strider on a water surface, capillary effects become detrimental to model the system correctly. Additionally, when there is an absence of body forces, such as in a zero-g environment of a satellite, capillary effects always need to be considered for a stationary system as there are no other forces to dominate over them.

5.1.3 Capillary Systems in Equilibrium

The surface separating two immiscible fluids can be divided into surfaces not intersecting a wall and surfaces that do, i.e. a system with a contact line. Primarily, surface tension effects away from the contact line will be investigated and afterwards, the special case at a contact line is dealt with.

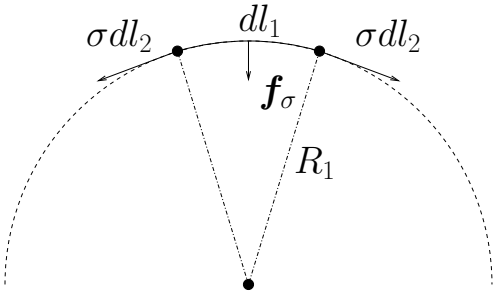

Figure 5.2: An excerpt of the rectangular piece of the $dl_1 \times dl_2$ surface, with the forces illustrated along the 1-direction, resulting in the normal force pointing to the center of the curvature.

In a stationary system, a pressure jump at the interface between two phases is caused by the curvature of the surface and the surface tension. Imagine a rectangular excerpt $(dl_1 \times dl_2)$ of a surface Γ, with the sides aligned along the principal directions. Unless the rectangular excerpt is planar it has two principal radii of curvature. Applying a force balance, the forces acting on this surface stem from the forces acting along the lines σdl_1 and σdl_2 and the pressure difference acting in the direction normal to the rectangular segment, see Figure 5.2 for an illustration of this in the 1-direction. As the line forces are acting from "opposite sides" the tangential component along the surface disappears (as long as the surface energy density is not varying). However, in the normal direction of the surface, a force $\boldsymbol{f}_\sigma$ pointing toward the center of the circle of curvature appears. This resulting force needs to be compensated by a pressure jump. The following force balance can be set up,

$$\boldsymbol{f}_\sigma(dl_1 \times dl_2) = 2\sigma(dl_1 \times dl_2)/2R_1 + 2(\sigma dl_2 \times dl_1)/2R_2 = \Delta p(dl_1 \times dl_2).$$

Given that the expression can be shortened by $(dl_2 \times dl_1)$, the Young–Laplace equation is retained as,

$$\sigma\kappa = \Delta p, \tag{5.1}$$

where $\kappa = 1/R_1 + 1/R_2$ is the mean curvature. The case of non-stationary systems will be treated later.

Remark 5.1 *From the Young–Laplace equation* (5.1) *it is clear that a contribution to the pressure discontinuity is always positive on the side of the surface containing the center of curvature, otherwise it is negative. This explains for instance why champagne bubbles pop louder than beer bubbles. As the bubbles of champagne are smaller, the pressure discontinuity is larger than*

the larger bubbles in beer. Hence, it is possible to hear the bubbles breaking the surface in champagne, whereas it is usually not in beer.

The next case is to study the equilibrium at a contact line. The forces acting on the point stem from three interfaces, $\Gamma_{\mathrm{FF}} = \Omega^+ \cap \Omega^-$, $\Gamma_{\mathrm{G}}^+ = \Omega^+ \cap \Gamma_{\mathrm{G}}$ and $\Gamma_{\mathrm{G}}^- = \Omega^- \cap \Gamma_{\mathrm{G}}$ and are depicted in Figure 5.3. For an ideal surface Γ_{G} (i.e. without roughness and impurities), Young's equation [281] holds at the contact line $\partial\Gamma_{\mathrm{FF}}$ in the tangential plane of the surface Γ_{G} as,

$$\begin{aligned} \mathbf{0} &= -\sigma \cos\theta_e \boldsymbol{m}_S - \sigma_{s+}\boldsymbol{m}_S + \sigma_{s-}\boldsymbol{m}_S \\ &= -\sigma \cos\theta_e \boldsymbol{m}_S - [\![\sigma_s]\!]\boldsymbol{m}_S. \end{aligned} \tag{5.2}$$

Here, σ is the surface energy of the interface Γ_{FF} between the two fluids in the domains Ω^+ and Ω^-, the vector $\boldsymbol{m}_S$ lies in the plane of Γ_{G} and normal to the line $\partial\Gamma_{\mathrm{FF}}$. Furthermore, the surface energy between the positive fluid phase Ω^+ and the surface Γ_{G} is defined as σ_{s+} and in the same fashion σ_{s-} is defined between the negative fluid phase Ω^- and Γ_{G}. The equilibrium contact angle

$$\cos(\theta_e) = \boldsymbol{m} \cdot \boldsymbol{m}_S,$$

can be constructed from the normals at the contact line $\partial\Gamma_{\mathrm{FF}}$, where $\boldsymbol{m}$ is the tangential vector of the surface Γ_{FF} intersecting the contact line as depicted in Figure 5.3. From the above Young's equation, the spreading parameter S can be defined as

$$S = E(\Gamma_{\mathrm{G}})_{\mathrm{dry}} - E(\Gamma_{\mathrm{G}})_{\mathrm{wet}} = \sigma_{s-} - (\sigma_{s+} + \sigma), \tag{5.3}$$

where $E(\Gamma_{\mathrm{G}})_{\mathrm{dry}}$ is the surface energy in the dry configuration (i.e. encapsulated in the negative fluid phase) and $E(\Gamma_{\mathrm{G}})_{\mathrm{wet}}$ is the surface energy in the wet configuration (i.e. the surface created from the positive fluid phase and the contact line). If $S < 0$ partial wetting occurs which implies that $\theta_e > 0$, else if $S > 0$ total wetting occurs instead, where the positive fluid phase spreads completely in a film with nanoscopic thickness on Γ_{G}. These results are well known and for a more thorough derivation of them see De Gennes *et al.* [85] or Lautrup [174].

Remark 5.2 *The normal component of the force $-\sigma\boldsymbol{m}$ to the surface Γ_{G} is usually not considered when force balances are set up at the contact line. The solid is often assumed to be rigid, and consequently, the force is absorbed by the solid. In practice, this force can deform a soft solid and the ensuing surface stresses, stemming from the interaction with the contact line, are of importance in thin films as reported by Style* et al. *[251]. For more details on this vertical deformation of the solid in the vicinity of the contact line, also known as a wetting ridge, the review article by Yu [282] and the references therein are recommended.*

Remark 5.3 *Young's equation is valid for a clean surface, however in practice all surfaces exhibit chemical or geometrical heterogeneities as reported by De Gennes [84]. This fact leads to the phenomenon known as contact angle hysteresis, in which the static contact angle has a range of $\theta_R < \theta_e < \theta_A$. Here θ_A is the advancing contact angle and θ_R the receding contact angle as detailed in Snoeijer and Andreotti [242]. It is owing to this contact line hysteresis that it is possible to capture a liquid column in a vertical capillarity. This equilibrium only holds true if*

$$\frac{2\sigma}{R}\left(\cos(\theta_R) - \cos(\theta_A)\right) > \rho g H,$$

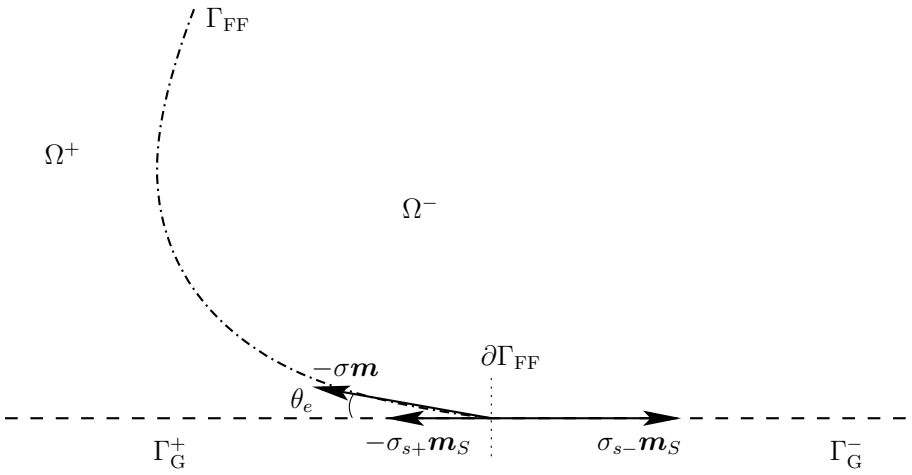

Figure 5.3: The illustration shows the interfaces Γ_{FF} between two fluid phases Ω^+ and Ω^- intersecting the solid boundary Γ_{G}, creating a contact line $\partial\Gamma_{\mathrm{FF}}$ and partitioning the boundary Γ_{G} into Γ_{G}^+ and Γ_{G}^-. Furthermore, the "pull" of these interfaces at the contact line $\partial\Gamma_{\mathrm{FF}}$ is depicted with the forces: $-\sigma\boldsymbol{m}$ from Γ_{FF}, $-\sigma_{s+}\boldsymbol{m}_S$ from Γ_{G}^+ and $\sigma_{s-}\boldsymbol{m}_S$ from Γ_{G}^-.

where R is the radius of the capillarity and H the height of the column. In the book by De Gennes et al. *[85] the hysteresis is estimated to be about $5°$ on a "good" surface and up to $50°$ on a "dirty" surface.*

5.1.4 Capillary Systems in Motion

The theory of capillary systems in equilibrium has been thoroughly studied and models such as Young's equation (5.2) have been derived and verified in practical experiments. By contrast, moving contact lines remain to this day an open field of research. It is still not well understood how exactly the contact line propagates, as reported by Kirkinis and Davis [168]. What was discovered early is the fact that a no-slip condition in the vicinity of the contact line is not a feasible choice, as it leads to the integrated shear stress of the fluid to be unbounded, which has been demonstrated in Huh and Scriven [151], Moffatt [194] and Dussan V and Davis [104].

When considering moving contact lines, the scale at which the system is observed becomes detrimental. For instance, on a microscopic scale it can be observed that the contact line does not slide along the surface, but rather exhibits a rolling motion, as reported in Dussan V and Davis [104] and Dussan V [103], whereas on the macroscopic scale this rolling motion is not observable. This issue of a macroscopic and microscopic view of the contact line, becomes prevalent also in measurements of the contact angle. When measurements are conducted, the *apparent contact angle* θ_a is measured which is on a macroscopic scale, whereas the actual contact angle, named the *dynamic contact angle* θ_d, is only observable at the microscopic scale. A depiction of this phenomena is given in Figure 5.4.

It is nowadays generally accepted that dissipation controls the dynamics of a moving contact line, as reported by de Ruijter *et al.* [86]. From the publication by De Gennes [84], the out-of-balance surface tension force

$$\boldsymbol{f}_{\theta_d} = \sigma(\cos(\theta_e) - \cos(\theta_d))\boldsymbol{m}_S, \tag{5.4}$$

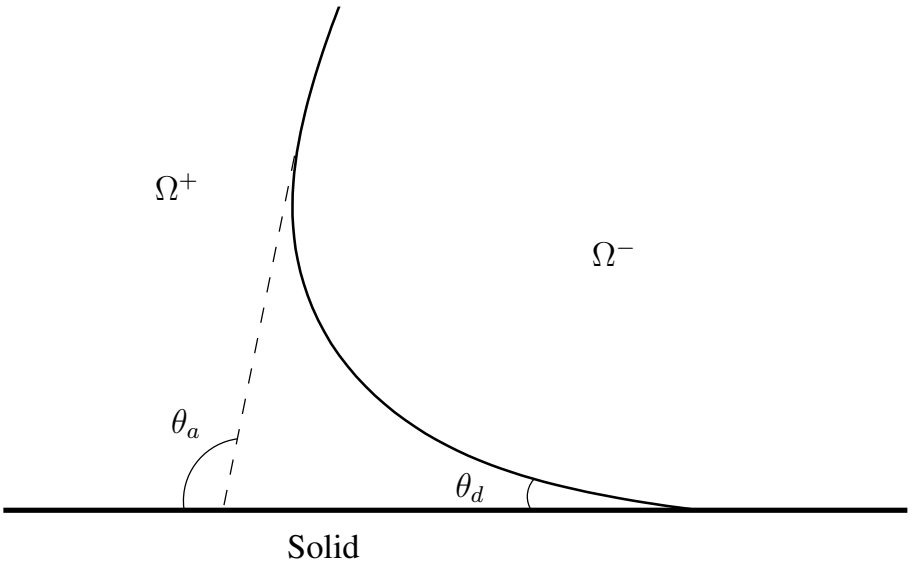

Figure 5.4: A visualization of the macroscopic measurable apparent contact angle θ_a and the actual microscopic dynamic contact angle θ_d.

can be compensated by three channels of dissipation: viscous dissipation, dissipation in the precursor film (only important in the case of complete wetting, i.e. $\theta_e = 0$) and dissipation in the close vicinity of the solid in proximity of the contact line. In the case of partial wetting, the viscous dissipation can be described by the the hydrodynamic approach as introduced by Voinov [275] and Cox [77] and the dissipation near the contact line by molecular-kinetic theory as first considered in Blake and Haynes [34]. It is suggested in the review article by Snoeijer and Andreotti [242] that for a sufficiently large capillary number

$$\mathrm{Ca} = \frac{\mu U_{\mathrm{CL}}}{\sigma} \sim \frac{\textit{viscous forces}}{\textit{surface tension}}, \tag{5.5}$$

where U_{CL} is the contact line velocity, the viscous dissipation will be dominating. The transition between where these two dissipations dominate is postulated to occur around $\mathrm{Ca} \approx 10^{-4}$ or $\mathrm{Ca} \approx 10^{-5}$. A difficulty in the modeling of the viscous dissipation is the fact that the dissipation of the contact line occurs between the macroscopic length determined by the capillary length l_σ ($\sim 10^{-3}$ [m]) and the microscopic scale ($\sim 10^{-9}$ [m]), determined by the molecular size. According to Snoeijer and Andreotti [242] each decade between these scales contributes a comparable amount to the viscous dissipation, thus showing the multiscale character of a wetting flow

An alternative model for the motion of the contact line stems from the interface formation theory suggested by Shikhmurzaev [240]. This model builds upon the publication by Bedeaux *et al.* [29] on non-equilibrium thermodynamics of two immiscible fluids and their interface, and extends it to include contact-lines. This approach has the advantage, compared to the theory by Cox for viscous dissipation, that it can take hydrodynamic assist into consideration, i.e. the case when the bulk flow affects the motion of the contact line strongly.

The possibility exists to model the contact line by molecular dynamics (MD) or hybrid-MD models, however these approaches are restricted to very small systems, as highlighted in Bonn *et al.* [38].

Even though different models have been proposed to describe the motion of a contact line, the difficulty in finding the correct model is discussed in Seveno *et al.* [236], where different models were fitted to experimental data and more than one was able to provide good results.

Remark 5.4 *Given that a no-slip condition has been deemed unfeasible from a modeling point of view, by for instance Huh and Scriven [151], a reasonable inquiry might be if slip can be measured or observed in the vicinity of a moving contact line? This can indeed be verified as large apparent slip velocities and slip lengths were observed in Qian* et al. *[214], even for low capillary numbers* Ca *and over a relatively large region around the contact line. Additionally, from molecular dynamics (MD) simulations it can be observed that almost complete slip occurs at the moving contact line as reported in Koplik* et al. *[170, 171] and Thompson and Robbins [264].*

5.2 Numerical Modeling of Moving Contact Lines

Given that the physics regarding the motion of the contact line is still an active topic of research, it comes as no surprise that there exist several approaches to simulate flows with moving contact lines. In the following, only macroscopic models will be considered, and hence, molecular dynamics or hybrid-molecular dynamics simulations will be omitted.

One of the more popular approaches is to model the interface Γ_{FF} between the two phases with a clean interface model, i.e. the surface mass density $\rho^{\Gamma_{\mathrm{FF}}} = 0$. The motion of the contact line $\partial\Gamma_{FF}$ can then be modeled with an out-of-balance force with the option of adding dissipation at the contact line. The publications by Bänsch [16] and Gerbeau and Lelievre [124] employ this approach with an ALE method to simulate free-surface flow with no dissipation considered at the contact line. This no-dissipation at the contact line approach has also been done in a VOF approach by Renardy *et al.* [219]. The publication by Ganesan and Tobiska [122] also does not consider dissipation at the contact line, however, a first attempt at incorporating contact line hysteresis is made. In the publications by Afkhami *et al.* [3] and Manservisi and Scardovelli [181], attempts at introducing dissipation for the moving contact line are done where the mesh size and Cox's theory [77] are used to model the viscous dissipation in the former and a power law in the latter. An important publication for clean interface models was done by Buscaglia and Ausas [68], where a derivation from the assumption of a sharp, clean interface with an associated surface energy was conducted. In this publication the principal of virtual work is utilized to derive the formulations associated with two phase flow and moving contact lines. It also correlates the above mentioned publications to the formulation in [68]. Recently, a publication by Reusken *et al.* [222] utilized the XFEM to simulate moving contact line flows with an out-of-force balance model. Nevertheless, this approach only uses a discontinuous space for the pressure, whereas the velocity is modeled as continuous.

In contrast to using a force at the contact line $\partial\Gamma_{\mathrm{FF}}$, the contact angle can be imposed instead. This type of approach utilizes Cox's theory to relate the velocity at the contact line to the contact angle. More on this method can be found in Dupont and Legendre [101], Spelt [245], Sui and

Spelt [256] and the references therein. Some methods try to circumvent the necessity of a slip condition in the vicinity of the contact line by introducing diffusion to the motion of the interface, mimicking the phase field method [154], while still adhering to a sharp interface model. This approach was first introduced by Zahedi *et al.* [284] and has later been used in the works by Sato and Ničeno [227] and Heimann [140].

In the diffusive interface model proposed by Jacqmin [154], also known as the phase field model, the interface is modeled with a finite thickness. The motion of the interface is driven by convection or diffusion determined by the chemical potential gradients. As such, this model can keep the no-slip condition at the solid interface and instead let the contact line move by diffusion, and has been applied in Dong [95, 96] and Ding *et al.* [91] with good results. Critics to this method will however claim that the thickness of the interface, which is on the molecular length scale, should not be resolved in a continuum model. This is demonstrated in Yue *et al.* [283], where the connection between a sharp interface model and the phase field model is investigated for moving contact lines. It is concluded that for systems on the macroscopic scale, the thickness of the interface needs an extremely fine resolution to produce convergent results. It is important to stress that the diffusive interface model is fundamentally different to the continuum surface force (CSF) model by Brackbill *et al.* [41], which smears the surface tension force over a finite thickness over the interface. The CSF is at its core still a sharp interface model, and does not permit a no-slip condition in the vicinity of the contact line.

Lastly the model by Shikhmurzaev [240] assumes a sharp interface, but deviates from the clean interface model, as it allows for some mass accumulation/exchange with the bulk from the interface. In the publication by Shikhmurzaev [239], the methods mentioned in the previous paragraphs are discredited as unphysical and instead the suggested method proposed by Shikhmurzaev is stressed to be the only sensible way forward. This suggested model is by far the most complex of the presented models, requiring a lot of parameters and the necessity to solve a surface-PDE on both the solid-fluid, Γ_{G}, and fluid-fluid, Γ_{FF}, interfaces. So far a computational approach has only been attempted in Sprittles and Shikhmurzaev [246] and tested only for small systems in the vicinity of the contact line.

In the following an out-of-balance force approach is pursued and the formulation by Buscaglia and Ausas [68] is extended to a CutFEM. This differentiates the approach taken here from the recently published method by Reusken *et al.* [222], which uses a continuous velocity space approximation. Additionally, the region of slip introduced in the vicinity of the contact line is modeled by the method introduced in Chapter 3 for general Navier slip. This makes it possible to guarantee no-slip far away from the contact line and next to full slip in its vicinity, even when the contact line moves.

5.2.1 Strong Formulation of a Two-Phase Flow with Moving Contact Lines

Given the assumption of a sharp and clean interface model, the following strong form for a two-phase flow with a moving contact line is proposed, as extended from the Stokes equations presented in Buscaglia and Ausas [68].

Two-phase flow in the domain $\widehat{\Omega} = \Omega^+ \cup \Omega^- \subset \mathbb{R}^d$, $d \in \{2, 3\}$, is considered. An interface Γ_{FF} divides the domain into two subdomains $\Omega^+(t)$ and $\Omega^-(t)$, representing the two fluid phases. Each fluid phase $\Omega^i \in \{\Omega^+, \Omega^-\}$ is governed by the incompressible Navier–Stokes equations and complemented by the associated outer boundary conditions Γ^i_{N} and Γ^i_{G}. Initial conditions

for the velocity are given as $\boldsymbol{u}_0^i$ for $\boldsymbol{u}^i$ at time $t = 0$, where $\boldsymbol{u}_0^i$ is divergence-free and satisfies the given boundary conditions. The interface Γ_{FF} separating the two phases is given an associated boundary normal $\boldsymbol{n}_\Gamma$ pointing from the positive phase Ω^+ to the negative phase Ω^-. Moreover, the normal $\boldsymbol{n}^i$ associated with the boundary $\Gamma^i = \Gamma^i_{\mathrm{N}} \cup \Gamma^i_{\mathrm{G}}$ is defined as pointing outward to the associated domain Ω^i. This leads to the strong form of a two-phase flow with a contact line as: for any time $t \in (0, T)$ find $\boldsymbol{u}(t) : \widehat{\Omega}(t) \to \mathbb{R}^d$, $p(t) : \widehat{\Omega}(t) \to \mathbb{R}$, restricted to $\boldsymbol{u}^i(t) = \boldsymbol{u}(t)|_{\Omega^i(t)}$ and $p^i(t) = p^i|_{\Omega^i(t)}$, such that

$$\rho^i \frac{\partial \boldsymbol{u}^i}{\partial t} + \rho^i \boldsymbol{u}^i \cdot \nabla \boldsymbol{u}^i - \nabla \cdot (2\mu^i \boldsymbol{\epsilon}(\boldsymbol{u}^i)) + \nabla p^i = \boldsymbol{f}^i \qquad \text{in } \Omega^i \times (0,T)\,, \tag{5.6}$$

$$\nabla \cdot \boldsymbol{u}^i = 0 \qquad \text{in } \Omega^i \times (0,T)\,, \tag{5.7}$$

$$\boldsymbol{\sigma}(\boldsymbol{u}^i, p^i) \cdot \boldsymbol{n}^i = \boldsymbol{h}^i \qquad \text{on } \Gamma^i_{\mathrm{N}} \times (0,T) \tag{5.8}$$

$$\left(\boldsymbol{u}^i - \boldsymbol{g}^i\right) \boldsymbol{P}_i^n = \boldsymbol{0} \qquad \text{on } \Gamma^i_{\mathrm{G}} \times (0,T)\,, \tag{5.9}$$

$$\left(\varepsilon(2\mu^i \boldsymbol{\epsilon}(\boldsymbol{u}^i)\boldsymbol{n}^i - \boldsymbol{h}^i) + \mu^i(\boldsymbol{u}^i - \boldsymbol{g}^i)\right) \boldsymbol{P}_i^t = \boldsymbol{0} \qquad \text{on } \Gamma^i_{\mathrm{G}} \times (0,T)\,, \tag{5.10}$$

$$[\![\boldsymbol{u}]\!] = \boldsymbol{0} \qquad \text{on } \Gamma_{\mathrm{FF}} \times (0,T)\,, \tag{5.11}$$

$$[\![\boldsymbol{\sigma}(\boldsymbol{u}, p)]\!] \cdot \boldsymbol{n}_\Gamma = -\sigma\kappa\boldsymbol{n}_\Gamma + \nabla_{\Gamma_{\mathrm{FF}}}\sigma \qquad \text{on } \Gamma_{\mathrm{FF}} \times (0,T)\,, \tag{5.12}$$

$$\sigma(\boldsymbol{m} \cdot \boldsymbol{m}_S) + [\![\sigma_s]\!] + \boldsymbol{f}_{\theta_d} \cdot \boldsymbol{m}_S = \boldsymbol{0} \qquad \text{on } \partial\Gamma_{\mathrm{FF}} \times (0,T)\,, \tag{5.13}$$

$$\boldsymbol{u}^i = \boldsymbol{u}_0^i \qquad \text{in } \Omega^i \times \{0\}, \tag{5.14}$$

with $i \in \{+,-\}$. The equations (5.6)–(5.10) and (5.14) are familiar from the single fluid case treated in Chapter 3, as such, focus will be put on the terms (5.11)–(5.13) stemming from the interface Γ_{FF} between the two fluid phases. The jump in velocity in (5.11) on Γ_{FF} is defined as

$$[\![\boldsymbol{u}]\!] = \boldsymbol{u}^+ - \boldsymbol{u}^-, \tag{5.15}$$

and set to $\boldsymbol{0}$. This implies that no mass flow occurs across the interface, and that the two phases can not slide in tangential direction of the interface. Owing to the surface energy σ associated with the interface Γ_{FF}, a jump in the traction between the two fluids exists, and is defined in (5.12). The jump acting in normal direction to the surface, that is $-\sigma\kappa\boldsymbol{n}_\Gamma$, can be identified as the classical *surface tension force*, as introduced for a stationary system in Section 5.1.3. The jump, $\nabla_{\Gamma_{\mathrm{FF}}}\sigma$, acting in the tangential plane of the interface Γ_{FF} is the so-called *Marangoni force*. This force appears if there exists a gradient in the surface tension owing to, for instance, temperature gradients or surfactants. Lastly the motion of the contact line $\partial\Gamma_{\mathrm{FF}}$ is defined by (5.13). Here $\boldsymbol{f}_{\theta_d}$ is an added term related to the dissipation associated with the motion of the contact line. This condition can also be rewritten with a contact angle, as

$$\boldsymbol{m} \cdot \boldsymbol{m}_S = \cos(\theta_d) \tag{5.16}$$

where θ_d is the angle created between Γ^+_{G} and Γ_{FF} and the normal vectors at the contact line $\boldsymbol{m}$ and $\boldsymbol{m}_S$ are defined as in Figure 5.3. Furthermore, define

$$M = \frac{\sigma_{s-} - \sigma_{s+}}{\sigma}. \tag{5.17}$$

If $|M| \leq 1$ the static contact angle can be defined as

$$\sigma\cos(\theta_e) = \sigma_{s-} - \sigma_{s+}. \tag{5.18}$$

If $|M| > 1$ the case of complete wetting occurs and one of the fluids spreads completely on the solid.

Even though the dissipative term $\boldsymbol{f}_{\theta_d}$ is an important component in modeling the motion of the contact line correctly, this chapter puts its focus on the computational model, and as such this term will be neglected (i.e. $\boldsymbol{f}_{\theta_d} = \mathbf{0}$) to simplify the formulations from hereon. Moreover, given that this thesis employs a CutFEM, which has a discontinuous velocity and test function space, it is not straightforward how to add this dissipation term, as in literature so far only approaches with continuous velocity, and its associated test function space, have been employed.

5.2.2 Weak Formulation of a Two-Phase Flow with Moving Contact Lines

The two phases are treated here as separate domains and the interaction between them at the interface Γ_{FF} is given as a coupling condition. Taking the same space as for the single fluid case presented in (3.9)–(3.12), with the spaces restricted to their respective domain, the following notations are introduced,

$$\mathcal{V}_{\boldsymbol{g}^i}^{n,i} := \{\boldsymbol{u} \in [H^1(\Omega^i)]^d \mid \boldsymbol{u}^i \boldsymbol{P}_i^n = \boldsymbol{g}^i \boldsymbol{P}_i^n \text{ on } \Gamma_{\mathrm{G}}^i \wedge \boldsymbol{u}^i = \boldsymbol{g}^i \text{ on } \Gamma_{\mathrm{D}}^i\}, \tag{5.19}$$

$$\mathcal{V}_{\boldsymbol{g}^i}^{i} := \begin{cases} \mathcal{V}_{\boldsymbol{g}^i}^{n,i} & \text{if } \Gamma_{\mathrm{G}}^{i,\varepsilon} \neq \emptyset \\ \mathcal{V}_{\boldsymbol{g}^i}^{n,i} \setminus RM(\Omega^i) & \text{if } \Gamma_{\mathrm{G}}^{i,\varepsilon} = \emptyset, \end{cases} \tag{5.20}$$

$$\mathcal{Q}^i := \begin{cases} L^2(\Omega^i) & \text{if } \Gamma_{\mathrm{N}}^i \neq \emptyset \\ L_0^2(\Omega^i) & \text{if } \Gamma_{\mathrm{N}}^i = \emptyset. \end{cases} \tag{5.21}$$

The weak form for the problem (5.6)–(5.14) is then defined as: find the velocity and pressure field $(\boldsymbol{u}^i, p^i) \in \mathcal{V}_{\boldsymbol{g}^i}^i \times \mathcal{Q}^i$ such that

$$\begin{aligned} &(\rho^i \frac{\partial \boldsymbol{u}^i}{\partial t}, \boldsymbol{v}^i)_{\Omega^i} + (2\mu^i \boldsymbol{\epsilon}(\boldsymbol{u}^i), \boldsymbol{\epsilon}(\boldsymbol{v}^i))_{\Omega^i} + (\rho^i(\boldsymbol{u}^i \cdot \nabla)\boldsymbol{u}^i, \boldsymbol{v}^i)_{\Omega^i} - (p^i, \nabla \cdot \boldsymbol{v}^i)_{\Omega^i} + (q^i, \nabla \cdot \boldsymbol{u}^i)_{\Omega^i} \\ &\quad - \langle (-p^i \boldsymbol{I} + 2\mu^i \boldsymbol{\epsilon}(\boldsymbol{u}^i)) \cdot \boldsymbol{n}^i, \boldsymbol{v}^i \rangle_{\Gamma_{\mathrm{G}}^i \cup \Gamma_{\mathrm{FF}}} + \langle \sigma_{s,i} \boldsymbol{m}_S, \boldsymbol{v}^i \rangle_{\partial \Gamma_{\mathrm{FF}}} \\ &\quad = (\boldsymbol{f}^i, \boldsymbol{v}^i)_{\Omega^i} + \langle \boldsymbol{h}^i, \boldsymbol{v}^i \rangle_{\Gamma_{\mathrm{N}}^i} \quad \forall (\boldsymbol{v}^i, q^i) \in \mathcal{V}_{\mathbf{0}}^i \times \mathcal{Q}^i, \end{aligned} \tag{5.22}$$

where $i \in \{+, -\}$ and $\sigma_{s,+} = \sigma_{s+}$ and $\sigma_{s,-} = -\sigma_{s-}$. To shorten the notation, the following weighted operators are introduced,

$$\{\cdot\} = \omega^+(\cdot)_+ + \omega^-(\cdot)_- \tag{5.23}$$

$$\langle\cdot\rangle = \omega^-(\cdot)_+ + \omega^+(\cdot)_-, \tag{5.24}$$

where the weights are restricted to the conditions that $\omega^+, \omega^- \in [0, 1]$ and $\omega^+ + \omega^- = 1$. Moreover, the identity

$$[\![ab]\!] = [\![a]\!] \{b\} + \langle a \rangle [\![b]\!] \tag{5.25}$$

holds for arbitrary functions a and b, which are sufficiently smooth in their subdomains. From this, the formulation can be rewritten as

$$\begin{aligned}(\rho\frac{\partial \boldsymbol{u}}{\partial t}, \boldsymbol{v})_{\widehat{\Omega}} + (2\mu\boldsymbol{\epsilon}(\boldsymbol{u}), \boldsymbol{\epsilon}(\boldsymbol{v}))_{\widehat{\Omega}} + (\rho(\boldsymbol{u}\cdot\nabla)\boldsymbol{u}, \boldsymbol{v})_{\widehat{\Omega}} - (p, \nabla\cdot\boldsymbol{v})_{\widehat{\Omega}} + (q, \nabla\cdot\boldsymbol{u})_{\widehat{\Omega}} \\ - \langle(-p\boldsymbol{I} + 2\mu\boldsymbol{\epsilon}(\boldsymbol{u}))\cdot\boldsymbol{n}, \boldsymbol{v}\rangle_{\Gamma_{\mathrm{G}}} \\ + \langle\{-p\boldsymbol{I} + 2\mu\boldsymbol{\epsilon}(\boldsymbol{u})\}\cdot\boldsymbol{n}_{\Gamma}, [\![\boldsymbol{v}]\!]\rangle_{\Gamma_{\mathrm{FF}}} + \langle[\![-p\boldsymbol{I} + 2\mu\boldsymbol{\epsilon}(\boldsymbol{u})]\!]\cdot\boldsymbol{n}_{\Gamma}, \langle\boldsymbol{v}\rangle\rangle_{\Gamma_{\mathrm{FF}}} \\ + \langle[\![\sigma_s]\!]\boldsymbol{m}_S, \langle\boldsymbol{v}\rangle\rangle_{\partial\Gamma_{\mathrm{FF}}} \\ = (\boldsymbol{f}, \boldsymbol{v})_{\widehat{\Omega}} + \langle\boldsymbol{h}, \boldsymbol{v}\rangle_{\Gamma_{\mathrm{N}}} \quad \forall\,(\boldsymbol{v}^i, q^i) \in \mathcal{V}_{\mathbf{0}}^i \times \mathcal{Q}^i, \end{aligned} \tag{5.26}$$

where the bi-linear forms are defined as

$$(\cdot,\cdot)_{\widehat{\Omega}} = (\cdot,\cdot)_{\Omega^+} + (\cdot,\cdot)_{\Omega^-}$$

and

$$(\cdot,\cdot)_{\Gamma_{\mathrm{G}}} = (\cdot,\cdot)_{\Gamma_{\mathrm{G}}^+} + (\cdot,\cdot)_{\Gamma_{\mathrm{G}}^-}.$$

The second term on the third line in equation (5.26) can be rewritten from the condition (5.12) and the contribution from the contact line $\partial\Gamma_{\mathrm{FF}}$ such that,

$$\begin{aligned}\langle([\![-p\boldsymbol{I} + 2\mu\boldsymbol{\epsilon}(\boldsymbol{u}))]\!]\cdot\boldsymbol{n}_{\Gamma}, \langle\boldsymbol{v}\rangle\rangle_{\Gamma_{\mathrm{FF}}} &= l^{\mathrm{ST}}(\boldsymbol{v}) \\ &= \langle(-\sigma\kappa\boldsymbol{n}_{\Gamma} + \nabla_{\Gamma_{\mathrm{FF}}}\sigma, \langle\boldsymbol{v}\rangle\rangle_{\Gamma_{\mathrm{FF}}} + \langle\sigma\boldsymbol{m}, \langle\boldsymbol{v}\rangle\rangle_{\partial\Gamma_{\mathrm{FF}}}. \end{aligned} \tag{5.27}$$

Alternatively, this can also be formulated with a Laplace–Beltrami formulation as

$$\langle[\![-p\boldsymbol{I} + 2\mu\boldsymbol{\epsilon}(\boldsymbol{u})]\!]\cdot\boldsymbol{n}_{\Gamma}, \langle\boldsymbol{v}\rangle\rangle_{\Gamma_{\mathrm{FF}}} = l^{\mathrm{LB}}(\boldsymbol{v}) = \langle\sigma, \boldsymbol{P}^t : \langle\nabla\boldsymbol{v}\rangle\rangle_{\Gamma_{\mathrm{FF}}}. \tag{5.28}$$

This way of rewriting the traction jump at the interface Γ_{FF} between the two-phases is a well-known approach first introduced by Bänsch [16]. The equivalence between the two formulations (5.27) and (5.28) is proven in Buscaglia and Ausas [68].

Remark 5.5 *From the formulation in (5.26) it is apparent that line integrals need to be evaluated. It is important to stress that these line integral terms are not bounded in $[H^1(\Omega)]^d$, as reported in Buscaglia and Ausas [68]. The well-posedness of the weak formulation is not guaranteed, however, upon discretization the integrals can be evaluated. Usually this ill-posedness is attributed to some physical phenomenon, involving some microscopic length scale to remove this singularity. Alternatively, it is argued by Snoeijer and Andreotti [242] that the lack of an energy scale causes this divergent pressure.*

5.2.3 A CutFEM Discretized Formulation of a Two-Phase Flow with Moving Contact Lines

As was already mentioned in the introduction to the CutFEM in Section 2.3.1, unfitted finite element methods have enjoyed success in simulating two-phase flows. However, for publications concerning flows with contact lines, this approach has as of yet not been as frequently utilized. In Buscaglia and Ausas [68] an unfitted method with an enriched pressure space is used and in

Reusken *et al.* [222] an XFEM is used to depict the discontinuity in the pressure. Nonetheless, both of these methods assume a continuous velocity space. For two-phase flows it holds true that the velocity at the interface Γ_{FF} is continuous, as $[\![\boldsymbol{u}]\!] = \mathbf{0}$ here. However, the gradient of the velocity is usually not continuous and, accordingly, the velocity solution has a kink. This kink becomes more pronounced as the difference in material parameters (μ and ρ) becomes larger between the two phases. To depict this correctly, an enrichment of the velocity function space is needed. In this section a discontinuous function space for both the velocity and pressure are employed. Furthermore, to permit slip in the vicinity of the contact line, the weak imposition of a general Navier condition from Chapter 3 and 4 is utilized. These two facts set the approach in this thesis apart from the publication by Reusken *et al.* [222], which, apart from the above mentioned differences, has a similar scope as this thesis.

First the necessary notation and function spaces are introduced for the discretized two-phase problem. Let $\mathcal{V}_h^i$ and $\mathcal{Q}_h^i$ be the discrete approximation spaces for the velocity and pressure associated with the respective fluid phase and time-dependent subdomain Ω_h^i, where

$$\mathcal{Q}_h^i := \mathcal{X}_h^i, \quad \mathcal{V}_h^i := [\mathcal{X}_h^i]^d, \tag{5.29}$$

and $\mathcal{W}_h^i := \mathcal{V}_h^i \times \mathcal{Q}_h^i$. Two identical coinciding background meshes are chosen to approximate each respective phase, i.e. $\widehat{\mathcal{T}}_h^+ = \widehat{\mathcal{T}}_h^-$. Nevertheless, the active parts of the meshes do not coincide, i.e. $\mathcal{T}_h^+ \neq \mathcal{T}_h^-$, nor do the associated fictitious domains $\Omega_h^{+,*}$ and $\Omega_h^{-,*}$. However, the overlap of the active meshes construe the subset of elements intersecting the boundary, i.e. $\mathcal{T}_h^+ \cap \mathcal{T}_h^- = \mathcal{T}_\Gamma^+ = \mathcal{T}_\Gamma^-$. The function space $\mathcal{X}_h^i$ is defined in a similar fashion as in (2.20). A continuous isoparametric function space for piecewise polynomials of order k for a given mesh $\mathcal{T}_h^i$ is introduced as

$$\mathcal{X}_h^i = \left\{ v_h^i \in C^0(\Omega_h^i) : v_h^i\big|_T \in \mathbb{V}^k(T) \; \forall \, T \in \mathcal{T}_h^i \right\}, \tag{5.30}$$

where $\mathbb{V}^k(T)$ is a polynomial function space on the element T.

To shorten the notation, the discrete space can be defined over the entire domain $\widehat{\Omega}_h$ as a product space $\mathcal{W}_h = \mathcal{W}_h^+ \oplus \mathcal{W}_h^-$ such that for $V_h = (\boldsymbol{v}_h, q_h) \in \mathcal{W}_h$ a velocity pressure pair is defined on $\widehat{\Omega}_h$, for which

$$V_h|_{\Omega_h^i} = V_h^i = (\boldsymbol{v}_h^i, q_h^i) \in \mathcal{V}_h^i \times \mathcal{Q}_h^i, \quad \text{for } i \in \{+,-\}. \tag{5.31}$$

For a more thorough exposition on the treatment of degrees of freedom and spatial discretization techniques for the CutFEM, with regards to coupled multi-physics problems, the interested reader is recommended the thesis by Schott [232] or the publication by Schott and Wall [229].

From these definitions, the discretized weak form for the two-phase flow with moving contact lines can be formulated as, find $U_h = (\boldsymbol{u}_h, p_h) \in \mathcal{W}_h$ such that for all $V_h = (\boldsymbol{v}_h, q_h) \in \mathcal{W}_h$ it holds

$$\begin{aligned}
&\sum_{i\in\{+,-\}} \left(\mathcal{A}^i(U_h, V_h) + \mathcal{S}_h^{i,*}(U_h, V_h) + \mathcal{G}_h^i(U_h, V_h) + \mathcal{N}_h^i(U_h, V_h) \right) \\
&\qquad + \mathcal{C}_h^{\Gamma_{\mathrm{FF}}}(U_h, V_h) + \mathcal{C}_h^{\partial\Gamma_{\mathrm{FF}}}(U_h, V_h) \\
&\quad = \sum_{i\in\{+,-\}} \left(\mathcal{L}^i(V_h) + \mathcal{L}_h^{\mathcal{N},i}(V_h) \right) + \mathcal{L}_h^{\Gamma_{\mathrm{FF}}}(U_h, V_h) + \mathcal{L}_h^{\partial\Gamma_{\mathrm{FF}}}(U_h, V_h).
\end{aligned} \tag{5.32}$$

where

$$\begin{aligned}\mathscr{A}^i(U_h, V_h) =& (\rho\frac{\partial \boldsymbol{u}_h}{\partial t}, \boldsymbol{v}_h)_{\Omega_h^i} + (2\mu\boldsymbol{\epsilon}(\boldsymbol{u}_h), \boldsymbol{\epsilon}(\boldsymbol{v}_h))_{\Omega_h^i} + (\rho(\boldsymbol{u}_h\cdot\nabla)\boldsymbol{u}_h, \boldsymbol{v}_h)_{\Omega_h^i} \\ & - (p_h, \nabla\cdot\boldsymbol{v}_h)_{\Omega_h^i} + (q_h, \nabla\cdot\boldsymbol{u}_h)_{\Omega_h^i} \\ & - \langle(-p_h\boldsymbol{I} + 2\mu\boldsymbol{\epsilon}(\boldsymbol{u}_h))\cdot\boldsymbol{n}_h, \boldsymbol{v}_h\rangle_{\Gamma^i_{\mathrm{N},h}\cup\Gamma^i_{\mathrm{G},h}} \end{aligned} \tag{5.33}$$

$$\mathscr{L}^i(V_h) = (\boldsymbol{f}^i, \boldsymbol{v}_h)_{\Omega_h^i} \tag{5.34}$$

$$\mathscr{L}_h^{i,\mathcal{N}}(V_h) = \mathscr{L}_h^{\Gamma^i_{\mathrm{N}}}(V_h) + \mathscr{L}_h^{\Gamma^i_{\mathrm{G}},n}(V_h) + \mathscr{L}_h^{\Gamma^i_{\mathrm{G}},t}(V_h) \tag{5.35}$$

$$\mathscr{N}_h^i(U_h, V_h) = \mathscr{N}_h^{\Gamma^i_{\mathrm{N}}}(U_h, V_h) + \mathscr{N}_h^{\Gamma^i_{\mathrm{G}},n}(U_h, V_h) + \mathscr{N}_h^{\Gamma^i_{\mathrm{G}},t}(U_h, V_h). \tag{5.36}$$

The terms (5.35)–(5.36) are defined in the same fashion as already introduced in Section 3.2.2 in the equations (3.18)–(3.19). The domain stabilization term $\mathscr{S}_h^{i,*}$ is defined, for its respective domain, as in Section 2.1.3 for residual-based stabilization in (2.23)–(2.25) or continuous interior penalty stabilization (2.31). Equivalently, the definition of the ghost penalty operator $\mathscr{G}_h^i$ for the respective domain can be found in (2.84). It remains to define the terms related to the interface between the two phases $\mathscr{C}_h^{\Gamma_{\mathrm{FF}}}(U_h, V_h)$ and $\mathscr{L}_h^{\Gamma_{\mathrm{FF}}}(U_h, V_h)$ and the terms related to the contact line $\mathscr{C}_h^{\partial\Gamma_{\mathrm{FF}}}(U_h, V_h)$ and $\mathscr{L}_h^{\partial\Gamma_{\mathrm{FF}}}(U_h, V_h)$.

Starting with the terms associated with the interface $\Gamma_{\mathrm{FF},h}$, the no-slip condition at the interface has to be imposed. This is once again done with the Nitsche's method. The added term is taken from the dissertation by Schott [232] and the publication by Schott *et al.* [230] and reads

$$\mathscr{C}_h^{\Gamma_{\mathrm{FF}}}(U_h, V_h) = \langle(\{-p_h\boldsymbol{I} + 2\mu\boldsymbol{\epsilon}(\boldsymbol{u}_h)\})\cdot\boldsymbol{n}_h, [\![\boldsymbol{v}]\!]\rangle_{\Gamma_{\mathrm{FF},h}} \tag{5.37}$$

$$\langle\frac{1}{2\gamma_{\mathrm{FF}}^n}\left\{\frac{\mu}{h}\right\}[\![\boldsymbol{u}_h]\!]\boldsymbol{P}^n, [\![\boldsymbol{v}_h]\!]\rangle_{\Gamma_{\mathrm{FF},h}} \tag{5.38}$$

$$-\zeta_u^{\mathrm{FF}}\langle[\![\boldsymbol{u}_h]\!], \{2\mu\boldsymbol{\epsilon}(\boldsymbol{v}_h)\}\boldsymbol{n}_h\rangle_{\Gamma_{\mathrm{FF},h}} - \langle[\![\boldsymbol{u}_h]\!]\boldsymbol{P}^n, \{q_h\}\boldsymbol{n}_h\rangle_{\Gamma_{\mathrm{FF},h}} \tag{5.39}$$

$$+\langle\frac{1}{2\gamma_{\mathrm{FF}}^n}\left\{\frac{\rho\phi_u}{h}\right\}[\![\boldsymbol{u}_h]\!]\boldsymbol{P}^n, [\![\boldsymbol{v}_h]\!]\rangle_{\Gamma_{\mathrm{FF},h}} \tag{5.40}$$

$$-\langle(\{\rho\boldsymbol{u}_h\}_m\cdot\boldsymbol{n}_h)[\![\boldsymbol{u}_h]\!], \{\boldsymbol{v}_h\}_m\rangle_{\Gamma_{\mathrm{FF},h}} \tag{5.41}$$

$$+\langle\gamma_{upw}|(\{\rho\boldsymbol{u}_h\}\cdot\boldsymbol{n}_h)|[\![\boldsymbol{u}_h]\!], [\![\boldsymbol{v}_h]\!]\rangle_{\Gamma_{\mathrm{FF},h}} \tag{5.42}$$

$$+\langle\frac{1}{2\gamma_{\mathrm{FF}}^t}\left\{\frac{\mu}{h}\right\}[\![\boldsymbol{u}_h]\!]\boldsymbol{P}^t, [\![\boldsymbol{v}_h]\!]\rangle_{\Gamma_{\mathrm{FF},h}} \tag{5.43}$$

where $\{\cdot\}_m$ is given the weights $\omega_m^+ = \omega_m^- = 1/2$, ϕ_u is defined in (2.82), $\zeta_u^{\mathrm{FF}} \in \{-1, 1\}$ defines whether an adjoint-consistent or adjoint-inconsistent method is chosen and the term $\gamma_{upw} \in \{0, 1\}$ determines whether upwinding stabilization is considered. The weights for the averaging operators $\{\cdot\}$ and $\langle\cdot\rangle$ are chosen as

$$\omega^+ = \frac{\mu^-}{\mu^+ + \mu^-}, \qquad \omega^- = \frac{\mu^+}{\mu^+ + \mu^-}. \tag{5.44}$$

For a more thorough explanation on the coupling terms the reader is referred to Schott [232, Chap. 4]. The right-hand-side is given as

$$\mathscr{L}_h^{\Gamma_{\mathrm{FF}}}(V_h) = l^*(V_h), \tag{5.45}$$

where $l^* \in \{l^{\mathrm{ST}}, l^{\mathrm{LB}}\}$, that is, either a curvature type formulation (5.27) or a Laplace–Beltrami formulation (5.28) can be chosen.

Continuing with the contributions from the contact line, it is clear that when no dissipation is assumed $\mathscr{C}_h^{\partial\Gamma_{\mathrm{FF}}}(U_h, V_h) = 0$ and that the right-hand-side term reads

$$\mathscr{L}_h^{\partial\Gamma_{\mathrm{FF}}}(V_h) = -\langle [\![\sigma_s]\!] \boldsymbol{m}_S, \langle \boldsymbol{v} \rangle \rangle_{\partial\Gamma_{\mathrm{FF},h}}. \tag{5.46}$$

With this last term defined, this completes the discretized weak form for a two-phase flow with a moving contact line.

What still remains to be defined is the motion of the interface $\Gamma_{\mathrm{FF},h}$, and by extension the deformation of the domains $\Omega_h^+(t)$ and $\Omega_h^-(t)$. Given the assumption that the motion of the interface $\Gamma_{\mathrm{FF},h}$ is determined completely by the convection of the flow of the two fluids, the level-set equation (2.56)–(2.57) can be used to describe the evolution of the interface. The discretization of the level-set equation on $\widehat{\Omega}_h = \Omega_h^+ \cup \Omega_h^-$ is given by the equations (2.59).

Remark 5.6 *As the velocity advecting the level-set field is set to the fluid solution $\boldsymbol{c} = \boldsymbol{u}_h$ and the level-set is needed for the cut of the domain and the calculations related to the curvature $\kappa(\phi_h)$, the fluid equations (5.32) and level-set equation (2.59) are strongly coupled. Hence, the two equations need to be coupled in a sensible way. In this thesis a partitioned approach is chosen, which entails solving the equations sequentially. For a new time step t^{n+1}, the level-set equation (2.59) is solved first with $\boldsymbol{u}_h^0(t^{n+1}) = \boldsymbol{u}_h(t^n)$ and $\phi_h^0(t^{n+1})$ is obtained. Next the fluid equations (5.32) are solved with $\phi_h^0(t^{n+1})$ and as such $\boldsymbol{u}_h^1(t^{n+1})$ can be calculated. Finally, $\phi_h^1(t^{n+1})$ is calculated, from solving the level-set equation with the updated velocity. Another fluid velocity - level-set iteration can be carried out until a set tolerance for $\Delta\boldsymbol{u}_h(t^{n+1}), \Delta p_h(t^{n+1})$ and $\Delta\phi_h(t^{n+1})$ is reached, where*

$$\Delta\boldsymbol{u}_h(t^{n+1}) = \boldsymbol{u}_h^k(t^{n+1}) - \boldsymbol{u}_h^{k-1}(t^{n+1}). \tag{5.47}$$

This way of constructing the partitioned method for a coupled fluid-scalar-transport problem has been shown to provide an improved accuracy and still maintain an efficient computational model, see for instance Gravemeier and Wall [128].

5.2.3.1 On the Construction of the Right-Hand-Side Surface Tension Related Terms

The terms $\mathscr{L}_h^{\Gamma_{\mathrm{FF}}}(V_h)$ and $\mathscr{L}_h^{\partial\Gamma_{\mathrm{FF}}}(V_h)$ need some extra treatment before they can be employed in a discretized setting. From hereon it will be assumed that the surface energy σ on Γ_{FF} is a constant, and consequently, the *Marangoni forces* can be neglected (i.e. $\nabla_{\Gamma_{\mathrm{FF}}}\sigma = \boldsymbol{0}$), simplifying the following terms.

Starting with the term $\langle(-\sigma\kappa\boldsymbol{n}_h, \langle\boldsymbol{v}\rangle\rangle_{\Gamma_{\mathrm{FF},h}}$ appearing in $l^{\mathrm{ST}}(\boldsymbol{v}_h)$, the curvature is given by equation (2.55) as

$$\kappa = -\nabla \cdot \boldsymbol{n} \quad \text{on } \Gamma_{\mathrm{FF}}, \tag{5.48}$$

from which it is is clear that if the piecewise constant normal $\boldsymbol{n}_h$ from $\Gamma_{\mathrm{FF},h}$ is used to evaluate the curvature, it will be zero as $\nabla \cdot \boldsymbol{n}_h = 0$. As the surface Γ_{FF} is described by the zero contour of a level-set function ϕ, the curvature can also be expressed as

$$\kappa(\nabla\phi) = \nabla \cdot \left(\frac{\nabla\phi}{|\nabla\phi|} \right). \tag{5.49}$$

The problem here is the fact that if a linear finite element discretization is employed for ϕ_h, the second derivatives in (5.49) partially vanish in the interior of the elements. Given that bi-linear elements are used for the discretizations in the following numerical examples, an alternative approach to calculating the curvature with $\boldsymbol{n}_h$ or $\nabla\phi_h$ is needed. In this thesis, this problem is resolved by constructing a smoothed gradient field $\widetilde{\nabla\phi_h}$ from one of the smoothing techniques introduced in Section 2.2.1.4 (Mean-value averaging, L^2-projection or super convergent patch recovery). As this smoothed gradient field is continuous, the calculation of the curvature $\kappa(\widetilde{\nabla\phi_h})$ from (5.49) becomes well defined. This approach is also popular in literature, where it has been applied in Marchandise *et al.* [182], Nagrath *et al.* [199], Sussman *et al.* [259], Zahedi *et al.* [285] and Schott *et al.* [230] to mention a few.

Next, the treatment of the Laplace–Beltrami term $l^{\mathrm{LB}} = \langle \sigma, \boldsymbol{P}^t : \langle \nabla \boldsymbol{v} \rangle \rangle_{\Gamma_{\mathrm{FF},h}}$ is dealt with. Different choices of creating the projection matrix $\boldsymbol{P}^t$ for the Laplace–Beltrami term exist in literature. Either the piecewise constant normal from the cut boundary

$$\boldsymbol{P}^t_{\boldsymbol{n}_h} = \boldsymbol{I} - \boldsymbol{n}_h \otimes \boldsymbol{n}_h \tag{5.50}$$

can be used, which is done in Ausas *et al.* [9], Bänsch [16] and Groß *et al.* [134], or a smoothed version of the normal

$$\boldsymbol{P}^t_{\widetilde{\boldsymbol{n}_h}} = \boldsymbol{I} - \widetilde{\boldsymbol{n}_h} \otimes \widetilde{\boldsymbol{n}_h} \tag{5.51}$$

can be employed, created from smoothed gradients of the level-set function as in Hysing [153] and Rasthofer *et al.* [217]. A third option was introduced in Groß and Reusken [131], where it is argued that the best performance is received with a concatenation of the two, that is

$$\widetilde{\boldsymbol{P}^t} = \boldsymbol{P}^t_{\widetilde{\boldsymbol{n}_h}} \boldsymbol{P}^t_{\boldsymbol{n}_h}, \tag{5.52}$$

which was verified with numerical examples in Groß and Reusken [132] to be the superior choice. It is postulated by Fries [118] that the Laplace–Beltrami formulation is preferable to the surface tension one as the calculation of the curvature is a delicate matter. Also, with this formulation it is not necessary to evaluate the divergence of the normal of the interface, hence reducing the required smoothness of this normal vector to achieve results.

Lastly the vectors at the contact line have to be calculated to enable the calculation of the contact line term $\langle \sigma \boldsymbol{m}, \langle \boldsymbol{v} \rangle \rangle_{\partial\Gamma_{\mathrm{FF},h}}$ and $\langle \llbracket \sigma_s \rrbracket \boldsymbol{m}_S, \langle \boldsymbol{v} \rangle \rangle_{\partial\Gamma_{\mathrm{FF},h}}$ appearing in $l^{\mathrm{ST}}(V_h)$ and $\mathcal{L}_h^{\partial\Gamma_{\mathrm{FF}}}(V_h)$, respectively. The tangential vector $\boldsymbol{m}$ to the interface Γ_{FF} and the tangential vector $\boldsymbol{m}_S$ to the solid surface Γ_{G}, as defined in Figure 5.3, need to be construed from the two known normal vectors $\boldsymbol{n}_{\Gamma_{\mathrm{G}}}$ and $\boldsymbol{n}_{\Gamma_{\mathrm{FF}}}$, i.e. the normal on the solid interface Γ_{G} and the normal of the two-phase interface Γ_{FF}. These vectors can be constructed following the approach by Gerbeau and Lelievre [124], where

$$\boldsymbol{t}_{\Gamma_{\mathrm{FF}}} = \boldsymbol{n}_{\Gamma_{\mathrm{FF}}} \otimes \boldsymbol{n}_{\Gamma_{\mathrm{G}}}, \tag{5.53}$$

$$\boldsymbol{m}_S = \boldsymbol{n}_{\Gamma_{\mathrm{G}}} \otimes \boldsymbol{t}_{\Gamma_{\mathrm{FF}}}, \tag{5.54}$$

$$\boldsymbol{m} = \boldsymbol{t}_{\Gamma_{\mathrm{FF}}} \otimes \boldsymbol{n}_{\Gamma_{\mathrm{FF}}}. \tag{5.55}$$

Alternatively, the approach by Reusken *et al.* [222] can be opted for, where

$$\boldsymbol{m}_S = \frac{\boldsymbol{P}^t_{\Gamma_\mathrm{G}} \boldsymbol{n}_{\Gamma_\mathrm{FF}}}{|\boldsymbol{P}^t_{\Gamma_\mathrm{G}} \boldsymbol{n}_{\Gamma_\mathrm{FF}}|}, \tag{5.56}$$

$$\boldsymbol{m} = \frac{\boldsymbol{P}^t_{\Gamma_\mathrm{FF}} \boldsymbol{n}_{\Gamma_\mathrm{G}}}{|\boldsymbol{P}^t_{\Gamma_\mathrm{FF}} \boldsymbol{n}_{\Gamma_\mathrm{G}}|}. \tag{5.57}$$

Here the projection matrices are defined as $\boldsymbol{P}^t_{\Gamma_\mathrm{G}} = \boldsymbol{I} - \boldsymbol{n}_{\Gamma_\mathrm{G}} \otimes \boldsymbol{n}_{\Gamma_\mathrm{G}}$ and $\boldsymbol{P}^t_{\Gamma_\mathrm{FF}} = \boldsymbol{I} - \boldsymbol{n}_{\Gamma_\mathrm{FF}} \otimes \boldsymbol{n}_{\Gamma_\mathrm{FF}}$.

In the following, $\boldsymbol{n}_{\Gamma_\mathrm{G}}$ is assumed to be the same as the discretized normal $\boldsymbol{n}_h$ on Γ_G, i.e. no smoothing is needed here. For $\boldsymbol{n}_{\Gamma_\mathrm{FF}}$, a choice between using the smoothed normal $\widetilde{\boldsymbol{n}_h}$ or the piecewise constant normal $\boldsymbol{n}_h$ from the piecewise linear approximation of Γ_FF has to be made. In the following, the choice will be restricted to only the smoothed normal case $\widetilde{\boldsymbol{n}_h}$, for the creation of the vectors $\boldsymbol{m}$ and $\boldsymbol{m}_S$ of the contact line terms.

5.3 Numerical Examples of Capillary Systems

To verify the viability of the discretized formulation (5.32), a stationary and an instationary example will corroborate the theoretical findings. First, a stationary two dimensional droplet will be studied. As there exists an analytic solution for this problem in the absence of gravity, different numerical approaches, as were discussed in Section 5.2.3.1, can be tested here. The most suitable of these approaches can then be used for the ensuing instationary spreading droplet.

In both numerical examples, the two-phase surface Γ_FF is cut and treated with a CutFEM approach, whereas the boundary Γ_G is discretized with a fitted mesh approach. The division of Γ_G into two surfaces Γ^+_G and Γ^-_G is however retrieved from cutting the background mesh $\widehat{\mathcal{T}}_h$, to impose the boundary condition in a consistent fashion. This also allows for the possibility to consistently simulate systems with large contrasts in material parameters.

Given that the CutFEM will be utilized in the following examples, the need arises to integrate cut elements of non-regular shapes. As the standard integration rules are not applicable, the non-regular shapes are decomposed into tetrahedra for which the integration rules are well defined (also known as *tessellation*). See Section 2.3.2.3, for a short discussion on the possible ways of carrying out the numerical integration for cut elements. The imposition of the continuity condition on the surface Γ_FF is given in (5.37)–(5.42). In the following simulations, the term (5.41) will be disregarded and $\gamma_{upw} = 1.0$, as proposed in Schott [232].

Imposition of the general Navier condition The general Navier condition is evaluated on $\Gamma^+_{\mathrm{G},h}$ and $\Gamma^-_{\mathrm{G},h}$, just as it would be in the single fluid case. In contrast to the previous chapters though, a strong imposition of the normal no-penetration condition ($\boldsymbol{u} \cdot \boldsymbol{n} = 0$) will be conducted. This choice will not violate the Babuška paradox, as the discretized boundary $\Gamma_{\mathrm{G},h}$ coincides with the physical boundary Γ_G. Nevertheless, it is important to stress that this approach is not viable for the general case, without either switching to a weak imposition in the normal direction or a careful creation of the normal vector at the nodes of $\Gamma_{\mathrm{G},h}$. To impose slip in the vicinity of the contact line, and no-slip further away, the following dependence of the slip length on the

level-set function is made,

$$\varepsilon(\phi) = \begin{cases} \frac{1}{2}\left(1.0 + \cos(\pi \frac{\phi}{l_\varepsilon})\right) e^{\log(\varepsilon_{\max})(1-2|\frac{\phi}{l_\varepsilon}|)} & \text{for } |\frac{\phi}{l_\varepsilon}| \leq l_\varepsilon \\ 0 & \text{for } |\frac{\phi}{l_\varepsilon}| > l_\varepsilon. \end{cases} \tag{5.58}$$

Where $\varepsilon_{\max}$ is chosen as the maximum slip length at the contact line, and l_ε the length surrounding the contact line which is affected by slip. This way of imposing slip at the contact line is a feasible way as long as no contact angles close to $0°$ or $180°$ are present, or thin films exist on the boundary $\Gamma_{\mathrm{G},h} = \Gamma^+_{\mathrm{G},h} \cup \Gamma^-_{\mathrm{G},h}$.

5.3.1 Static Droplet on a Plate

With the absence of gravity, i.e. $\mathrm{Bo} = 0$, a 2D-droplet with an initial radius of R_0 and the shape of a semi-circle, i.e. $\theta_e^* = 90°$, will have the final radius at equilibrium of

$$R = R_0 \sqrt{\frac{\pi}{2(\theta_e^* - \sin(\theta_e^*)\cos(\theta_e^*))}}. \tag{5.59}$$

The height of the bubble is given as

$$e = R\left(1 - \cos(\theta_e^*)\right), \tag{5.60}$$

and the pressure jump across the interface is $\Delta p = \sigma / R$. In the following study, an initial radius

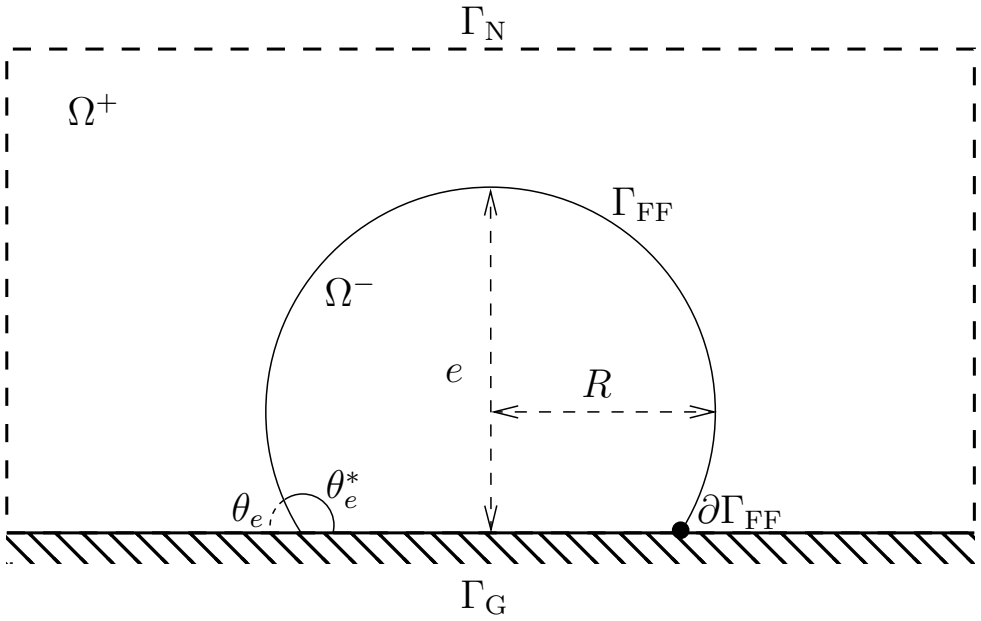

Figure 5.5: Setup of a bubble, depicted by Ω^-, at rest on a planar surface. In the sketch, the prescribed equilibrium contact angle θ_e^* is defined, alongside the height e of the bubble and the radius R of the bubble. Furthermore, the boundaries Γ_{FF}, Γ_{G} and Γ_{N} and the contact line $\partial\Gamma_{\mathrm{FF}}$ are depicted in this illustration.

of $R_0 = 0.25$ [m] is set for the droplet, and the equilibrium contact angle θ_e^*, as depicted in

Figure 5.5, is set to $120°$. Moreover, the setup of the problem and the introduced variables are also depicted in the aforementioned figure. A bubble, defined by the negative domain Ω^-, is at rest on a surface Γ_G, which is prescribed a general Navier boundary. The other boundaries are set as Neumann boundaries Γ_N with $\boldsymbol{h} = \mathbf{0}$. Given this premise, the analytic solution for the velocity is $\boldsymbol{u} = \mathbf{0}$ and for the pressure is

$$p = \begin{cases} \sigma/R & \text{in } \Omega^- \\ 0 & \text{in } \Omega^+. \end{cases} \tag{5.61}$$

As the analytic solution is known, the obtained results from applying the discretized equations (5.32) to this setup can be assessed quantitatively. Deviancy from the analytic solution stem from the error introduced in the discretized pressure space to the exact one, and results in the creation of spurious velocities. To demonstrate how this takes shape in practice, the pressure and the magnitude of the velocity for a 32×16 mesh are depicted in Figure 5.6, where the simulation was conducted with a mixed Laplace–Beltrami formulation for the surface tension force, i.e. (5.52), and a super convergent patch recovery technique is employed for the smoothing of the gradient field.

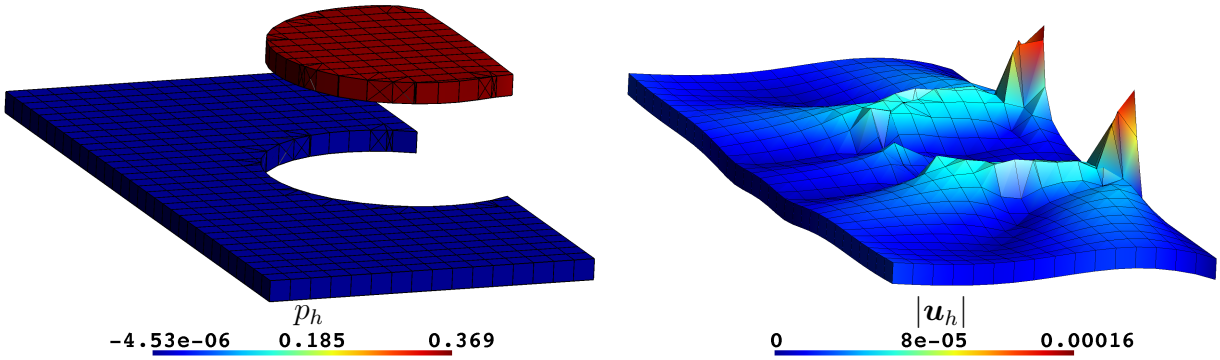

(a) Pressure solution

(b) Velocity magnitude

Figure 5.6: Solution of the primary variables $\boldsymbol{u}_h$ and p_h for a 32×16 mesh. On the left the discontinuous pressure solution is depicted, whereas the magnitude of the velocity $|\boldsymbol{u}_h|$ is depicted on the right.

To test the capabilities of employing a CutFEM for the velocity and pressure space, a large contrast in the physical parameters between the two phases is chosen. Accordingly, in the following simulation the viscosity and density are chosen as: $\mu^+ = 10^{-3}$, $\rho^+ = 10^{-3}$, $\mu^- = 1.0$, $\rho^- = 1.0$. The maximum slip length at the contact line is set as $\varepsilon_{\text{max}} = 10^6$ [m], with a spread around the contact line of $l_\varepsilon = 0.08$ [m]. Parameters related to the capillarity are chosen as $\sigma = 0.072$ [N/m] and, in accordance with the contact angle $\theta_e^* = 120°$, the forces at the contact line are given by $[\![\sigma_s]\!] = 0.036$ [N/m].

In Section 5.2.3.1 a variety of approaches to compute the surface tension and contact line forces found in literature were presented. The aim of this numerical example is to find the most suitable of these formulations for the proposed discretization. Given the initial conclusion that the Laplace–Beltrami approach is simpler to implement than the curvature one, as it does not necessitate the computation of the normal divergence on the surface, variations of this method are investigated in Section 5.3.1.1. Next, the best performing of the different Laplace–Beltrami methods is investigated in Section 5.3.1.2 to determine the best smoothing technique

from Section 2.2.1.4. Finally, the best performing Laplace–Beltrami technique is compared to the curvature formulations with the best performing smoothing technique in Section 5.3.1.3 to determine whether differences between the approaches exists.

To perform the convergence studies, the following parameters are employed for the simulations.

Mesh refinement parameters for the convergence studies The domain $\Omega = \Omega^+ \cup \Omega^-$ is a two-dimensional rectangle with the dimensions $[-0.5, 0.5] \times [-0.5, 0.0]$ $[\mathrm{m}]^2$. The interface condition on Γ_{FF} and the tangential boundary condition on Γ_{G} are imposed by means of an adjoint-inconsistent ($\zeta_u = -1$) Nitsche method, and the penalty parameters for these impositions are chosen as $1/\gamma^t = 1/\gamma^t_{\mathrm{FF}} = 1/\gamma^n_{\mathrm{FF}} = 100.0$. To reiterate what was mentioned in the introduction of this section, the wall-normal no-penetration condition of Γ_{G} is imposed strongly. For the Neumann boundary Γ_{N}, a classic Galerkin substitution method is used to enforce this boundary condition. The mesh sizes used to partition the domain for the convergence studies are chosen between 16×8 and 384×192 for bi-linear $\mathbb{Q}^1$ elements. The L^2-norms are evaluated on the computational domain $\widehat{\Omega}_h = \Omega^+_h \cup \Omega^-_h$.

Defining the computational domain by a level-set function The domain is defined by a level-set function, depending on the height of the bubble e and its radius R

$$\phi = \sqrt{(x - x_0)^2 + (y - y_0 - (R - e))^2} - R, \tag{5.62}$$

where $x_0 = 0$ and $y_0 = -0.5$. The height and radius are readily calculated from equations (5.60) and (5.59) respectively. This constructed level-set field is then projected by a nodal projection onto the background mesh, to create ϕ_h. The cut of this background mesh with ϕ_h is carried out as explained in Section 2.2.1.1.

Stabilization of the discretized weak form The nature of an equal-order finite element discretization necessitates the addition of stabilization terms to guarantee stability. In the following examples, the domain stabilization is conducted with a CIP-stabilization (2.31) and the instabilities arising from the cut interface are taken care of by the addition of ghost penalty terms (2.84). The constants for the stabilization terms are chosen the same as for the 2D Box Flow problem in Section 3.3.7, that is, $\gamma_\beta = \gamma_p = 0.01$, $\gamma_u = \gamma_\beta = \gamma_\nu = 0.05$ and $\gamma_\sigma = 0.005$ for the first order ghost penalty terms and the CIP terms. The second order ghost penalty terms are scaled with 0.05 to their first order counter parts. Higher order terms than second order for the ghost penalty terms are omitted, with the same reasoning as in the publication by Winter *et al.* [279]. The terms of ϕ_u, ϕ_β and ϕ_p appearing in the ghost penalty and CIP terms are defined as in (2.36) and (2.37) and the constants are given as $c_u = 1/6$ and $c_\sigma = 1/12$, as suggested in Schott *et al.* [230]. Additionally the simplified implementation for the CIP term $\overline{s}_\beta$ and the higher order approximations, i.e. $k > 1$, of the ghost penalty term $\overline{g}_\beta$ is employed. For a discussion on this simplification see Remark 3.6.

5.3.1.1 Comparison of Laplace–Beltrami Methods

In Section 5.2.3.1 three different ways of creating the Laplace–Beltrami projection matrix were shown in the equations (5.50)–(5.52). The different methods are given abbreviations to easier

distinguish between them. The projection defined in (5.50), where $\boldsymbol{P}^t_{\boldsymbol{n}_h} = \boldsymbol{I} - \boldsymbol{n}_h \otimes \boldsymbol{n}_h$, i.e. the normal is taken from the piecewise linear surface Γ_h, is abbreviated as **LB-NS**, for *Laplace–Beltrami no smoothing*. Next the approach in (5.51), where $\boldsymbol{P}^t_{\widetilde{\boldsymbol{n}_h}} = \boldsymbol{I} - \widetilde{\boldsymbol{n}_h} \otimes \widetilde{\boldsymbol{n}_h}$, is abbreviated as **LB-S**, for *Laplace–Beltrami with smoothing*. Finally, the option with a concatenation of the two, presented in (5.52), where $\widetilde{\boldsymbol{P}^t} = \boldsymbol{P}^t_{\widetilde{\boldsymbol{n}_h}} \boldsymbol{P}^t_{\boldsymbol{n}_h}$, is given the abbreviation **LB-MS**, short for *Laplace–Beltrami with mixed smoothing*. As the **LB-S** and **LB-MS** necessitate a smoothing of the gradient field $\nabla \phi_h$, a super convergent patch recovery (SPR), explained in Section 2.2.1.4, is chosen for this purpose. Alternative smoothing methods will be covered in the subsequent Section 5.3.1.2.

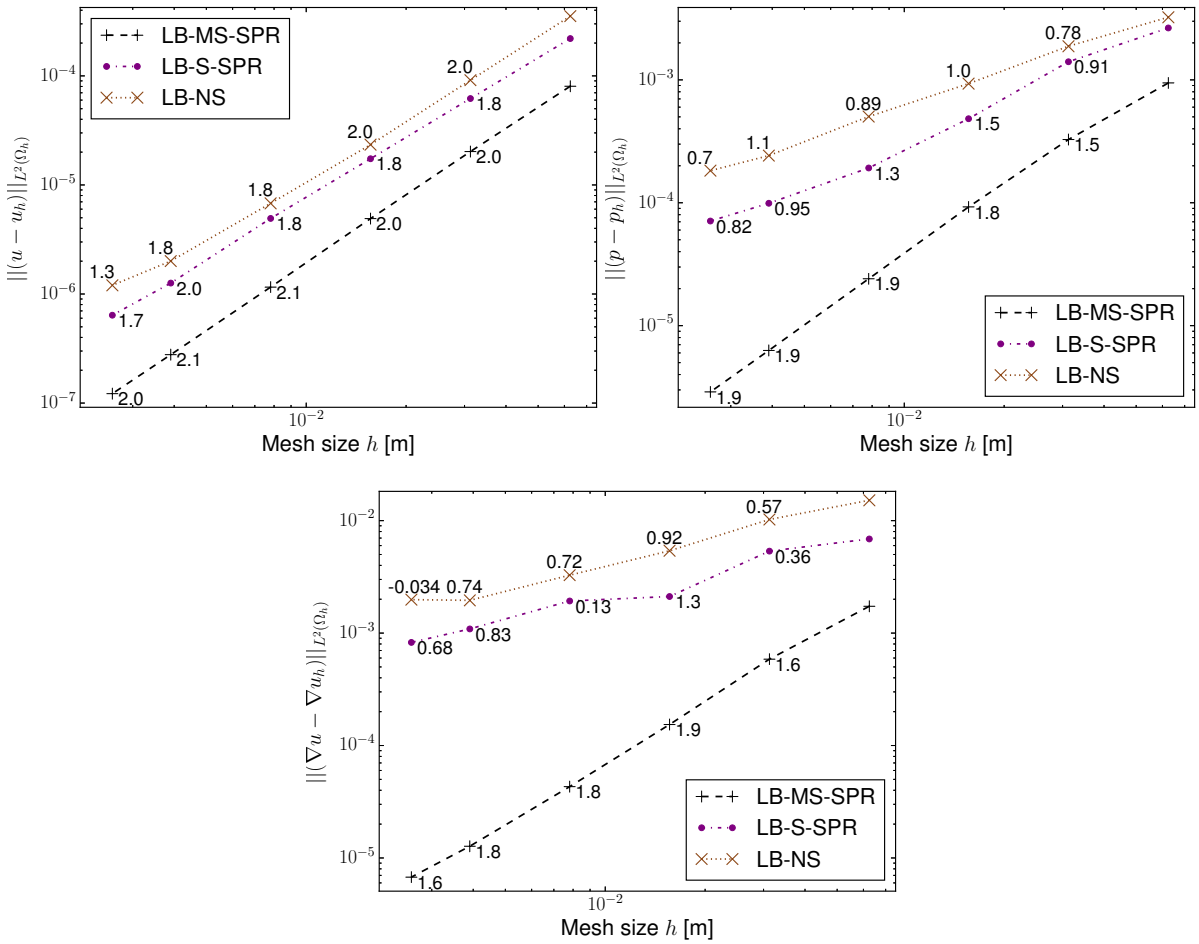

Figure 5.7: Error study for a static bubble with a 120 degrees equilibrium contact angle, comparing different Laplace–Beltrami configurations with a superconvergent patch recovery smoothing technique of the gradient. The upper row shows the bulk error of the velocity (to the left) and pressure (to the right) and on the lower row the bulk error of the velocity gradient. The numbers depicted in the plots are the logarithmic slopes of the curves, calculated from the current and previous data points for the respective study.

The results of the convergence study for the different approaches are shown in Figure 5.7, where the L^2-error for the velocity, pressure and velocity gradient on $\widehat{\Omega}_h$ are depicted. In these results, it is apparent that **LB-MS** delivers the best results. The method converges with

optimal order for the velocity L^2-norm and with super-convergence in the cases for the pressure and the velocity gradient. This super convergence stems most likely from the simplicity of the constant velocity solution ($\boldsymbol{u} = 0$ in Ω) and the constant solution of the pressure in the respective subdomain Ω^+ and Ω^-. Both the cases of **LB-S** and **LB-NS** have obvious convergence issues for both the pressure and the velocity gradient solution. The theoretical results from Groß and Reusken [132], conducted for a closed surface $\Gamma_{\mathrm{FF},h}$, can here be seen to also extend to the case where a contact line is included, as **LB-MS** clearly outperforms the other two approaches.

5.3.1.2 Smoothing Methods for the Mixed Laplace–Beltrami Method

Given the results from the previous Section 5.3.1.1, the mixed method Laplace–Beltrami approach (**LB-MS**) is chosen to further investigate the effects of the different smoothing techniques introduced in Section 2.2.1.4. The smoothing techniques are abbreviated as **SPR** for the super

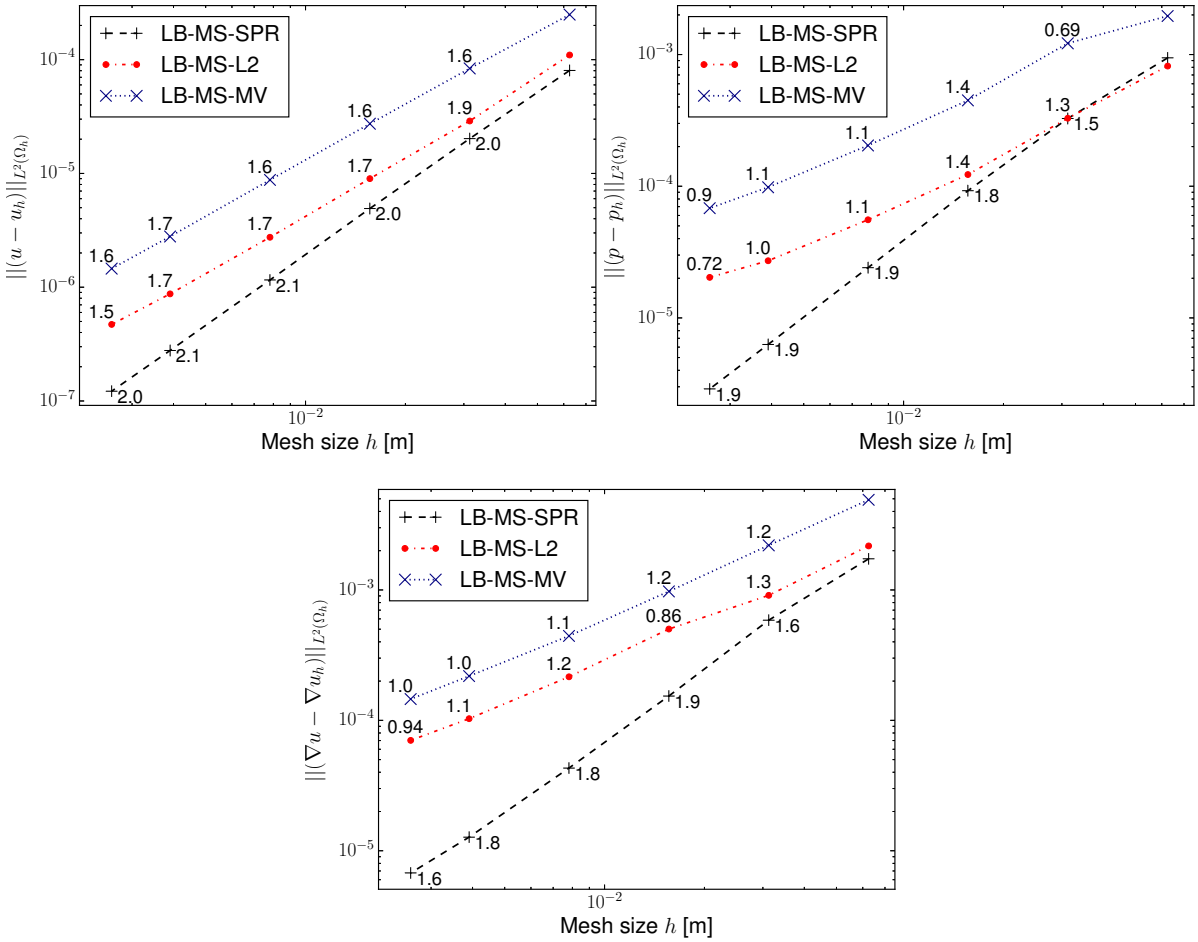

Figure 5.8: Error study for a static bubble with a 120 degree equilibrium contact angle, comparing different smoothing techniques for the mixed Laplace–Beltrami approach. The upper row shows the bulk error of the velocity (to the left) and pressure (to the right) and on the lower row the bulk error of the velocity gradient is shown. The numbers depicted in the plots are the logarithmic slopes of the curves, calculated from the current and previous data points for the respective study.

convergent patch recovery, **L2** for the L^2-projection and **MV** for the mean-value averaging. In

Figure 5.8 the convergence study is exhibited. The mean-value averaging and L^2-projection smoothing techniques have similar orders of convergence, i.e. $\mathcal{O}(h^{1.5})$ for the velocity and $\mathcal{O}(h)$ for the pressure and velocity gradient. Important to mention though, is the fact that the L^2-projection has a lower base error than the mean-value averaging. Nonetheless, the best performance is obtained in the SPR case, where optimal order of convergence for the velocity and super convergence for both the pressure and velocity gradients can be observed.

To quantify the differences between the smoothing methods, the smoothed normal $\widetilde{\boldsymbol{n}_h}$ is compared to the analytic one on $\Gamma_{\mathrm{FF},h}$. Given that the shape of the droplet is known, the analytic normal can be construed as,

$$\boldsymbol{n}(\boldsymbol{x}) = \frac{1}{r}\begin{pmatrix}(x - x_0)\\(y - y_0) + (R - e)\end{pmatrix}, \tag{5.63}$$

where

$$r = \sqrt{(x - x_0)^2 + (y - y_0 + (R - e))^2}. \tag{5.64}$$

The L^2-error on the interface $\Gamma_{\mathrm{FF},h}$ of the smoothed normal vectors $\widetilde{\boldsymbol{n}}_h$ compared against the

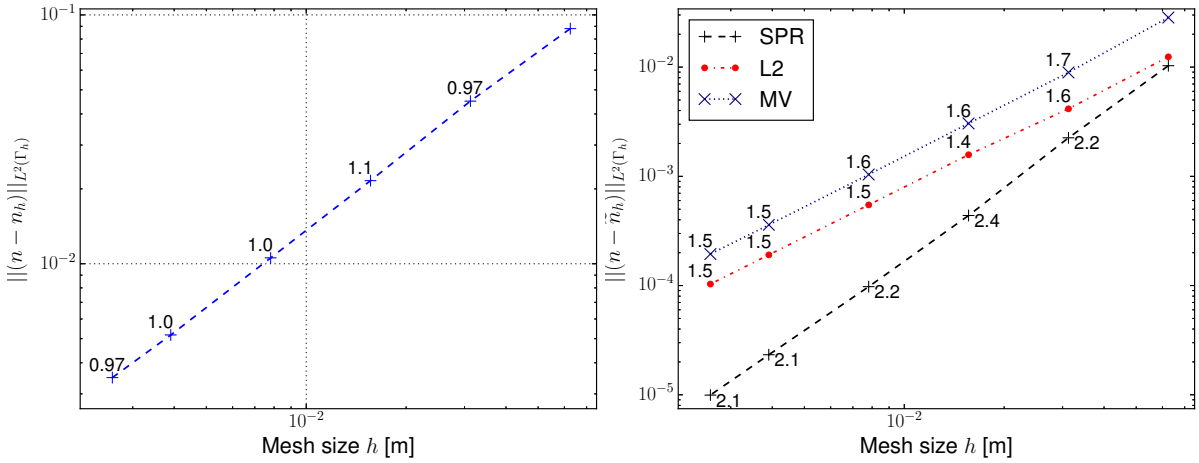

Figure 5.9: Error study for the normal vector on $\Gamma_{\mathrm{FF},h}$, comparing the convergence of different smoothing techniques to the analytic normal. On the left, the piecewise constant normal $\boldsymbol{n}_h$ taken from the approximated piecewise linear surface $\Gamma_{\mathrm{FF},h}$, is shown and on the right, the smoothed normal $\widetilde{\boldsymbol{n}_h}$ with different smoothing techniques is illustrated. The numbers depicted in the plots are the logarithmic slopes of the curves, calculated from the current and previous data points for the respective study.

analytic normal $\boldsymbol{n}(\boldsymbol{x})$, given by equation (5.63), is depicted in Figure 5.9. Here the differences between the proposed smoothing techniques become apparent. The approximation of the normal vector $\widetilde{\boldsymbol{n}_h}$ is about half an order of convergence better for the SPR than for the L2 or MV cases. Hence, it is concluded that for the cases with droplets on surfaces, the SPR method should be employed for normal vector smoothing purposes. Nevertheless, it is important to stress that an improvement is made for any choice of smoothing technique in comparison to using the normal vector $\boldsymbol{n}_h$ originating from the cut surface. This normal taken from the cut surface only enjoys a first order convergence, whereas a normal created from one of the presented smoothing techniques achieves at least an order of $\mathcal{O}(h^{1.5})$ as seen in the results presented in Figure 5.9.

Remark 5.7 *In Figure 4.10 a smoothing of normals on circular surfaces are also conducted with a L^2-projection. In contrast to the obtained order of convergence of $\mathcal{O}(h^{1.5})$ in Figure 5.9 for the L^2-projection, an order of $\mathcal{O}(h^2)$ could be observed. The difference between these two cases is the fact that the zero iso-contour of the level-set (i.e. the boundary/interface of interest) intersects the boundary of the computational mesh in the former. Accordingly, it can be postulated that this smoothing of normals close to the boundary of the computational mesh leads to a loss of convergence for the L^2-projection.*

5.3.1.3 The Mixed Laplace–Beltrami Method Compared to Curvature Formulations

Lastly, the most successful approach for the Laplace–Beltrami with the best smoothing technique is compared to curvature formulation approaches. Accordingly, the abbreviation

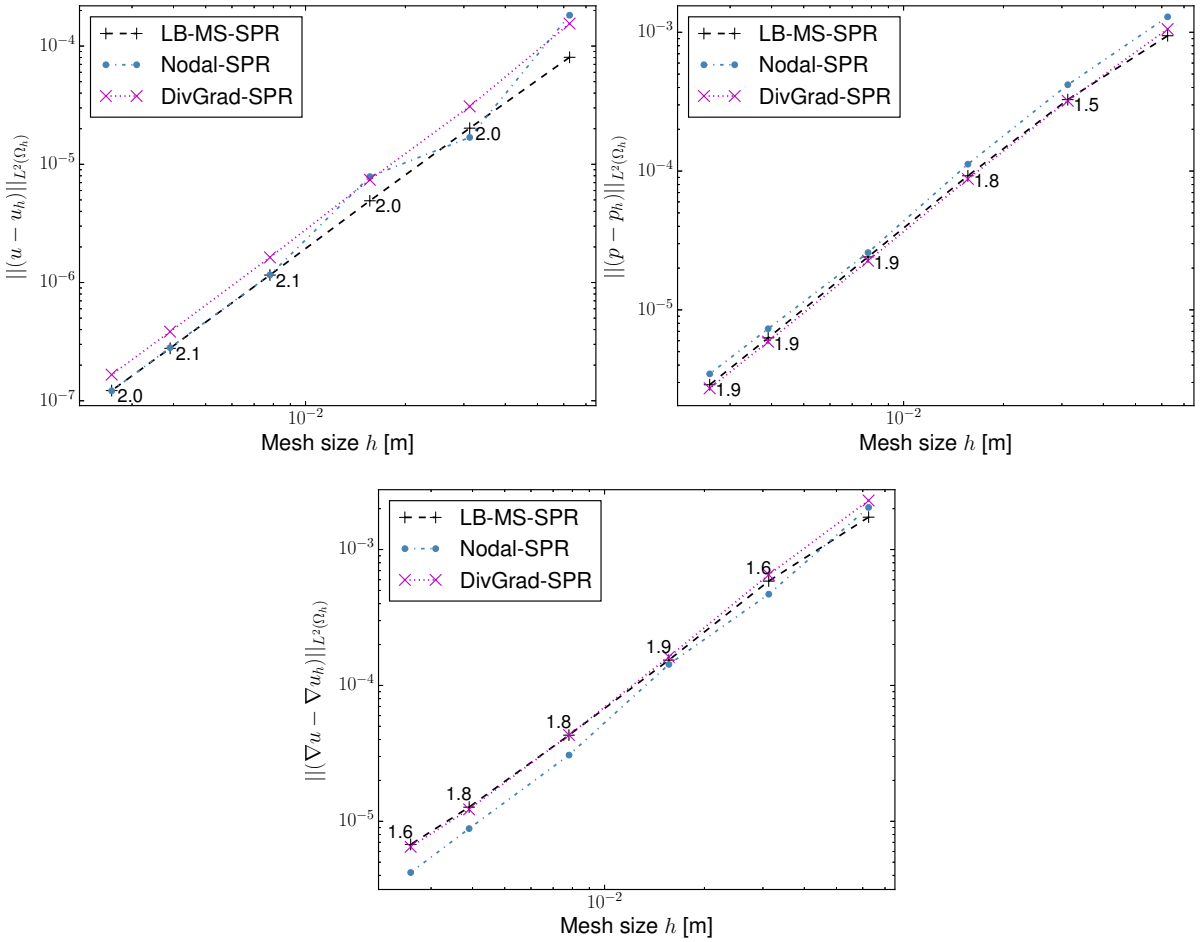

Figure 5.10: Error study for a bubble with 120 degree equilibrium contact angle, comparing different approaches to calculate the surface tension forces. The upper row shows the bulk error of the velocity (to the left) and pressure (to the right) and on the lower row the bulk error of the velocity gradient is shown. The numbers depicted in the plots is the logarithmic slope of the **LB-MS-SPR**, calculated from the current and previous data points.

LB-MS-SPR denotes the mixed Laplace–Beltrami approach with SPR smoothing of the level-

set gradient field. The **DivGrad** option denotes the approach described in (5.49), which in short calculates the curvature $\kappa(\widetilde{\nabla\phi_h})$ from the smoothed level-set field. Given that this curvature field is not continuous, an L^2-projection, as described in Section 2.2.1.4, can be applied to obtain a smoothed curvature field $\widetilde{\kappa(\phi_h)}$. This approach with extra L^2 smoothing of the curvature is named **Nodal** in the following.

The results in Figure 5.10 demonstrate that, at least for this setup, the choice between a Laplace–Beltrami and curvature formulation makes no big difference. All three approaches show more or less the same order of convergence with slight differences in the level of the error for the velocity, pressure and velocity gradient. What seems to be conclusive from the results, is the fact that any choice of method seems to perform satisfactorily as long as a good smoothing technique is employed.

5.3.2 Spreading Droplet on a Plate

To conclude this section, a final example is demonstrated with a moving contact line. The premise for the static bubble in the previous Section 5.3.1 is repeated, but in this case the droplet starts in an non-equilibrium position. The droplet will be given an initial contact angle of $\theta_0^* = 120°$ whereas the equilibrium contact angle is set to $\theta_e^* = 80°$. Hence, when $t \to \infty$ the solution should converge to the equilibrium state of $\theta_e^* = 80°$, with the associated solution $\boldsymbol{u} = \mathbf{0}$ and the pressure p given by (5.61). Another measure to quantify the accuracy of the simulation is the wetted radius L, given by

$$L = R\sin(\theta_e^*). \tag{5.65}$$

The position of the contact line $\partial\Gamma_{\mathrm{FF}}$ can be measured and, over time, its position should converge to the equilibrium wetted radius. Given, the above input, the asymptotic solution for the pressure jump is

$$\Delta p(t \to \infty) \approx 0.254358,$$

and for the wetted radius

$$L(t \to \infty) \approx 0.27876514.$$

As the final shape of the droplet is independent of the fluid properties, the parameters are chosen the same for both fluid phases, that is, $\mu^+ = \mu^- = 1.0$, $\rho^+ = \rho^- = 1.0$. To evaluate the ensuing wetting process, the motion of the droplet is simulated for $t \in [0, t_{\text{end}}]$, with $t_{\text{end}} = 50$ [s]. For the time integration a backward Euler scheme is used (i.e. a one-step theta scheme with $\Theta = 1$) with $\Delta t = 0.01$ [s], see Section 2.3.3 for more details on how time integration for moving interfaces are dealt with in a CutFEM framework.

The imposition of the surface tension force is done with a mixed Laplace–Beltrami formulation for the surface tension force, i.e. (5.52), and an SPR-technique is employed for the smoothing of the gradient field. This setup was found to provide good performance in the static droplet case, which was investigated in the previous Section 5.3.1. In the simulations, the surface tension is set to $\sigma = 0.072$ [N/m] on the surface Γ_{FF} and the equilibrium contact angle is chosen as $\theta_e^* = 80°$, which corresponds to $[\![\sigma_s]\!] \approx 0.0125$ [N/m] (as calculated from (5.18)). Furthermore, as already mentioned in Section 5.2.1, no dissipation at the contact line, i.e. $\boldsymbol{f}_{\theta_d} = \mathbf{0}$, is assumed in the following simulations.

The domain $\widehat{\Omega}_h$ is defined by a two-dimensional rectangle of the dimensions $[-0.5, 0.5] \times [0.0, 0.5]$ $[\mathrm{m}]^2$. The interface condition on Γ_{FF} and the tangential boundary condition on Γ_{G} are imposed by means of an adjoint-inconsistent ($\zeta_u = -1$) Nitsche method, and the penalty parameters for these impositions are chosen as $1/\gamma^t = 1/\gamma^t_{\mathrm{FF}} = 1/\gamma^n_{\mathrm{FF}} = 200.0$. A strong imposition is employed for the wall-normal no-penetration condition on Γ_{G} and a classic Galerkin substitution method is used for the Neumann boundary Γ_{N}. The domain is partitioned into three distinct mesh sizes of 60×30, 100×50 and 140×70 to study the effects of the simulation upon refinement of the mesh. For these meshes, equal-order $\mathbb{Q}^1$ continuous bi-linear elements are employed. Given the setup, stabilizations in the domain and at the interface are necessary. For these simulations, residual based stabilization (2.23)–(2.25) are employed in the domain, and ghost penalty stabilization terms (2.84) at the interface between the two phases.

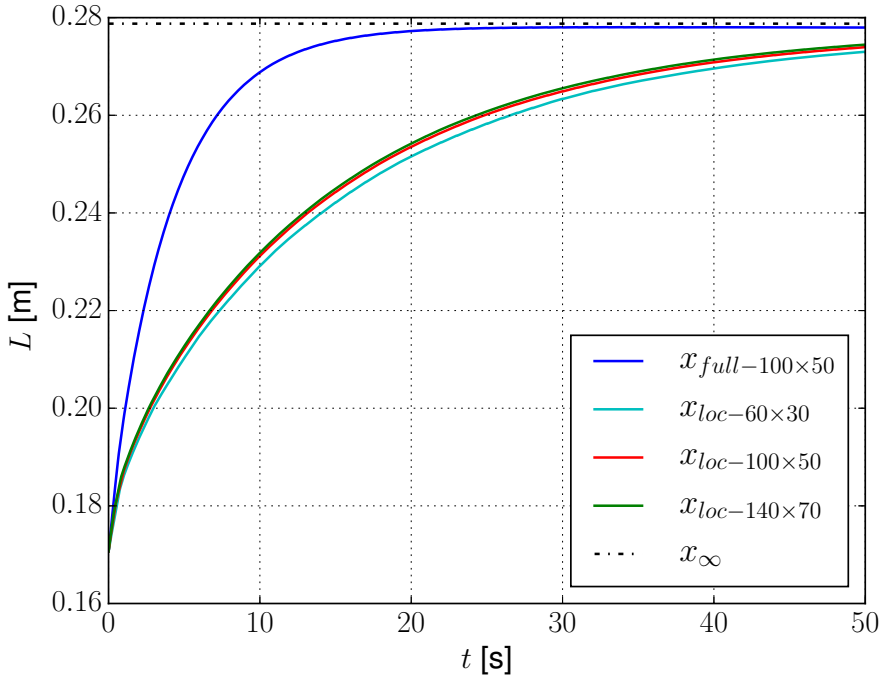

Figure 5.11: The motion of the contact line $\partial\Gamma_{\mathrm{FF}}$ along the positive x-axis for the simulation is depicted in this figure. The lines defined as x_{loc} show the results for the localized slip method for different mesh sizes. A reference solution with full slip on the plate is demonstrated for the label x_{full}, and the asymptotic solution for $t \to \infty$ is given by x_∞.

The initial shape of the droplet is given by the equations (5.59)–(5.60), which give the height e and radius R provided the initial contact angle θ_0^*. These two properties can be plugged into (5.62), with $x_0 = y_0 = 0$, to obtain the associated level-set function ϕ at time $t = 0$. Given that in the following simulations the interface $\Gamma_{\mathrm{FF},h}$ is not stationary, both the fluid equations (5.32) and the level-set equation (2.59) need to be solved at the same time. The coupling between these two discretized fields was briefly explained in Remark 5.6. To combat the deterioration of the signed-distance property of the level-set, a geometric reinitialization technique is employed, explained in Section 2.2.1.2. Reinitialization of the signed-distance field is undertaken every 100 time steps, which corresponds to every 1 second. Given the issue of mass conservation of

the phases when the level-set field is advected, explained in Section 2.2.1.3, the hybrid-particle method by Enright *et al.* [107] is employed to combat this.

In Figure 5.11 the wetted radius L is tracked over time, where the position of the contact line $\partial\Gamma_{\mathrm{FF}}$ is calculated along the positive x-axis. Three different mesh sizes are shown, 60×30, 100×50 and 140×70, with the localized slip length method presented in (5.58), for the parameters $\varepsilon_{\max}=10^6$ [m] and $l_\varepsilon=0.08$ [m]. These three simulations are named $x_{loc-60\times30}$, $x_{loc-100\times50}$ and $x_{loc-140\times70}$ respectively in the subsequent figures. Additionally, a simulation with full slip, i.e. $\varepsilon_{\max}=\infty$ and $l_\varepsilon=\infty$, for the mesh size 100×50 is conducted as a reference solution to quantify the effect of the localized slip approach. From Figure 5.11 it is clear that there is a noticeable effect coming from the inclusion of a localized slip model in comparison to a full slip model. It takes longer to reach the asymptotic solution for a localized slip model, which is expected given that there is more friction between the fluid and the plate. Additionally, upon mesh refinement, it would seem as if the obtained solution converges towards a common solution for a fixed l_ε and $\varepsilon_{\max}$, as seen from the x_{loc}-cases.

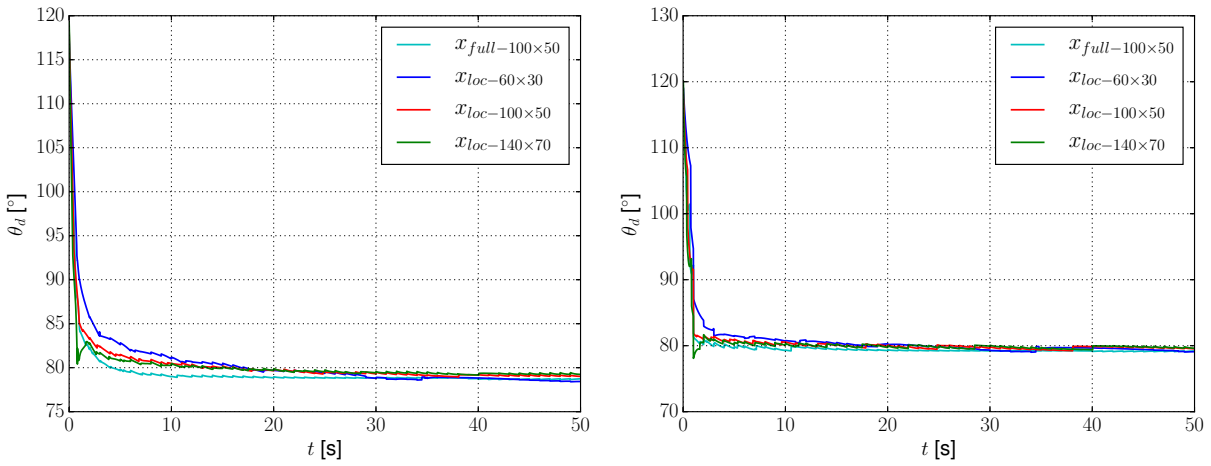

(a) θ_d (from cut-geometry) against t time.

(b) θ_d (from smoothed gradient field) against t time.

Figure 5.12: Contact angle evolution in time for different mesh mesh sizes of the localized slip case, depicted as x_{loc} in the above results, and the reference simulation with full slip given by x_{full}.

Another quantity of interest is the dynamic contact angle θ_d. In Figure 5.12 the dynamic contact angles are plotted against time for the contact line created by the intersection of the interface $\Gamma_{\mathrm{FF},h}$ with the boundary Γ_{G} on the positive half plane, i.e. $x>0$.

The contact angle can be computed from the normal $\boldsymbol{n}_{\Gamma_{\mathrm{FF}}}$ of the interface Γ_{FF} and the normal $\boldsymbol{n}_{\Gamma_{\mathrm{G}}}$ of the boundary Γ_{G} at the point $\partial\Gamma_{\mathrm{FF}}$ in the following fashion,

$$\boldsymbol{t}_{\Gamma_{\mathrm{G}}}(\boldsymbol{n}_{\Gamma_{\mathrm{G}}},\boldsymbol{n}_{\Gamma_{\mathrm{FF}}})=\boldsymbol{n}_{\Gamma_{\mathrm{G}}}\times(\boldsymbol{n}_{\Gamma_{\mathrm{FF}}}\times\boldsymbol{n}_{\Gamma_{\mathrm{G}}}) \tag{5.66}$$

$$\boldsymbol{t}_{\Gamma_{\mathrm{FF}}}(\boldsymbol{n}_{\Gamma_{\mathrm{G}}},\boldsymbol{n}_{\Gamma_{\mathrm{FF}}})=(\boldsymbol{n}_{\Gamma_{\mathrm{FF}}}\times\boldsymbol{n}_{\Gamma_{\mathrm{G}}})\times\boldsymbol{n}_{\Gamma_{\mathrm{FF}}}, \tag{5.67}$$

and

$$\theta_d^*(\boldsymbol{n}_{\Gamma_{\mathrm{G}}},\boldsymbol{n}_{\Gamma_{\mathrm{FF}}})=\cos^{-1}\left(\boldsymbol{t}_{\Gamma_{\mathrm{G}}}\cdot\boldsymbol{t}_{\Gamma_{\mathrm{FF}}}\right). \tag{5.68}$$

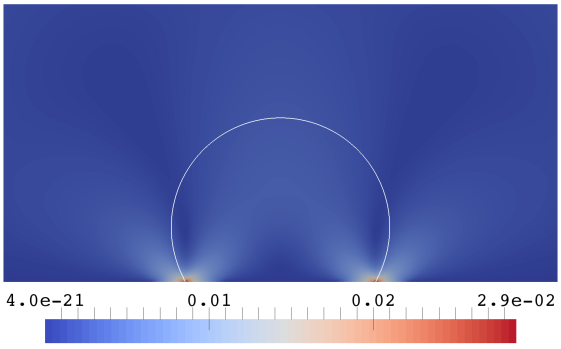

(a) $t = 0.02$, $||\boldsymbol{u}_h||_\infty \approx 0.029$

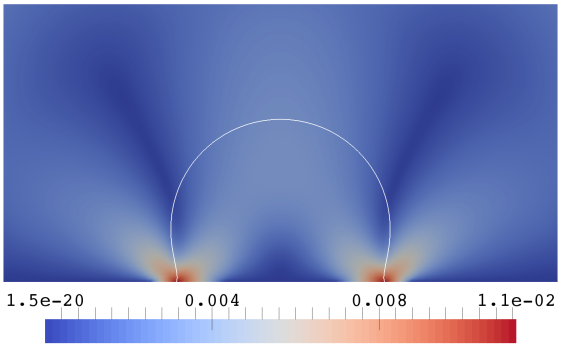

(b) $t = 1.0$, $||\boldsymbol{u}_h||_\infty \approx 0.011$

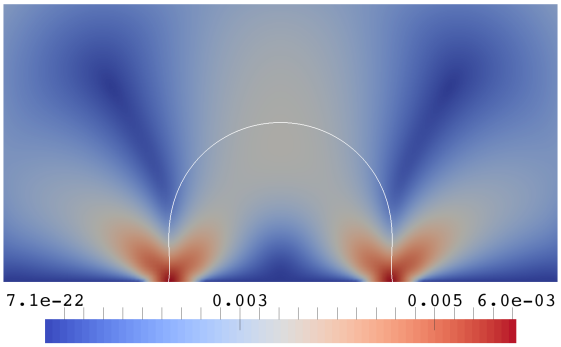

(c) $t = 3.0$, $||\boldsymbol{u}_h||_\infty \approx 0.006$

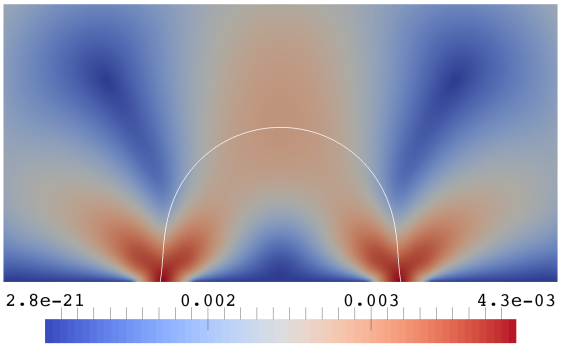

(d) $t = 6.0$, $||\boldsymbol{u}_h||_\infty \approx 0.0043$

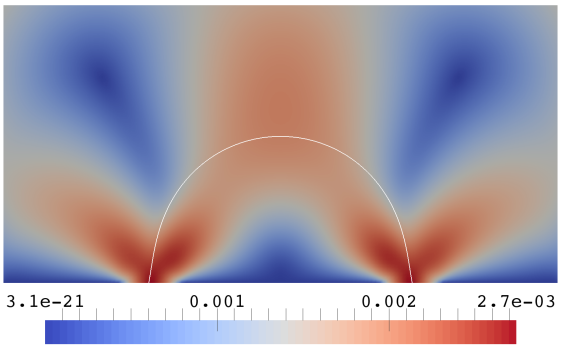

(e) $t = 12.0$, $||\boldsymbol{u}_h||_\infty \approx 0.0027$

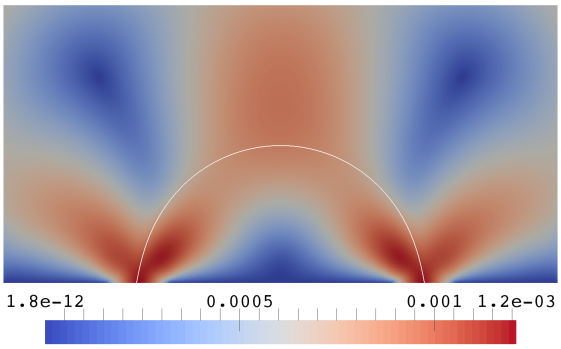

(f) $t = 24.0$, $||\boldsymbol{u}_h||_\infty \approx 0.0012$

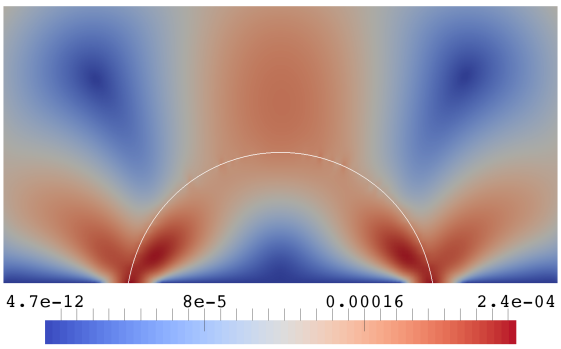

(g) $t = 50.0$, $||\boldsymbol{u}_h||_\infty \approx 0.00024$

Figure 5.13: A time series of $t = [0.02, 1.0, 3.0, 6.0, 12.0, 24.0, 50.0]$ of the velocity magnitude $||\boldsymbol{u}_h||_\infty$ for the spreading droplet with localized slip for a 140×70 mesh. Keep in mind that the color scale changes throughout the time series.

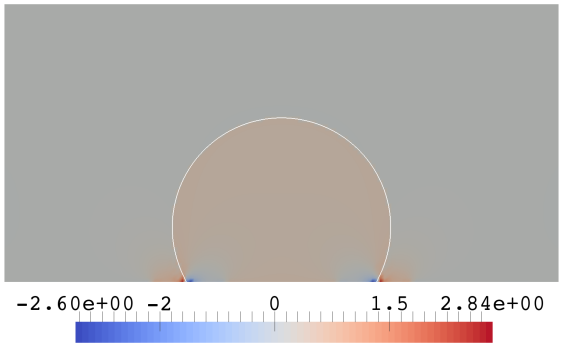

(a) $t = 0.02$, $\Delta_\infty p_h \approx 5.4$

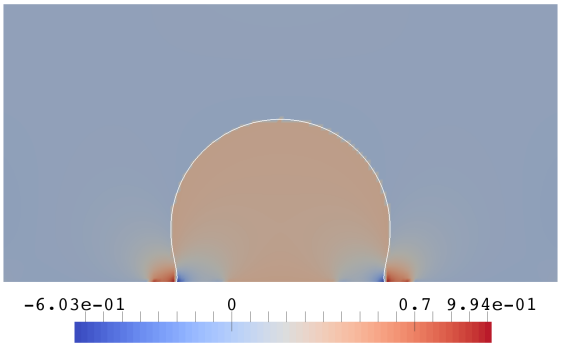

(b) $t = 1.0$, $\Delta_\infty p_h \approx 1.6$

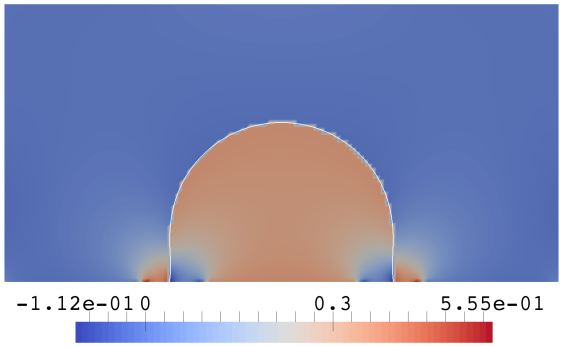

(c) $t = 3.0$, $\Delta_\infty p_h \approx 0.66$

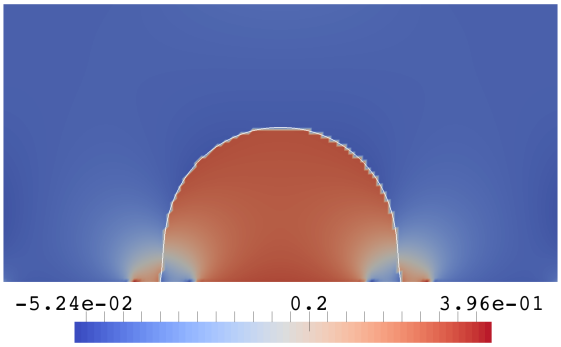

(d) $t = 6.0$, $\Delta_\infty p_h \approx 0.45$

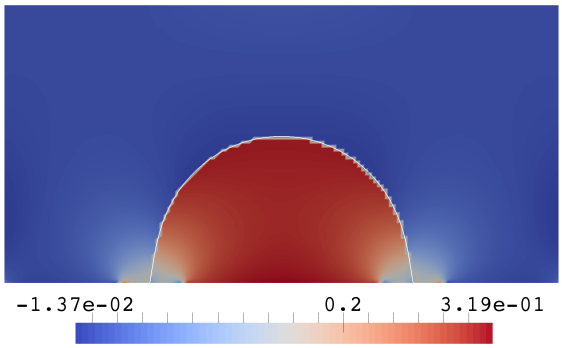

(e) $t = 12.0$, $\Delta_\infty p_h \approx 0.33$

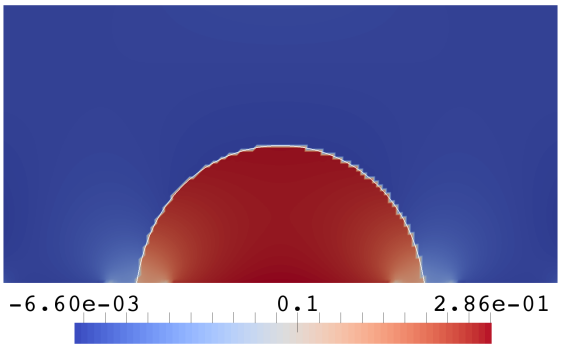

(f) $t = 24.0$, $\Delta_\infty p_h \approx 0.29$

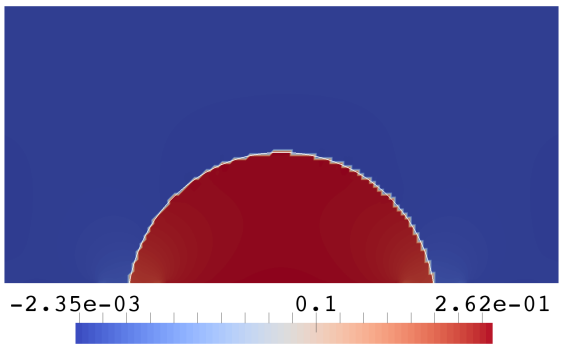

(g) $t = 50.0$, $\Delta_\infty p_h \approx 0.264$

Figure 5.14: A time series of $t = [0.02, 1.0, 3.0, 6.0, 12.0, 24.0, 50.0]$ of pressure solution p_h for the spreading droplet with localized slip for a 140×70 mesh. Keep in mind that the color scale changes throughout the time series.

In Figure 5.12a, the contact angle is created from the piecewise linear surface, that is $\theta_d^*(\boldsymbol{n}_{\Gamma_\mathrm{G}}, \boldsymbol{n}_{\Gamma_{\mathrm{FF},h}})$, whereas in Figure 5.12b the smoothed normal, after applying the SPR on $\nabla\phi_h$, is used to calculated the contact angle, i.e. $\theta_d^*(\boldsymbol{n}_{\Gamma_\mathrm{G}}, \widetilde{\boldsymbol{n}_{\Gamma_{\mathrm{FF},h}}})$. In both of the figures it is apparent that the contact angle decreases within a short period of time to the prescribed $\theta_e^* = 80°$, and then stays around this prescribed value. This is in agreement with the observations in Buscaglia and Ausas [68] that without a dissipative force $\boldsymbol{f}_{\theta_d} = \boldsymbol{0}$, the contact angle will will change almost immediately to θ_e^* and then keep this value for the remainder of the simulation. The observed oscillations of the contact angle in the figures stem from the reinitialization of the level-set and the passage of the interface from one element to another.

Next, the primary variables $\boldsymbol{u}_h$ and p_h are investigated at the times $t = [0.02, 1.0, 3.0, 6.0, 12.0, 24.0, 50.0]$. Throughout these time series, the color scale is changing, which needs to be kept in mind when viewing the following results. In Figure 5.13 the velocity magnitude $|\boldsymbol{u}_h|$ is depicted. As is expected, the velocity is the largest close to the contact line and decreases with time as the droplet starts to approach the equilibrium condition. Furthermore, the localized slip is clearly visible around the contact line region, while away from the smeared slip region, the no-slip condition is fulfilled. Next, the pressure is depicted in Figure 5.14, where large pressure peaks are visible in the vicinity of the contact line at $t = 0.02$. These peaks decreases successively in magnitude as the droplet approaches its equilibrium shape. The measure between the maximum and minimum values of the pressure solution is defined as

$$\Delta_\infty p_h = \max_{\widehat{\Omega}}(p_h) - \min_{\widehat{\Omega}}(p_h), \tag{5.69}$$

and is provided in the caption of the subfigures to quantify the evolution of the peaks. This quantity starts of at $\Delta_\infty p_h \approx 5.4$ for $t = 0.02$ and decreases with time until it arrives at $\Delta_\infty p_h \approx 0.264$ for $t = 50.0$, which is close to the analytic solution $\Delta p \approx 0.254$.

The magnitude of the initial pressure peaks increases with mesh refinement, as demonstrated in Figure 5.15. For $t = 0.02$ the measure $\Delta_\infty p_h$ is reproduced with the mesh sizes, 60×30, 100×50 and 140×70. From Figure 5.15a and Figure 5.15c the measure $\Delta_\infty p_h$ increases from 2.2 to 5.4. This divergence of the pressure solution at the contact line upon refinement is a known phenomena for this type of formulation, and has also been reported in the works by Heimann [140] and Boelens and de Pablo [35]. Given that the contact line introduces line forces in 3D (or point forces in 2D), the support of the element which needs to "absorb" this force becomes smaller upon mesh refinement, and hence the pressure jump needs to become larger to compensate the line force at the contact line. The obvious drawback of this diverging pressure solution is that it sets a limit on how fine a mesh can be refined before the conditioning of the global system starts to deteriorate. This diverging pressure solution can also be argued to be a manifestation of the ill-posedness of the weak form discussed in Remark 5.5.

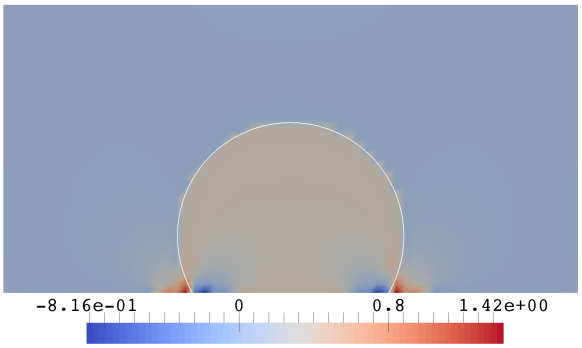

(a) p_h at $t = 0.02$ for mesh 60×30, $\Delta_\infty p_h \approx 2.2$

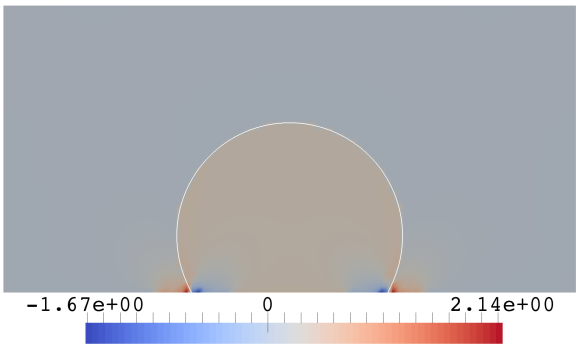

(b) p_h at $t = 0.02$ for mesh 100×50, $\Delta_\infty p_h \approx 3.8$

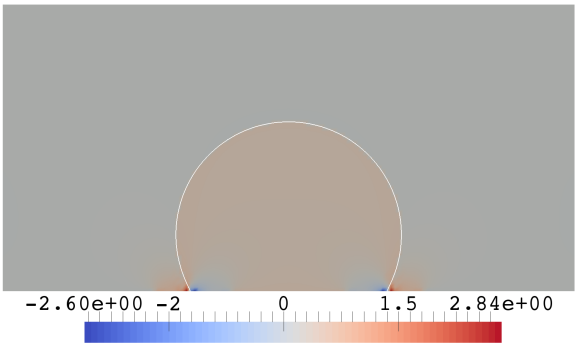

(c) p_h at $t = 0.02$ for mesh 140×70, $\Delta_\infty p_h \approx 5.4$

Figure 5.15: Pressure solution at $t = 0.02$ with the CutFEM localized slip method for mesh sizes 60×30, 100×50 and 140×70. Keep in mind that the color scales are not the same for the subfigures.

Chapter 6

Summary and Outlook

The research presented in this thesis has made strides to improve the usability of the general Navier boundary condition (GNBC). Even though this boundary condition arises in several flows in nature and industry, it has only been studied at depth in a handful of previous publications.

One of the main issues in the way the general Navier boundary condition has been imposed in literature thus far, is the fact that both the Dirichlet and Neumann limits of the tangential Robin condition could not be incorporated by the Galerkin substitution method. In particular, the Dirichlet limit caused problems. This thesis has demonstrated a method to overcome this issue by employing the Nitsche's method for this tangential Robin condition. To ensure that the proposed formulation is indeed applicable for an arbitrary choice of slip length, i.e. any linear combination of the Dirichlet and Neumann contributions, a thorough mathematical analysis was conducted for the linearized Navier–Stokes equations, i.e. the Oseen problem. In this analysis, inf-sup stability, optimal a-priori estimates and a L^2-optimal estimate for the velocity were demonstrated. A numerical example was carried out to corroborate the theoretical findings, and good agreement to theory could be observed. As the aforementioned mathematical analysis was conducted for the more general case of an unfitted finite element approach, here the CutFEM, this incorporates also the analysis of the fitted approach. The proposed formulation for the general Navier condition lays the foundation for extensions of the Nitsche's method from only imposing Dirichlet conditions to also include the imposition of Robin conditions for the Navier–Stokes equations. Future work could try to incorporate the findings of this thesis to impose a Robin condition, viable in both the Dirichlet and Neumann limits. Given the robust numerical analysis of the imposition of the GNBC by a Nitsche method, the proposed imposition could be extended to other similar boundary or interface conditions. Two possible extensions for future research could be found in the coupling of incompressible fluid flow with poroelasticity, or in the numerical modeling of contact between immersed bodies. Nevertheless, these are most certainly not the only possible extensions, as the techniques introduced in this thesis might also be beneficial for other fields, apart from solid or fluid mechanics.

A well-known issue for the general Navier boundary condition is the importance of accounting for geometrical approximations errors. One of the more notable errors, is the error introduced when the normal $\boldsymbol{n}_h$ of the discretized domain Ω_h and the normal $\boldsymbol{n}$ of the physical domain Ω do not match. In the context of the GNBC, when $\boldsymbol{n}_h$ is chosen as a piecewise constant, this

error is more commonly known as the Babuška paradox [12]. The effects of using a smoothed normal field of an underlying level-set function was demonstrated in this thesis to have an improving effect on the convergence of the solution. Moreover, in the results obtained with the proposed Nitsche's method, it was discovered that to achieve optimal order of convergence, the convergence of the discretized normal needed to be of at least the same order as the expected order of convergence for the velocity. Nevertheless, this correlation has only been demonstrated heuristically in this thesis by a numerical example. As such, a thorough mathematical analysis on the introduced geometrical error of the discretized normal vector $\boldsymbol{n}_h$ remains to be carried out in future work on the GNBC. Additionally, the smoothed normal field utilized to improve the convergence was always taken to be a continuous field in this thesis. This restriction might be impractical in the case of discontinuous Galerkin methods. Hence, investigations into the possibility of a discontinuous normal field on the discretized boundary Γ_h with sufficiently high convergence in a L^2-norm, should be undertaken.

When discretizations with higher order elements are used, not only errors from the approximations of the normal become important to consider for the imposition of the GNBC, but also errors stemming from the approximation of the physical domain. Given that a CutFEM was employed in this thesis, a piecewise linear approximation Ω_h is created of the physical domain Ω. This geometrical approximation error introduces an error of order $\mathcal{O}(h^2)$, hence, corrective measures have to be undertaken to achieve optimal order of convergence when higher order than first order elements are considered. In this thesis this was remedied by the addition of boundary value correction terms in the Nitsche terms imposing the GNBC. These corrective terms were calculated by creating extensions of the solution on the approximated boundary to the physical boundary through a Taylor expansion. With this approach, optimal order of convergence for bi-quadratic elements could be demonstrated in a numerical example with curved boundaries. On a side note, the method applied here is also viable for Dirichlet boundaries, as it is but a subset of the GNBC. Given that no thorough mathematical analysis was provided in this thesis, work remains to be done in this area. Moreover, only second order elements were considered in this thesis. Accordingly, it remains to demonstrate the effect of the boundary value correction also for elements of higher order than second order. In this thesis the distance of the approximated boundary Γ_h and Γ was assumed to be of the order $\mathcal{O}(h^2)$; even though in the analysis in Burman *et al.* [66] this is not a necessary requirement. With the addition of sufficiently high order terms in the Taylor expansion, a distance of the order $\mathcal{O}(h)$ could be sufficient, at least in the case of a Dirichlet boundary. This possibility remains to be investigated in future work. Lastly, given that the Dirichlet and general Navier boundary conditions have shown good results for the boundary value correction method, attempts to use this method for the Neumann condition should be done as well. What makes the Neumann condition more complex though, is that it necessitates extensions of both the pressure and velocity solutions. For the Dirichlet and general Navier boundary this was not the case, as extensions of only the velocity were sufficient. Consequently, care has to be taken when developing boundary value corrections for the Neumann condition as the suggested extensions for the velocity might not be readily applicable for the pressure.

Finally, this thesis dealt with the subject of two-phase flows, and in particular on flows with contact lines, i.e. at the line where two phases and a solid wall intersect. As is commonly known, the no-slip condition at a moving contact line for wetting processes is an unfeasible boundary condition, as it leads to a divergent shear stress of the fluid. Accordingly, a different approach needs to be pursued at the contact line. In this thesis, this is resolved with a localized

slip model, i.e. close to the contact line slip is allowed whereas further away no-slip is imposed. The localized slip model was realized here by the proposed imposition of the general Navier condition by the Nitsche's method. It was combined with a CutFEM for the two-phase flow, making it possible to conduct simulations with large contrasts in material parameters between the two phases. Alternative approaches, to the one chosen, for modeling the motion of contact lines were also presented, and their strengths and weaknesses were discussed. For the static case, investigations into different techniques for imposing the surface tension on the interface between the two phases were conducted. In particular, different smoothing techniques for the normal vector of the interface were compared, and for the studied example, it was found that the super convergent patch recovery achieved the best results. Additionally, it was found that both the Laplace–Beltrami and curvature formulations gave equally good results, when the same smoothing technique was applied. For the dynamic case, the spreading of a partial wetting droplet was studied. Qualitatively, convergence could be observed when the mesh was refined, as the solution approached the expected asymptotic solution. However, an important term neglected in this thesis is the dissipation occurring at the contact line. A natural next step for this formulation would be to implement a dissipative term at the contact line to allow for a more physically sound model. In the approach pursued in this thesis, it became obvious that around the contact line, the pressure diverges upon mesh refinement, as was demonstrated for the spreading droplet example. This is an inherent property of the chosen sharp-interface model, and it is not well investigated or discussed in literature how it is to be resolved when molecular length scales are approached. As such, this makes it an important priority for future research. Moreover, it is important to recognize that the modeling and computing of systems containing moving contact lines, are still an active field of research. An important contribution to this field would be a comparison of the three major approaches, i.e the sharp-interface, phase-field and Shikmurzaev model for a simulation with a moving contact line.

Appendix A

Linearization of Projected Nitsche Terms for the General Navier Condition

With the splitting of the boundary condition for the general Navier condition, projection matrices are applied on the conditions. This introduction of projection matrices brings about some changes in how the linearization of the boundary terms need to be created. Given that,

$$u_{h,k} := \sum_{ic=0}^{\mathrm{n_{node}}} N^{ic} u_{h,k}^{ic} \tag{A.1}$$

$$p_h := \sum_{ic=0}^{\mathrm{n_{node}}} N^{ic} p_h^{ic}, \tag{A.2}$$

and $\boldsymbol{v}_h$ and q_h construed similarly. The terms added should be rewritten to have the form (in the following the subscript h will be dropped to shorten notation),

$$v_i^{ir}[\boldsymbol{A}_{i,j}^{ir,ic}]u_j^{ic} \quad \text{and} \quad q^{ir}[\boldsymbol{B}^{ir,ic}]p^{ic} \tag{A.3}$$

where $\boldsymbol{A}_{i,j}^{ir,ic}$ and $\boldsymbol{B}^{ir,ic}$ correspond directly to the Jacobian $\frac{\partial R(U_h,V_h)}{\partial U_h}$ as the added terms are linear.

From the Nitsche terms introduced in Section 3.2, four cases can be highlighted as standard cases which are $\langle \boldsymbol{v}, \boldsymbol{uP} \rangle$, $\langle 2\boldsymbol{\epsilon}(\boldsymbol{v}) \cdot \boldsymbol{n}, \boldsymbol{uP} \rangle$, $\langle \boldsymbol{v}, (2\boldsymbol{\epsilon}(\boldsymbol{u}) \cdot \boldsymbol{n})\boldsymbol{P} \rangle$, $\langle 2\boldsymbol{\epsilon}(\boldsymbol{v}) \cdot \boldsymbol{n}, (2\boldsymbol{\epsilon}(\boldsymbol{u}) \cdot \boldsymbol{n})\boldsymbol{P} \rangle$. As computational efficiency is of importance, four variables have been identified which can be precomputed to reduce the number of operations

$$\begin{aligned} c(ir) &= \frac{\partial N^{ir}}{\partial x_k} n_k \\ p_1(ir,j) &= \frac{\partial N^{ir}}{\partial x_k} P_{jk} \\ p_2(ic,i) &= \frac{\partial N^{ic}}{\partial x_k} P_{ki} \\ C_{12}(ir,ic) &= \frac{\partial N^{ir}}{\partial x_l} P_{kl} \frac{\partial N^{ic}}{\partial x_k}, \end{aligned}$$

where index summation is carried out by standard Einstein notation.

The four aforementioned bilinear products are rewritten in the following in the form of (A.3),

$$\begin{aligned}\langle \boldsymbol{v}, \boldsymbol{uP} \rangle = \left\langle v_i^{ir} N^{ir}, u_k^{ic} N^{ic} P_{ki} \right\rangle = \\ v_i^{ir} [N^{ir} P_{ji} N^{ic}] u_j^{ic}\end{aligned} \tag{A.4}$$

$$\begin{aligned}\langle 2\boldsymbol{\epsilon}(\boldsymbol{v}) \cdot \boldsymbol{n}, \boldsymbol{uP} \rangle = \left\langle \left(v_k^{ir} \frac{\partial N^{ir}}{\partial x_i} + v_i^{ir} \frac{\partial N^{ir}}{\partial x_k} \right) n_k, u_j^{ic} N^{ic} P_{ji} \right\rangle = \\ \left(v_i^{ir} P_{ji} \left[\frac{\partial N^{ir}}{\partial x_k} n_k \right] + v_k^{ir} n_k \left[\frac{\partial N^{ir}}{\partial x_i} P_{ji} \right] \right) N^{ic} u_j^{ic} = \\ \text{Change of indices} = \\ v_i^{ir} \left[P_{ji} \left(\frac{\partial N^{ir}}{\partial x_k} n_k \right) N^{ic} + n_i \left(\frac{\partial N^{ir}}{\partial x_k} P_{jk} \right) N^{ic} \right] u_j^{ic} = \\ v_i^{ir} \left[N^{ic} \mathbf{c}(ir) P_{ji} + N^{ic} \mathbf{p_1}(ir, j) n_i \right] u_j^{ic}\end{aligned} \tag{A.5}$$

$$\begin{aligned}\langle \boldsymbol{v}, (2\boldsymbol{\epsilon}(\boldsymbol{u}) \cdot \boldsymbol{n}) \boldsymbol{P} \rangle = \left\langle v_i^{ir} N^{ir}, \left(u_k^{ic} \frac{\partial N^{ic}}{\partial x_j} + u_j^{ic} \frac{\partial N^{ic}}{\partial x_k} \right) n_k P_{ji} \right\rangle = \\ v_i^{ir} N^{ir} \left(u_k^{ic} n_k \left[\frac{\partial N^{ic}}{\partial x_j} P_{ji} \right] + u_j^{ic} P_{ji} \left[\frac{\partial N^{ic}}{\partial x_k} n_k \right] \right) = \\ v_i^{ir} \left[N^{ir} P_{ji} \left(\frac{\partial N^{ic}}{\partial x_k} n_k \right) + N^{ir} n_j \left(\frac{\partial N^{ic}}{\partial x_k} P_{ki} \right) \right] u_j^{ic} = \\ v_i^{ir} \left[N^{ir} \mathbf{c}(ic) P_{ji} + N^{ir} \mathbf{p_2}(ic, i) n_j \right] u_j^{ic}\end{aligned} \tag{A.6}$$

$$\begin{aligned}\langle 2\boldsymbol{\epsilon}(\boldsymbol{v}) \cdot \boldsymbol{n}, (2\boldsymbol{\epsilon}(\boldsymbol{u}) \cdot \boldsymbol{n}) \boldsymbol{P} \rangle = \left\langle \left(v_l^{ir} \frac{\partial N^{ir}}{\partial x_i} + v_i^{ir} \frac{\partial N^{ir}}{\partial x_l} \right) n_l, \left(u_k^{ic} \frac{\partial N^{ic}}{\partial x_j} + u_j^{ic} \frac{\partial N^{ic}}{\partial x_k} \right) n_k P_{ji} \right\rangle = \\ v_l^{ir} n_l \left(\frac{\partial N^{ir}}{\partial x_i} P_{ji} \frac{\partial N^{ic}}{\partial x_j} \right) u_k^{ic} n_k + v_l^{ir} n_l \frac{\partial N^{ir}}{\partial x_i} P_{ji} u_j^{ic} \left(\frac{\partial N^{ic}}{\partial x_k} n_k \right) + \\ v_i^{ir} \left(\frac{\partial N^{ir}}{\partial x_l} n_l \right) P_{ji} \frac{\partial N^{ic}}{\partial x_j} u_k^{ic} n_k + v_i^{ir} \left(\frac{\partial N^{ir}}{\partial x_l} n_l \right) P_{ji} \left(\frac{\partial N^{ic}}{\partial x_k} n_k \right) u_j^{ic} = \\ v_i^{ir} [n_i \left(\frac{\partial N^{ir}}{\partial x_l} P_{kl} \frac{\partial N^{ic}}{\partial x_k} \right) n_j + n_i \frac{\partial N^{ir}}{\partial x_l} P_{jl} \left(\frac{\partial N^{ic}}{\partial x_k} n_k \right) + \\ \left(\frac{\partial N^{ir}}{\partial x_l} n_l \right) P_{ki} \frac{\partial N^{ic}}{\partial x_k} n_j + \left(\frac{\partial N^{ir}}{\partial x_l} n_l \right) P_{ji} \left(\frac{\partial N^{ic}}{\partial x_k} n_k \right)] u_j^{ic} = \\ v_i^{ir} [n_i \mathbf{C}_{12}(ir, ic) n_j + n_i \mathbf{p_1}(ir, j) \mathbf{c}(ic) + n_j \mathbf{p_2}(ic, i) \mathbf{c}(ir) + P_{ji} \mathbf{c}(ir) \mathbf{c}(ic)] u_j^{ic}\end{aligned} \tag{A.7}$$

$$\begin{aligned}\langle q\boldsymbol{n}, \boldsymbol{uP} \rangle = \langle q n_k, u_j \mathbf{P}_{jk} \rangle = \\ q \left[\mathbf{P}_{jk} n_k \right] u_j\end{aligned} \tag{A.8}$$

As the projection matrix is symmetric it can be applied from either the left or the right of the condition, and hence $\boldsymbol{uP} = \boldsymbol{Pu}$. This covers the linearization of the added projected terms.

BIBLIOGRAPHY

[1] D. Adalsteinsson and J. A. Sethian, The fast construction of extension velocities in level set methods, *Journal of Computational Physics* **148**, 2–22, 1999.

[2] P. M. Adler and H. Brenner, Multiphase flow in porous media, *Annual Review of Fluid Mechanics* **20**, 35–59, 1988.

[3] S. Afkhami, S. Zaleski, and M. Bussmann, A mesh-dependent model for applying dynamic contact angles to VOF simulations, *Journal of Computational Physics* **228**, 5370–5389, 2009.

[4] C. Amrouche and V. Girault, On the existence and regularity of the solution of Stokes problem in arbitrary dimension, *Proceedings of the Japan Academy, Series A, Mathematical Sciences* **67**, 171–175, 1991.

[5] C. Annavarapu, M. Hautefeuille, and J. E. Dolbow, A robust Nitsche's formulation for interface problems, *Computer Methods in Applied Mechanics and Engineering* **225**, 44–54, 2012.

[6] L. Antiga, J. Peiró, and D. A. Steinman, From image data to computational domains, *Cardiovascular Mathematics*, 123–175, 2009.

[7] U. M. Ascher and L. R. Petzold, *Computer methods for ordinary differential equations and differential-algebraic equations*, Volume 61, SIAM, 1998.

[8] J. Aubin, Behavior of the error of the approximate solutions of boundary value problems for linear elliptic operators by Galerkin's and finite difference methods, *Annali della Scuola Normale Superiore di Pisa* **21**, 599–637, 1967.

[9] R. F. Ausas, F. S. Sousa, and G. C. Buscaglia, An improved finite element space for discontinuous pressures, *Computer Methods in Applied Mechanics and Engineering* **199**, 1019 – 1031, 2010.

[10] I. Babuška and U. Banerjee, Stable generalized finite element method (SGFEM), *Computer Methods in Applied Mechanics and Engineering* **201**, 91–111, 2012.

[11] I. Babuska and J. M. Melenk, The partition of unity method, *International Journal of Numerical Methods in Engineering* **40**, 727–758, 1996.

[12] I. Babuška, The theory of small changes in the domain of existence in the theory of partial differential equations and its applications, *Differential equations and their applications*, 13–26, 1963.

[13] I. Babuška, The finite element method with Lagrangian multipliers, *Numerische Mathematik* **20**, 179–192, 1973.

[14] S. Badia and F. Verdugo, Robust and scalable domain decomposition solvers for unfitted finite element methods, *Journal of Computational and Applied Mathematics*, 2017.

[15] J. Baiges, R. Codina, F. Henke, S. Shahmiri, and W. A. Wall, A symmetric method for weakly imposing Dirichlet boundary conditions in embedded finite element meshes, *International Journal for Numerical Methods in Engineering* **90**, 636–658, 2012.

[16] E. Bänsch, Finite element discretization of the Navier–Stokes equations with a free capillary surface, *Numerische Mathematik* **88**, 203–235, 2001.

[17] E. Bänsch and K. Deckelnick, Optimal error estimates for the Stokes and Navier–Stokes equations with slip–boundary condition, *ESAIM: Mathematical Modelling and Numerical Analysis* **33**, 923–938, 1999.

[18] E. Bänsch and B. Höhn, Numerical treatment of the Navier–Stokes equations with slip boundary condition, *SIAM Journal on Scientific Computing* **21**, 2144–2162, 2000.

[19] H. J. Barbosa and T. J. Hughes, The finite element method with Lagrange multipliers on the boundary: circumventing the Babuška–Brezzi condition, *Computer Methods in Applied Mechanics and Engineering* **85**, 109–128, 1991.

[20] H. J. Barbosa and T. J. Hughes, Boundary Lagrange multipliers in finite element methods: error analysis in natural norms, *Numerische Mathematik* **62**, 1–15, 1992.

[21] A. Basson and D. Gérard-Varet, Wall laws for fluid flows at a boundary with random roughness, *Communications on pure and applied mathematics* **61**, 941–987, 2008.

[22] C. Basting and D. Kuzmin, A minimization-based finite element formulation for interface-preserving level set reinitialization, *Computing* **95**, 13–25, 2013.

[23] Y. Bazilevs, C. Michler, V. Calo, and T. Hughes, Weak Dirichlet boundary conditions for wall-bounded turbulent flows, *Computer Methods in Applied Mechanics and Engineering* **196**, 4853–4862, 2007.

[24] Y. Bazilevs and T. J. Hughes, Weak imposition of Dirichlet boundary conditions in fluid mechanics, *Computers & Fluids* **36**, 12–26, 2007.

[25] G. S. Beavers and D. D. Joseph, Boundary conditions at a naturally permeable wall, *Journal of Fluid Mechanics* **30**, 197–207, 1967.

[26] É. Béchet, N. Moës, and B. Wohlmuth, A stable Lagrange multiplier space for stiff interface conditions within the extended finite element method, *International Journal for Numerical Methods in Engineering* **78**, 931–954, 2009.

[27] R. Becker, Mesh adaptation for Dirichlet flow control via Nitsche's method, *International Journal for Numerical Methods in Biomedical Engineering* **18**, 669–680, 2002.

[28] R. Becker, E. Burman, and P. Hansbo, A Nitsche extended finite element method for incompressible elasticity with discontinuous modulus of elasticity, *Computer Methods in Applied Mechanics and Engineering* **198**, 3352–3360, 2009.

[29] D. Bedeaux, A. Albano, and P. Mazur, Boundary conditions and non-equilibrium thermodynamics, *Physica A: Statistical Mechanics and its Applications* **82**, 438 – 462, 1976.

[30] M. Behr, On the application of slip boundary condition on curved boundaries, *International Journal for Numerical Methods in Fluids* **45**, 43–51, 2004.

[31] T. Belytschko and T. Black, Elastic crack growth in finite elements with minimal remeshing, *International Journal for Numerical Methods in Engineering* **45**, 601–620, 1999.

[32] T. Belytschko, N. Moës, S. Usui, and C. Parimi, Arbitrary discontinuities in finite elements, *International Journal for Numerical Methods in Engineering* **50**, 993–1013, 2001.

[33] T. Belytschko, R. Gracie, and G. Ventura, A review of extended/generalized finite element methods for material modeling, *Modelling and Simulation in Materials Science and Engineering* **17**, 043001, 2009.

[34] T. Blake and J. Haynes, Kinetics of liquid/liquid displacement, *Journal of Colloid and Interface Science* **30**, 421 – 423, 1969.

[35] A. M. P. Boelens and J. J. de Pablo, Generalised navier boundary condition for a volume of fluid approach using a finite-volume method, *Physics of Fluids* **31**, 021203, 2019.

[36] T. Boiveau and E. Burman, A penalty-free Nitsche method for the weak imposition of boundary conditions in compressible and incompressible elasticity, *IMA Journal of Numerical Analysis* **36**, 770–795, 2016.

[37] T. Boiveau, E. Burman, S. Claus, and M. G. Larson, Fictitious domain method with boundary value correction using penalty-free Nitsche method, *Journal of Numerical Mathematics*, 2017.

[38] D. Bonn, J. Eggers, J. Indekeu, J. Meunier, and E. Rolley, Wetting and spreading, *Reviews of Modern Physics* **81**, 739, 2009.

[39] R. Bonnerot and P. Jamet, Numerical computation of the free boundary for the two-dimensional Stefan problem by space-time finite elements, *Journal of Computational Physics* **25**, 163–181, 1977.

[40] M. Braack, E. Burman, V. John, and G. Lube, Stabilized finite element methods for the generalized Oseen problem, *Computer Methods in Applied Mechanics and Engineering* **196**, 853–866, 2007.

[41] J. Brackbill, D. B. Kothe, and C. Zemach, A continuum method for modeling surface tension, *Journal of Computational Physics* **100**, 335–354, 1992.

[42] J. H. Bramble, T. Dupont, and V. Thomée, Projection methods for Dirichlet's problem in approximating polygonal domains with boundary-value corrections, *Mathematics of Computation* **26**, 869–879, 1972.

[43] S. C. Brenner, Poincaré–Friedrichs inequalities for piecewise H1 functions, *SIAM Journal on Numerical Analysis* **41**, 306–324, 2003.

[44] S. C. Brenner, Korn's inequalities for piecewise H1 vector fields, *Mathematics of Computation*, 1067–1087, 2004.

[45] S. Brenner and L. Scott, *The mathematical theory of finite element methods*, Volume 15 of *Texts in Applied Mathematics*, Springer-Verlag, 3. Edition, 2008.

[46] F. Brezzi, On the existence, uniqueness and approximation of saddle-point problems arising from Lagrangian multipliers, *Revue française d'automatique, informatique, recherche opérationnelle. Analyse numérique* **8**, 129–151, 1974.

[47] F. Brezzi and M. Fortin, *Mixed and hybrid finite element methods*, Volume 15, Springer Verlag, 1991.

[48] E. Burman, Interior penalty variational multiscale method for the incompressible Navier–Stokes equation: Monitoring artificial dissipation, *Computer Methods in Applied Mechanics and Engineering* **196**, 4045–4058, 2007.

[49] E. Burman, Ghost penalty, *Comptes Rendus Mathematique* **348**, 1217–1220, 2010.

[50] E. Burman, A penalty-free nonsymmetric Nitsche-type method for the weak imposition of boundary conditions, *SIAM Journal on Numerical Analysis* **50**, 1959–1981, 2012.

[51] E. Burman, Projection stabilization of Lagrange multipliers for the imposition of constraints on interfaces and boundaries, *Numerical Methods for Partial Differential Equations* **30**, 567–592, 2014.

[52] E. Burman and A. Ern, A continuous finite element method with face penalty to approximate Friedrichs' systems, *ESAIM: Mathematical Modelling and Numerical Analysis* **41**, 55–76, 2007.

[53] E. Burman and M. A. Fernández, Continuous interior penalty finite element method for the time-dependent Navier–Stokes equations: space discretization and convergence, *Numerische Mathematik* **107**, 39–77, 2007.

[54] E. Burman and M. A. Fernández, Galerkin finite element methods with symmetric pressure stabilization for the transient Stokes equations: stability and convergence analysis, *SIAM Journal on Numerical Analysis* **47**, 409–439, 2009.

[55] E. Burman and M. A. Fernández, An unfitted Nitsche method for incompressible fluid–structure interaction using overlapping meshes, *Computer Methods in Applied Mechanics and Engineering* **279**, 497–514, 2014.

[56] E. Burman and P. Hansbo, Edge stabilization for Galerkin approximations of convection–diffusion–reaction problems, *Computer Methods in Applied Mechanics and Engineering* **193**, 1437–1453, 2004.

[57] E. Burman and P. Hansbo, Edge stabilization for the generalized Stokes problem: a continuous interior penalty method, *Computer Methods in Applied Mechanics and Engineering* **195**, 2393–2410, 2006.

[58] E. Burman and P. Hansbo, A unified stabilized method for Stokes' and Darcy's equations, *Journal of Computational and Applied Mathematics* **198**, 35–51, 2007.

[59] E. Burman and P. Hansbo, Fictitious domain finite element methods using cut elements: I. A stabilized Lagrange multiplier method, *Computer Methods in Applied Mechanics and Engineering* **199**, 2680–2686, 2010.

[60] E. Burman and P. Hansbo, Fictitious domain finite element methods using cut elements: II. A stabilized Nitsche method, *Applied Numerical Mathematics* **62**, 328–341, 2012.

[61] E. Burman and P. Hansbo, Fictitious domain methods using cut elements: III. A stabilized Nitsche method for Stokes' problem, *ESAIM: Mathematical Modelling and Numerical Analysis* **48**, 859–874, 2014.

[62] E. Burman and P. Zunino, Numerical approximation of large contrast problems with the unfitted Nitsche method, In *Frontiers in Numerical Analysis-Durham 2010*, pages 227–282, Springer, 2012.

[63] E. Burman, M. A. Fernández, and P. Hansbo, Continuous interior penalty finite element method for Oseen's equations, *SIAM Journal on Numerical Analysis* **44**, 1248–1274, 2006.

[64] E. Burman, S. Claus, P. Hansbo, M. G. Larson, and A. Massing, CutFEM: Discretizing geometry and partial differential equations, *International Journal for Numerical Methods in Engineering* **104**, 472–501, 2015.

[65] E. Burman, A. Ern, and M. A. Fernández, Fractional-step methods and finite elements with symmetric stabilization for the transient Oseen problem, *ESAIM: Mathematical Modelling and Numerical Analysis* **51**, 487–507, 2017.

[66] E. Burman, P. Hansbo, and M. G. Larson, A cut finite element method with boundary value correction, *Mathematics of Computation*, 2017.

[67] E. Burman, P. Hansbo, M. G. Larson, and A. Massing, Cut finite element methods for partial differential equations on embedded manifolds of arbitrary codimensions, *ESAIM: M2AN* **52**, 2247–2282, 2018.

[68] G. C. Buscaglia and R. F. Ausas, Variational formulations for surface tension, capillarity and wetting, *Computer Methods in Applied Mechanics and Engineering* **200**, 3011–3025, 2011.

[69] K. Cheng and T.-P. Fries, Higher-order XFEM for curved strong and weak discontinuities, *International Journal for Numerical Methods in Engineering* **82**, 564–590, 2010.

[70] J. Chessa and T. Belytschko, An enriched finite element method and level sets for axisymmetric two-phase flow with surface tension, *International Journal for Numerical Methods in Engineering* **58**, 2041–2064, 2003.

[71] J. Chessa, P. Smolinski, and T. Belytschko, The extended finite element method (XFEM) for solidification problems, *International Journal for Numerical Methods in Engineering* **53**, 1959–1977, 2002.

[72] T. Clopeau, A. Mikelić, and R. Robert, On the vanishing viscosity limit for the 2D incompressible Navier–Stokes equations with the friction type boundary conditions, *Nonlinearity* **11**, 1625, 1998.

[73] B. Cockburn and M. Solano, Solving Dirichlet boundary-value problems on curved domains by extensions from subdomains, *SIAM Journal on Scientific Computing* **34**, A497–A519, 2012.

[74] B. Cockburn and M. Solano, Solving convection-diffusion problems on curved domains by extensions from subdomains, *Journal of Scientific Computing* **59**, 512–543, 2014.

[75] B. Cockburn, D. Gupta, and F. Reitich, Boundary-conforming discontinuous Galerkin methods via extensions from subdomains, *Journal of Scientific Computing* **42**, 144, 2009.

[76] B. Cockburn, W. Qiu, and M. Solano, A priori error analysis for HDG methods using extensions from subdomains to achieve boundary conformity, *Mathematics of Computation* **83**, 665–699, 2014.

[77] R. Cox, The dynamics of the spreading of liquids on a solid surface. Part 1. Viscous flow, *Journal of Fluid Mechanics* **168**, 169–194, 1986.

[78] R. Croce, M. Griebel, and M. A. Schweitzer, Numerical simulation of bubble and droplet deformation by a level set approach with surface tension in three dimensions, *International Journal for Numerical Methods in Fluids* **62**, 963–993, 2010.

[79] C. Cuvelier, A. Segal, and A. A. Van Steenhoven, *Finite element methods and Navier–Stokes equations*, Volume 22, Springer Science & Business Media, 1986.

[80] C. D'Angelo and P. Zunino, Numerical approximation with Nitsche's coupling of transient Stokes'/Darcy's flow problems applied to hemodynamics, *Applied Numerical Mathematics* **62**, 378–395, 2012.

[81] A. A. Darhuber and S. M. Troian, Principles of microfluidic actuation by modulation of surface stresses, *Annual Review of Fluid Mechanics* **37**, 425–455, 2005.

[82] F. Dassi, S. Perotto, L. Formaggia, and P. Ruffo, Efficient geometric reconstruction of complex geological structures, *Mathematics and Computers in Simulation* **106**, 163–184, 2014.

[83] M. A. Day, The no-slip condition of fluid dynamics, *Erkenntnis* **33**, 285–296, 1990.

[84] P.-G. De Gennes, Wetting: statics and dynamics, *Reviews of Modern Physics* **57**, 827, 1985.

[85] P.-G. De Gennes, F. Brochard-Wyart, and D. Quéré, *Capillarity and wetting phenomena: drops, bubbles, pearls, waves*, Springer Science & Business Media, 2004.

[86] M. de Ruijter, J. De Coninck, and G. Oshanin, Droplet spreading: Partial wetting regime revisited, *Langmuir* **15**, 2209–2216, 1999.

[87] M. M. Denn, Issues in viscoelastic fluid mechanics, *Annual Review of Fluid Mechanics* **22**, 13–32, 1990.

[88] W. Dettmer and D. Perić, An analysis of the time integration algorithms for the finite element solutions of incompressible Navier–Stokes equations based on a stabilised formulation, *Computer Methods in Applied Mechanics and Engineering* **192**, 1177–1226, 2003.

[89] V. K. Dhir, Boiling heat transfer, *Annual Review of Fluid Mechanics* **30**, 365–401, 1998.

[90] P. Diez, R. Cottereau, and S. Zlotnik, A stable extended FEM formulation for multi-phase problems enforcing the accuracy of the fluxes through Lagrange multipliers, *International Journal for Numerical Methods in Engineering* **96**, 303–322, 2013.

[91] H. Ding, P. D. Spelt, and C. Shu, Diffuse interface model for incompressible two-phase flows with large density ratios, *Journal of Computational Physics* **226**, 2078 – 2095, 2007.

[92] F. T. Dodge, *The new "dynamic behavior of liquids in moving containers"*, Southwest Research Inst. San Antonio, Texas, 2000.

[93] J. Dolbow, N. Moës, and T. Belytschko, Discontinuous enrichment in finite elements with a partition of unity method, *Finite Elements in Analysis and Design* **36**, 235–260, 2000.

[94] J. Donea and A. Huerta, *Finite element methods for flow problems*, John Wiley & Sons, 2003.

[95] S. Dong, On imposing dynamic contact-angle boundary conditions for wall-bounded liquid–gas flows, *Computer Methods in Applied Mechanics and Engineering* **247**, 179–200, 2012.

[96] S. Dong, An efficient algorithm for incompressible n-phase flows, *Journal of Computational Physics* **276**, 691–728, 2014.

[97] J. Douglas and T. Dupont, Interior penalty procedures for elliptic and parabolic Galerkin methods, *Computing Methods in Applied Sciences*, 207–216, 1976.

[98] K. Dréau, N. Chevaugeon, and N. Moës, Studied X-FEM enrichment to handle material interfaces with higher order finite element, *Computer Methods in Applied Mechanics and Engineering* **199**, 1922 – 1936, 2010.

[99] C. A. Duarte, I. Babuška, and J. T. Oden, Generalized finite element methods for three-dimensional structural mechanics problems, *Computers & Structures* **77**, 215–232, 2000.

[100] R. Duddu, S. Bordas, D. Chopp, and B. Moran, A combined extended finite element and level set method for biofilm growth, *International Journal for Numerical Methods in Engineering* **74**, 848–870, 2008.

[101] J.-B. Dupont and D. Legendre, Numerical simulation of static and sliding drop with contact angle hysteresis, *Journal of Computational Physics* **229**, 2453–2478, 2010.

[102] T. Dupont, L2 error estimates for projection methods for parabolic equations in approximating domains, In C. d. Boor (ed.), *Mathematical Aspects of Finite Elements in Partial Differential Equations*, pages 313 – 352, Academic Press, 1974.

[103] E. B. Dussan V, On the spreading of liquids on solid surfaces: static and dynamic contact lines, *Annual Review of Fluid Mechanics* **11**, 371–400, 1979.

[104] E. B. Dussan V and S. H. Davis, On the motion of a fluid-fluid interface along a solid surface, *Journal of Fluid Mechanics* **65**, 71–95, 1974.

[105] C. D'Angelo and A. Scotti, A mixed finite element method for Darcy flow in fractured porous media with non-matching grids, *ESAIM: Mathematical Modelling and Numerical Analysis* **46**, 465–489, 2012.

[106] M. Engelman, R. Sani, and P. Gresho, The implementation of normal and/or tangential boundary conditions in finite element codes for incompressible fluid flow, *International Journal for Numerical Methods in Fluids* **2**, 225–238, 1982.

[107] D. Enright, R. Fedkiw, J. Ferziger, and I. Mitchell, A hybrid particle level set method for improved interface capturing, *Journal of Computational Physics* **183**, 83–116, 2002.

[108] A. Ern and J. L. Guermond, *Theory and Practice of Finite Elements*, Volume 159 of *Applied Mathematical Sciences*, Springer-Verlag, 2004.

[109] S. O. R. Fedkiw and S. Osher, *Level set methods and dynamic implicit surfaces*, Springer, 2002.

[110] M. A. Fernández and M. Landajuela, Unfitted mesh formulations and splitting schemes for incompressible fluid/thin-walled structure interaction, Research Report RR-8908, Inria, 2016. Submitted to ESAIM: Mathematical Modelling and Numerical Analysis.

[111] S. Fernández-Méndez and A. Huerta, Imposing essential boundary conditions in mesh-free methods, *Computer Methods in Applied Mechanics and Engineering* **193**, 1257–1275, 2004.

[112] J. H. Ferziger and M. Peric, *Computational methods for fluid dynamics*, Springer Science & Business Media, 2012.

[113] R. Finn, The contact angle in capillarity, *Physics of Fluids* **18**, 047102, 2006.

[114] R. Finn, Comments related to my paper "the contact angle in capillarity", *Physics of Fluids* **20**, 107104, 2008.

[115] C. Förster, *Robust methods for fluid-structure interaction with stabilised finite elements*, PhD thesis, University of Stuttgart, 2007.

[116] M. Fortunato and P.-O. Persson, High-order unstructured curved mesh generation using the Winslow equations, *Journal of Computational Physics* **307**, 1 – 14, 2016.

[117] L. P. Franca and S. L. Frey, Stabilized finite element methods: II. The incompressible Navier–Stokes equations, *Computer Methods in Applied Mechanics and Engineering* **99**, 209–233, 1992.

[118] T.-P. Fries, The intrinsic XFEM for two-fluid flows, *International Journal for Numerical Methods in Fluids* **60**, 437–471, 2009.

[119] T.-P. Fries and T. Belytschko, The extended/generalized finite element method: an overview of the method and its applications, *International Journal for Numerical Methods in Engineering* **84**, 253–304, 2010.

[120] G. P. Galdi and W. J. Layton, Approximation of the larger eddies in fluid motions II: A model for space-filtered flow, *Mathematical Models and Methods in Applied Sciences* **10**, 343–350, 2000.

[121] P. Gamnitzer, *Residual-based variational multiscale methods for turbulent flows and fluid-structure interaction*, PhD thesis, Technical University of Munich, 2010.

[122] S. Ganesan and L. Tobiska, Modelling and simulation of moving contact line problems with wetting effects, *Computing and Visualization in Science* **12**, 329–336, 2009.

[123] D. Gérard-Varet, M. Hillairet, and C. Wang, The influence of boundary conditions on the contact problem in a 3D Navier–Stokes flow, *Journal de Mathématiques Pures et Appliquées* **103**, 1–38, 2015.

[124] J.-F. Gerbeau and T. Lelievre, Generalized Navier boundary condition and geometric conservation law for surface tension, *Computer Methods in Applied Mechanics and Engineering* **198**, 644–656, 2009.

[125] A. Gerstenberger and W. Wall, An embedded Dirichlet formulation for 3D continua, *International Journal for Numerical Methods in Engineering* **82**, 537–563, 2010.

[126] A. Gerstenberger and W. A. Wall, An extended finite element method/Lagrange multiplier based approach for fluid–structure interaction, *Computer Methods in Applied Mechanics and Engineering* **197**, 1699–1714, 2008.

[127] V. Girault and P. A. Raviart, *Finite Element Methods for Navier–Stokes Equations*, Volume 5 of *Springer Series in Computational Mathematics*, Springer-Verlag, 1986.

[128] V. Gravemeier and W. A. Wall, An algebraic variational multiscale–multigrid method for large-eddy simulation of turbulent variable-density flow at low Mach number, *Journal of Computational Physics* **229**, 6047 – 6070, 2010.

[129] P. M. Gresho and R. L. Sani, *Incompressible flow and the finite element method. Volume 1: Advection-diffusion and isothermal laminar flow*, John Wiley and Sons, Inc., New York, NY (United States), 1998.

[130] P. Gresho and R. Sani, *Incompressible flow and the finite element method. Volume 2: Incompressible flow and finite element*, John Wiley and Sons, Inc., New York, NY (United States), 1998.

[131] S. Groß and A. Reusken, Finite element discretization error analysis of a surface tension force in two-phase incompressible flows, *SIAM Journal on Numerical Analysis* **45**, 1679–1700, 2007.

[132] S. Groß and A. Reusken, An extended pressure finite element space for two-phase incompressible flows with surface tension, *Journal of Computational Physics* **224**, 40–58, 2007.

[133] S. Groß and A. Reusken, *Numerical methods for two-phase incompressible flows*, Volume 40, Springer Science & Business Media, 2011.

[134] S. Groß, V. Reichelt, and A. Reusken, A finite element based level set method for two-phase incompressible flows, *Computing and Visualization in Science* **9**, 239–257, 2006.

[135] J. Guzmán and M. Olshanskii, Inf-sup stability of geometrically unfitted Stokes finite elements, *Mathematics of Computation* **87**, 2091–2112, 2018.

[136] A. Hansbo and P. Hansbo, An unfitted finite element method, based on Nitsche's method, for elliptic interface problems, *Computer Methods in Applied Mechanics and Engineering* **191**, 5537–5552, 2002.

[137] A. Hansbo and P. Hansbo, A finite element method for the simulation of strong and weak discontinuities in solid mechanics, *Computer Methods in Applied Mechanics and Engineering* **193**, 3523–3540, 2004.

[138] P. Hansbo, J. Hermansson, and T. Svedberg, Nitsche's method combined with space–time finite elements for ale fluid–structure interaction problems, *Computer Methods in Applied Mechanics and Engineering* **193**, 4195–4206, 2004.

[139] M. Hautefeuille, C. Annavarapu, and J. E. Dolbow, Robust imposition of Dirichlet boundary conditions on embedded surfaces, *International Journal for Numerical Methods in Engineering* **90**, 40–64, 2012.

[140] F. Heimann, *An Unfitted Higher-Order Discontinuous Galerkin Method for Incompressible Two-Phase Flow with Moving Contact Lines*, PhD thesis, Heidelberg University, 2013.

[141] M. Hematiyan, A general method for evaluation of 2D and 3D domain integrals without domain discretization and its application in BEM, *Computational Mechanics* **39**, 509–520, 2007.

[142] F. Henke, M. Winklmaier, V. Gravemeier, and W. Wall, A semi-Lagrangean time-integration approach for extended finite element methods, *International Journal for Numerical Methods in Engineering* **98**, 174–202, 2014.

[143] F. Henke, *An extended finite element method for turbulent premixed combustion*, PhD thesis, Technical University of Munich, 2013.

[144] J. S. Hesthaven and T. Warburton, *Nodal Discontinuous Galerkin Methods: Algorithms, Analysis, and Application*, Volume 54 of *Texts in Applied Mathematics*, Springer, 2008.

[145] M. Hillairet and T. Takahashi, Collisions in three-dimensional fluid structure interaction problems, *SIAM Journal on Mathematical Analysis* **40**, 2451–2477, 2009.

[146] C. W. Hirt and B. D. Nichols, Volume of fluid (VOF) method for the dynamics of free boundaries, *Journal of Computational Physics* **39**, 201–225, 1981.

[147] A. Huerta, A. Angeloski, X. Roca, and J. Peraire, Efficiency of high-order elements for continuous and discontinuous Galerkin methods, *International Journal for Numerical Methods in Engineering* **96**, 529–560, 2013.

[148] T. J. R. Hughes, G. Scovazzi, and L. P. Franca, Multiscale and Stabilized Methods, In *Encyclopedia of Computational Mechanics*, John Wiley & Sons, Chichester, 2007.

[149] T. J. Hughes, Multiscale phenomena: Green's functions, the Dirichlet-to-Neumann formulation, subgrid scale models, bubbles and the origins of stabilized methods, *Computer Methods in Applied Mechanics and Engineering* **127**, 387–401, 1995.

[150] C. Huh and S. Mason, Effects of surface roughness on wetting (theoretical), *Journal of Colloid and Interface Science* **60**, 11 – 38, 1977.

[151] C. Huh and L. Scriven, Hydrodynamic model of steady movement of a solid/liquid/fluid contact line, *Journal of Colloid and Interface Science* **35**, 85–101, 1971.

[152] J. C. R. Hunt, A. A. Wray, and P. Moin, Eddies, Stream, and Convergence Zones in Turbulent Flows, *Center For Turbulence Research* **Report CTR-S88**, 1988.

[153] S. Hysing, A new implicit surface tension implementation for interfacial flows, *International Journal for Numerical Methods in Fluids* **51**, 659–672, 2006.

[154] D. Jacqmin, Contact-line dynamics of a diffuse fluid interface, *Journal of Fluid Mechanics* **402**, 57–88, 2000.

[155] W. Jäger and A. Mikelić, On the roughness-induced effective boundary conditions for an incompressible viscous flow, *Journal of Differential Equations* **170**, 96 – 122, 2001.

[156] W. Jäger and A. Mikelić, Couette flows over a rough boundary and drag reduction, *Communications in Mathematical Physics* **232**, 429–455, 2003.

[157] P. Jamet and R. Bonnerot, Numerical solution of the Eulerian equations of compressible flow by a finite element method which follows the free boundary and the interfaces, *Journal of Computational Physics* **18**, 21–45, 1975.

[158] K. E. Jansen, S. S. Collis, C. Whiting, and F. Shaki, A better consistency for low-order stabilized finite element methods, *Computer Methods in Applied Mechanics and Engineering* **174**, 153–170, 1999.

[159] K. E. Jansen, C. H. Whiting, and G. M. Hulbert, A generalized-α method for integrating the filtered Navier–Stokes equations with a stabilized finite element method, *Computer Methods in Applied Mechanics and Engineering* **190**, 305–319, 2000.

[160] H. Ji, D. Chopp, and J. Dolbow, A hybrid extended finite element/level set method for modeling phase transformations, *International Journal for Numerical Methods in Engineering* **54**, 1209–1233, 2002.

[161] V. John, Slip with friction and penetration with resistance boundary conditions for the Navier–Stokes equations—numerical tests and aspects of the implementation, *Journal of Computational and Applied Mathematics* **147**, 287–300, 2002.

[162] V. John and A. Liakos, Time-dependent flow across a step: the slip with friction boundary condition, *International Journal for Numerical Methods in Fluids* **50**, 713–731, 2006.

[163] V. John and N. Sahin, Derivation and analysis of near wall models for channel and recirculating flows, *Computers & Mathematics with Applications* **48**, 1135–1151, 2004.

[164] V. John, G. Matthies, and J. Rang, A comparison of time-discretization/linearization approaches for the incompressible Navier–Stokes equations, *Computer Methods in Applied Mechanics and Engineering* **195**, 5995 – 6010, 2006.

[165] Y. C. Jung and B. Bhushan, Biomimetic structures for fluid drag reduction in laminar and turbulent flows, *Journal of Physics: Condensed Matter* **22**, 035104, 2010.

[166] M. Juntunen and R. Stenberg, Nitsche's method for general boundary conditions, *Mathematics of Computation* **78**, 1353–1374, 2009.

[167] G. E. Karniadakis, M. Israeli, and S. A. Orszag, High-order splitting methods for the incompressible Navier–Stokes equations, *Journal of Computational Physics* **97**, 414 – 443, 1991.

[168] E. Kirkinis and S. Davis, Hydrodynamic theory of liquid slippage on a solid substrate near a moving contact line, *Physical Review Letters* **110**, 234503, 2013.

[169] P. Knobloch, *Variational crimes in a finite element discretization of 3D Stokes equations with nonstandard boundary conditions*, Otto-von-Guericke-Univ., Graduiertenkolleg Modellierung, Berechnung und Identifikation mechanischer Systeme, 1997.

[170] J. Koplik, J. R. Banavar, and J. F. Willemsen, Molecular dynamics of Poiseuille flow and moving contact lines, *Physical Review Letters* **60**, 1282, 1988.

[171] J. Koplik, J. R. Banavar, and J. F. Willemsen, Molecular dynamics of fluid flow at solid surfaces, *Physics of Fluids A: Fluid Dynamics* **1**, 781–794, 1989.

[172] D. J. Korteweg, Sur la forme que prennent les équations du mouvement des fluides si l'on tient compte des forces capillaires causées par des variations de densité considérables mais continues et sur la théorie de la capillarité dans l'hypothese d'une variation continue de la densité, *Archives Néerlandaises des Sciences exactes et naturelles* **6**, 6, 1901.

[173] H.-O. Kreiss and J. Lorenz, *Initial-boundary value problems and the Navier–Stokes equations*, Academic Press, 1989.

[174] B. Lautrup, *Physics of continuous matter: exotic and everyday phenomena in the macroscopic world*, CRC Press, 2004.

[175] P. Lax, *Functional analysis*, Pure and applied mathematics, Wiley, 2002.

[176] C. Lee, J. Dolbow, and P. J. Mucha, A narrow-band gradient-augmented level set method for multiphase incompressible flow, *Journal of Computational Physics* **273**, 12–37, 2014.

[177] A. Legay, J. Chessa, and T. Belytschko, An Eulerian–Lagrangian method for fluid–structure interaction based on level sets, *Computer Methods in Applied Mechanics and Engineering* **195**, 2070–2087, 2006.

[178] C. Lehrenfeld, High order unfitted finite element methods on level set domains using isoparametric mappings, *Computer Methods in Applied Mechanics and Engineering* **300**, 716–733, 2016.

[179] C. Li, C. Xu, C. Gui, and M. D. Fox, Distance regularized level set evolution and its application to image segmentation, *IEEE Transactions on Image Processing* **19**, 3243–3254, 2010.

[180] A. Liakos, Discretization of the Navier–Stokes equations with slip boundary condition, *Numerical Methods for Partial Differential Equations* **17**, 26–42, 2001.

[181] S. Manservisi and R. Scardovelli, A variational approach to the contact angle dynamics of spreading droplets, *Computers & Fluids* **38**, 406–424, 2009.

[182] E. Marchandise, P. Geuzaine, N. Chevaugeon, and J.-F. Remacle, A stabilized finite element method using a discontinuous level set approach for the computation of bubble dynamics, *Journal of Computational Physics* **225**, 949–974, 2007.

[183] K. A. Mardal and R. Winther, An observation on Korn's inequality for nonconforming finite element methods, *Mathematics of Computation* **75**, 1–6, 2005.

[184] A. Massing, B. Schott, and W. Wall, A stabilized Nitsche cut finite element method for the Oseen problem, *Computer Methods in Applied Mechanics and Engineering* **328**, 262 – 300, 2018.

[185] A. Massing, M. G. Larson, A. Logg, and M. E. Rognes, A stabilized Nitsche fictitious domain method for the Stokes problem, *Journal of Scientific Computing* **61**, 604–628, 2014.

[186] A. Massing, M. Larson, A. Logg, and M. Rognes, A Nitsche-based cut finite element method for a fluid-structure interaction problem, *Communications in Applied Mathematics and Computational Science* **10**, 97–120, 2015.

[187] W. C. H. McLean, *Strongly elliptic systems and boundary integral equations*, Cambridge university press, 2000.

[188] J. M. Melenk and I. Babuška, The partition of unity finite element method: basic theory and applications, *Computer Methods in Applied Mechanics and Engineering* **139**, 289–314, 1996.

[189] R. Merle and J. Dolbow, Solving thermal and phase change problems with the extended finite element method, *Computational mechanics* **28**, 339–350, 2002.

[190] B. Merriman, J. K. Bence, and S. J. Osher, Motion of multiple junctions: A level set approach, *Journal of Computational Physics* **112**, 334–363, 1994.

[191] P. Minev, T. Chen, and K. Nandakumar, A finite element technique for multifluid incompressible flow using Eulerian grids, *Journal of Computational Physics* **187**, 255–273, 2003.

[192] N. Moës, J. Dolbow, and T. Belytschko, A finite element method for crack growth without remeshing, *International Journal for Numerical Methods in Engineering* **46**, 131–150, 1999.

[193] N. Moës, E. Béchet, and M. Tourbier, Imposing Dirichlet boundary conditions in the extended finite element method, *International Journal for Numerical Methods in Engineering* **67**, 1641–1669, 2006.

[194] H. Moffatt, Viscous and resistive eddies near a sharp corner, *Journal of Fluid Mechanics* **18**, 1–18, 1964.

[195] B. Mohammadi and O. Pironneau, *Analysis of the k–ϵ turbulence model*, Editions MASSON, 1993.

[196] A. Montlaur, S. Fernandez-Mendez, and A. Huerta, High-order implicit time integration for unsteady incompressible flows, *International Journal for Numerical Methods in Fluids* **70**, 603–626, 2012.

[197] H. M. Mourad, J. Dolbow, and I. Harari, A bubble-stabilized finite element method for Dirichlet constraints on embedded interfaces, *International Journal for Numerical Methods in Engineering* **69**, 772–793, 2007.

[198] D. Moxey, M. Green, S. Sherwin, and J. Peiró, An isoparametric approach to high-order curvilinear boundary-layer meshing, *Computer Methods in Applied Mechanics and Engineering* **283**, 636 – 650, 2015.

[199] S. Nagrath, K. E. Jansen, and R. T. Lahey, Computation of incompressible bubble dynamics with a stabilized finite element level set method, *Computer Methods in Applied Mechanics and Engineering* **194**, 4565–4587, 2005.

[200] C. Navier, Mémoire sur les lois du mouvement des fluides, *Mémoires de l'Académie Royale des Sciences de l'Institut de France* **6**, 389–440, 1823.

[201] C. Neto, D. R. Evans, E. Bonaccurso, H.-J. Butt, and V. S. Craig, Boundary slip in Newtonian liquids: a review of experimental studies, *Reports on Progress in Physics* **68**, 2859, 2005.

[202] J. Neustupa and P. Penel, A weak solvability of the Navier–Stokes equation with Navier's boundary condition around a ball striking the wall, In *Advances in Mathematical Fluid Mechanics*, pages 385–407, 2010.

[203] N. C. Nguyen, J. Peraire, and B. Cockburn, An implicit high-order hybridizable discontinuous Galkerin method for the incompressible Navier–Stokes equations, *Journal of Computational Physics* **230**, 1147–1170, 2011.

[204] J. Nitsche, Über ein Variationsprinzip zur lösung von Dirichlet-Problemen bei Verwendung von teilräumen, die keinen Randbedingungen unterworfen sind, *Abhandlungen aus dem Mathematischen Seminar der Universität Hamburg* **36**, 9–15, 1971.

[205] J. Nitsche, Ein Kriterium für die Quasi-Optimalität des Ritzschen Verfahrens, *Numerische Mathematik* **11**, 346–348, 1968.

[206] W. F. Noh and P. Woodward, Slic (simple line interface calculation), In *Proceedings of the Fifth International Conference on Numerical Methods in Fluid Dynamics June 28–July 2, 1976 Twente University, Enschede*, pages 330–340. Springer, 1976.

[207] J. Ou, B. Perot, and J. P. Rothstein, Laminar drag reduction in microchannels using ultrahydrophobic surfaces, *Physics of Fluids* **16**, 4635–4643, 2004.

[208] R. L. Panton, *Incompressible flow*, John Wiley & Sons, 2013.

[209] J. Pedlosky, *Geophysical fluid dynamics*, Springer Science & Business Media, 2013.

[210] J. Pereira, C. Duarte, D. Guoy, and X. Jiao, hp-generalized FEM and crack surface representation for non-planar 3-D cracks, *International Journal for Numerical Methods in Engineering* **77**, 601–633, 2009.

[211] J. Pitkäranta, Boundary subspaces for the finite element method with Lagrange multipliers, *Numerische Mathematik* **33**, 273–289, 1979.

[212] J. Pitkäranta, Local stability conditions for the Babuška method of Lagrange multipliers, *Mathematics of Computation* **35**, 1113–1129, 1980.

[213] E. Puckett and P. Colella, *Finite Difference Methods for Computational Fluid Dynamics*, Cambridge University Press, 2005.

[214] B. Qian, J. Park, and K. S. Breuer, Large apparent slip at a moving contact line, *Physics of Fluids* **27**, 091703, 2015.

[215] Y. H. Qian, D. D'Humières, and P. Lallemand, Lattice BGK models for Navier–Stokes equation, *EPL (Europhysics Letters)* **17**, 479, 1992.

[216] A. Quarteroni, *Numerical Models for Differential Problems*, Modeling, Simulation and Applications, Springer-Verlag, 2009.

[217] U. Rasthofer, F. Henke, W. Wall, and V. Gravemeier, An extended residual-based variational multiscale method for two-phase flow including surface tension, *Computer Methods in Applied Mechanics and Engineering* **200**, 1866 – 1876, 2011.

[218] U. Rasthofer, *Computational multiscale methods for turbulent single and two-phase flows*, PhD thesis, Technical University of Munich, 2015.

[219] M. Renardy, Y. Renardy, and J. Li, Numerical simulation of moving contact line problems using a volume-of-fluid method, *Journal of Computational Physics* **171**, 243 – 263, 2001.

[220] A. Reusken, Analysis of an extended pressure finite element space for two-phase incompressible flows, *Computing and visualization in science* **11**, 293–305, 2008.

[221] A. Reusken and T. H. Nguyen, Nitsche's method for a transport problem in two-phase incompressible flows, *Journal of Fourier Analysis and Applications* **15**, 663–683, 2009.

[222] A. Reusken, X. Xu, and L. Zhang, Finite element methods for a class of continuum models for immiscible flows with moving contact lines, *International Journal for Numerical Methods in Fluids* **84**, 268–291, 2017.

[223] O. Rodrigues, Des lois geometriques qui regissent les desplacements d'un systeme solide dans l'espace et de la variation des coordonnees provenant de deplacements consideres independamment des causes qui peuvent les produire, *Journal de Mathématiques* **5**, 380–440, 1840.

[224] E. Rothe, Zweidimensionale parabolische Randwertaufgaben als Grenzfall eindimensionaler Randwertaufgaben, *Mathematische Annalen* **102**, 650–670, 1930.

[225] E. Ruiz-Gironés, J. Sarrate, and X. Roca, Generation of curved high-order meshes with optimal quality and geometric accuracy, *Procedia Engineering* **163**, 315 – 327, 2016.

[226] P. G. Saffman, On the boundary condition at the surface of a porous medium, *Studies in Applied Mathematics* **50**, 93–101, 1971.

[227] Y. Sato and B. Ničeno, A new contact line treatment for a conservative level set method, *Journal of Computational Physics* **231**, 3887–3895, 2012.

[228] H. Sauerland and T.-P. Fries, The extended finite element method for two-phase and free-surface flows: a systematic study, *Journal of Computational Physics* **230**, 3369–3390, 2011.

[229] B. Schott and W. Wall, A new face-oriented stabilized XFEM approach for 2D and 3D incompressible Navier–Stokes equations, *Computer Methods in Applied Mechanics and Engineering* **276**, 233–265, 2014.

[230] B. Schott, U. Rasthofer, V. Gravemeier, and W. A. Wall, A face-oriented stabilized Nitsche-type extended variational multiscale method for incompressible two-phase flow, *International Journal for Numerical Methods in Engineering* **104**, 721–748, 2015.

[231] B. Schott, S. Shahmiri, R. Kruse, and W. Wall, A stabilized Nitsche-type extended embedding mesh approach for 3D low-and high-Reynolds-number flows, *International Journal for Numerical Methods in Fluids* **82**, 289–315, 2016.

[232] B. Schott, *Stabilized Cut Finite Element Methods for Complex Interface Coupled Flow Problems*, PhD thesis, Technical University of Munich, 2017.

[233] J. Serrin, Mathematical principles of classical fluid mechanics, *Handbuch der Physik* **8**, 125–263, 1959.

[234] J. A. Sethian, A fast marching level set method for monotonically advancing fronts, *Proceedings of the National Academy of Sciences* **93**, 1591–1595, 1996.

[235] J. A. Sethian, *Level set methods and fast marching methods: evolving interfaces in computational geometry, fluid mechanics, computer vision, and materials science*, Volume 3, Cambridge university press, 1999.

[236] D. Seveno, A. Vaillant, R. Rioboo, H. Adao, J. Conti, and J. De Coninck, Dynamics of wetting revisited, *Langmuir* **25**, 13034–13044, 2009.

[237] S. Shahmiri, *A Hybrid Fixed-Grid-ALE Approach for Fluid-Structure Interaction*, PhD thesis, Technical University of Munich, 2017.

[238] S. Shahmiri, A. Gerstenberger, and W. A. Wall, An XFEM-based embedding mesh technique for incompressible viscous flows, *International Journal for Numerical Methods in Fluids* **65**, 166–190, 2011.

[239] Y. D. Shikhmurzaev, Some dry facts about dynamic wetting, *The European Physical Journal Special Topics* **197**, 47, 2011.

[240] Y. D. Shikhmurzaev, *Capillary flows with forming interfaces*, CRC Press, 2008.

[241] K. A. Smith, F. J. Solis, and D. L. Chopp, A projection method for motion of triple junctions by level sets, *Interfaces and Free Boundaries* **4**, 263–276, 2002.

[242] J. H. Snoeijer and B. Andreotti, Moving contact lines: scales, regimes, and dynamical transitions, *Annual Review of Fluid Mechanics* **45**, 269–292, 2013.

[243] V. A. Solonnikov, Solvability of a three-dimensional boundary value problem with a free surface for the stationary Navier–Stokes system, *Journal of Soviet Mathematics* **21**, 427–450, 1983.

[244] A. Sommariva and M. Vianello, Product Gauss cubature over polygons based on Green's integration formula, *BIT Numerical Mathematics* **47**, 441–453, 2007.

[245] P. D. Spelt, A level-set approach for simulations of flows with multiple moving contact lines with hysteresis, *Journal of Computational Physics* **207**, 389–404, 2005.

[246] J. E. Sprittles and Y. D. Shikhmurzaev, Finite element simulation of dynamic wetting flows as an interface formation process, *Journal of Computational Physics* **233**, 34–65, 2013.

[247] E. Stein, *Singular Integrals and Differentiability Properties of Functions*, Princeton University Press, 1970.

[248] R. Stenberg, On some techniques for approximating boundary conditions in the finite element method, *Journal of Computational and Applied Mathematics* **63**, 139–148, 1995.

[249] G. Strang and G. Fix, *An analysis of the finite element method*, Wellesley Cambridge Press, 2008.

[250] T. Strouboulis, I. Babuška, and K. Copps, The design and analysis of the generalized finite element method, *Computer Methods in Applied Mechanics and Engineering* **181**, 43–69, 2000.

[251] R. W. Style, R. Boltyanskiy, Y. Che, J. Wettlaufer, L. A. Wilen, and E. R. Dufresne, Universal deformation of soft substrates near a contact line and the direct measurement of solid surface stresses, *Physical Review Letters* **110**, 066103, 2013.

[252] S. Succi, The lattice Boltzmann equation – for fluid dynamics and beyond, *Clarendon Pres*, 2001.

[253] Y. Sudhakar and W. A. Wall, Quadrature schemes for arbitrary convex/concave volumes and integration of weak form in enriched partition of unity methods, *Computer Methods in Applied Mechanics and Engineering* **258**, 39–54, 2013.

[254] Y. Sudhakar, J. M. de Almeida, and W. A. Wall, An accurate, robust, and easy-to-implement method for integration over arbitrary polyhedra: application to embedded interface methods, *Journal of Computational Physics* **273**, 393–415, 2014.

[255] Y. Sudhakar, *An embedded interface finite element method for fluid-structure-fracture interaction*, PhD thesis, Technical University of Munich, 2015.

[256] Y. Sui and P. D. Spelt, An efficient computational model for macroscale simulations of moving contact lines, *Journal of Computational Physics* **242**, 37–52, 2013.

[257] Y. Sui, H. Ding, and P. D. Spelt, Numerical simulations of flows with moving contact lines, *Annual Review of Fluid Mechanics* **46**, 97–119, 2014.

[258] N. Sukumar, N. Moës, B. Moran, and T. Belytschko, Extended finite element method for three-dimensional crack modelling, *International Journal for Numerical Methods in Engineering* **48**, 1549–1570, 2000.

[259] M. Sussman, K. M. Smith, M. Y. Hussaini, M. Ohta, and R. Zhi-Wei, A sharp interface method for incompressible two-phase flows, *Journal of Computational Physics* **221**, 469–505, 2007.

[260] C. A. Taylor, T. J. Hughes, and C. K. Zarins, Finite element modeling of blood flow in arteries, *Computer Methods in Applied Mechanics and Engineering* **158**, 155–196, 1998.

[261] R. Temam, *Navier–Stokes equations*, Volume 2, North-Holland Amsterdam, 1984.

[262] T. E. Tezduyar, M. Behr, S. Mittal, and J. Liou, A new strategy for finite element computations involving moving boundaries and interfaces—the deforming-spatial-domain/space-time procedure: II. Computation of free-surface flows, two-liquid flows, and flows with drifting cylinders, *Computer Methods in Applied Mechanics and Engineering* **94**, 353–371, 1992.

[263] T. Tezduyar, M. Behr, and J. Liou, A new strategy for finite element computations involving moving boundaries and interfaces—the deforming-spatial-domain/space-time procedure: I. The concept and the preliminary numerical tests, *Computer Methods in Applied Mechanics and Engineering* **94**, 339 – 351, 1992.

[264] P. A. Thompson and M. O. Robbins, Simulations of contact-line motion: slip and the dynamic contact angle, *Physical Review Letters* **63**, 766, 1989.

[265] T. Toulorge, J. Lambrechts, and J.-F. Remacle, Optimizing the geometrical accuracy of curvilinear meshes, *Journal of Computational Physics* **310**, 361 – 380, 2016.

[266] G. Tryggvason, R. Scardovelli, and S. Zaleski, *Direct numerical simulations of gas–liquid multiphase flows*, Cambridge University Press, 2011.

[267] J. M. Urquiza, A. Garon, and M.-I. Farinas, Weak imposition of the slip boundary condition on curved boundaries for Stokes flow, *Journal of Computational Physics* **256**, 748 – 767, 2014.

[268] F. Van der Bos and V. Gravemeier, Numerical simulation of premixed combustion using an enriched finite element method, *Journal of Computational Physics* **228**, 3605–3624, 2009.

[269] R. Verfürth, Finite element approximation of steady Navier–Stokes equations with mixed boundary conditions, *RAIRO-Modélisation mathématique et analyse numérique* **19**, 461–475, 1985.

[270] R. Verfürth. Finite element approximation of stationary Navier–Stokes equations with slip boundary condition. Habilitationsschrift, Report No. 75, Univ. Bochum, 1986.

[271] R. Verfürth, Finite element approximation of incompressible Navier–Stokes equations with slip boundary condition II, *Numerische Mathematik* **59**, 615–636, 1991.

[272] R. Verfürth, Finite element approximation on incompressible Navier–Stokes equations with slip boundary condition, *Numerische Mathematik* **50**, 697–721, 1986.

[273] C. Vergara, Nitsche's method for defective boundary value problems in incompressibile fluid-dynamics, *Journal of Scientific Computing* **46**, 100–123, 2011.

[274] H. K. Versteeg and W. Malalasekera, *An introduction to computational fluid dynamics: the finite volume method*, Pearson Education, 2007.

[275] O. V. Voinov, Hydrodynamics of wetting, *Fluid Dynamics* **11**, 714–721, 1976.

[276] G. Wagner, N. Moës, W. Liu, and T. Belytschko, The extended finite element method for rigid particles in Stokes flow, *International Journal for Numerical Methods in Engineering* **51**, 293–313, 2001.

[277] W. A. Wall, C. Ager, M. Grill, M. Kronbichler, A. Popp, B. Schott, and A. Seitz, BACI: A multiphysics simulation environment, Technical report, Institute for Computational Mechanics, Technical University of Munich, 2017.

[278] C. H. Whiting and K. E. Jansen, A stabilized finite element method for the incompressible Navier–Stokes equations using a hierarchical basis, *International Journal for Numerical Methods in Fluids* **35**, 93–116, 2001.

[279] M. Winter, B. Schott, A. Massing, and W. Wall, A Nitsche cut finite element method for the Oseen problem with general Navier boundary conditions, *Computer Methods in Applied Mechanics and Engineering* **330**, 220 – 252, 2018, https://doi.org/10.1016/j.cma.2017.10.023.

[280] A. Yarin, Drop impact dynamics: Splashing, spreading, receding, bouncing…, *Annual Review of Fluid Mechanics* **38**, 159–192, 2006.

[281] T. Young, An essay on the cohesion of fluids, *Philosophical Transactions of the Royal Society of London*, 65–87, 1805.

[282] Y.-s. Yu, Substrate elastic deformation due to vertical component of liquid-vapor interfacial tension, *Applied Mathematics and Mechanics* **33**, 1095–1114, 2012.

[283] P. Yue, C. Zhou, and J. J. Feng, Sharp-interface limit of the Cahn–Hilliard model for moving contact lines, *Journal of Fluid Mechanics* **645**, 279–294, 2010.

[284] S. Zahedi, K. Gustavsson, and G. Kreiss, A conservative level set method for contact line dynamics, *Journal of Computational Physics* **228**, 6361–6375, 2009.

[285] S. Zahedi, M. Kronbichler, and G. Kreiss, Spurious currents in finite element based level set methods for two-phase flow, *International Journal for Numerical Methods in Fluids* **69**, 1433–1456, 2012.

[286] H.-K. Zhao, T. Chan, B. Merriman, and S. Osher, A variational level set approach to multiphase motion, *Journal of Computational Physics* **127**, 179–195, 1996.

[287] O. C. Zienkiewicz and J. Z. Zhu, The superconvergent patch recovery and a posteriori error estimates. Part 2: Error estimates and adaptivity, *International Journal for Numerical Methods in Engineering* **33**, 1365–1382, 1992.

[288] O. C. Zienkiewicz and J. Z. Zhu, The superconvergent patch recovery and a posteriori error estimates. Part 1: The recovery technique, *International Journal for Numerical Methods in Engineering* **33**, 1331–1364, 1992.

[289] A. Zilian and A. Legay, The enriched space–time finite element method (EST) for simultaneous solution of fluid–structure interaction, *International Journal for Numerical Methods in Engineering* **75**, 305–334, 2008.

[290] S. Zlotnik and P. Díez, Hierarchical X-FEM for n-phase flow (n $>$ 2), *Computer Methods in Applied Mechanics and Engineering* **198**, 2329–2338, 2009.

VERZEICHNIS DER BETREUTEN STUDIENARBEITEN

Im Rahmen dieser Dissertation entstanden am Lehrstuhl für Numerische Mechanik (LNM) in den Jahren von 2014 bis 2017 unter wesentlicher wissenschaftlicher, fachlicher und inhaltlicher Anleitung des Autors die im Folgenden aufgeführten studentischen Arbeiten.

Studierende(r)	**Studienarbeit**
Tobias Bremicker	*Investigation of a Continuum Surface Force Model in the FEM for Two-Phase Flows*, Bachelorarbeit, 2015
Nils Much	*Parameter- und Modell-Validierungsstudie von schwappenden Tanks*, Bachelorarbeit, 2017
Moustafa Alsayed Ahmad	*Discretization and Implementation of Level set Equation using Hybridizable Discontinuous Galerkin Method*, Honours project, 2017